Physik

Structural Reorientation, Hybridization, and Excitonic States in Organic Molecules on Surfaces

Dissertation

Ralf Hemm

RPTU Rheinland-Pfälzische Technische Universität Kaiserslautern Landau

Structural Reorientation, Hybridization, and Excitonic States in Organic Molecules on Surfaces

Dissertation

Ralf Hemm

Vom Fachbereich Physik der Rheinland-Pfälzischen Technischen Universität Kaiserslautern-Landau zur Verleihung des akademischen Grades „Doktor der Naturwissenschaften“ genehmigte Dissertation

Betreuer: **Prof. Dr. Benjamin Stadtmüller**
Zweitgutachter: **Prof. Dr. Martin Aeschlimann**

Datum der wissenschaftlichen Aussprache:
28.07.2025

DE-386

“Life is full of surprises, but never when you need one.”

B. Watterson
The Complete Calvin and Hobbes
Andrews McMeel Publishing, 2005
ISBN: 0-7407-4847-5

Abstract

Electronic coupling and correlated electron phenomena are increasingly important for the design of next-generation electronic and optoelectronic devices, as they critically influence a system's band structure and subsequently its electronic properties, and overall device performance. π-Conjugated organic molecules on surfaces provide a versatile platform for investigating these effects due to their chemically tunable properties. In such systems, various types of electronic coupling can arise simultaneously. First, intramolecular dispersion results from π-electron delocalization within individual molecules. Second, intermolecular dispersion emerges from π-orbital overlap between adjacent molecules in multilayer films. Third, hybridization at molecule–substrate interfaces arises from wave function overlap between adsorbate and substrate, potentially altering the electronic structure significantly. Moreover, strong Coulomb interactions and reduced dielectric screening in these materials give rise to correlated electron phenomena upon optical excitation, such as the formation of bound electron–hole pairs, so-called excitons.

To contribute to the fundamental understanding of band structure design in π-conjugated molecular systems on surfaces this work investigates the coupling of electronic wave functions and correlated electronic effects in these systems. The focus is on how molecular interactions, adsorption geometry, and interfacial coupling influence energy level alignment, band dispersion, and excitonic structure. A combination of angle-resolved photoelectron spectroscopy (ARPES) in the form of momentum microscopy and photoemission orbital tomography (POT) is used to probe the momentum- and real-space distribution of electronic states. Three prototypical systems are examined, including cesium-doped PTCDA monolayers on Ag(111), monolayer C_{60} on Cu(111), and C_{60} multilayer films on Cu(111).

In the first system, cesium doping of weakly chemisorped PTCDA induces a stoichiometry-dependent reorientation of the molecular layer. The results show that energy level alignment is predominantly governed by intermolecular interactions determined by molecular orientation. For monolayer C_{60} on Cu(111), a strongly chemisorbed system, significant hybridization between molecular and substrate states leads to pronounced modifications of the band structure. Varying adsorption configurations result in different degrees of hybridization, with the most reconstructed surfaces exhibiting the strongest coupling. In the C_{60} multilayer films, the first three excitonic states were investigated, revealing clear dispersion features attributed to intramolecular interactions. A complementary variant of the exciton photoemission orbital tomography (exPOT) technique was conceptually explored, employing ultraviolet probe photon energies at tens of MHz repetition rates. This approach is limited to probing within the first surface Brillouin zone of the C_{60} films. However, it enables the acquisition of high-statistics photoemission angular distributions (PADs), thereby increasing sensitivity to delocalization effects and intermolecular interactions. Although a definitive momentum-space distinction between Frenkel and charge-transfer excitons was not observed, the method offers valuable insight into the excitonic momentum space signatures. To address complications arising from dispersive, scattered final states that obscure PADs, approximate correction and validation strategies are proposed.

Zusammenfassung

Elektronische Kopplung und korrelierte Elektronenphänomene sind für die Entwicklung elektronischer und optoelektronischer Bauelemente der nächsten Generation von zunehmender Bedeutung, da sie die Bandstruktur eines Systems und damit seine elektronischen Eigenschaften und die Gesamtleistung des Bauelements entscheidend beeinflussen. π-Konjugierte organische Moleküle auf Oberflächen bieten aufgrund ihrer chemisch abstimmbaren Eigenschaften eine vielseitige Plattform zur Untersuchung dieser Effekte. In solchen Systemen können verschiedene Arten von elektronischer Kopplung gleichzeitig auftreten. Erstens resultiert die intramolekulare Dispersion aus der Delokalisierung von π-Elektronen in einzelnen Molekülen. Zweitens ergibt sich die intermolekulare Dispersion aus dem Überlapp von π-Orbitalen zwischen benachbarten Molekülen in Multilagenfilmen. Drittens entsteht die Hybridisierung an den Molekül-Substrat-Grenzflächen durch die Überlappung der Wellenfunktionen von Adsorbat und Substrat, wodurch sich die elektronische Struktur erheblich verändern kann. Darüber hinaus führen starke Coulomb-Wechselwirkungen und reduzierte dielektrische Abschirmung in diesen Materialien bei optischer Anregung zu korrelierten Elektronenphänomenen, wie der Bildung von gebundenen Elektron-Loch-Paaren, so genannten Exzitonen.

Als Beitrag zum grundlegenden Verständnis der Bandstrukturgestaltung in π-konjugierten molekularen Systemen auf Oberflächen wird in dieser Arbeit die Kopplung von elektronischen Wellenfunktionen und korrelierten elektronischen Effekten in diesen Systemen untersucht. Der Schwerpunkt liegt darauf, wie molekulare Wechselwirkungen, Adsorptionsgeometrie und Grenzflächenkopplung die Lage der Energieniveaus, Banddispersion und exzitonische Struktur beeinflussen. Eine Kombination aus winkelaufgelöster Photoelektronenspektroskopie (ARPES) in Form von Impulsmikroskopie und Photoemissionsorbitalmographie (POT) wird verwendet, um die Impuls- und Realraumverteilung der elektronischen Zustände zu untersuchen. Es werden drei prototypische Systeme untersucht, darunter Cäsium-dotierte PTCDA-Monolagen auf Ag(111), C_{60}-Monolagen auf Cu(111) und C_{60}-Multilagenfilme auf Cu(111).

Im ersten System führt die Cäsiumdotierung von schwach chemisorbiertem PTCDA zu einer von der Stöchiometrie abhängigen Neuausrichtung der Molekülschicht. Die Ergebnisse zeigen, dass die Lage der Energieniveaus überwiegend durch intermolekulare Wechselwirkungen bestimmt wird, die durch die molekulare Orientierung bedingt sind. Bei der Monolage C_{60} auf Cu(111), einem stark chemisorbierten System, führt eine signifikante Hybridisierung zwischen Molekül- und Substratzuständen zu ausgeprägten Veränderungen der Bandstruktur. Unterschiedliche Adsorptionskonfigurationen führen zu verschiedenen Graden der Hybridisierung, wobei die am stärksten rekonstruierte Oberfläche die stärkste Kopplung aufweist. In den C_{60}-Multilagenfilmen wurden die ersten drei exzitonischen Zustände untersucht, wobei sich deutliche Dispersionsmerkmale zeigten, die auf intramolekulare Wechselwirkungen zurückzuführen sind. Eine ergänzende Variante der Exzitonen-Photoemissionsorbitaltomographie (exPOT) wurde konzeptionell erforscht, bei der Abfragepulse mit ultravioletten Photonenenergien und Repititionsraten von einigen zehn MHz verwendet werden. Dieser Ansatz ist auf die Untersuchung innerhalb der ersten Brillouin-Zone der C_{60}-Filme beschränkt. Er ermöglicht jedoch die Erfassung von Photoemissionswinkelverteilungen (PADs) mit hoher

Statistik und erhöht damit die Empfindlichkeit gegenüber Delokalisierungseffekten und intermolekularen Wechselwirkungen. Obwohl eine definitive Impulsraum-Unterscheidung zwischen Frenkel- und Ladungstransferexzitonen nicht beobachtet werden konnte, bietet die Methode wertvolle Einblicke in die Impulsraumsignaturen der Exzitonen. Um Komplikationen zu begegnen, die sich aus dispersiven, gestreuten Endzuständen ergeben, die die PADs überlagern, werden Korrektur- und Validierungsstrategien vorgeschlagen.

Contents

1 Introduction

Designing the next generation of electronic and optoelectronic devices requires precise control over the electronic structure of materials. As device architectures continue to shrink and low-dimensional or molecular materials become more prevalent, a deeper understanding of the fundamental interactions governing electronic behavior becomes essential. Effects such as geometric structure variations, many-body interactions, and orbital hybridization are playing an increasingly significant role in shaping the electronic properties of materials. Electronic coupling and correlated electron phenomena are central to these developments. These phenomena are key aspects of current surface and material science research and are also growing in technological importance [1–4]. These interactions significantly influence the behavior of materials at the electronic level, yet many aspects remain unexplored [5–7]. Therefore, gaining a clearer understanding of these phenomena at a fundamental level is critical for continued progress in the field.

The band structure is a fundamental property that governs the behavior and interactions of a material's electronic system and directly manifests electronic coupling and correlated phenomena. It encodes the energy and symmetry of electronic states, as well as their degree of delocalization, dispersion, and many-body character. Changes in these properties differently affect and shape the band structure. In crystalline solids, coupling between the wave functions of neighboring electrons leads to extended Bloch states. These delocalized states result in well-defined, dispersive energy bands, in which the electron energy varies with momentum. This dispersion reflects the coherent overlap of wave functions across the lattice. Conversely, when electrons are more localized due to structural confinement, disorder, or weak inter-site coupling, their wave functions overlap less. Depending on the degree of localization, this can lead to flatter, less dispersive bands or even discrete energy levels. Narrow bandwidths are a typical signature of localization and are often accompanied by enhanced sensitivity to electron-electron interactions.

The balance between localization and delocalization directly impacts Coulomb interactions. In delocalized systems, electron-electron repulsion is reduced by the spatial spread of electronic wave functions and efficient dielectric screening. In systems with strong localization, such as molecular crystals or organic semiconductors, screening is poor and Coulomb interactions become significant. These strong many-body interactions can reshape the band structure itself, leading to a breakdown of conventional band theory, as evidenced by phenomena such as band renormalization. In the excited-state regime, reduced screening and strong Coulomb attraction between electrons and holes result in the formation of excitons rather than single electronic excitations. Excitons are collective electronic excitations in which an excited electron leaves behind a positively charged vacancy, called a hole, that cannot be completely screened. The hole then interacts with the excited electron, forming a bound electron-hole pair called an exciton. In inorganic semiconductors, which exhibit stronger electronic screening and larger dispersion for electrons and holes, excitons have weak binding energies compared to the total electronic interactions [8, 9]. However, in 2D materials (e.g., transition metal dichalcogenides) and especially in organic molecular crystals, screening is reduced and localization is enhanced, resulting in strongly bound excitons with complex internal structure [10–13].

The formation of a molecule from single atoms serves as a precursor example for the formation of band-like states. The properties of (de-)localization, Coulomb interactions, and electronic coupling can be manipulated through material design in these systems. In two-dimensional conjugated molecular systems, the π-orbital system is delocalized above and below the molecular plane. When these molecules are assembled into ordered multilayer films or molecular crystals, their electronic structure evolves through intermolecular coupling. The π-orbitals of adjacent molecules overlap, creating dispersive electronic bands [14–16]. This process, referred to as intermolecular dispersion, gives rise to band formation in otherwise discrete systems, thus enhancing charge transport. It is directionally dependent and primarily occurs along the stacking direction, which is perpendicular to the molecular plane, where π-orbital overlap is significant. In contrast, along the plane of the molecule, i.e., perpendicular to the π-orbitals, there is minimal wave function overlap, and thus no significant dispersion occurs in that direction. This anisotropic behavior underscores the significance of molecular orientation in defining the dimensionality and character of band formation in molecular materials.
The delocalized π-electron system of conjugated molecules can exhibit intramolecular dispersion, a variation of orbital energies with momentum [15]. This dispersion is discrete because the molecules are of finite size. Infinitely extended molecules would exhibit smooth band dispersion. Thus, conjugated molecules are well suited to study electron coupling effects in a confined system due to their limited size.
The bands in molecular crystals can resemble those in atomic solids in specific cases [17]. However, the bandwidths are typically much smaller, resulting in mostly flat bands that are generally sensitive to molecular orientation and packing density. Nonetheless, highly dispersive valence states have been observed in 3D molecular systems such as rubrene [18–20] and C_{60} [21–23], but the band oscillation is confined to an energy region in the order of 500 meV.
In addition to intramolecular and intermolecular interactions, the molecule-substrate interface of molecular thin films on surfaces adds another layer of complexity due to possible coupling of molecular and substrate electron wave functions [24–26]. This can even lead to the formation of new hybridized states as a result of electron wave function overlap [27, 28]. Such interface effects can reshape the entire band structure of the system. The adsorption geometry, depending on factors such as molecular orientation, bond distance, and registry with the substrate lattice, is a dominant factor that affects the strength and character of the interface [29–31].
An investigative approach to intra- and intermolecular interactions, hybridization and excitonic states is possible with angle-resolved photoelectron spectroscopy (ARPES) from the experimental side and photoemission orbital tomography (POT) from the theoretical side [15, 27, 32–35]. The techniques provide direct insight into the electronic structure of molecular systems from different directions. ARPES allows a mapping of the electronic band structure including all hybridization signatures and correlated electronic effects. POT facilitates the theoretical calculation of orbital-resolved angular distributions of photoelectrons, enabling a direct assignment of molecular orbitals and energy levels to signatures in the ARPES experiments. Furthermore, since POT is based on density functional theory (DFT) calculations, it provides information about the expansion of the electronic wave functions in real space. The combination of both techniques provides a unique access to momentum and real space distribution of the electron wave functions and allows a comprehensive analysis of electronic structure, interactions and wave function distributions of molecular systems.

The goal of this work is to contribute to the understanding of the coupling of electronic wave functions and correlated electronic effects in organic molecular systems on surfaces. Therefore, the above mentioned combination of ARPES and POT will be used in the study of π-conjugated organic molecules, accessing the band structure and real space distributions

of the electronic wave functions. Of particular interest is the influence of the substrate and the adsorption geometry on the dispersion and energy level alignment of the molecular layers. The study of the excitonic states in organic multilayer films focuses on excitonic dispersion and aims to determine the excitonic character based on signatures observed in the band structure. Furthermore, the use of ultraviolet photon energies within the (exciton) photoemission orbital tomography framework is conceptually tested.

This thesis is divided into three main parts. After an introduction to the fundamental physics of the experimental techniques employed, the first main part in Chapter 3 presents a study of cesium-doped 3,4,9,10-Perylenetetracarboxilic Dianhydride (PTCDA) monolayers on Ag(111). The interaction of PTCDA with the Ag(111) surface is rather weak, resulting in weak chemisorptive bonding and negligible hybridization. The cesium doping induces a stoichiometry-dependent reorientation of the molecules. The aim of this chapter is to quantify the structural geometric changes and investigate the influence of the different molecular orientations and the resulting different intermolecular and molecule-substrate interactions on the energy level alignment.
The next main part in Chapter 4 discusses the sample system of a C_{60} monolayer on the Cu(111) surface. In contrast to the weakly hybridized PTCDA/Ag(111), C_{60}/Cu(111) shows considerable hybridization. The formation of an interface state as a result of this strong hybridization is discussed. This chapter also focuses on different adsorption geometries of the C_{60} molecules accompanied by different changes in the band structure and aims at a qualitative understanding of considerably hybridized molecule-metal interfaces.
The last main part in Chapter 5 is an investigation of the excitonic landscape in C_{60} multilayer films. The aim of this chapter is to observe a dispersion of the excitonic states and to determine the excitonic character (Frenkel versus charge transfer) based on momentum space signatures. In addition, the use of ultraviolet photon energies, which provide an easy access with good statistics to the first surface Brillouin zone, is tested conceptually in the framework of (exciton) photoemission orbital tomography.

2 Theoretical Background and Experimental Techniques

In the course of this work, the structural and electronic properties of organic semiconductor films on metal surfaces were investigated. This chapter delineates the experimental techniques and theoretical frameworks that were employed, offering a comprehensive introduction to the fundamental physics underpinning the research. The most salient aspects necessary for comprehending the measurement principle, the obtained data, or the theoretical approach will be elucidated. Supplemental explanations of the theoretical background will be provided subsequently, when appropriate. For any additional information, the relevant specialized literature is referenced.

2.1. Low Energy Electron Diffraction

Low energy electron diffraction (LEED) is a prevalent experimental technique employed to investigate the crystallographic structure and quality of surfaces. In this process, an electron beam with a typical kinetic energy of 20 to 500 eV is directed onto a sample close to normal incidence and elastically backscattered at the periodic lattice of the surface. The scattered electrons are subsequently visualized on a fluorescence screen forming diffraction spots [36]. A schematic drawing of a LEED setup is shown in Figure 2.1.

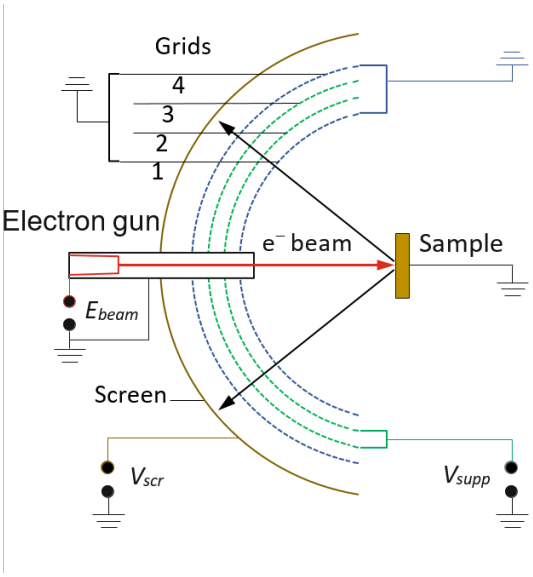

Figure (2.1) Schematic drawing of a LEED setup. A low-energy electron beam is emitted from an electron gun towards the sample. The electrons are elastically backscattered from the lattice potential of the sample surface, and the resulting diffraction pattern is imaged on a fluorescence screen. The retarding grids function as electrostatic lenses for an improved imaging of the diffraction pattern. Modified with permission from Lu Lyu [37].

The origin of the spot formation is the interference of elastically scattered electron waves. The LEED pattern is defined by this interference, representing the reciprocal lattice and providing information on the periodicity of the structure in real space.
Therefore, a vice versa determination of the lattice structure based on a LEED image is possible. Considering a perfect two-dimensional (2D) lattice the condition for constructive interference and the formation of a diffraction spot is given by the Laue equation. Its 2D analog is given by the following equation

$$\mathbf{K}_{||} = \mathbf{k}'_{||} - \mathbf{k}_{||} = \mathbf{G}_{||}. \tag{2.1}$$

In the equation, $\mathbf{K}_{||}$ is referred to as the "scattering vector component parallel to the surface" and it is expressed as the difference between the parallel moment of the incident electron ($\mathbf{k}_{||}$) and scattered electron ($\mathbf{k}'_{||}$). The 2D Laue equation posits that the scattering vector must be equal to a reciprocal lattice vector $\mathbf{G}_{||}$ of the 2D surface lattice [36].

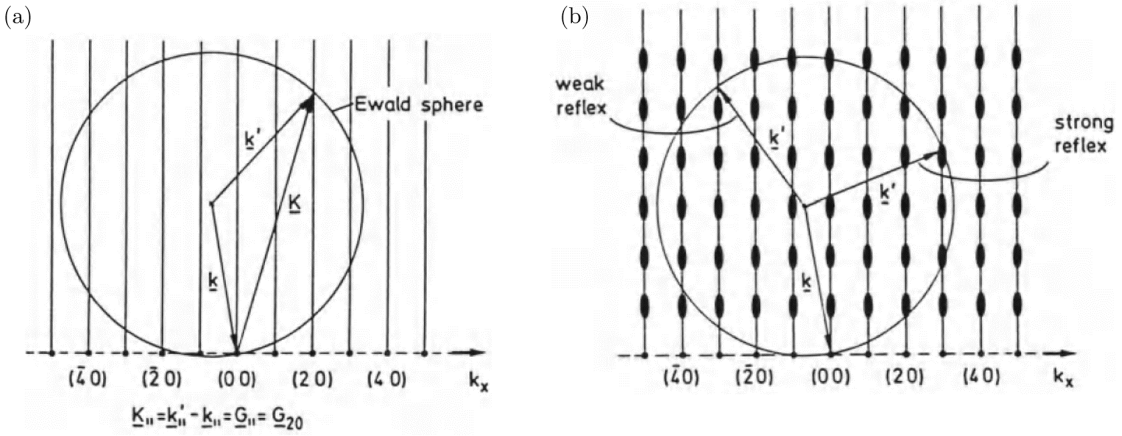

Figure (2.2) Ewald constructions in LEED. (a) Scattering on a perfect two-dimensional surface lattice. (b) Scattering on a quasi-two-dimensional surface lattice. Broader regions of the reciprocal rods represent higher intensity originating from the Laue condition perpendicular to the surface which cannot be neglected anymore. Taken with permission from [36]. Copyright © 2015 Springer-Verlag Berlin Heidelberg.

The construction of the diffraction pattern for a two-dimensional layer is analogous to that in three dimensions, with an Ewald sphere as depicted in Figure 2.2 (a). In the two-dimensional case, the reciprocal lattice spots in the direction perpendicular to the surface are extended into rods, thereby relaxing the third Laue condition in this direction [36]. To obtain all possible momentum vectors of the scattered electron beam ($\mathbf{k}'$), the wave vector of the incident beam ($\mathbf{k}$) is placed at the (0,0) order of the reciprocal lattice. A sphere with radius $|\mathbf{K}| = |\mathbf{k}' - \mathbf{k}|$ around this center is then constructed, called an Ewald sphere. Each intersection of the Ewald sphere with a reciprocal lattice rod fulfills the 2D Laue condition in Equation 2.1 and determines the position of a diffraction spot. It is imperative to note that the validity of this procedure is contingent upon the assumption of a purely two-dimensional periodic lattice. In the case of thicker films, the electrons penetrate a few layers deep into the solid, a phenomenon determined by their mean free path [38]. Consequently, the Laue condition perpendicular to the surface becomes imperative, resulting in an oscillating intensity along the reciprocal lattice rods, as illustrated in Figure 2.2 (b). Varying the kinetic energy of the incident electrons, and thus changing the magnitude of $\mathbf{k}$, causes the Ewald sphere to change size accordingly. Consequently, the Ewald sphere traverses through distinct intensity regions of the reciprocal lattice rod, thereby inducing a variation in the intensity

of a selected diffraction spot. In the limit of the bulk crystal, the region of higher intensity condenses onto the diffraction spots of the three-dimensional (3D) lattice.
The surface sensitivity of LEED is derived from the mean free path of the electrons in the specified energy interval, which is approximately equal to a few Ångstroems [38]. For the majority of materials, only electrons scattered on the initial layers can contribute to the signal. Consequently, LEED is regarded as an optimal technique for examining the crystallographic structure, purity, and ordering of surfaces and adsorbate layers [39].
In the course of this work, a multi-channel plate (MCP) LEED by Scienta Omicron was utilized, which has a planar fluorescence screen compared to the hemispherical one depicted in the schematic drawing in Figure 2.1. This results in a distortion of the diffraction pattern in the acquired images. This distortion was corrected for the determination of adsorption geometries in Chapter 3.
The LEED system was connected to an ultra-high vacuum chamber with a pressure lower than $2 \cdot 10^{-9}$ mbar. This ensured a sufficient mean free path of the electrons to reach the screen and prevented the sample surfaces from contamination.

2.2. Introduction to Photoelectron Spectroscopy

Photoelectron spectroscopy is a powerful technique for investigating the electronic structure of solid surfaces and interfaces. It is the primary experimental technique employed in this work. This section first discusses the physical foundations of photoemission spectroscopy (PES) and then describes the technical implementations used.
The fundamental process of PES is based on the photoelectric effect, which was discovered by Hertz [40] and Hallwachs [41] and describe by Einstein [42]. The process states that the absorption of a photon by a solid can result in the emission of an electron, provided that the photon possesses sufficient energy. Since its initial discovery and subsequent theoretical elucidation, PES has emerged as a standard technique for investigating the electronic structures of solids. The subsequent discussion will commence with a thorough exposition of the fundamental principle underlying PES, namely the photoemission process itself. Subsequently, the correlation between the emission angle of the photoelectron and its momentum will be elucidated, thereby giving rise to the technique of angle-resolved photoelectron spectroscopy (ARPES), which enables the measurement of band structures of solids. The technical implementation of an ARPES experiment as momentum microscopy will be explained. Ultimately, the theoretical framework of photoemission orbital tomography (POT) that enables an interpretation of ARPES data will be presented.

2.2.1. The Photoemission Process

In the photoemission process, an electron is excited from an initial state (Ψ_i) to a final state (Ψ_f) upon the absorption of a photon of energy $h\nu$. This process is treated as instantaneous, with the remaining *N-1*-electron system not interacting with the outgoing photoelectron. This assumption is called the sudden approximation [43]. The photoemission process can be described by Fermi's golden rule, with ω representing the transition probability between the initial and final states and the operator $\hat{\Delta}$ in the transition matrix element describing the coupling of the photon to be absorbed with the electron system under the assumption of a small perturbation.

$$\omega \propto \frac{2\pi}{\hbar} |\langle \Psi_f | \hat{\Delta} | \Psi_i \rangle|^2 \delta(E_f - E_i - h\nu) \tag{2.2}$$

The δ function is instrumental in ensuring the conservation of energy.
It is imperative to acknowledge that both Ψ_i and Ψ_f represent states of a N-electron system, thereby signifying that the final state includes the remaining electron system, in addition to the outgoing photoelectron.

The operator $\hat{\Delta}$ encompasses the electron momentum $\mathbf{p}$ and the vector potential $\mathbf{A}$. Within the dipole approximation [44], spatial variations in the vector potential $\mathbf{A}$ are disregarded. This approximation is applicable under the condition that the wavelength of the absorbed photon is considerably larger than the electron's orbital radius, a requirement that is met in all experiments within this body of work. Employing the Coulomb gauge and further neglecting transitions involving the simultaneous absorption of multiple photons, the operator $\hat{\Delta}$ can be expressed as

$$\hat{\Delta} = \frac{e}{mc}\mathbf{Ap} \tag{2.3}$$

In order to perform a more extensive evaluation of the transition matrix element, it is necessary to undertake a more thorough examination of the electron wave functions. In a simplified representation, the wave functions of the N-electron system can be considered as the result of the product of the wave function of the photoexcited electron and the wave function of the remaining $N-1$ electron system [44].

$$\Psi_i = C\phi_{i,k}\Psi_i^k(N-1) \tag{2.4}$$

$$\Psi_f = C\phi_{f,k}\Psi_f^k(N-1) \tag{2.5}$$

It can thus be concluded $\phi_{i,k}$ and $\phi_{f,k}$ are the initial and final state wave functions of the photoexcited electron with quantum number k and $\Psi_i^k(N-1)$ and $\Psi_f^k(N-1)$ are the corresponding wave functions of the remaining $N-1$ electrons. The operator C ensures the correct antisymmetry of the wave function. The transition matrix element in Equation 2.2 can be expressed using the above wave function products of initial and final states and the expression for the $\hat{\Delta}$ operator in Equation 2.3 as follows:

$$\langle\Psi_f|\mathbf{Ap}|\Psi_i\rangle = \langle\phi_{f,k}|\mathbf{Ap}|\phi_{i,k}\rangle\,\langle\Psi_f^k(N-1)|\Psi_i^k(N-1)\rangle \tag{2.6}$$

The matrix element of the N-electron system simplifies to a matrix element with only one electron multiplied by an overlap integral of the initial and final states of the remaining $N-1$ electron system.

In the frozen orbital approximation it is assumed that the orbitals of the electrons not involved in the photoelectron transition are unperturbed, i.e. $\Psi_i(N-1) = \Psi_f(N-1)$ and only the one-electron matrix element prevails in Equation 2.6. This leads to the simplified expression for the transition probability:

$$\omega \propto \frac{2\pi}{\hbar}|\,\langle\phi_{f,k}|\mathbf{Ap}|\phi_{i,k}\rangle\,|^2\delta(E_f - E_i - h\nu) \tag{2.7}$$

The frozen orbital approximation is a rather crude approximation because the $N-1$ electron system will attempt to screen the photohole, leading to a relaxation to a more energetically favourable state. The organic materials used in this work are highly polarisable and can therefore sufficiently screen the hole generated in the photoemission process. A discrepancy between experiment and employed theory within the frozen orbital approximation may then lie in the energetic positions and broadening of the molecular orbitals [45, 46].

After simplifying the transition matrix element and the wave functions, the conservation of energy should be revisited to ascertain how the expression inside the δ-function in Equation 2.2 is simplified, given the steps taken above. Applying the separation of wave functions into the wave function of the electron undergoing the phototransition and the wave function of the remaining electron system, a similar apportionment can be made regarding the energy. The energy of the final state, E_f, is thus separated into the kinetic energy of the photoelectron outside of the solid, $E_{\mathrm{kin,o}}$, and the energy of the abiding $N-1$ electron system, $E_f(N-1)$. Subsequent rearrangement of the equation for the kinetic energy using the frozen orbital approximation ($E_i(N-1) = E_f(N-1)$ since $\Psi_i(N-1) = \Psi_f(N-1)$) results in the

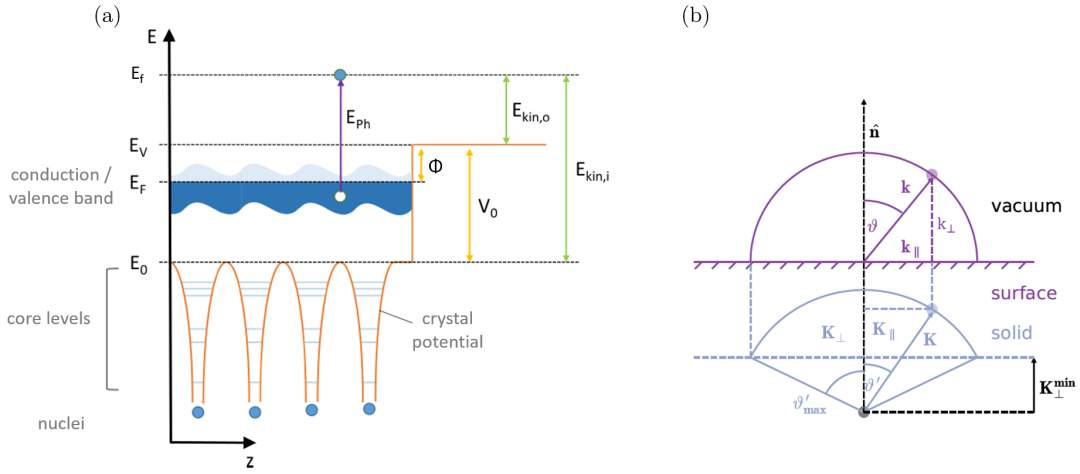

Figure (2.3) Schematic drawing of the energy (left) and momentum relations (right) during the photoemission process. Left image modified with permission from [47]. Right image adopted with small changes from [48], original from [44]. Copyright © 2003 Springer-Verlag Berlin Heidelberg.

following expression:

$$E_{\text{kin,o}} = h\nu - (E_f(N-1) - E_i(N)) = h\nu - (E_i(N-1) - E_i(N)) = h\nu - E_{\text{B}} - \Phi \quad (2.8)$$

As illustrated in Figure 2.3 (a), the energetic relations of the aforementioned expression are represented. The excited photoelectron can leave the solid if the photon energy $E_{\text{Ph}} = h\nu$ exceeds the sum of the electron binding energy E_{B} (the energetic distance between the electron's inital energy level and the Fermi energy E_{F}) and the material's work function Φ. The excess energy is transferred to the photoelectron in the form of kinetic energy ($E_{\text{kin,o}}$). Consequently, the energy level alignment of a system can be determined by analysing the kinetic energy of photoelectrons emitted from it.
During the photoemission process, electrons can inelastically scatter, thereby losing some of their kinetic energy, yet still manage to leave the solid. Consequently, the electrons cease to contribute to the primary photoemission signal, instead forming a broad and continuous background, designated as the secondary electron background.
The defining properties of the electronic states of a material are not only their energetic positions, but also the relation between energy and momentum, i.e. the band structure, $E(\mathbf{k})$, of the system. This can be determined through a photoemission experiment, as will be elucidated in the following section.

2.2.2. Angel-Resolved Photelectron Spectroscopy

The measurement of the band structure of a material system is pivotal in determining its complete set of electronic properties. In order to achieve this with a photoemission experiment, it is necessary to record the emission angles of the outgoing photoelectrons, as these are connected to the electronic momentum parallel to the surface. The corresponding experimental technique is then termed angle-resolved photoelectron spectroscopy (ARPES). It is important to note that a straightforward measurement of the electronic momentum perpendicular to the surface inside the sample is challenging, as this changes when the electron traverses the surface [44]. This phenomenon will be further delineated in the ensuing section.
To elaborate further on the momentum relations of the photoemission process, the reader is directed to Figure 2.3 (b), in which the electron momentum inside the solid is designated as $\mathbf{K}$ and outside as $\mathbf{k}$. In the process of photoexcitation, electrons travel from the bulk to

the surface, where they are distributed along a cone (see the grey cone segment in Figure 2.3 (b)). The Schrödinger equation is utilised to describe their propagation in a periodic potential, yielding the solution

$$E_f = E_{\text{kin,i}} - |E_0| = \frac{\hbar^2|\mathbf{K}|^2}{2m^*} - |E_0|, \tag{2.9}$$

where E_f is the energy of the final state, E_0 denotes the energetic start of the potential Coulomb wells of the nuclei, i.e. the start of the free electron parabola, and m^* is the effective electron mass. All energies are determined with respect to the Fermi level. In the case of large photon energies, electrons are excited at a considerable distance from the periodic Coulomb potentials of the nuclei. Outside the solid, the potential changes to zero, thereby resulting in the energy relation of a free electron:

$$E_{\text{kin,o}} = \frac{\hbar^2|\mathbf{k}|^2}{2m_e}. \tag{2.10}$$

The alteration in potential between the interior and exterior of the solid results in disparate kinetic energies. A direct comparison of Equations 2.9 and 2.10 reveals that the change in energy is directly associated with a change in momentum. Consequently, the potential step at the surface induces a change in the momentum of the photoelectron perpendicular to the surface, analogous to Snell's law of refraction [44].
From an alternative perspective, the Noether theorem can be contested on the grounds that the momentum parallel to the surface must be conserved up to multiples of the reciprocal surface lattice vector, $\mathbf{G}_{||}$, as a consequence of the discrete translation symmetry of the crystal surface [49].

$$\mathbf{K}_{||} = \mathbf{k}_{||} + \mathbf{G}_{||} \tag{2.11}$$

Subsequently, due to the symmetry breaking in the direction perpendicular to the surface, the momentum of the photoelectron must change along that direction. This can also be seen in Figure 2.3 (b), where $K_{||} = k_{||}$, but $K_\perp > k_\perp$. It is possible to derive a key relationship that is fundamental to the ARPES technique between the escape angle of the photoelectron and its parallel momentum,

$$K_{||} = k_{||} = \sqrt{\frac{2m_e}{\hbar^2}E_{\text{kin,o}}}\, sin(\theta). \tag{2.12}$$

Splitting the photoelectron momentum in Equation 2.9 in a component parallel and a component perpendicular to the surface and utilizing the expression of the final state energy $E_f = E_{\text{kin,o}} + \Phi$

$$E_f + |E_0| = E_{\text{kin,o}} + \Phi + |E_0| = \frac{\hbar^2}{2m^*}[K_{||}^2 + K_\perp^2] \tag{2.13}$$

an expression for the momentum component in the solid perpendicular to the surface can be obatined:

$$\begin{aligned} K_\perp &= \sqrt{\frac{2m^*}{\hbar^2}(E_{\text{kin,o}} + \Phi + |E_0|) - K_{||}^2)} \\ &= \sqrt{\frac{2m^*}{\hbar^2}(E_{\text{kin,o}} + V_0) - \frac{2m_e}{\hbar^2}E_{\text{kin,o}}sin^2(\theta)} \end{aligned} \tag{2.14}$$

The term $V_0 = \phi + |E_0|$, denoted as the inner potential, is a measure of the positive attraction exerted by the nuclei on the valence electrons. As the inner potential is a material property that is not easily accessible, measuring the full band structure $E(\mathbf{K})$ of a sample system is challenging. Consequently, one usually only measures $E(\mathbf{k}_{||})$. It is possible to make an

experimental determination of $K_\perp$ (and thus V_0) by continuously changing the wavelengths of the incident photons [50].
From Equation 2.14 it is feasible to deduce an escape condition

$$K_{\perp,\min} = \sqrt{\frac{2m^*}{\hbar^2}V_0} \tag{2.15}$$

signifying that the photoelectron must possess a minimum of perpendicular momentum to the surface, $K_{\perp,\min}$, in order to escape the solid. This expression for the minimal momentum perpendicular to the surface helps to connect the perpendicular momenta inside ($K_\perp$) and outside of the solid ($k_\perp$).

$$k_\perp = K_\perp - K_{\perp,\min} = K_\perp - \sqrt{\frac{2m^*}{\hbar^2}V_0} \tag{2.16}$$

Equation 2.16 demonstrates that the inner potential V_0 is responsible for the reduction of the momentum perpendicular to the surface when the photoelectron leaves the solid. Additionally, the disparity between the perpendicular momentum inside $K_\perp$ and outside $k_\perp$ of the solid result in different curvatures of the photoemission horizon (compare circular segments in Figure 2.3 (b)).
Before concluding the fundamental momentum relations in an ARPES experiment and providing an outline of the used experimental setup, three points must be noted: Firstly, due to the change in the perpendicular momentum component the photoelectrons inside and outside of the solid are distributed on sphere segments with different radii (compare Figure 2.3 (b)). In detail, the sphere segment inside of the solid has a larger radius because of the issue of the inner potential. This is a crucial consideration in any theoretical simulation of the photoemission angular distribution (PAD).
Secondly, the scheme employed in the aforementioned outline of the momentum relations is the three-step model of photoemission [44]. In this model, the photoemission process is divided into three stages: optical excitation of the electron, transport towards the surface, and transmission of the electron into the vacuum. The third stage of the process involves the refraction of electrons passing through the surface into the vacuum.
The three-step model is highly illustrative, yet lacks physically accuracy [44]. A physically accurate description is provided by the one-step model, in which the entire photoemission process is treated as a single coherent transition from an initial state to a final state. This model also describes the photoemission process using Fermi's golden rule, as outlined in Section 2.2.1, but employs an accurate description of the final state. The final states in question are referred to as time-reversed LEED states, which consist of a plane wave outside the solid that couples to an exponentially damped Bloch wave inside [44]. The finite mean free path of the photoelectrons is taken into account by introducing damping inside the solid. These states are also employed in the description of a LEED experiment, but in LEED, the electrons are incident onto the sample. In the context of photoemission, these states are referred to as time-reversed, as the direction of propagation is reversed.
The third and final point to be deliberated upon pertains to the characterisation of the final state. It has been demonstrated that, for a multitude of systems, the assumption of a plane wave final state constitutes a sufficient description of the photoemission process in great detail [15, 16, 23, 32, 51–67]. Nevertheless, this assertion is predominantly valid for sufficiently large excitation energies, such that the photoexcited electron no longer experiences the periodic potential of the crystal lattice. Conversely, for low excitation energies, but still sufficient to permit the electron to enter the vacuum, it is necessary to treat the final state as a scattered Bloch-like state [68–72]. This treatment of the final state as a scattered Bloch state is crucial for subsequent analyses, and thus, it is necessary to elaborate further on this

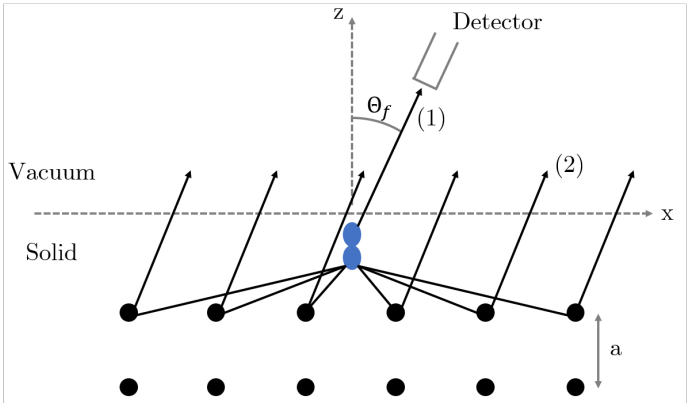

Figure (2.4) Schematic drawing of the photoemission processes from a p_z orbital of a molecular adsorbate (drawn in blue) on a metal substrate with different final states. Process (1) indicates the direct emission of the photoelectron wave into a plane wave final state towards the photoelectron detector. Process (2) shows the part of the photoelectron wave that is backscattered by the substrate, indirectly reaching the detector. Redrawn from [68].

point.
As illustrated in Figure 2.4, the process of photoemission of an electron from a molecular adsorbate on a metal surface can be conceptualised as follows: the electron wave is divided into two distinct components. The first component is directed towards the photoelectron detector (1), while the second component propagates towards the bulk [68–70]. The first component can be treated as a direct emission into a plane wave final state, which is characterised by its propagation in vacuum. The other component of the electron wave undergoes backscattering upon the periodic lattice potential of the surface, resulting in the Bloch character of this state. The interference of both components of the photoelectron wave on the detector gives rise to a photoelectron final state that contains information regarding the lattice periodicity due to its Bloch state share. It is evident that, due to the coherent superposition of the direct-emitted electron wave and the backscattered one, a straightforward separation of initial and final state information is not possible.
Following the exposition of the underlying physics of ARPES, the succeeding section is dedicated to the presentation of the more technical aspects of the experimental setup utilized.

2.2.3. Momentum Microscopy

The NanoESCA system, developed by FOCUS GmbH, is employed in all photoemission experiments presented in this work. This system is a momentum microscope, which is built upon a photoemission electron microscope (PEEM) that can detect the photoelectron distribution in real space. The momentum microscope can additionally discern the momentum distribution of the photoelectrons [73, 74].

As illustrated in Figure 2.5, the NanoESCA instrument is composed of three primary components: the PEEM column (1), the imaging double energy analyser (IDEA) (2), and the detection unit (3) [73]. In the PEEM column, photoelectrons from the sample are collected, and an image of the sample is formed. An octopole stigmator can be used to optimise the image before a set of projective lenses project the image onto the entrance slit of the energy analyser or directly onto the first charge-coupled device (CCD) detector for energy-integrated real space imaging. The IDEA is a double hemispherical analyser. Each hemisphere is a domed plate capacitor in which electrons of different kinetic energies propagate on trajectories with different radii. Only electrons with a specified kinetic energy are capable of exiting the IDEA at the exit slit. While the use of one hemispherical energy analyser is sufficient

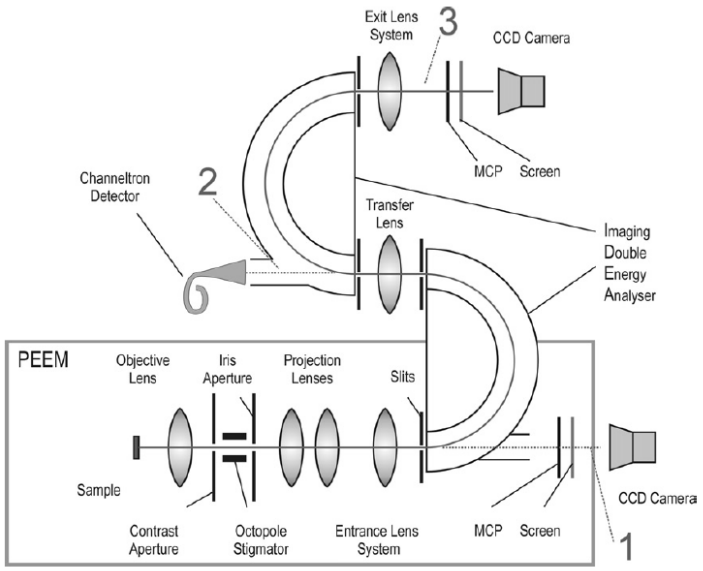

Figure (2.5) Schematic drawing of the NanoESCA system. The three major parts of the device are highlighted: (1) The PEEM column, (2) the IDEA and (3) the detection unit. Taken with permission from [73]. Copyright © 2005 IOP Publishing Ltd.

to obtain energy resolution [75], the second substantially reduces spherical aberrations in the trajectory plane and thus enhances image quality [73]. The rationale behind this phenomenon can be elucidated by considering the electron distribution in the trajectory plane. It has been demonstrated that, following 180° revolution, the electron distribution exhibits the largest spread due to aberrations. Conversely, after a complete revolution, all lateral electron positions are aligned with the initial spread [73]. This phenomenon can be likened to the motion of planets in accordance with Kepler's law.
The third and final component of the NanoESCA comprises an additional set of projector lenses, enabling the adjustment of magnification, in conjunction with an imaging unit. The imaging unit itself consists of two coupled multi-channel plates (MCPs), a fluorescence screen, and a CCD camera.

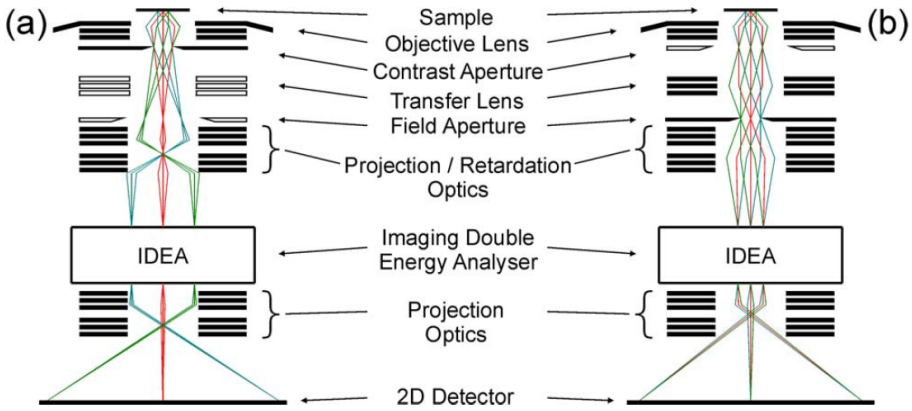

Figure (2.6) Schematic drawing of the NanoESCA system with the electrostatic lens optics and sketched electron trajectories. For real space imaging (a) photoelectrons originating from the same sample spot are focused in the same spot on the detector, whereas for imaging k-space (b) photoelectrons emitted under the same angle to the surface normal contribute to the same spot on the detector. With permission from [74], copyright © 2008 American Institute of Physics.

A momentum microscope is distinguished by its capacity to alternate between real space and momentum space imaging. Figure 2.6 provides a visual representation of this functionality, illustrating the electron trajectories for both modes in the NanoESCA. In this figure, electron paths originating from the same sample spot are designated by matching colour. As expected, for mapping a real space image of the sample, electrons originating from the same sample spot (i.e. trajectories with the same colour) impinge on the same detector spot (see Figure 2.6 (a)). For imaging momentum space, an additional electrostatic lens is used, the so-called transfer lens (see Figure 2.6 (b)). This lens projects the back focal plane, in which electrons emitted under the same angle are focused into a single spot, on the entrance slit of the IDEA (see Figure 2.6 (b)) [74]. It thus enables momentum space to be imaged (see Section 2.2.2).
A momentum microscope differentiates itself from a conventional ARPES setup by the simultaneous mapping of the full accessible momentum space.

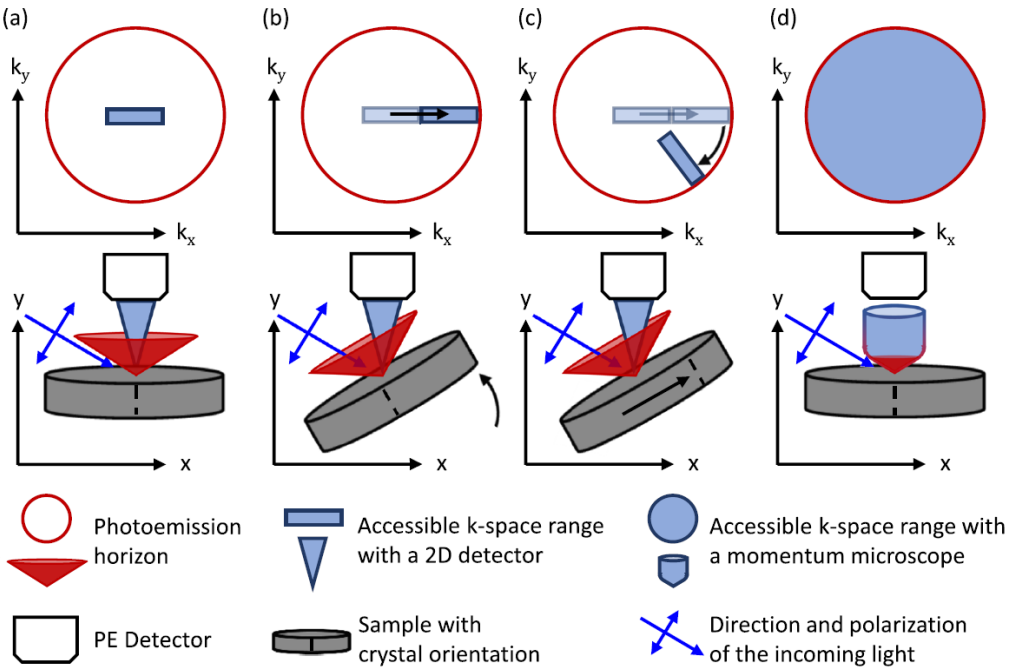

Figure (2.7) Comparison of the measurement principles of ARPES and momentum microscopy. (a) Detected photoemission angular distribution with a conventional ARPES system and set acceptance angle at normal emission. (b)-(c) Required sample rotation and tilt to map the complete accessible momentum space. (d) Simultaneous acquisition of the full accessible momentum space due to the applied extractor voltage in momentum microscopy. With permission from [76].

This is illustrated in Figure 2.7, which compares the data acquisition procedures of the two techniques. The standard ARPES setup is distinguished by an acceptance angle of photoelectrons emitted into the solid angle above the sample. It is therefore possible to measure a specific slice of the photoemission angular distribution (PAD) (see Figure 2.7 (a)). In order to map the complete accessible momentum space indicated by the red circular photoemission horizon, it is necessary to vary the sample's azimuth and polar angles (Figure 2.7(b-c)), moving the detection window over the entire area. In contrast, momentum microscopy enables the simultaneous measurement of the entire momentum space. This is achieved by applying an extractor voltage, which accelerates electrons emitted from every angle into the device. Given the energy filtering IDEA, the momentum distributions of electrons at a constant kinetic energy $I(E = const, k_x, k_y)$ can be measured. This is called a constant energy map (CE map) and is shown as the horizontal discs in Figure 2.8. Detecting electrons with different kinetic energies allows for the acquisition of a full 3D data cube $I(E, k_x, k_y)$, i.e. a

full band structure with momentum parallel to the surface, as shown in Figure 2.8.

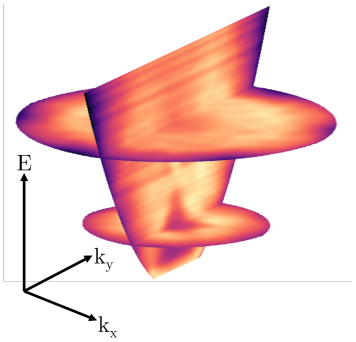

Figure (2.8) Structure of the data cubes $I(E, k_x, k_y)$ measured with momentum microscopy. Simultaneously only constant energy maps (CE maps) $I(E = const, k_x, k_y)$ are measured. By scanning through the kinetic energy of the electrons the data cubes are obtained. Similar to [76].

An advantage of a momentum microscope lies in the fixed experimental geometry. Due to the absence of any rotation or tilting of the sample the incident angle of light as well as the light polarization are unaltered throughout the experiment.
The NanoESCA system was connected to an ultra-high vacuum chamber and operated at a base pressure lower than $2 \cdot 10^{-9}$ mbar to ensure the cleanliness of the sample surfaces for a sufficiently long time, which is a prerequisite given the surface sensitivity of the photoemission process. Similar to LEED, the surface sensitivity results from the fact that the mean free path of the photoexcited electrons is within a few surface layers for the photon energies applied [38].
In the studies, three distinct light sources were employed in conjunction with the NanoESCA system. Initially, a vacuum ultraviolet (VUV) gas discharge lamp was utilised, operating with helium gas and emitting the He I_α line ($h\nu = 21.2$ eV). The presence of the He I_β line was found to be negligible, contributing only 1.2 to 1.8 % of the He I_α intensity [77], as observed in all conducted experiments. The utilisation of this light source was driven by the objective of emitting electrons with higher binding energies and accessing larger momenta compared to the other utilized light sources.
Furthermore, two distinct titanium sapphire ($Ti^{3+} : Al_2O_3$, abbreviated Ti:Sa) oscillator lasers were employed, with both lasers demonstrating the capability to generate ultrashort pulses with a duration ranging from 12 to 100 fs through mode-locking within an adjustable wavelength range, and exhibiting a repetition rate of approximately 80 MHz [78, 79]. The pulse powers of the lasers are sufficiently high to drive nonlinear processes such as second harmonic generation (SHG) and parametric amplification. The predominantly used Ti:Sa laser is a *Mai Tai* oscillator by Spectra-Physics. The pulses exhibit a duration of less than 100 fs with an average power of 2.5 W. The central wavelength can be adjusted from 690 to 1040 nm, depending on the experimental requirements. In certain instances, the second and fourth harmonic of the fundamental wavelength have been created using SHG. Furthermore, to cover an additional wavelength interval in Section 4 the *Mai Tai* was used to seed an *Inspire* optical parametric oscillator (OPO) by Spectra-Physics. Using parametric amplification the OPO enables a gap-free tuning of the wavelength from 345 nm to 2.5 µm with pulse duration between 80 and 250 fs [80].
The other Ti:Sa laser utilised was a *Griffin-10* by KMLABS, which was exclusively employed for the C_{60} multilayer experiments at ambient temperature in Section 5.7. It possesses an average power of 1.4 W and emits approximately 12 fs short pulses [79]. The adjustable repetition rate was set to approximately 80 MHz. Operated at a central wavelength of 840 nm, the second and fourth harmonic of the fundamental were created before the excitation of

photoelectrons.

2.3. Photoemission Orbital Tomography

In the preceding sections, the fundamental physics of a photoemission experiment was elucidated, and the practical implementation of this experiment using a momentum microscope was discussed. In the employed measurement setup photoemission angular distributions (PADs) at constant energies ($I(E = const, k_x, k_y)$), termed constant energy maps (CE maps), are measured. Obtaining these CE maps for a molecular film, conducting an analysis of the data, and correctly assigning measured PADs to their corresponding molecular orbitals can be ambiguous and challenging. Photoemission orbital tomography (POT), as introduced by Puschnig et al. [32], is a theoretical framework that aids in overcoming these challenges. The objective is to utilise density functional theory (DFT) to simulate PADs. Subsequent to comparing the theoretical results with experimental data sets, an assignment is made of molecular orbitals to their corresponding PADs due to the unambiguous nature of the latter. The aforementioned objective is accomplished by implementing the approximation of a plane wave final state, $\phi_{f,k} = Ce^{i\mathbf{kr}}$ [32, 52], a concept initially proposed by Gadzuk [51, 69]. The photoemission intensity at a constant energy of the electrons is directly proportional to the transition probability, a subject that is elaborated upon in Section 2.2.1. The expression in Equation 2.7 is then further simplified to

$$I(E = const, k_x, k_y) \propto \omega \propto |\langle e^{i\mathbf{kr}}|\mathbf{Ap}|\phi_{i,k}\rangle|^2 = |\mathbf{Ak}|^2 \cdot |FT[\phi_{i,k}]|^2 \tag{2.17}$$

$FT[\phi_{i,k}]$ hereby defines the Fourier transform of the initial state wave function of the photoelectron. The polarization factor $\mathbf{A} \cdot \mathbf{k}$ modulates the photoemission pattern, which is dependent on the angle of the incident light and its polarization. This modulation leads to an intensity gradient.
It is evident that the depiction of the final state as a plane wave can yield erroneous outcomes in certain scenarios [81]. A notable example is the final states of Bloch-like character [68–72], as eloborated in Section 2.2.2. Furthermore, POT predicts a vanishing intensity in the case of $\mathbf{A} \perp \mathbf{k}$, yet this can be observed in experiment, e.g. for a CO molecule on a Ni(100) substrate with its axis oriented along the surface normal [82]. Nevertheless, POT has been demonstrated to be a reliable technique for investigating the electronic structure of large π-conjugated molecular systems [15, 32, 52], determining molecular orientation [53, 59], investigating molecular interaction [15, 57] or identifying surface reactions [62]. First steps have also been taken to advance the simple picture of POT to systems with final state effects by extending the framework [66].
In the simplest POT approach, the initial state wave function is approximated by the molecular wave function of a free gas phase molecule [32, 52–54, 59]. This assumption is valid for weakly interacting systems with no or weak hybridisation, i.e. systems bound by physisorption or weak chemisorption. For more strongly interacting systems, or for a more detailed calculation including interaction effects, a sufficient model of the sample must be calculated [23, 58, 61, 62, 65, 83].
Figure 2.9 illustrates the process of a POT calculation. The starting point is the calculation of the gas phase molecular orbitals. Figure 2.9 shows on the left an isosurface contour plot of the highest occupied molecular orbital (HOMO) of pentacene. The orbitals obtained in this way are then Fourier transformed, resulting in their corresponding appearance in momentum space (middle panel of Figure 2.9). The hemispherical cut in red at constant momentum $k = \sqrt{(2m/\hbar^2)E_{\text{kin}}}$ corresponding to a defined kinetic energy shows the areas of emitted photoelectrons. A 2D projection and taking the absolute value gives the simulated POT CE map of the pentacene HOMO as shown on the right in Figure 2.9. Since the molecular

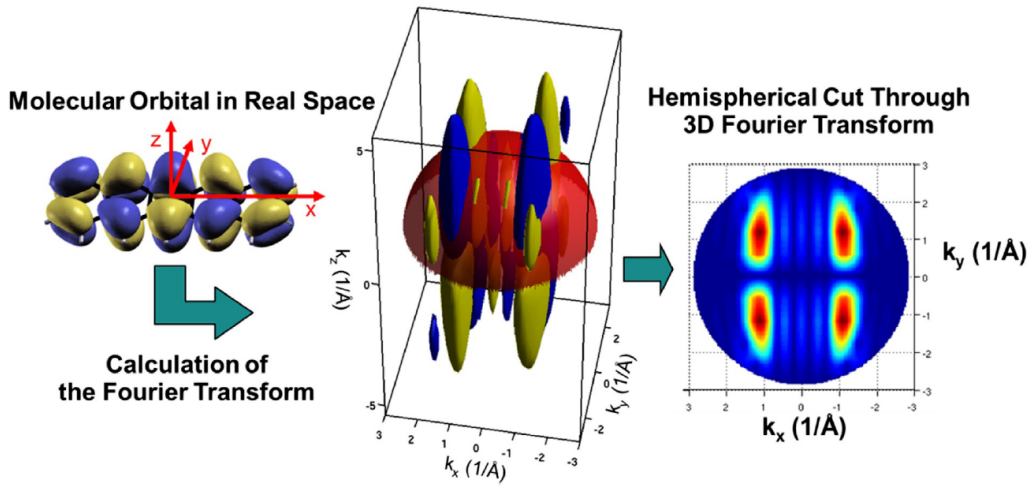

Figure (2.9) Main calculation steps of photoemission orbital tomography. Left: The starting point is a molecular orbital wave function obtained from DFT. Here shown as an isosurface contour plot of the HOMO of pentacene next to its schematic drawing. Blue and yellow represent the phase of the wave function, with the former showing negative and the latter positive values. Middle: Representation of the pentacene HOMO in momentum space after Fourier transformation. The red hemisphere represents a cut with constant momentum $k = \sqrt{(2m/\hbar^2)E_{\mathrm{kin}}}$ along which photoelectrons are detected. Right: 2D projection of the absolute value of the PAD along the hemispherical cut in the middle image, representing the unique emission pattern of the gas-phase pentacene HOMO. Taken with permission from [54].

orbital has a unique structure in real space, both the momentum space representation and the resulting 2D PAD are also exclusive in shape. Thus the calculated PAD can be used as a fingerprint to identify molecular orbitals in ARPES experiments.

A direct comparison of a calculated CE map from a gas phase molecule as in the right part of Figure 2.9 is only valid if there is only one molecular orientation present on the surface. In the case of multiple molecular orientations (in the unit cell or due to rotation or mirror domains of the surface) a combination of the calculated gas phase CE map must be assembled [53], which is illustrated in Section 3.3. In addition, any tilt of the molecules with respect to the surface must be taken into account [32].
As demonstrated in the middel panel of Figure 2.9, the hemispherical cut is determined by the total momentum of the photoelectron outside of the solid. As outlined in Section 2.2.2, electrons are refracted upon exiting the solid due to the potential step of the surface, originating from the inner potential (see Equation 2.16 and Figure 2.3 (b) in Section 2.2.2). This results in a change in the size of the hemispherical cut according to Equation 2.13. In order to calculate PADs comparable with the results of an ARPES experiment, knowledge of the inner potential is required. However, its determination is rather challenging [84], and so it is often neglected for planar molecules, as its impact is negligible for these systems [23, 32, 52]. Yet for 3D molecules, the inner potential leads to a severe alteration of the calculated PADs. The significance of the inner potential for POT of 3D molecules and its negligibility for planar molecules that are (almost) flat on the substrate, will be further elucidated.
As a planar molecule the case of 3,4,9,10-Perylenetetracarboxilic Dianhydride (PTCDA) is considered. The electron wave function of its HOMO is illustrated as an isosurface contour plot in Figure 2.10 (a), with the z-axis aligned perpendicular to the surface. In the framework of POT, i.e. assuming a plane wave final state, the electron wave function is Fourier transformed to obtain the corresponding electron wave function in momentum space. An excerpt of this Fourier transform is plotted in Figure 2.10 (b) with the momentum perpendicular to the surface versus the momentum parallel to the surface. Two spherical cuts through the

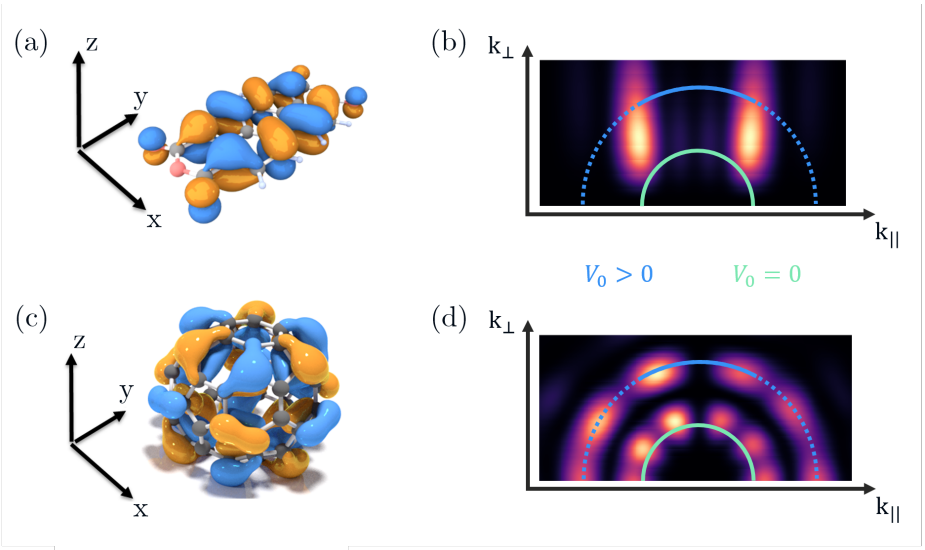

Figure (2.10) Differences in the PAD for planar and 3D molecules due to the inner potential. Isosurface of the PTCDA HOMO (a) and a momentum cut through its corresponding Fourier transform. The semicircles are of constant energy and indicate the PAD obtained by POT considering the inner potential (blue semicircle) and neglecting it (green semicircle). Due to the change in the perpendicular momentum that is dependent on the inner potential, only electrons located on the solid blue arc can leave the solid. (c,d) Analogous to (a,b) but for the C_{60} HOMO. DFT images by courtesy of Norman Haag adapted from [47].

3D momentum distribution corresponding to the same photon energy are indicated by the green and blue semicircles. The green semicircle thus signifies a cut with $V_0 = 0$, thereby neglecting the inner potential in the POT formalism. Conversely, the blue semicircle incorporates a non-zero inner potential. In this case it also has to be taken into account, that due to the change of momentum perpendicular to the surface that is defined by the inner potential, only electrons located on the solid blue arc can leave the solid.

While the hemispherical cuts including (green semicircle) and neglecting (blue solid arc) the inner potential differ in their absolute location, the resulting PADs are very similar. This is attribute to the cigar-like structure of the 3D Fourier transform, which is a consequence of its 2D character and exhibits minimal dependency on $K_\perp$.

In the case of a 3D molecule such as C_{60}, the situation differs. Figure 2.10 (c) illustrates the isosurface of the C_{60} HOMO, and its corresponding cut through the 3D Fourier transform is shown in (d). It is evident that there is an absence of momentum direction with minimal altercations of intensity, in contrast to the case of the planar PTCDA. In fact neglecting the inner potential will result in substantially different PADs (illustrated as a green semicircle), contrasting to the scenario when it is taken into account (blue semicircle). Consequently, a knowledge of the inner potential is imperative for the analysis of POT in systems comprising 3D molecules [23].

Finally, it should be noted that the inner potential does not only affect the location of the hemispherical cut through the 3D Fourier transform, but also the curvature of the angular distribution of photoelectrons of this cut. This, in turn, results in variations in the distances between features subsequent to the projection of the hemispherical cut onto a 2D plane. However, in the case of planar molecules, this effect can be considered negligible. This assertion is supported by further research, which will be presented in the case of the Cs-doped PTCDA on Ag(111) in Section 3.3. However, its impact is evident for 3D molecules, such as the C_{60} monolayer on Cu(111), as illustrated in Section 4.4.

2.4. Multi-Photon Photoemission Processes

All prior discourse has considered only the absorption of one photon per photoelectron for a transition from an occupied initial state $|i\rangle$ to a final state $|f\rangle$ above the vacuum energy E_V. This process is henceforth referred to as a one-photon photoemission (1PPE) process, as illustrated in Figure 2.11 (a). The transition between the initial and final states $|i\rangle \rightarrow |f\rangle$, can also occur through the absorption of multiple photons, provided that the sum of all absorbed photon energies is equivalent to the energetic distance between $|i\rangle$ and $|f\rangle$ [85–87]. It is noteworthy that the smaller the photon energy, the greater the number of photons required to contribute to a single photoemission process. A more thorough exposition of these nPPE processes can be found below.

The two-photon photoemission (2PPE) process is the subsequent possible higher order process. As illustrated in Figure 2.11 (b), the 2PPE process can be divided into two cases: In the transition depicted on the left, the electron simultaneously absorbs two photons. In contrast, for the 2PPE transition on the right, the electron is excited stepwise from the initial state into an unoccupied intermediate state ($|int\rangle$) and from there into the final state. Consequently, nPPE processes can be utilized to access the unoccupied states of a material in a photoemission experiment. In the context of the process involving an intermediate state, the photoelectron will carry information regarding the momentum distribution of that state. Conversely, in the context of a simultaneous absorption of two photons, the photoelectron contributes to the photoemission angular distribution of the initial state, as no intermediate state is involved in the transition (note that this assumes a plane wave final state).
In this context, the scenario of tuning the photon energy by $\Delta h\nu$ in the case of a 2PPE process as shown in Figure 2.11 (c) is considered. In the case of a simultaneous absorption

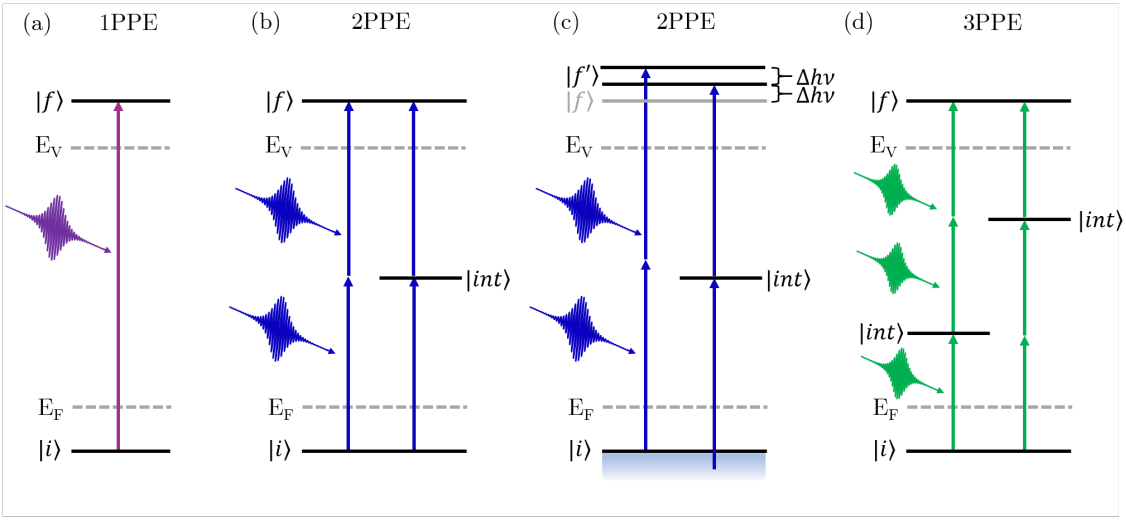

Figure (2.11) Comparison of a one-photon photoemission (1PPE) process (a) with multi-photon photoemisssion (nPPE) processes (b-d). (a) For a 1PPE process the photon energy is sufficiently large to excited the electron from an occupied initial state $|i\rangle$ to a final state $|f\rangle$ above the vacuum energy E_V. (b) For a two-photon photoemission (2PPE) process one electron needs to absorb two photons in order to be excited above the vacuum energy. Depicted are the two cases of a simultaneous adsorption and a transition via an intermediate state $|int\rangle$. (c) 2PPE process with by $\Delta h\nu$ increased photon energy. The new final state for a transition by simultaneous absorption of two photons is shifted by $2\Delta h\nu$ to higher energies, whereas the final state of stepwise transition involving the intermediate state is only shifted by $\Delta h\nu$ given the initial state is sufficiently broad in energy. (d) A 3PPE process is exemplary illustrated as a higher nPPE process. Only the two process with one intermediate state are depicted.

of two photons, the new final state $|f'\rangle$ will be shifted by $2\Delta h\nu$ to larger energies compared to the previous final state $|f\rangle$. Conversely, the final state of the stepwise transition will only be shifted by $\Delta h\nu$ [88]. It is imperative to note that this phenomenon occurs under the condition that the initial state ($|i\rangle$) possesses a sufficient bandwidth, thereby enabling the intermediate state to undergo resonant excitation. This criterion of a sufficient energetic width of the initial state is typically observed for most molecular orbitals, as well as for metallic states. The criterion of a differential shift in energy upon photon energy tuning facilitates the differentiation between initial and intermediate states and will be employed later on [87]. In the given example of a 2PPE process, the shift of the peak in the photoelectron spectrum by $2\Delta h\nu$ is indicative of an initial state, while a shift by $\Delta h\nu$ signifies an intermediate state.
As a further nPPE process, the case of a 3PPE event is to be considered, as illustrated in Figure 2.11 (d) with two possible paths involving one intermediate state. The cases of a transition with the simultaneous absorption of three photons, as well as a stepwise transition including two intermediate states, are henceforth neglected. A comparison of the 2PPE process (Figure 2.11 (b)) involving an intermediate state with the depicted 3PPE processes (Figure 2.11 (d)) reveals that the utilization of higher order photoemission processes facilitates the excitation and probing of intermediate states that are closer to the Fermi level and vacuum energy for the same initial and final states.
This possibility to excite different unoccupied states with different photon energies is used to determine the energetic positions of excited states in the monolayer C_{60} on Cu(111) sample system in Section 4.5. The magnitude of the shift of the corresponding peak in the photoelectron spectrum allows for a distinction between intermediate and initial states. Before delving into the introduction of investigating dynamics using the technique of photoemission, it is important to make a few remarks: Firstly, it should be noted that the nPPE processes ($n > 1$) depicted in Figure 2.11 are monochromatic. While bichromatic nPPE transitions are possible, they require an intermediate state. Secondly, the investigation of systems using nPPE processes necessitates high photon densities. As the transitions are processes of n-th order, they follow the product of the n involved pulse intensities [86]. This demands the use of ultrashort laser pulses with high peak intensities.

2.5. Time-Resolution and the Pump-Probe scheme

The investigation of dynamics in a photoemission experiment invariably necessitates the employment of multi-photon photoemisssion processes, as at least one photon is required for the optical excitation of the system under study, and the subsequent absorption of one or more photons leads to the emission of the electron from the solid [85, 86]. In this section the simplest case of a time-resolved two-photon photoemission (tr-2PPE) process as shown in Figure 2.12 is considered. The first laser pulse excites electrons from the initial state $|i\rangle$ into the intermediate state $|int\rangle$. In the event that the second laser pulse is not simultaneous with the first one, but rather arrives with a delay, designated as Δt, the excitation in the intermediate state can undergo partial decay. The resultant photoemission signal is consequently weaker in comparison to a transition in which no time delay exists between the laser pulses. By systematically varying the time delay between laser pulses and recording the photoemission signal for each delay step, the temporal resolution of the intermediate state's photoemission signal can be achieved, facilitating the investigation of excited state dynamics [85, 86].
In experimental settings, the temporal resolution is realized through the implementation of the so-called pump-probe scheme [85]. In this method, laser pulses are separated into two distinct pulses using a Mach-Zehnder interferometer. Within one interferometer arm, a linear translation stage (delay stage) is employed to modify the optical path, thereby in-

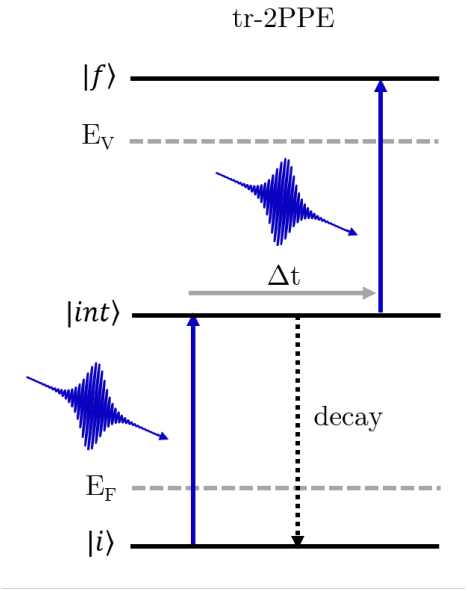

Figure (2.12) Schematic depiction of a time-resolved (tr) 2PPE process. The two laser pulses do not arrive on the sample at the same time anymore, but with a delay Δt. The first pulse (pump pulse) excites electrons from the initial state $|i\rangle$ to the intermediate state $|int\rangle$. Until the next laser pulse (probe pulse) arrives, the electronic excitation can partially decay. The electron yield excited by the second laser pulse from the intermediate state above the vacuum level thus depends on the delay between the two laser pulses.

troducing a delay between the two pulses within the interferometer. The nomenclature of this process is derived from the two laser pulses involved in the photoemission process. The pulse that arrives at the sample first is designated as the pump pulse, as it functions to pump electrons from the initial into the intermediate state. The second pulse, designated as the probe pulse, subsequently probes the excitation by photoemitting electrons into the vacuum. As illustrated in Figure 2.13, the experimental implementation of the employed pump-probe scheme is demonstrated. Laser pulses with a central photon energy of 2.95 eV enter the Mach-Zehnder interferometer. The generation of these pulses is accomplished by second harmonic generation (SHG) in front of the interferometer (not shown in Figure 2.13). The laser pulses are separated into the two beam arms by a beam splitter. A translation stage integrated into an interferometer arm serves to impose a precise temporal delay between the two laser pulses. The other arm contains another nonlinear β-Barium borate (BBO) crystal to further up-convert the laser pulses to the fourth harmonic ($h\nu = 5.9\,\mathrm{eV}$) of the fundamental photon energy.

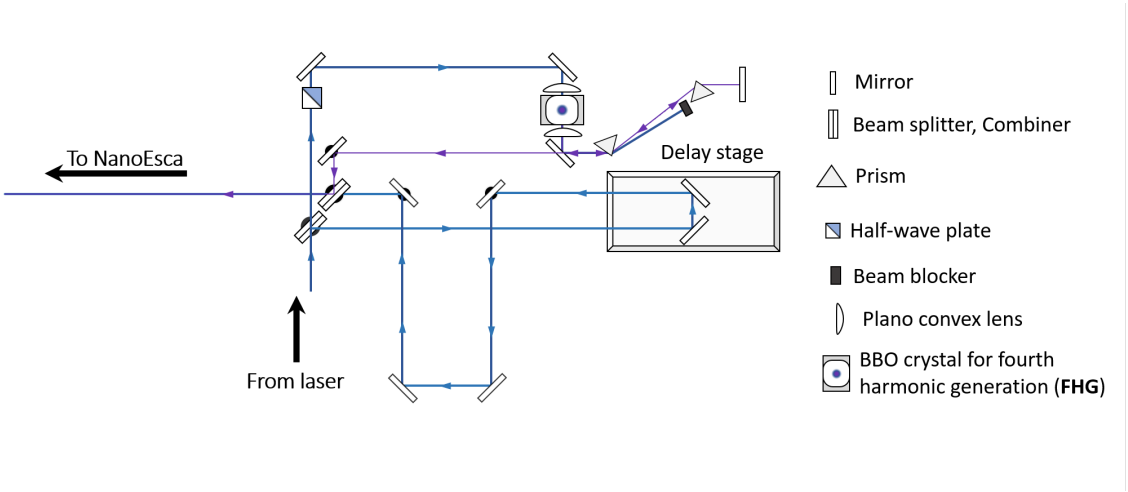

Figure (2.13) Schematic depiction of the bichromatic laser beam line used for the pump-probe experiments. The setup consist of a Mach-Zehnder interferometer with a linear translation stage (delay stage) in one interferometer arm enabling the delay of the laser pulses with respect to each other. The second harmonic is created in front of the interferometer, whereas only laser pulses in the interferometer arm not containing the delay stage are further up-converted to the fourth harmonic.

The pump-probe scheme is employed in Chapter 5 for the investigation of the excitonic structure and dynamics in multilayer C_{60} films. The creation of the fourth harmonic is necessary to overcome the substantial work function of the the C_{60} multilayer film ($\Psi = 4.9\,\mathrm{eV}$) [89] using a 1PPE process.
Following the presentation of the experimental and theoretical techniques employed, along with their physical foundations, the subsequent chapters of this dissertation will present the three distinct projects that form the basis of this research.

3 Charge-Transfer and Structural Reorientation of PTCDA on Ag(111) upon Alkali Metal Doping

As a first experimental part of this work, the electronic coupling of a weakly interacting molecule/metal interface and the influence of the adsorption geometry on the energy level alignment will be investigated. Therefore, this chapter explores the structural alterations of the molecular ordering and the concomitant modifications of the electron system of a monolayer film of the 3,4,9,10-Perylenetetracarboxilic Dianhydride (PTCDA) ($C_{24}O_6H_8$) molecule on a Ag(111) single crystal upon cesium doping. The investigation commences with an introduction to the undoped reference system of a single monolayer PTCDA/Ag(111), as PTCDA is a subject of extensive study due to its prevalence as an organic semiconductor, particularly with regard to its growth and electronic structure at interfaces. It has emerged as a "drosophila" model system in surface science with potential applications (see [90–94] and references therein). The Ag(111) surface is an intriguing surface template for the study of doping-induced effects on molecular ordering and electronic properties. Its interaction with molecular adsorbates is rather weak (see, for example, [95]). This gives the molecular adsorbates a high mobility with only little perturbation and hybridization of the molecular orbitals. Furthermore, the molecule-substrate interaction on Ag(111) is of the same order of magnitude as the intermolecular interactions of most organic adsorbates. Small changes in the system, e.g. by doping, can lead to very different molecular ordered structures [96].
Due to the already extensive research and literature on PTCDA on surfaces, this chapter will start with an overview of the most relevant work. Therefore, Section 3.1 commences with an introduction of the molecules followed by a summary of the geometric properties of PTCDA on Ag(111). After an introduction to the electronic properties of the pristine PTCDA/Ag(111) system, the approach of photoemission orbital tomography (POT) of highly symmetric adsorbate systems [53] to investigate the molecular-resolved electronic structure of pristine PTCDA/Ag(111) will be highlighted. This approach will be followed in the study of the Cs-doped system. In Section 3.2 an overview of the literature on the reference system of potassium-doped PTCDA/Ag(111) will be given. After this overview and classification of relevant literature the studies on cesium-doped PTCDA/Ag(111) will be presented in Section 3.3. Comparisons to literature, especially to a similar study on potassium-doped PTCDA/Ag(111) [97–99], will be made.
The focus of this chapter is the determination of the caesium induced structural changes in the adsorption geometry and the investigation of the subsequent influence on the intermolecular interactions and the energy level alignment.

3.1. The Undoped Reference System: PTCDA on Ag(111)

PTCDA/Ag(111) is a well-studied interface with regard to molecular ordering as well as electronic properties. It serves as a starting point and reference for the present investigation [53, 90, 92, 100–106]. Therefore, an overview of the system will be provided by elucidating

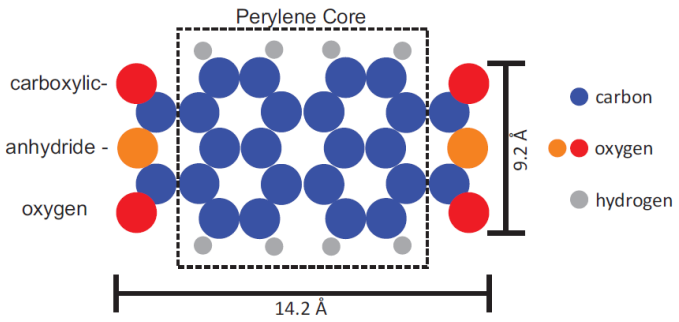

Figure (3.1) Ball model of the atomic structure of PTCDA. By courtesy of Benjamin Stadtmüller [109], copyright © 2013 Forschungszentrum Jülich GmbH.

the geometric properties of the ordered structure, with particular emphasis on the molecular orientation and the geometrical alteration of the molecular geometry due to interaction with the surface. It is further intended to discuss the molecule-substrate interaction in detail, focusing especially on the charge transfer and the orbital structure.
Figure 3.1 illustrates the atomic structure of the planar PTCDA molecule in the form of a ball model. The molecule consists of a perylene core with two types of different oxygen groups, two carboxylic- and one anhydride-oxygen group, located at both ends of its long molecular axis. The oxygen atoms located at the molecule's short edges, in contrast to the hydrogen atoms populating the long molecular edges, result in a quadrupole moment on the molecule. This quadrupole moment exerts a significant influence on the formation and ordering of islands on substrates [91, 92, 107]. The oxygen atoms bear negative partial charges, while the hydrogen atoms carry positive charges. π-Conjugated delocalized orbitals expand mainly over the perylene core originating from the sp^2 hybridization of the carbon atoms. These out-of-plane π-orbitals are a significant factor in molecule-substrate interactions, determining the geometric structure of the molecular layers [53, 92, 104–106]. In multilayer systems, the molecules arrange in a $\pi - \pi$ stacking configuration, which exerts a substantial influence on the optical properties [108].
In the subsequent section, an outline will be provided of the adsorption and geometric properties of one monolayer PTCDA on a Ag(111) surface. This will be followed by a more detailed discussion of the electronic properties.

3.1.1. Adsorption Geometry

The initial focus will be on the ordering and structural characteristics of a single monolayer of PTCDA on an Ag(111) surface.
PTCDA grows on Ag(111) in two structurally distinct phases, depending on the sample temperature during deposition [25, 106]. The properties of the phase prepared at room temperature will be discussed in the following section, as this is the relevant phase for the subsequent experiments of the doped system.
Upon deposition, PTCDA grows in a Stranski-Krastanov fashion on the Ag(111) surface kept at room temperature [110]. A corresponding low energy electron diffraction (LEED) pattern of a monolayer coverage is shown in Figure 3.2 (a), indicating a commensurate structure with a super structure matrix of $\left(\begin{smallmatrix} 7 & 1 \\ 2 & 5 \end{smallmatrix}\right)$. It is noteworthy, that this superstructure matrix corresponds to a description of the $p3m1$-symmetric Ag(111) substrate with an obtuse angle between the substrate basis vectors. This matches the supersturcture matrix $\left(\begin{smallmatrix} 6 & 1 \\ -3 & 5 \end{smallmatrix}\right)$ in the depiction of an acute angle between the substrate unit cell vectors, which is also commonly found in literature [100–103]. Both molecules are found to be in a flat configuration on the surface. The unit cell of the PTCDA monolayer on Ag(111) is nearly rectangular (angle between adsorbate unit cell vectors, $\alpha = 89°$) and is slightly smaller than in its bulk phase

owing to the molecule-substrate interaction [101].

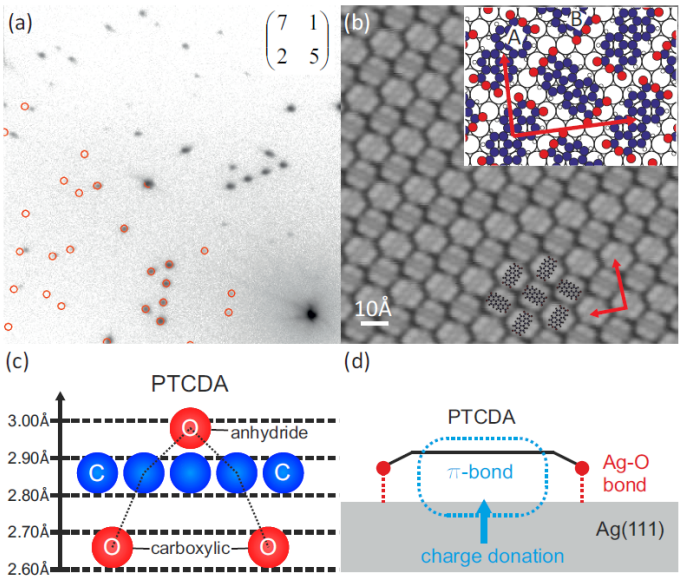

Figure (3.2) Structural properties of a PTCDA monolayer on Ag(111). (a) LEED image taken at a kinetic energy of $E_{\mathrm{kin}} = 27.2\,\mathrm{eV}$. The red dots indicate diffraction spots according to the superstructure matrix in the inset. (b) STM image ($U_{\mathrm{Bias}} = -0.34\,\mathrm{V}, I = 0.2\,\mathrm{nA}$) of the PTCDA structure on Ag(111) with an inset depicting the molecular orientation of the two inequivalent molecules A and B inside the unit cell. (c) Molecular distortion and vertical adsorption geometry from a lateral perspective of one monolayer PTCDA on Ag(111) based on [106]. (d) Schematic drawing of the different interactions between a PTCDA molecule and the Ag substrate. By courtesy of Benjamin Stadtmüller [109], copyrighted by Forschungszentrum Jülich GmbH.

Figure 3.2 (b) presents a scanning tunneling microscopy (STM) image of the monolayer PTCDA/Ag(111) system, revealing a herringbone structure [100–103]. Each unit cell thus contains two molecules with differing orientations, which are labeled A and B (see inset in Figure 3.2 (b)). Molecule A exhibits a near alignment (2° off) with its long axis along a high-symmetry direction of the Ag(111) surface, whereas molecule B is rotated by 77° compared to A [24, 104].
The perylene core of each molecule is centered on a bridge site of the Ag(111) surface, resulting in different relative positions of the oxygen atoms of molecules A and B with respect to the silver atoms (see inset in Figure 3.2 (b)) [24]. The carboxylic oxygen atoms of molecule A are situated directly above the Ag atoms, whereas the carboxylic oxygen atoms of molecule B are laterally misplaced from the top site. This variation significantly impacts the molecule-substrate interaction and the formation of covalent bonds between the oxygen atoms and the Ag atoms for the differently oriented molecules.
The adsorption height and structural geometry of the PTCDA molecules were investigated with normal incident X-ray standing wave (NIXSW), revealing a deformation of the molecules from their planar geometry [106, 111]. While most of the perylene backbone (20 out of 24 carbon atoms) are located in a plane 2.86 Å above the Ag surface, the oxygen atoms are vertically strongly distorted (see Figure 3.2 (c)). The carboxylic oxygen atoms exhibit a bending toward the surface, while the anhydride oxygen atoms are located above the plane of the carbon atoms. The down-bending of the carboxylic oxygen atoms causes a saddle-like distortion of the PTCDA molecules (see Figure 3.2 (d)), which further indicates a localized bond between the oxygen and silver atoms. The molecular distortion, in conjunction with the registry of the perylene cores on bridge sites, enables the commensurate registry of PTCDA on the Ag(111) surface.

A more detailed view on the electronic properties and interactions of the PTCDA layer on Ag(111) will be given in the next section.

3.1.2. Electronic Structure

The electronic structure of PTCDA on Ag(111) is defined by an interplay between the intermolecular and the molecule-substrate interactions [24]. A significant overlap exists between the molecular π-orbitals and the orbitals of the silver sp-bands, resulting in the formation of a new hybrid π-bond. However, the mixing of substrate states to the molecular orbital is only approximately 10% [26]. Subsequently, the LUMO is partially filled (see Figure 3.2 (d)) [103–105]. Additionally, localized covalent bonds form between the Ag atoms and the carboxylic oxygens. The formation of these hybrid bonds explains the low adsorption height of PTCDA, which is much smaller than the corresponding van der Waals radii.
The formation of π-bonds, as well as the emergence of the localized O-Ag bonds at the carboxylic groups, result in a redistribution of charges within the adsorbate and the substrate [111]. An orbital-resolved density functional theory (DFT) study determined that the charge transfer from the substrate to the LUMO is partially compensated by a reverse donation of electrons from the PTCDA to the silver. This process does not result in a resolvable depopulation of any molecular orbital, as up to 20 occupied orbitals are affected [105]. The charge donation strengthens the local bonds between the carboxylic groups and the Ag atoms, pulling the molecule closer to the surface [111]. This reduction in adsorption height further promotes charge transfer, leading to a repetition of the mutual interactions.
A determination of the energy level alignment in the PTCDA/Ag(111) system is possible by means of scanning tunneling spectroscopy (STS) [24] or ultraviolet photoelectron spectroscopy (UPS) [103]. The local density of states can be measured with high spatial and energy resolution using STS compared to UPS. Conversely, its high spatial resolution can also be disadvantageous. STS is only capable of probing the energy level alignment of one specific molecule at a time. As a result, local impurities, defects or perturbations have a significant influence, and thus no averaged signal of a broad area can be obtained. Moreover, STS can only be performed at very low sample temperatures. In contrast, UPS suffers from the shortcoming that energetic differences between the differently oriented molecules in the unit cell are hardly resolvable, and an assignment of the spectral peaks to corresponding molecular orbitals can be challenging. However, these deficits can be overcome by employing angle-resolved photoelectron spectroscopy (ARPES) in combination with photoemission orbital tomography (POT), as was demonstrated by Stadtmüller et al. [53]. The remainder of this section is dedicated to their findings and the approach, as a similar procedure will be followed in the analysis of the Cs-doped system in Section 3.3.2. The exemplary case of the undoped system will be elucidated in the following.

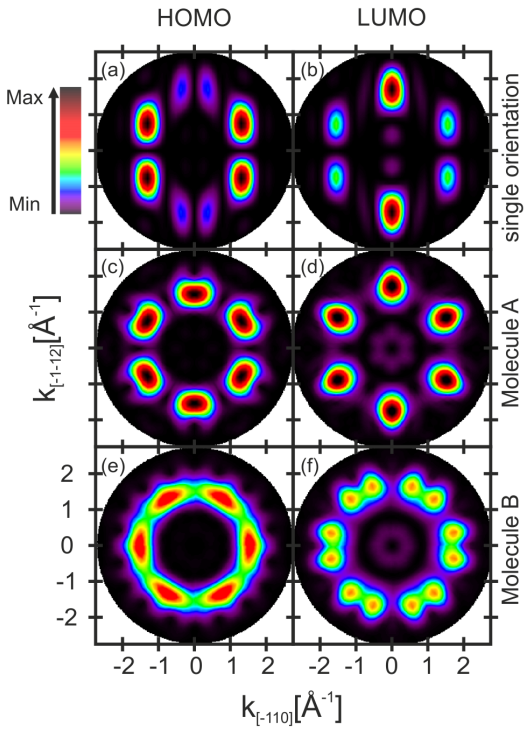

Figure (3.3) DFT calculations of the HOMO and LUMO CE maps of PTCDA for a gas phase molecule (a, b) with its longs axis aligned horizontally. (c, d) CE maps of molecule A considering the possible rotation and mirror domains of the $p3m1$ symmetry. (e, f) The same as in (c, d) but for molecule B which is rotated by 77° with respect to A. Taken with permission from [53]. Copyright © EPLA, 2012.

In accordance with the approach of photoemission orbital tomography (POT), the objective is to replicate the constant energy maps (CE maps) of the PTCDA/Ag(111) system as observed in experiment. This facilitates the identification of the observed orbitals. Additionally, a tomographic fitting approach enables the deconvolution of the photoelectron spectrum into the contributions of the two inequivalent molecules within the unit cell. As a preliminary step, the CE maps of the HOMO and LUMO for a gas-phase PTCDA molecule were computed using density functional theory (DFT). These maps are illustrated in Figure 3.3 (a) and (b), with each map belonging to a single molecule oriented with its long axis positioned horizontally. To calculate the CE maps of the entire PTCDA layer on Ag(111), it is necessary to consider all possible molecular orientations. This is achieved by summing appropriate multiples of the calculated CE maps in (a) and (b) after proper rotations and mirroring. This includes CE maps for molecules with different orientations within the unit cell (A and B), as well as all mirror and rotation domains.
Molecule A is approximately aligned with its long axis along high-symmetry directions of the Ag surface, e.g. the $[\bar{1}01]$ direction or any equivalent one. Figure 3.3 (c) and (d) depict the corresponding calculated CE maps including all rotation and mirror domains according to its $p3m1$ symmetry of the Ag surface. The formation of six main maxima is observed, originating from the three distinct rotational domains. The mirror domains do not contribute to the formation of new distinct maxima, as the deviation of molecule A from a high-symmetry direction of the Ag(111) surface is only 2°. Consequently, this results in a minor broadening of the six main intensity maxima, which is hardly perceptible in the POT simulations.
In the case of molecule B, the long axis deviates by 77° from a high-symmetry direction of the Ag(111) surface, resulting in a different outcome. The CE map of the HOMO and LUMO, calculated according to surface symmetry, are displayed in Figure 3.3 (e) and (f), respectively. In this case, the deviation of the molecular axis from a high-symmetry direc-

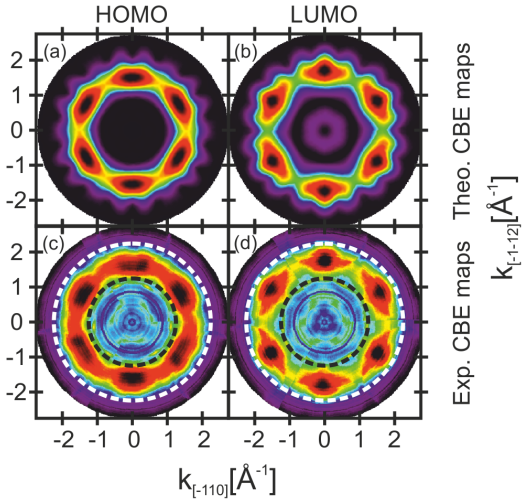

Figure (3.4) Comparison of the theoretical (a, b) and experimental (c, d) CE maps of the PTCDA/Ag(111) HOMO and LUMO. The theoretical CE maps include both molecular orientations in the unit cell as well as all rotation and mirror domains according to the $p3m1$ substrate symmetry. The experimental CE maps were measured at a binding energy of 1.6 (c) and 0.3 eV (d). Taken with permission from [53]. Copyright © EPLA, 2012.

tion leads to a splitting of the emission maxima due to the mirror domains, best seen for the LUMO CE map in Figure 3.3 (f). For the HOMO the maxima are smeared out to a ring-like structure.

The combination of the calculated CE maps for molecules A and B provides an estimate of the overall photoemission angular distribution (PAD) of the frontier orbitals of a monolayer PTCDA/Ag(111). The result is demonstrated in Figure 3.4 (a) and (b). It is important to note that a direct combination is not precisely accurate because the orbitals of molecules A and B must be at the same energy, which is not the case in this system. Nevertheless, they are sufficiently similar that a direct sum of the CE maps provides a reliable estimate. This can be verified by comparing the in this way obtained theoretical CE maps in Figure 3.4 (a) and (b) with the experimental ones in (c) and (d). The remarkable agreement between the CE maps underscores the validity of the photoemission orbital tomography approach, particularly in the case of highly symmetric adsorbate systems [53]. This demonstrates that despite the additional rotation and mirror domains of highly symmetric surfaces such as the (111)-surface, the identification of the different molecular orbitals by means of POT is still possible. In this particular instance, it is confirmed that the molecular orbital near the Fermi edge is the partially filled LUMO that becomes populated by charge transfer from the Ag substrate.
As previously mentioned in Section 2.3, the modeling of the CE maps based on DFT calculations of a free-standing molecule is only valid for systems with weak interaction and minimal hybridization. However, in the case of PTCDA/Ag(111), the carboxylic oxygen atoms form covalent bonds with underlying Ag atoms, and the LUMO also hybridizes with the substrate orbitals due to charge transfer, resulting in a deformation of the molecule (see Section 3.1.1). This interaction can still be regarded as weak because it does not involve d-bands, which are known to be energetically deep-lying for Ag surfaces [112]. In addition, the substantial congruence between experiment and theory demonstrates that the emerging hybrid orbitals bear a significant resemblance to the molecular ones, thereby serving as a reliable, albeit approximate, starting point.
A tomographic approach was employed by Stadtmüller et al. [53] to deconvolve the contributions of the differently oriented molecules A and B to the individual CE maps and thus

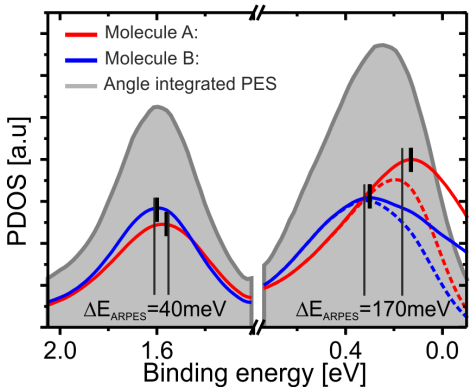

Figure (3.5) Molecular and orbital resolved energy spectra of PTCDA/Ag(111) for the different molecular orientations inside the unit cell. The dotted lines for the LUMO represent the orbital contributions according to the fitting parameters a_i, whereas the solid curves are broadened by the Fermi distribution function. The filled gray curves are the photoelectron spectrum extracted by an integration over the ring in the CE maps in Figure 3.4 (a) and (d). Short thick lines indicate peak positions obtained from the POT analysis. For comparison the long thin vertical lines show the peak positions measured with STS in [24]. Taken with permission from [53]. Copyright © EPLA, 2012.

the photoemission spectrum [52, 53]. For each energy, the measured CE maps were fitted by a linear combination of the calculated ones in Figure 3.3 (c-f) using a least-square method. The fit function is as follows:

$$F(k_k, k_y, E_\mathrm{B}) = \sum_i a_i(E_\mathrm{B})\Phi_i(k_x, k_y) + b(E_\mathrm{B})I_\mathrm{sub}(k_x, k_y, E_\mathrm{B}) + c(E_\mathrm{B}). \tag{3.1}$$

The sum of calculated CE maps, denoted by $\Phi(k_x, k_y)$, is included in the fit along with a contribution from the substrate, $I_\mathrm{sub}(k_x, k_y, E_\mathrm{B})$, as well as an energy-dependent offset, $c(E_\mathrm{B})$. The fit parameters $a_i(E_\mathrm{B})$ represent the energy-resolved density of states projected onto the different molecular orbitals (projected density of states, PDOS) multiplied by the Fermi distribution function [53]. The function $F(k_x, k_y, E_\mathrm{B})$ was fitted to the ARPES intensity $I(k_x, k_y, E_\mathrm{B})$ by Stadtmüller et al. in the highlighted rings illustrated in Figure 3.4 (c) and (d). This region encompasses the predominant intensity, and the restriction of the fitting procedure to this domain has been shown to enhance the outcomes [53].

As depicted in Figure 3.5, the tomographic fitting approach yielded notable results. The angle-integrate ARPES intensity of the HOMO and LUMO (illustrated as filled gray curves) could be deconvoluted into the contributions from molecules with different orientations. Subsequent division of these contributions for the LUMO by the Fermi distribution function yielded the corresponding PDOS. The tomographic approach revealed higher binding energies for the HOMO and LUMO in molecule B, whose alignment deviates from the high-symmetry directions of the Ag surface. The results are corroborated by scanning tunneling spectroscopy (STS) measurements, which attribute the shift of orbital energies between differently oriented molecules to an alteration of molecule-substrate and intermolecular interactions [24, 104]. The molecule-substrate interactions differ between the two molecules in the unit cell because they are differently aligned to the Ag substrate and thus show a different degree of hybridization with the Ag atoms. This effect is more pronounced for the LUMO than for the HOMO, as the former is more involved in the bonding to the substrate. It was found that the LUMO of molecule A has its lobes of high electron probability centered on top of Ag atoms, enhancing hybridization [24]. This is not the case for molecule B, resulting in weaker interaction with the surface. The second effect of different orbital energy positions of molecule A and B results from intermolecular interactions. The 1° deviation of

the PTCDA unit cell from a rectangular shape enforces different distances of the O-H bonds for the two molecules [24]. This leads to different quadrupole moments at the position of molecule A compared to B thus changing the energy level positions [104, 113]. In the case of PTCDA/Ag(111), the effects of the molecule substrate and intermolecular interactions on the energy level alignment are countervailing. This results in a reduction of energy offsets due to the molecule substrate interaction [24, 25].

It should be noted, that the effect of the different orbital energies of the two PTCDA molecules in the unit cell is not limited to the Ag(111) surface; it also occurs in a smaller but still considerable magnitude for the herringbone PTCDA monolayer on Ag(110) [112, 113]. In this system, the phenomenon can be attributed to the configuration of the herringbone structure, where the aggregate of all quadrupole fields differs between the positions of the two molecules. Therefore, the differing orbital energies are a consequence of intermolecular interactions.
Following this introduction to the undoped reference system of PTCDA/Ag(111) and the tomographic deconvolution approach based on POT, an overview of the reported effects of potassium doping of PTCDA/Ag(111) will be given. This is due to the remarkable strong similarities between the potassium doped system and the cesiated system. These similarities become evident later on in the discussion.

3.2. K-doped PTCDA on Ag(111)

The influence of alkali metal doping on PTCDA, a prototypical organic semiconductor, has been a subject of ongoing research. Studies have investigated effects on transport properties [114], electron-phonon coupling [115], dopant distribution in bulk PTCDA [116], as well as structural [97, 99] and electronic changes [98, 117]. In this section, the effects of potassium doping on the PTCDA/Ag(111) interface [97–99] will be elucidated, as this system shares numerous similarities with the investigated cesium-doped PTCDA/Ag(111) system, as will become evident subsequently.
Potassium doping of a PTCDA monolayer on Ag(111) results in the formation of two stable, compact and distinct phases, designated as K_2PTCDA and K_4PTCDA, respectively [97]. The index denoting the number of potassium atoms per PTCDA molecule serves as a quantitative descriptor of these structural phases. It is noteworthy that the phase formations occur spontaneously, affecting all molecular domains, and are solely depending on the dopant concentration. It has been observed that variable dopant concentrations do not result in the formation of phases with different K-stoichiometry; rather, they give rise to a coexistence of the aforementioned phases.
Post-deposition annealing of the sample at temperatures below 473 K results in the complete decay of the K_4PTCDA phase, while the K_2PTCDA phase remains unaltered. This observation indicates that a higher potassium concentration destabilizes the structure [99]. Furthermore, the annealing process facilitates the formation of a new phase with a lower potassium stoichiometry, designated as $K_{0.5}$PTCDA. This phase does not occur for direct potassium deposition. The activation energy provided by annealing the sample is needed for its formation.
All observed K_xPTCDA phases exhibit a point-on-line epitaxy [97, 99]. The focus of this section will be on the $K_{0.5}$PTCDA and K_2PTCDA phases, whose properties are listed in Table 3.1 for comparison. Their properties are similar to the ones of the cesiated and subsequently annealed PTCDA/Ag(111) systems, which will be the subject of this thesis.
In order to facilitate the discussion of the structural properties of the K_xPTCDA, an illustration of their real space geometry is necessary. Figure 3.6 compares scanning tunneling microscopy (STM) images of the two different K-doped PTCDA phases in comparison to the

Table (3.1) Structural properties of the different K_xPTCDA phases on Ag(111) (x = 0, 0.5 and 2). a_1 and a_2 are the length of the real space unit cell vectors, α the angle between $\mathbf{a_1}$ and $\mathbf{a_2}$, β the angle between $\mathbf{a_1}$ and the $[\bar{1}01]$ direction of the Ag substrate, γ the angle of the long molecular axes to the nearest high-symmetry direction of the surface and A as the unit cell area. The superstructure matrix refers to a unit cell of the Ag(111) surface with an obtuse angle of 120° between the unit cell vectors. The values of the pristine phase are taken from [24, 100] and the values of the K-doped phases from [97, 99].

K atoms per PTCDA molecule	Superstructure matrix	a_1 (Å)	a_2 (Å)	α(°)	β(°)	γ(°)	A (Å^2)
0	$\begin{pmatrix} 7 & 1 \\ 2 & 5 \end{pmatrix}$	18.9	12.6	89.0	7.6	2 17	238.6
0.5	$\begin{pmatrix} 6.04 & 5.00 \\ -2.44 & 4.00 \end{pmatrix}$	16.10	16.23	91.25	50.77	3 32	264.0
2	$\begin{pmatrix} 3.16 & 0.16 \\ 0.98 & 5.98 \end{pmatrix}$	8.92	16.05	108.60	2.63	21	135.7

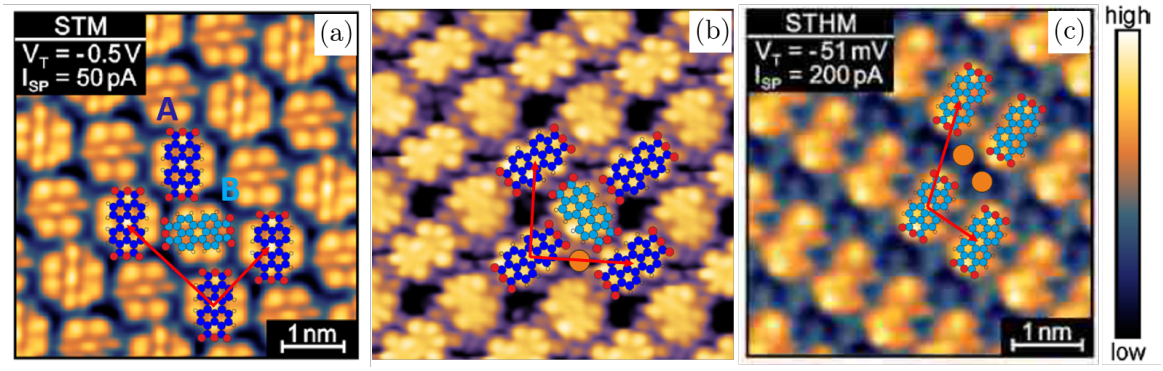

Figure (3.6) STM images for different K_xPTCDA phases. (a) Pristine PTCDA, (b) $K_{0.5}$PTCDA and (c) K_2PTCDA on Ag(111). Superimposed are the real space models and unit cells of the different structures. PTCDA molecules oriented along (off) high-symmetry directions of the Ag substrate are depicted in light (dark) blue and K atoms in orange. (a) and (c) adapted with permission from Ref. [97]. Copyright © 2015 American Chemical Society. (b) adapted with permission from Ref. [99]. By courtesy of Torsten Fritz. Copyright © 2019 American Physical Society.

pristine PTCDA/Ag(111) phase discussed in the section above. The images were obtained from references [97] and [99]. The real space models and unit cells have been superimposed.

In the pristine phase, the molecules occur in a herringbone structure with an angle between the molecules of 89°. One molecule is almost aligned to a high-symmetry direction of the Ag(111) surface (2° discrepancy), while the other molecule forms an angle of 17° to the nearest high-symmetry direction of the surface [24]. Subsequent to potassium doping, a "windmill" structure emerges for the $K_{0.5}$PTCDA phase, thereby forming a nearly rectangle alignment between neighboring molecules. A total of four molecules are found to surround a potassium atom in close proximity to their short edges, resulting in the K atom exclusively neighboring the carboxylic oxygen atoms of the PTCDA molecule [99]. The molecular reorientation is accompanied by an enlargement of the unit cell size. The real space unit cell is composed of two molecules, one aligned approximately along a high-symmetry direction of the Ag substrate (approximately 3° discrepancy; light blue molecule in Figure 3.6 (b)), while the other molecule is oriented 32° to the nearest high-symmetry direction of the surface. It has been determined that every unit cell contains only one potassium atom. Since there are two PTCDA molecules per unit cell the phase is designated as $K_{0.5}$PTCDA. Each PTCDA molecule interacts with two potassium atoms. However, a nonuniform distribution of elec-

tron density indicates that the molecules interact more strongly with one potassium atom than with the other, suggesting that the two molecules in the unit cell are not equivalent. The effect on the orbital energies of the different molecules, as observed in the case of the pristine PTCDA system, remains to be elucidated.
A thorough examination of the $K_{0.5}$PTCDA structure in STM unveils a 1×2 superstructure manifested as intensity modulations [99]. The superstructure is undetectable in LEED experiments due to the striking similarity of the scattering form factors among the distinct molecules, resulting in diffraction spots that are barely discernible and mostly below the detection threshold. The origin and the consequence of the superstructure on the electronic properties of the system remain uncharted in the extant literature [99].
Further doping of the $K_{0.5}$PTCDA phase results in a parallel alignment of the molecules in the K_2PTCDA phase, exhibiting alternating rows of potassium atoms and PTCDA molecules [97]. The adsorbate unit cell closely follows the direction of the substrate unit cell, with a 2.63° discrepancy. However, the molecular orientation significantly deviates from the nearest high-symmetry direction of the Ag(111) surface by 21° (4° uncertainty). The adsorbate unit cell angle undergoes an expansion and adopts an obtuse configuration. This transformation is accompanied by a substantial decrease in the unit cell's area, as it now contains only a single molecule.
An investigation of the electronic structure of the K_2PTCDA phase reveals a shift of the molecular orbitals to higher binding energies and a complete filling of the LUMO. This phenomenon indicates a metal-to-semiconductor phase transition, as the pristine PTCDA phase has already metallic character due to its partially filled LUMO [98]. This transition is a well-documented occurrence in the field of doped organic semiconductors [118–120], though it stands in contrast to the behavior exhibited by inorganic semiconductors under similar conditions. The occupation of the LUMO is the result of an accumulation of electron density in the π-orbital system, in proximity to the potassium atoms. The charge transfer predominantly originates from the potassium atoms. This process is accompanied by a back-donation of electrons around the oxygen atoms [98]. The manifestation of this phenomenon is evident in an increased electron density between the potassium atoms and the oxygen groups (carboxylic and anhydride), accompanied by a decrease in electron density between the oxygen atoms and their neighboring carbon atoms. The alteration in the work function upon the introduction of dopant atoms is attributed to this rearrangement of charges. The electronic structure of the $K_{0.5}$PTCDA phase remains elusive.
NIXSW measurements of the K_2PTCDA phase reveal that the observed change in the electronic properties is concomitant with an increase in adsorption height of the entire molecule [98]. This observation indicates that potassium doping leads to the decoupling of the π-electron system from the surface, despite the occurrence of additional electron transfer to the LUMO. Additionally, a structural change in the molecules occurs. The carboxylic oxygens are no longer bend towards the surface, as it is the case for the pristine phase (see Section 3.1.1). In the K_2PTCDA phase, these oxygen atoms exhibit a bending upwards, analogous to the anhydride oxygens, resulting in their placement above the potassium atoms. This observation signifies the interaction of the oxygen groups with the dopant atoms. Notably, the geometrical information concerning the PTCDA molecules within the $K_{0.5}$PTCDA remains to be elucidated.
Following the comprehensive overview of the pristine PTCDA and potassium-doped systems, the subsequent sections of this chapter present the results of the research on cesium-doped monolayers of PTCDA on an Ag(111) surface.

3.3. Cs-doped PTCDA on Ag(111)

Following the presentation of the structure and electronic properties of the pristine PTCDA/Ag(111) system and the two potassium-doped phases $K_{0.5}$PTCDA and K_2PTCDA on Ag(111), the focus will shift to the research on cesium-doped PTCDA monolayers on Ag(111). The research will be mainly concentrated on two aspects: the geometric properties of the system and its electronic structure. With respect to the geometric structure, the primary inquiries pertain to the occurrence of dopant-dependent formations of well-ordered structures, as evidenced by the potassium-doped PTCDA phase, and the distinguishing characteristics of these phases in comparison to the case of potassium doping. A central question is whether the larger size of cesium compared to potassium (1.08× larger van der Waals radius [121] and 1.26× larger ionic radius [122]) has any effect on the geometric properties of the systems. It is reasonable to hypothesize that steric effects might lead to a different molecular arrangement in the cesium-doped phases compared to the potassium-doped phases discussed in Section 3.2. Moreover, the greater electrostatic attraction of potassium compared to cesium can be attributed to its smaller size. This prompts the question of whether this phenomenon also exerts influence on the molecular ordering process upon doping. However, given the relatively minor disparity in electrostatic attractions between cesium and potassium, the resulting influence is expected to be less significant than that of steric effects.
In the course of the investigation into the electronic properties, the objective is to ascertain whether the electrostatic interaction of the molecular system with the cesium atoms exerts a substantial influence on the orbital structure. Furthermore, the investigation will explore how the doping process affects the balance between molecule-substrate and intermolecular interactions. A particular emphasis is placed on structural phases comprising more than one molecule per unit cell. This study will explore whether the energetic difference between differently oriented molecules in the unit cell, as seen in pristine PTCDA/Ag(111), prevails and, if so, whether it is reduced or amplified.
The structural properties of the systems will be investigated using low energy electron diffraction (LEED). Following this investigation, the electronic structures of the systems examined by momentum microscopy will be discussed.

3.3.1. Structural Reorientation of PTCDA on Ag(111) upon Cs-doping

Several samples of one monolayer PTCDA on Ag(111) were doped with cesium using varying dopant concentrations for the purpose of investigating the effect of cesium doping on the films' structural and electronic properties. Subsequent to this process, the samples were subjected to annealing at 373 K, a step which resulted in phase transitions and the emergence of two distinct, well-ordered, compact phases. The present section is devoted to the analysis of the cesium-induced structural changes of the PTCDA monolayer films.

Figure 3.7 displays LEED images of the Cs_xPTCDA phases for increasing concentrations of cesium. The images were recorded by Benjamin Stadtmüller at the Peter-Grünberg Institute in Jülich using a spot profile analysis low energy electron diffraction (SPA-LEED). The diffraction image in Figure 3.7 (a) corresponds to the phase with lower Cs concentration, while the image in (d) corresponds to the phase with higher Cs concentration. The phases are designated as $Cs_{0.5}$PTCDA and Cs_2PTCDA, respectively, as will be elucidated subsequently. The LEED images in (b) and (c) illustrate intermediate dopant concentrations. For the $Cs_{0.5}$PTCDA and Cs_2PTCDA phases, LEED patterns were found to be entirely distinct from those of the pristine phase (see Figure 3.7 and Figure 3.2 (a)). The former is predominantly composed of ring-like arrangements of diffraction spots, while the latter exhibits distinct pairs and elliptical motifs of diffraction spots. For intermediate dopant concentrations, a transition from the $Cs_{0.5}$PTCDA phase towards the Cs_2PTCDA phase is

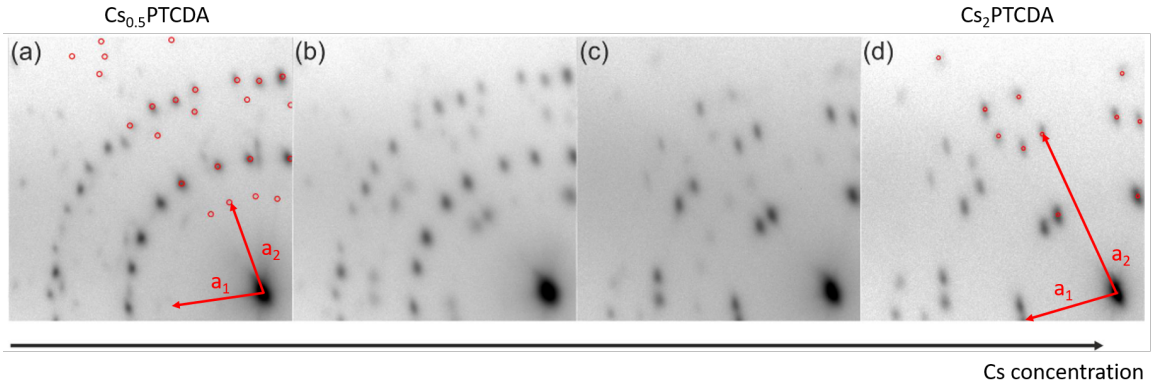

Figure (3.7) LEED images for different concentrations of cesium doped PTCDA on Ag(111). (a) $Cs_{0.5}$PTCDA phase. (b), (c) transition of the LEED pattern upon further Cs doping. (d) Cs_2PTCDA phase. The red dots mark the registered spots for the fitting procedure and the arrows indicate the momentum space unit cell vectors. LEED images captured by Benjamin Stadtmüller.

Table (3.2) Structural properties of the different Cs_xPTCDA phases on Ag(111) (x = 0, 0.5 and 2). a_1 and a_2 are the length of the real space unit cell vectors, α the angle between $\mathbf{a_1}$ and $\mathbf{a_2}$, β the angle between $\mathbf{a_1}$ and the $[\bar{1}01]$ direction of the Ag substrate, γ the angle of the long molecular axes to the nearest high-symmetry direction of the surface and A as the unit cell area. The superstructure matrix refers to a unit cell of the Ag(111) surface with an obtuse angle of 120° between the unit cell vectors. The values of the pristine phase are taken from [24, 100].

Cs atoms per PTCDA molecule	Superstructure matrix	a_1 (Å)	a_2 (Å)	α(°)	β(°)	γ(°)	A (Å^2)
0	$\begin{pmatrix} 7 & 1 \\ 2 & 5 \end{pmatrix}$	18.9	12.6	89.0	7.6	2 17	238.6
0.5	$\begin{pmatrix} 6.07 & 0.98 \\ 2.49 & 6.42 \end{pmatrix}$	16.3	16.2	88.7	8.6	0 30	264.0
2	$\begin{pmatrix} 6.12 & 1.07 \\ 0.30 & 3.35 \end{pmatrix}$	16.4	9.3	105.9	9.4	30	145.8

visible (see Figure 3.7 (b) and (c)) with both phases coexisting on the surface. The absence of any additional spots indicates that no stable phase with an intermediate Cs-stoichiometry exists.
The superstructure matrices and structural properties of the different cesiated PTCDA monolayer films on Ag(111) were extracted by fitting the experimental LEED images (red circles in Figure 3.7). The resulting data are enumerated in Table 3.2. For the pristine PTCDA phase, the obtained values are in agreement with literature [100–103]. The superstructure matrices for the doped phases in addition to the LEED images confirm a point-on-line growth with respect to the substrate. This loss of commensurability can result in different molecule-substrate interaction strengths as the contributions of local bonds can be weakened.

Upon cesium doping, the unit cell undergoes a transition from a rectangular to a more square-like configuration, accompanied by an increase in the area of the $Cs_{0.5}$PTCDA unit cell. The angle between the unit cell vectors and the orientation towards the high-symmetry direction of the silver substrate remains approximately constant. In the Cs_2PTCDA phase, the unit cell undergoes a reduction in size along the direction of $\mathbf{a_2}$. Concurrently, the angle between the two unit cell vectors becomes more obtuse. Notably, the unit cell's orientation with respect to the high-symmetry direction of Ag(111) remains largely unchanged.
A comparison of the area of the unit cells of the cesiated systems to the size of a PTCDA

molecule ($A = 119.5\,\text{Å}^2$ estimated from the area per molecule in the pristine PTCDA/Ag(111) unit cell) reveals that the $Cs_{0.5}$PTCDA phase consists of two molecules per unit cell, while the Cs_2PTCDA unit cell contains only one molecule.
The assignment of the stoichiometry of 0.5 cesium atoms per PTCDA molecule for the phase with low dopant concentration and 2 cesium atoms per PTCDA molecule for the phase with high dopant concentration is determined by a comparison of the LEED images in Figure 3.7 to LEED images of the potassium-doped system in the studies of Zwick et al. [97, 99]. The strong resemblances of the diffraction patterns and the striking similarity of the derived structural properties of the low Cs-concentration phase and the $K_{0.5}$PTCDA phase, as well as for the high Cs-concentration phase and the K_2PTCDA phase, substantiate the conclusion that the stoichiometries of the Cs-doped phases are equal to that of the K-doped phases. Furthermore, molecular orientations in the unit cells are similar between the cesium- and potassium-doped phases, as will be deduced from a POT analysis in the next section.
The cesium-doped phases bear a striking resemblance to the potassium-doped PTCDA phases regarding their structural properties. This similarity is notable despite the larger size of cesium, which has a van der Waals radius that is 1.08× larger [121] and an ionic radius that is 1.26× larger [122] than that of potassium. The similarities in the structural properties of the Cs_xPTCDA and the K_xPTCDA films suggest that the electrostatic potential of the alkali metal atoms is a principal factor in determining these properties, independent of atomic size. The outermost orbital of alkali metals is invariably a s-orbital, occupied by one electron. This results in an overall similar dopant-molecule and dopant-substrate interaction behavior for all alkali metals. Nonetheless, the interactions within the unit cell appear to deviate, as evidenced by the documented observation that the Cs_2PTCDA phase exhibits enhanced stability in comparison to the K_2PTCDA phase [116].
A Cs_4PTCDA phase analogous to the K_4PTCDA phase reported by Zwick et al [97, 99] and Baby et al. [98] could not be observed. This is most likely due to the annealing of the sample above 100 K following the doping process. Given the documented degradation of K_4PTCDA at such elevated temperatures [99], it is reasonable to anticipate a similar behavior from a possible Cs_4PTCDA phase.
After elucidating the structural properties of the cesium-doped PTCDA monolayer films on Ag(111), the focus will shift to the electronic structures of the systems. A primary objective of this study is to address the question of whether the two molecules comprising the $Cs_{0.5}$PTCDA phase unit cell are nonequivalent. This question arises in light of the observation that, in pristine PTCDA/Ag(111), the molecules in the unit cell exhibit nonequivalence [53]. Additionally, studies utilizing STM for the investigation of the $K_{0.5}$PTCDA phase have indicated the presence of nonequivalence, attributed to a divergent distribution of electron density on the molecules [99].

3.3.2. Charge-Transfer and Electronic Structure of Cs-Doped PTCDA on Ag(111)

Following the identification of the various cesiated PTCDA phases, the samples were examined using momentum microscopy to ascertain the effects of doping on the electronic properties. Subsequent to this, the molecular orientations will be determined from the photoemission angular distributions (PADs). Furthermore, the difference in the orbital energy level alignment of molecules with different orientations will be discussed. The investigation's focal point is the two frontier orbitals, HOMO and LUMO. These orbitals are pivotal in understanding the interaction of the molecules with the substrate and the dopant atoms [92, 98, 99].
The $Cs_{0.5}$PTCDA phase was studied using unpolarized light of the He I_α line of a vacuum ultraviolet light source at the NanoESCA setup in Kaiserslautern. For the reference system of a pristine PTCDA layer and the Cs_2PTCDA phase, p-polarized synchrotron radiation

with an energy of $h\nu = 35\,\text{eV}$ was utilized at the NanoESCA setup of the ELETTRA synchrotron in Trieste. The data of the latter phases were acquired by Benjamin Stadtmüller. Despite the utilization of different photon energies, the obtained data sets are comparable due to the negligible dispersion of PTCDA as a 2D molecule along the k_z direction and its flat orientation on the surface [56]. Any potential damage to the molecular layer due to significant photon flux of the high energy incident synchrotron radiation was mitigated by rapidly scanning the sample surface with the synchrotron beam.

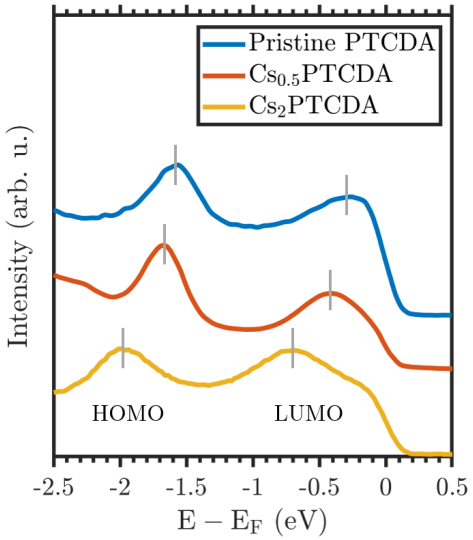

Figure (3.8) Photoelectron spectra of the different Cs_xPTCDA (x = 0, 0.5, 2) phases in the energy region of the HOMO and LUMO. The LUMO is filled by charge transfer from the Ag substrate. The gray lines indicate the central energetic positions of the molecular orbital peaks.

Angle-resolved photoemission data were recorded in the energy region of the two frontier valence orbitals. The corresponding photoelectron spectra are presented in Figure 3.8. As previously mentioned in Section 3.1, the LUMO of the pristine PTCDA phase on Ag(111) becomes partially occupied by charge transfer from the substrate in a hybridization process of the LUMO which has π-orbital character, with the orbitals of the Ag atoms. Upon cesium doping, the LUMO becomes further occupied, with a 89 % filling for the $Cs_{0.5}PTCDA$ and a complete filling for the Cs_2PTCDA phase. This occupation behavior indicates a metal-to-semiconductor phase transition, which is a common transition to occur for the doping of 2D organic semiconductors [118–120]. The extent to which the higher occupation of the LUMO is attributable to increased charge transfer into the molecule or reduced backdonation of electrons at the O-Ag bonds remains to be elucidated. It is proposed, that the latter has a discernible effect as the system transitions from a commensurate superstructure for pristine PTCDA/Ag(111) to a point-on-line one for the $Cs_{0.5}PTCDA$ phase. This transition results in altered adsorption sites for every unit cell leading to a different alignment of carboxylic oxygen atoms and silver atoms, influencing the formation of covalent bonds. Additionally, molecular orientation undergoes a change, as will be seen later. The complete filling of the LUMO for the point-on-line Cs_2PTCDA phase is likely attributable to the presence of additional charge-transfer to the molecule, in comparison to the $Cs_{0.5}PTCDA$ phase.
Furthermore, with increasing dopant concentration, the orbitals shift to larger binding energies while the width of the HOMO-LUMO gap reduces (see Table 3.3). This phenomenon can be attributed to a shift in the energy levels, resulting from a distortion of the charged molecule [123]. A similar behavior in the change of the electronic structure upon doping has been observed for the potassium-doped systems [98], as previously discussed.

Table (3.3) Energetic properties of the HOMO and LUMO of Cs_xPTCDA/Ag(111) phases (x = 0.5, 2). The values are obtained by fitting Gaussian functions to the spectral peaks taking an energy-dependent background and the Fermi distribution into account. The accuracy amounts to 0.02 eV for the energetic positions of the orbitals and to 0.04 eV for the FWHM. All values are given in eV and energetic positions are referenced to the Fermi edge.

	HOMO	LUMO	HOMO-LUMO gap	$FWHM_{HOMO}$	$FWHM_{LUMO}$
PTCDA /Ag(111)	-1.58	-0.215	1.365	0.56	0.44
$Cs_{0.5}$PTCDA /Ag(111)	-1.64	-0.36	1.28	0.30	0.58
Cs_2PTCDA /Ag(111)	-1.95	-0.71	1.18	0.44	0.49

In contrast to the results observed in the potassium-doped systems, no discernible trend has been identified in the behavior of the full width at half maximum (FWHM) of the HOMO or LUMO. Baby et al. discovered a reduction of the linewidth of the spectral features upon potassium deposition, attributing this phenomenon to a doping-induced decoupling of the molecules from the substrate [98]. However, no statement regarding the $K_{0.5}$PTCDA phase was made, as only the K_2PTCDA and K_4PTCDA phases were investigated. The absence of a discernible trend in the studies conducted can be attributed to the inhomogeneous broadening of the spectral features, a consequence of the constrained experimental energy resolution. The presence of defects and contamination is suggested as another source of frontier orbital broadening. The extent to which these phenomena may influence the observed outcomes remains uncertain and requires further investigation. An analysis of the spectral features regarding the effect of doping on the molecule-substrate interaction is not as conclusive in this case as in the literature for the potassium-doped systems.

An examination of the collective behavior of cesium- or potassium-doped PTCDA on Ag(111) reveals that the disparate size and electronic properties of cesium and potassium do not exert a discernible influence on the resultant system. To obtain a more detailed perspective, the focus will now be shifted to angle- and momentum-resolved photoemission data. This approach will allow for a comprehensive analysis of the characteristic orbital emission patterns of the HOMO and LUMO.
As illustrated in Figure 3.9, a comparison is made between the momentum space images of the two frontier valence orbitals of the pristine PTCDA phase and the cesiated phases. For the latter, the CE maps are divided into two sections, with the left halves illustrating the experimental data. The right halves of the CE maps depict a reconstruction of the experimental data based on a tomographic 2D fitting approach, which will be discussed later on. All experimental CE maps were symmetrized in accordance with the Ag(111) surface symmetry to account for the linear dichroism in the angular distribution (compare Appendix A.2).

Figure 3.9 (a) and (d) show the well-known emission patterns of a pristine PTCDA monolayer caused by two differently oriented PTCDA molecules in the unit cell (compare Table 3.2) [53]. The photoemission angular distributions of the HOMO and LUMO each consist of six main intensity maxima. As already introduced above in Section 3.1, one molecule in the unit cell is oriented along a high-symmetry direction of the Ag(111) surface, while the other deviates from a high-symmetry axis by 17°. This deviation leads to the formation of side-maxima [53]. The momentum space emission patterns are unique and allow for the

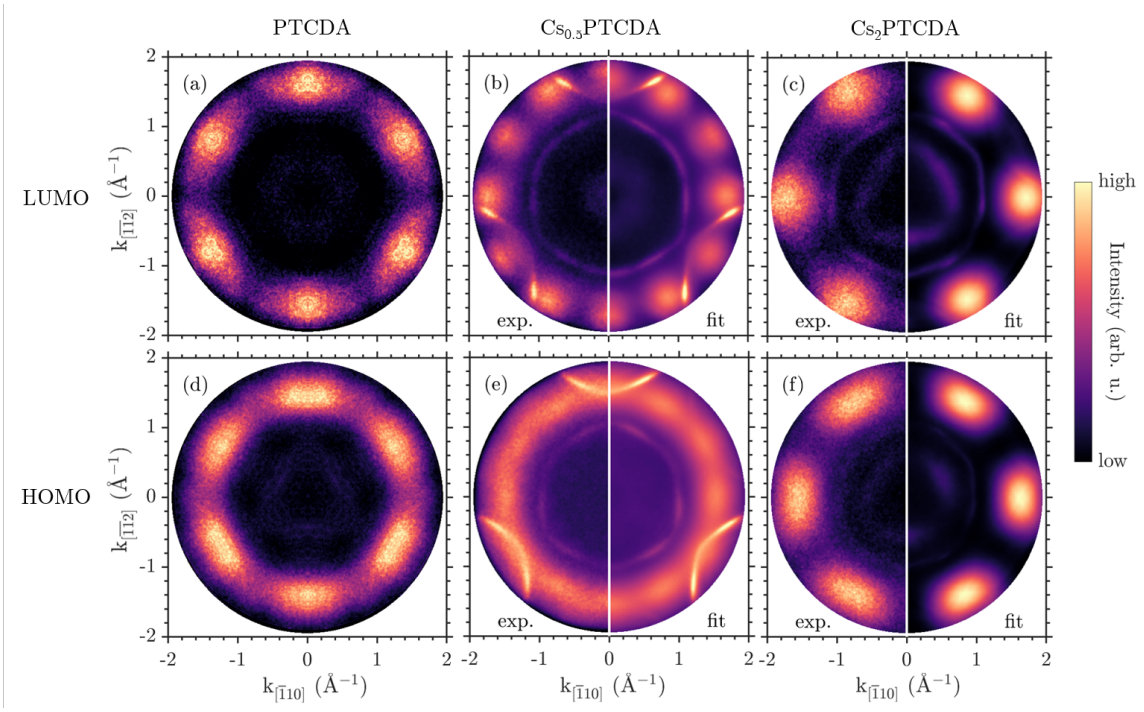

Figure (3.9) Constant energy maps of the HOMO and LUMO of the pristine PTCDA (left column), the $Cs_{0.5}$PTCDA (middle column) and the Cs_2PTCDA phase (right column) extracted at the energetic peak position of the corresponding molecular orbitals. The images of the cesiated systems are split in two. The left halves show the experimental photoemission data, while the right halves show the result of the 2D fitting procedure. The CE maps of the pristine and Cs_2PTCDA phase were obtained using a photon energy of $h\nu = 35\,\mathrm{eV}$, whereas the CE maps of the $Cs_{0.5}$PTCDA phase were acquired using a photon energy of $h\nu = 21.2\,\mathrm{eV}$.

identification of the molecular orbitals.
Upon cesium doping, a substantial change in the photoemission angular distributions is observed. For the $Cs_{0.5}$PTCDA phase, as illustrated in Figures 3.9 (b) and (e), the measured CE maps exhibit twelve intensity maxima for the LUMO and a ring-like structure for the HOMO. Conversely, for the Cs_2PTCDA phase, and thus for a higher cesium concentration, the patterns in the CE maps revert to six main emission maxima for LUMO and HOMO (see Figure 3.9 (c), (f)). For both orbitals the position of the intensity maxima exhibit a 30° rotation with respect to the maxima observed in the pristine PTCDA phase.
It is apparent that the Ag sp-bands are particularly evident in the $Cs_{0.5}$PTCDA phase, manifesting as prominent arcs in Figure 3.9 (b) and (e). The pronounced manifestation of these bands can be attributed to the utilization of an unpolarized light source during the experimental procedure. The experiments on the pristine PTCDA and the Cs_2PTCDA phase were conducted using p-polarized synchrotron radiation. It has been established that p-polarized radiation results in enhanced emission from the molecular π-orbitals when compared to the silver substrate. Consequently, the contributions of the sp-bands to the respective CE maps are comparatively weaker. This phenomenon is further elucidated by the comparison of the centers of the CE maps in Figure 3.9, where only weak molecular features occur. Consequently, employing an unpolarized light source in the experiments of the $Cs_{0.5}$PTCDA phase results in comparatively stronger emission from the Ag sp-bands.
In order to gain further insight into the composition of the measured CE maps and the molecular orientation in the different cesiated systems, a tomographic approach is employed to reconstruct and thereby disentangle the photoemission data [52]. This approach, as previously outlined in Section 3.1.2, has also been utilized in the investigation of the pristine PTCDA/Ag(111) layer by Stadtmüller et al. [53] and Willenbockel et al. [112]. In the following, a comparison will be made between the findings of this work and their results for the pristine phase.
As delineated in Section 3.1.2, the objective is to match the experimentally obtained CE maps with theoretically calculated ones. The theoretical CE maps of the involved LUMO and HOMO are calculated following the photoemission orbital tomography approach using density functional theory [32, 52, 53]. A plane-wave final state is assumed and a single free molecule rotated with its long axis horizontally is considered, as depicted in Figure 3.1. This modeling approach of the systems' CE maps, initiated from a single free molecule, assumes a weakly interacting system with a negligible effect on the overall electronic structure of the molecules. The subsequent theoretical CE maps of the PTCDA LUMO and HOMO are displayed in Figure 3.10 (a) and (b).

In order to reconstruct the experimental data, it is necessary to create a CE map for each molecule in the unit cell. In addition to this, all rotational and mirror domains must be considered when developing each CE map. All CE maps combined, this approach then encompasses all possible in-plane molecular orientations within the cesiated phase.
Assuming that the molecules for the CE maps in Figure 3.10 (a) and (d) are aligned along a high-symmetry of the Ag surface, all rotation and mirror domains are considered by applying the $p3m1$ substrate symmetry onto the CE maps of a single molecular orientation. The resulting CE maps of the LUMO and HOMO are depicted in Figure 3.10 (b) and (e). Finally, other molecular orientations that deviate from the high-symmetry directions of the Ag(111) surface may also be considered, if present. In the case of the $Cs_{0.5}$PTCDA phase, it is evident that the unit cell must comprise a second molecule with a different orientation, as can be seen by the twelve prominent intensity maxima in the LUMO CE map (Figure 3.9 (b)) in comparison to the six maxima in the theoretical CE map (Figure 3.10 (b)). It is apparent immediately that the second molecule in the unit cell must be rotated by about 30° with respect to the high-symmetry directions of the Ag(111) surface. The corresponding CE

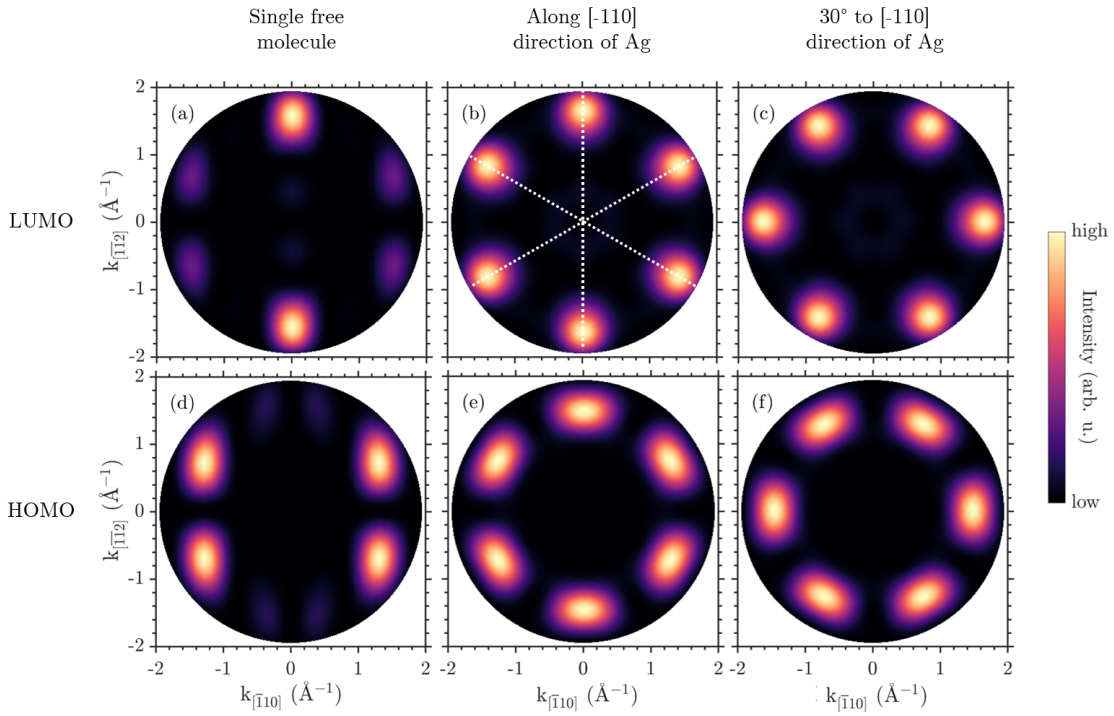

Figure (3.10) DFT calculated CE maps of the HOMO and LUMO considering different molecular orientations and domains. (a, d) HOMO and LUMO of a single molecular orientation without rotation or mirror domains. (b, e) CE maps considering all rotation and mirror domains of the Ag(111) surface for one molecule in the unit cell oriented along a high-symmetry direction of the Ag surface (molecule A). The high-symmetry directions of the Ag(111) surface are superimposed by white dashed lines in (b). (c, f) as in (b, e) but for one molecule in the unit cell deviating by 30° from the nearest high-symmetry direction of the Ag surface (molecule B).

maps of the LUMO and HOMO for this molecular orientation and all its mirror and rotation domains are shown in Figure 3.10 (c) and (f). In the preceding section, it was determined that, due to the small size of the unit cell, the Cs_2PTCDA phase contains only one molecule. As evidenced by the measured CE maps, the molecules form an angle of approximately 30° with their long axes and the nearest high-symmetry direction of the Ag(111) surface. A further examination of the molecular orientations will be presented later on.
For the tomographic reconstruction approach the function in Equation 3.1

$$F(k_k, k_y, E) = \sum_i a_i(E)\Phi_i(k_x, k_y) + b(E)I_{\text{sub}}(k_x, k_y, E) + c(E). \tag{3.2}$$

is fitted to the photoemission intensity of each measured CE map independently by means of a least-square fit routine. The fit parameters $a_i(E)$ represent the energy-resolved projected density of states (PDOS). The fitting yields a reconstructed CE map for each energy as the ones in the right halves of Figure 3.9. The components of the fit function are as follows: a constant energy-dependent background and homogeneous offset $c(E)$, a contribution from the Ag(111) substrate $I_{\text{sub}}(k_x, k_y, E)$ and a sum of the CE maps of all involved molecular orbitals and different orientation in the unit cell $\Phi_i(k_x, k_y)$.
In brief, for the 2D fit of the $Cs_{0.5}$PTCDA phase, the theoretical CE maps for molecules oriented with their long axis along the high-symmetry directions of the Ag surface (Figure 3.10 (b) and (d)) and for molecules rotated by 30° to this (Figure 3.10 (c) and (f)) will be used as a basis set. The basis set for the Cs_2PTCDA phase consists exclusively of the theoretical CE maps corresponding to a 30° rotated molecular orientation.
The execution of the fitting procedure is done by splitting the photoemission data cube into two halves along the energy direction, allowing a separate fit for the HOMO and LUMO for both cesiated phases. This is necessary to avoid contributions from the respective other orbital as their intensity maxima strongly overlap in momentum space positions. The CE maps utilized for the substrate contributions were obtained by experimental means on a clean Ag(111) surface, employing the respective photon energy. The fits are carried out in a circular ring containing the main intensity maxima ($k_{||}$ = 1.25 to 1.9 Å). The limitation of the fit to an area in momentum space only containing the main intensity maxima leads to a more robust performance. Moreover, this approach enhances the estimation of the contribution from the Ag substrate, which is frequently overestimated when regions in the center of the CE map with only weak molecular features, but comparatively significant Ag sp-bands, are included. For smaller $k_{||}$, molecular features become obscured by substrate contributions, leading to suboptimal fit performance. This phenomenon was also observed by Stadtmüller et al. [53].
The results of the 2D fitting approach for both cesiated phases are depicted in the right halves of their respective CE maps in Figures 3.9. A substantial degree of correspondence is found between the experimental data and the reconstructed images. It is evident that all features have been accurately reproduced. However, minor discrepancies in the radial extension of molecular features can be attributed to the neglect of the inner potential in the DFT calculations of the orbitals. In the absence of consideration for the inner potential, the momentum perpendicular to the surface remains constant during the transmission of the photoelectron into the vacuum. Consequently, the curvature of the PAD differs in the DFT calculation compared to the experiment. This discrepancy leads to variations in the spacing between momentum space signatures when the PAD is subsequently projected onto a 2D plane for detection. A slight displacement of the silver sp-bands is observed in the reconstructed images for the $Cs_{0.5}$PTCDA phase compared to the experimental data. This discrepancy can be attributed to a minor misalignment between the CE maps of the silver substrate and those of the cesiated phases. Furthermore, it was determined that the intensity maxima in the experiment exhibit an inhomogeneous broadening of the linewidth that is not

included in the DFT calculations. This discrepancy is most evident in the Cs_2PTCDA phase, where the maxima of the LUMO and HOMO exhibit a conspicuously larger extension in the experimental data. This phenomenon also results in a more homogeneously distributed ring for the $Cs_{0.5}$PTCDA phase HOMO. The corresponding reconstructed CE map accurately reproduces the intensity ring, while the presence of distinct single maxima on top of it is clearly discernible. This outcome is further enhanced by the existence of local impurities and defects within the sample systems.
The potassium-doped PTCDA monolayers on Ag(111) have been observed to demonstrate a dependence on the distribution of electron density on the molecule, influenced by the dopant atoms. As outlined in Section 3.2, an accumulation of electron density was found in the π-orbital system in proximity to the potassium atoms [98]. Concurrently, a reduction in electron density was observed between the oxygen atoms and their neighboring carbon atoms within the σ-orbital system, resulting in weakened bonds. It is anticipated that a comparable redistribution of electron density will occur in the cesiated systems, given the analogous electronic properties exhibited by potassium and cesium, both of which are classified as alkali metals. The CE maps of the frontier orbitals in Figure 3.9 are well replicated using calculated CE maps of a free PTCDA molecule without the consideration of any interaction with a nearby alkali atom. This strong similarity suggests that the influence of the dopant atoms on the electronic structure of the LUMO and HOMO is negligible. This outcome is in line with the expectation that the electron density of both orbitals is predominantly distributed within the perylene core, thereby rendering the orbital structure largely unaffected by changes in the oxygen groups in the vicinity of the dopant atoms. However, it is possible that this is not the case for energetically deeper-lying σ-orbitals, as it was reported for the K_2PTCDA phase that the electron density at the oxygen atoms of the molecules is influenced. A similar behavior is possible in the cesium-doped system, which could influence the momentum space signatures of the corresponding σ-orbitals. However, the σ-orbitals were not investigated in the experimental series. In such cases, a potential for distinction might emerge in the CE maps observed in experiments and those calculated by POT using a free molecule.
A more thorough examination of the $Cs_{0.5}$PTCDA phase is warranted, with the objective of discerning potential energetic disparities among the molecules with different orientations within the unit cell, as it occurs in the pristine PTCDA phase [53, 112]. To do so, an energy distribution curve (EDC) is extracted along a circular path through the intensity maxima of the molecular orbitals' PADs. The result is displayed in Figure 3.11 (a). The molecular orbitals are clearly identifiable: the HOMO forms a broad intensity region around $-1.5\,\mathrm{eV}$ and the LUMO consists of distinct intensity maxima close to the Fermi edge. The vertically propagating bright lines correspond to the Ag sp-bands. An examination of the LUMO reveals an energy offset between neighboring intensity maxima. The maxima closer to the Fermi edge, as indicated by the dark blue line, correspond to the molecular orientation along the high-symmetry directions of the Ag(111) surface. In contrast, the intensity maxima that are energetically lower lying (indicated by the light blue line) stem from molecules deviating by approximately 30° from the high-symmetry directions of the Ag surface. The discrepancy in energy is discernible for the HOMO as well; however, it is less pronounced due to the superposition of momentum space features exhibited by molecules with different orientations. Moreover, the silver sp-bands exhibit increased proximity and elevated intensity at this particular energy. This complicates the determination of an energy offset between different directions in momentum space.

The energy disparity between the two molecules in the unit cell can be ascertained by implementing the 2D fitting procedure outlined above for each energy. This approach yields the energy dependence of the fit parameters a_i. Subsequent to this, the Fermi distribution

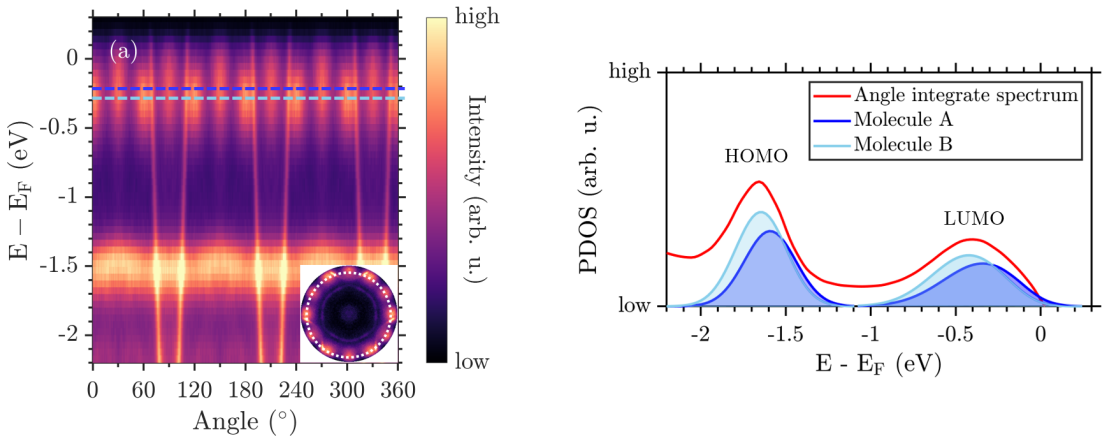

Figure (3.11) (a) EDC of the $Cs_{0.5}$PTCDA phase extracted along a circular path through the centers of the intensity maxima of the molecular orbitals. The inset shows the CE map of the LUMO withe the EDC path highlighted as a white dashed line. The blue lines highlight the energy difference of the differently oriented molecules in the unit cell (molecule A in dark blue, molecule B in light blue). (b) Angle integrated photoelectron spectrum of $Cs_{0.5}$PTCDA with projected density of states (PDOS) for the two frontier orbitals for both molecular orientations in the unit cell. The PDOS of the LUMO were divided by the Fermi distribution. The PDOS are not to scale compared to the photoelectron spectrum.

is utilized to transform the aforementioned parameters into the density of states projected onto the different molecular orbitals (PDOS). In the case of the $Cs_{0.5}$PTCDA phase, this approach enables the differentiation of the PDOS between different molecular orientations, which are incorporated into separate CE maps within the basis set of the fitting routine.
As illustrated in Figure 3.11 (b), the angle-integrated photoelectron spectrum of the $Cs_{0.5}$PTCDA phase is depicted in red, alongside the PDOS of the two molecules with different orientations within the unit cell. To enhance visibility, the height of the PDOS has been increased compared to the photoelectron spectrum. As previously evident in the EDC in Figure 3.11 (a), the PDOS resulting from the tomographic fitting reveals an energy difference between the differently oriented molecules in the unit cell. The molecule deviating from high-symmetry directions of the Ag(111) surface (designated as molecule B) has energetically deeper-lying orbitals compared to the molecule aligned along high-symmetry directions (molecule A).
The energetic positions of the individual orbitals are listed in Table 3.4 and compared with values of the pristine PTCDA/Ag(111) and heringbone (HB) PTCDA/Ag(110) phases taken from literature [53, 112]. It should be noted that the labeling of the molecules for the herringbone PTCDA phase on Ag(110) has been switched compared to literature so that the molecule oriented along the more close-packed direction of the Ag surface ($[\bar{1}01]$ direction or symmetry equivalent) is labeled as A. The energy difference between the HOMO of differently oriented molecules is 50 meV in the $Cs_{0.5}$PTCDA phase, similar to the PTCDA/Ag(111) phase. For the LUMO, the $Cs_{0.5}$PTCDA phase has an energy difference of 90 meV, approximately half that of the pristine PTCDA/Ag(111) system.

The observed energy differences of the molecules A and B are consistent with the differences in the herringbone PTCDA phase on Ag(110). Given the point-on-line nature of both phases, there is an absence of a common adsorption site for molecules A or B. Consequently, all effects caused by site-specific molecule-substrate interactions are averaged out. Therefore, the difference in energy levels is predominantly due to intermolecular interactions. Given the comparable molecular alignment in the $Cs_{0.5}$PTCDA phase and the HB PTCDA/Ag(110) phase, it is anticipated that the energetic differences originate from similar mechanisms. For

Table (3.4) Energetic properties of the HOMO and LUMO of Cs_xPTCDA/Ag(111) (x = 0.5, 2), PTCDA/Ag(111) and heringbone (HB) PTCDA/Ag(110) for the differently oriented molecules in the unit cell. Molecule A is oriented along a high-symmetry direction of the Ag surface, molecule B deviates from a high-symmetry direction. The values of the $Cs_{0.5}$PTCDA phase are obtained by fitting the parameters a_i of the tomographic approach. The accuracy amounts to 0.02 eV. The values of the pristine phases are taken from literature [53, 112, 113]. The labeling of the molecules for the HB PTCDA phase on Ag(110) has been switched compared to literature so that the molecule oriented along the more close packed direction of the Ag surface ($[\bar{1}01]$ direction or symmetry equivalent) is labeled as A. All values are given in eV and energetic positions are referenced to the Fermi edge.

	$HOMO_A$	$HOMO_B$	$LUMO_A$	$LUMO_B$
PTCDA /Ag(111)	-1.56	-1.60	-0.13	-0.30
HB PTCDA /Ag(110)	-1.85	-1.89	-0.60	-0.69
$Cs_{0.5}$PTCDA /Ag(111)	-1.60	-1.65	-0.33	-0.42
Cs_2PTCDA /Ag(111)	-	-1.95	-	-0.71

the HB phase on Ag(110), it was found that the herringbone structure's non-orhtogonal unit cell angle of 91° leads to different lengths of the O-H bonds between the two molecules. This results in the emergence of distinct quadrupole fields at the molecular locations, thereby inducing alterations in the energy offsets of the molecular orbitals [112, 113].
It should be noted that only the molecular arrangement and, by extension, the intermolecular interactions in the $Cs_{0.5}$PTCDA phase on Ag(111) and the PTCDA/Ag(110) are comparable. This is not the case for the molecule substrate interaction, which is significant for PTCDA on Ag(110) [112, 124]. In this case, the LUMO is found to be fully occupied and positioned well below the Fermi edge.
In conclusion, cesium doping exerts a significant impact on the electronic properties of the system by diminishing the influence of the substrates, thereby enabling a pronounced predominance of intermolecular interactions. This phenomenon can be attributed to a change in the geometric structure of the adsorbate layer becoming point-on-line. The molecular alignment of the $Cs_{0.5}$PTCDA phase becomes analogous to the HB phase on Ag(110), with comparable energy offsets for the two molecules in the unit cell. This emphasises the aforementioned defining influence of the molecular environment.
In order to draw parallels between the $Cs_{0.5}$PTCDA to the $K_{0.5}$PTCDA phase, it is reasonable to expect similar electronic properties and a comparable energetic splitting between the orbitals of the different molecules in the unit cell. This expectation is predicated on the similar geometric structure and molecular orientation (see Tables 3.1 and 3.2) [99]. Consequently, a predominant influence of the intermolecular interactions and the molecular environment on the electronic properties of the system is proposed.
The PDOS of molecules A and B, obtained from the tomographic fitting approach and illustrated in Figure 3.11 (b), can be used to calculate the degree of occupation of the LUMO for the two molecules. The results obtained indicate an 88 % filling of the LUMO for molecule A and a 94 % filling for molecule B, with a margin of error of ±3 %. This finding corresponds to the 89 % occupation of the averaged LUMO, as listed in Table 3.3.
A 1×2 superstructure was identified in STM studies of the $K_{0.5}$PTCDA phase. As outlined in Section 3.2, the differences in the scattering form factor are too subtle for the superstructure to be visible in LEED. Two possible origins for the emergence of the superstructure that result in intensity variations between neighbouring molecules of the same orientation in

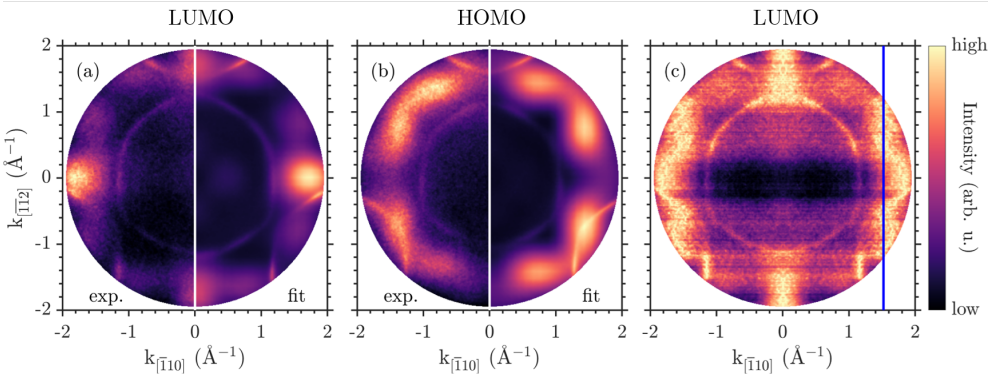

Figure (3.12) Not symmetrized CE maps of the $Cs_{0.5}$PTCDA phase LUMO (a) and HOMO (b) depicting a fourfold symmetry. The signal originates predominantly from a single domain. The left halves of the CE maps show the experimental data, the right halves show the result of the 2D fitting procedure. (c) CE map of the $Cs_{0.5}$PTCDA phase LUMO with each row of pixels along k_{-110} normalized to its maximum intensity. The blue line indicates the position of the side-maxima.

STM can be postulated. The first explanation is that the adsorption height of each second molecule may be different. This can result in an energetically favourable configuration from the upwards bending of the oxygen groups due to the interaction with the dopant atoms. Alternatively, an energetic shift of the molecular orbitals resulting from different intermolecular or molecule-substrate interactions could be a contributing factor. The consequence of both of these factors would be an energetic offset of every second molecule with the same orientation. As demonstrated in Figure 3.11 (a), the EDC does not reveal any indications of a superstructure in momentum microscopy. Moreover, the analysis of the tomographic fitting approach revealed no energetic splitting of the PDOS for the same molecular orientation. The absence of signatures of a possible superstructure can be attributed to the magnitude of the effects on the electronic structures. It is noteworthy that both explanations would result in only a marginal alteration to the properties of the frontier orbitals. Any such effects would be negligible in comparison to the experimental resolution, particularly given that the measurements were conducted at ambient sample temperatures.

In relation to the preceding analysis and discussion of the $Cs_{0.5}$PTCDA phase, it is important to note that the experimental images obtained do not align with the $p3m1$-symmetry of the Ag(111) surface prior to symmetrization. As illustrated in Figure 3.12 (a) and (b), the CE maps of the $Cs_{0.5}$PTCDA phase LUMO and HOMO, that were not symmetrized according to the substrate's $p3m1$ symmetry, reveal a deviation from the expected symmetry. It is evident that the molecular features exhibit a symmetry of $p4mm$, which is in contrast to the $p3m1$ symmetry of the Ag(111) surface. It is important to note that the data in Figure 3.12 was mirrored along the $k_{[\overline{1}12]}$-direction to enhance contrast and visibility. It has previously been verified that this symmetry is also present in the raw data. The recorded photoemission angular distributions of the molecular orbitals resemble the expected emission pattern of a single domain consisting of only two present molecular orientations aligned approximately 90° to each other. In order to verify this, the tomographic fitting approach presented above was employed to reconstruct the experimental raw data. As a molecular basis, the DFT calculated CE maps of single molecules in Figure 3.10 (a) and (d) and their by 90° rotated counterparts are used. The resulting reconstructed CE maps of the LUMO and HOMO are displayed in the right halves of Figure 3.12 (a) and (b). The substantial similarity between the experimental and reconstructed CE maps serves to reinforce the supposition that the presence of a single domain is predominant. In order to conduct a more thorough investigation into the impact of any potential rotation or mirror domain, a detailed analysis of the

distribution of the intensity maxima of the LUMO is necessary. In contrast to the HOMO, the superimposed emission features of the LUMO lead to twelve distinct maxima, enabling a better identification compared to the emerging ring-like structure of the HOMO (see Figure 3.9 (b) and (e)). The question is whether the side-maxima in Figure 3.12 (a) stem from a single domain or if they also contain contributions from rotation or mirror domains. In the event that the latter is the case, the side-maxima should display a more circular distribution. Conversely, if they originate from a single domain, they should be distributed along straight lines. In order to resolve this issue, Figure 3.12 (c) present the CE map of the LUMO, but with adjusted contrast. It is evident that the side-maxima follow a straight line (highlighted by the vertical blue line), contradicting the circular arrangement expected for rotation or mirror domains. Furthermore, no indication of any additional feature arising from a rotation or mirror domain is visible. Consequently, it can be deduced that the measured sample spot is predominantly constituted by a single domain. The influence of other rotation or mirror domains is negligible.

It is surprising that only a single domain is probed with the momentum microscopy setup, given that the field of view is several hundred μm in size. It is clear that there are other rotation and mirror domains on the surface, as demonstrated by the LEED measurements presented in Section 3.3.1, but incidentally an area that is predominantly occupied by a single domain was measured with momentum microscopy. It is expected that the observed state is a special case of thermodynamic non-equilibrium that is energetically favorable in this specific condictions due to some kind of perturbation of the system. The fabrication of the $Cs_{0.5}$PTCDA structure commences with the growth of a PTCDA multilayer on Ag(111). It is acknowledged that, within this structure, all rotation and mirror domains co-exist in equal measure in a state of thermodynamic equilibrium. Subsequent to the cesium-doping of the monolayer samples, the necessary activation energy for the formation of the $Cs_{0.5}$PTCDA phase is provided by annealing (see Appendix A.1). It is proposed that after the annealing process, thermodynamic equilibrium is lost, resulting in the formation of large domains with the predominance of the observed one. It is hypothesised that the formation of large domains may occur in a manner analogous to the growth of NTCDA on Cu(001) [125]. It has been observed that NTCDA grows in a dendrite-like structure with dilute molecular chains of long-range order for low coverages. In the initial phase, the molecules arrange themselves into a well-ordered two-dimensional network structure that extends over a substantial surface area, while also leaving numerous voids. Subsequent deposition of molecules occurs, gradually filling these voids and thereby occupying the available space within the predefined structure. The process of molecular deposition leads to the formation of a fractal, dendrite-like growth, which is facilitated by the molecular structure. The molecules exhibit a preferential attachment behaviour, attaching to the ends of the molecular chains rather than to their sides. This results in the enlargement of the predefined space for the single domain.

The formation of the $Cs_{0.5}$PTCDA phase is hypothesized to occur through fractal expansion at the inception of the annealing process, resulting from perturbations other than the annealing process, such as ordered contaminations, for instance carbon clusters. Consequently, the dendrites of a solitary $Cs_{0.5}$PTCDA domain infiltrate different rotation and mirror domains of the previous herringbone PTCDA/Ag(111) structure. Subsequently, the regions between the dendrites transition into the $Cs_{0.5}$PTCDA phase, assimilating into the large-scale ordered domain spanned by the dendrites.

In the initial presentation of the CE maps of the $Cs_{0.5}$PTCDA phase, the maps were symmetrized according to the $p3m1$ surface symmetry. This approach was adopted because the electronic properties of different rotation and mirror domains are equivalent. This was done in order to simulate the emission patterns of the whole sample, thus eliminating the influence of an accidentally obtained sample out of thermodynamic equilibrium. The observation

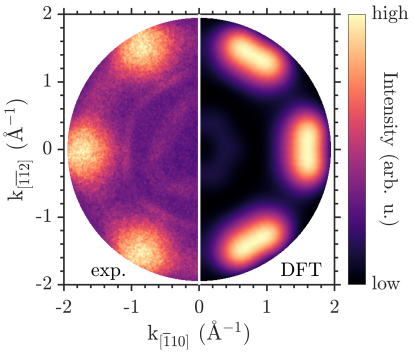

Figure (3.13) Comparison of the experimentally obtained CE map of the Cs_2PTCDA LUMO (left half) with DFT calculated one (right half). For the calculated CE map the molecular orientation with respect to the nearest high-symmetry direction of the Ag(111) substrate was chosen to be 21° according to the molecular orientation found by Zwick et al. in the K_2PTCDA phase [99].

of a dominant single domain in momentum microscopy, with a relatively extensive field of view, constitutes a non-equilibrium exception in sample growth. Therefore, the objective in symmetrizing the data according to the $p3m1$-symmetry was to provide a representation of the electronic properties of the entire structure. The latter allows a better comparability with the literature and possible further experiments. It is important to note that all analysis steps that were carried out for the $p3m1$-symmetrized data were also performed on the data set that has only been mirrored along the $k_{[\bar{1}\bar{1}2]}$-direction. All analysis steps, particularly the tomographic fitting procedure and the analysis of the energetic offsets of the molecular orbitals for molecules A and B, yielded the same results within the established error bounds regardless of the applied symmetrization.

Finally, the aim is to reexamine the subject of molecular orientation in relation to the substrate. As illustrated in Figure 3.12, the $p4mm$-symmetric CE maps reveal that the two molecules per unit cell are oriented approximately 90° to each other. Specifically, one molecule (A) is aligned along a high-symmetry direction of the Ag(111) surface. These observations align with the findings reported by Zwick et al. for the $K_{0.5}$PTCDA phase (refer to Tables 3.1 and 3.2) [99]. The minor discrepancies observed are likely attributable to the limitations of the experimental setup.
With respect to the molecular orientation in the Cs_2PTCDA, the findings indicate a 30° deviation from the high-symmetry direction of the silver surface, contrasting with the 21° angle proposed for the K_2PTCDA phase (see Tables 3.1 and 3.2 for comparison) [97]. The present study aims to ascertain whether a molecular alignment of 21° would correspond to the experimental findings. To this end, the CE map in Figure 3.13 compares the experimentally observed PAD (left half) with a DFT-calculated CE map representing a molecular alignment of 21° to the nearest high-symmetry direction of the substrate (right half). It is evident that the orbital features in the calculated CE map are considerably broader than those observed in the experiment. This discrepancy can be attributed to the presence of mirror domains, whose contributions no longer align with the experimental data. Consequently, it is concluded that the molecular orientation in the Cs_2PTCDA phase is approximately 30° with respect to the nearest high-symmetry axis of the Ag(111) surface, rather than 21° as observed for the K_2PTCDA phase. The observed discrepancy in molecular orientation between the cesium- and potasssium-doped systems can be hypothesized to originate from the larger size of the cesium atoms. However, given the structural similarity between the potassium- and cesium-doped phases, it is also conceivable that the molecular orientation in the K_2PTCDA phase may as well approximate 30° with respect to the nearest high-symmetry axis of the Ag(111) surface. A definitive statement cannot be made as the difference in orientation lies

at the boundary of the combined error bars of the experiment and for the K_2PTCDA phase reported in the literature [97]. The electronic structure of the K_2PTCDA phase could be investigated using a momentum microscopy study, which would provide further insight into this matter.
The molecular orientation in the cesiated PTCDA/Ag(111) systems has been determined, and the structural properties of the unit cell from the LEED experiments in the previous section have been taken into account. The adsorption geometry of the systems is therefore finalized. Figure 3.14 presents ball models that illustrate the various Cs_xPTCDA/Ag(111) phases (x = 0, 0.5, 2), integrating all pertinent structural information. The proposed structural models bear a strong resemblance to the potassium-doped PTCDA phases that were presented in Section 3.2 (see Figure 3.6). Consequently, it can be concluded that there is no structural difference between potassium- or cesium-doped PTCDA monolayers on Ag(111), despite the larger size of the cesium atoms. It is plausible that the electronic structures of these phases are comparable, as the electrostatic properties of potassium and cesium are analogous due to their shared classification as alkali metals.
In the subsequent section, a concise summary of the findings concerning the structural and electronic properties of cesium-doped PTCDA on Ag(111) will be provided. This will be followed by a discussion of potential avenues for further research.

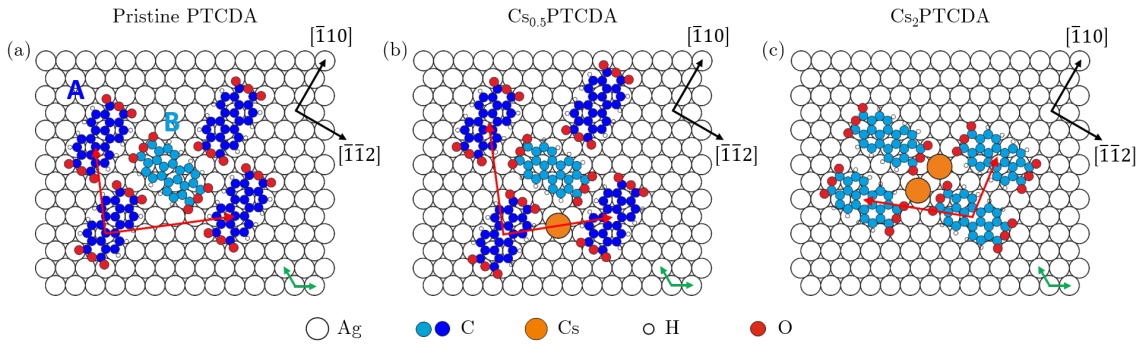

Figure (3.14) Ball model of the different Cs_xPTCDA phases (x = 0, 0.5, 2) on Ag(111). Molecules oriented along (molecule A) and off (molecule B) high-symmetry directions of the Ag surface are painted dark and light blue respectively. The green arrows indicate the unit cell of the silver substrate. The black arrows highlight the high-symmetry axes of the Ag(111) surface that served as reference axes for the displayed constant energy maps.

3.3.3. Summary and Outlook

In this section, the findings are summarized. The investigation focused on cesium-doped monolayers of PTCDA/Ag(111), leading to the identification of two distinct, well-ordered, and close-packed structural phases that are contingent upon the dopant concentration. The structural properties of the two phases were determined using low energy electron diffraction (LEED), revealing a point-on-line growth. The observed phases exhibited geometric properties analogous to those of the $K_{0.5}$PTCDA and K_2PTCDA phases, thereby facilitating the determination of the cesium stoichiometry as a $Cs_{0.5}$PTCDA and Cs_2PTCDA phase. A momentum microscopy study was conducted to ascertain the molecular orientation within the unit cell. The combination of these findings with structural information concerning the adsorbate layers, as determined by LEED, facilitated the development of a real-space model that comprehensively characterizes both cesium-doped PTCDA phases.
Despite the differences in size and electrostatics between cesium and potassium analog molecular structures form. This observation indicates that the common electronic properties of the two elements, as alkali metals, are determining factors in the molecular ordering.

In consideration of the electronic structures of the Cs_xPTCDA phases on Ag(111), it was observed that the LUMO was further filled upon cesium doping, resulting in a complete filling for the Cs_2PTCDA phase. This phenomenon is indicative of a doping-induced metal-to-semiconductor phase transition, which is commonly found in organic semiconducting materials. A comparison to literature based on the K_xPTCDA systems suggests a concomitant increased adsorption height and decoupling from the substrate.
The constant energy maps that were measured could be reconstructed using the photoemission orbital tomography (POT) approach of a free-standing PTCDA molecule. This finding suggests that the molecule substrate interaction and the electrostatic interactions with the cesium dopant atoms are sufficiently weak to not alter the orbital structure of the molecular adlayer. Furthermore, a tomographic fitting approach based on POT revealed an energy difference of the two differently oriented molecules in the $Cs_{0.5}$PTCDA phase unit cell. This energy difference is comparatively diminished in relation to that observed in the pristine PTCDA/Ag(111) system. The observed alteration in the energy offset can be attributed to different adsorption sites and changes in molecular orientation. The first results from a transition from a commensurate to a point-on-line superstructure. The latter is responsible for the variation in intermolecular interactions, thereby defining the energy level offset within the system, irrespective of the presence of dopant atoms.
Alkali metal doping of organic semiconductors on noble metal surfaces thus results in the formation of ordered, close-packed structures that exclusively depend on the stoichiometry of the dopant atoms. The reorientation of the molecules is thereby independent of the species of alkali metals. Energetic offsets between differently oriented molecules in the unit cell of point-on-line systems are solely dependent on the molecular orientation and thus on the intermolecular interactions.

In the end, an outlook on further possible research directions will be given. Doping, particularly with alkali metals, has emerged as a potent and adaptable approach for manipulating the structure and properties of molecular adlayers. The process of doping involves the transfer of electrons from the dopant to the adsorbate system, resulting in a redistribution of charge within the system. This charge transfer modifies the molecule–substrate coupling, influencing the molecular orientation and, consequently, altering intermolecular interactions. This results in significant changes in the potential energy landscape of the adsorbate system. Consequently, alkali metal doping can facilitate the formation of compact, ordered molecular layers through electrostatic interactions. Furthermore, the doping level can often be precisely tuned, allowing systematic control over the resulting molecular architectures and their associated electronic properties.
Given the substantial research that has already been conducted on the subject of alkali metal doping of organic adsorbate layers on metallic and insulating surfaces [97–99, 114, 116, 117, 119, 120, 126–131], it is recommended to redirect the focus to other substrates. The growth of molecular layers on surfaces with weak interaction has recently attracted considerable attention with respect to potential future applications [132–136]. These surfaces exhibit a passive nature, predominantly interacting with molecular layers through weak physisorption. Consequently, the growth of ordered structures that are stable at room temperature poses a significant challenge [132, 134, 135, 137]. This hinders the practical applications of these hybrid interfaces [134]. However, this very property also offers an ideal platform for studying subtle intermolecular interactions and doping-induced effects without strong hybridization obscuring the picture.
An approach of utilizing alkali metal doping for the purpose of achieving the formation of compact, ordered molecular layers on weakly interacting surfaces is proposed. The hypothesis is that the electrostatic forces induced by alkali metal doping could favor the structure formation by strengthening intermolecular interactions. Furthermore, the growth of different

phases by an adjustment of the dopant concentration would be highly desirable. Consequently, alkali metal doping would facilitate a straightforward modification of the geometric and electronic properties of the system.
An intriguing class of materials that has recently attracted considerable interest is topological insulators (TIs), which are characterized by weak (surface-)interactions. These materials exhibit a unique electronic structure, characterized by conducting surface states protected by time-reversal symmetry, coexisting with an insulating bulk. The surfaces of topological insulator exhibit a passive nature, predominantly interacting with molecular adlayers through weak physisorption [137, 138], thereby preserving the unperturbed character of the topological surface state [135, 138]. The aim of these studies is primarily to either exploit the topological nature of the surface state of the substrate or to break the time-reversal symmetry with the adsorbate layer and thus change the physical properties of the substrate [135, 136, 138–141].
It is suggested to start the investigation with potassium or cesium doping of PTCDA or tetracyanoquinodimethane (TCNQ) monolayers on Bi_2Se_3. It has been established that both molecular species are capable of forming close-packed, self-assembled layers on the TI Bi_2Se_3 [135, 137]. Consequently, they serve as a suitable model system to investigate dopant-induced changes in the electronic and geometric structures. Thermal desorption measurements, in conjunction with mass spectrometry, serve as a means to ascertain whether the doping has resulted in a reduction or augmentation of the structural stability of the hybrid system.
In the subsequent phase of this study, the exploration of alkali metal doping of (metal-) phthalocyanines on TI surfaces is proposed. PCs exhibit a strong interaction with the underlying TI, resulting in the formation of ordered and resilient adsorbate layers [134, 136, 139, 141]. The occupation of the central metal d-orbital determines the structural properties of the PC superstructure. The objective of this study is to manipulate this occupation (or the occupation of a corresponding molecular orbital with high electron density on the central metal atom) through alkali metal doping, with the aim of inducing a structural phase transition.
Finally, the doping of disordered molecular monolayers, such as C_{60} [139], is proposed. In this instance, the objective is to establish a structural organization in the adsorbate layer facilitated by the electrostatic interactions initiated by the dopant atoms.
It is hereby envisioned that all proposed sample systems shall be investigated through a combined study of low energy electron diffraction (LEED), scanning tunneling microscopy (STM) and momentum microscopy. Utilizing LEED and STM, the aim is to ascertain the (long-)range order of the adsorbate layer and to characterize its structural properties. The implementation of momentum microscopy will facilitate the investigation of the electronic structure of the systems and the determination of molecular orientations within the unit cell. In addition, thermal desorption experiments employing mass spectrometry can provide insights into the robustness of the achieved superstructures.

Following an investigation of a system with weak molecule-substrate interactions, the subsequent chapter explores the opposite regime of strong hybridization in the monolayer C_{60} on Cu(111) system.

4 Photoemission Orbital Tomography Study of a Monolayer C_{60} on Cu(111)

In the preceding chapter, the focus was on a hybrid interface characterized by a weak electronic coupling between the molecules and the metal surface. In contrast, this chapter examines a monolayer of considerably hybridized C_{60} molecules on the Cu(111) surface. C_{60} was selected as a prototypical sample system due to its chemical robustness and high symmetry. In combination with the Cu(111) substrate several different adsorption geometries with varying degrees of wave function overlap can be observed [142, 143]. Following a presentation of the molecular properties, a summary is provided of the geometric and electronic properties of the interface system. A momentum microscopy study, accompanied by photoemission orbital tomography calculations, was performed to examine the influence of hybridization and different adsorption geometries on the band structure of the hybrid system. The objective of this study is to achieve a qualitative understanding of considerably hybridized molecule-metal interfaces and quantify the adsorption-induced changes of the electron wave functions.

4.1. The Molecule C_{60}

C_{60} is a molecule composed of 60 carbon atoms. It is classified as a fullerene, which is an allotrope of carbon. Theoretical predictions of C_{60} were first made by Eiji Osawa in 1970 [144], and it was synthesized and correctly identified in 1985 by a team led by Harold Kroto, Robert Curl, and Richard Smalley [145], who were awarded the 1996 Nobel Prize in Chemistry for their discovery. The synthesis was accomplished through laser-induced vaporization of carbon from a graphite disc into a high-density helium flow. A more efficient technique for synthesizing C_{60} in large quantities (up to several grams) involves the creation of an arc discharge between graphite electrodes in a helium atmosphere [146].
The 60 carbon atoms in the molecule are arranged in the form of a truncated icosahedron with a diameter of approximately 7 Å [147]. A ball-and-stick model of the C_{60} molecule is displayed in Figure 4.1 (a). In honor of the architect Richard Buckminster Fuller, C_{60} has been designated as "Buckminsterfullerene," an honorable tribute to its resemblance to Fuller's iconic geodesic domes. The icosahedral symmetry of the C_{60} molecule is described by the point group I_h, which is the point group of highest possible symmetry [148]. This elevated degree of molecular symmetry contributes to a notable degree of robustness [149–151]. The molecule's structure consists of 12 pentagons and 20 hexagons. Each pentagon is completely surrounded by hexagons. Conjugated double bonds separate neighboring hexagons. As a member of the icosahedral point group, C_{60} exhibits three distinct types of high symmetry axes: C_2 axes through the center of double bonds, C_3 axes through the faces of two opposite hexagons, and C_5 axes through the center of opposite pentagons.

Each carbon atom is bonded to its neighboring atoms by either a single bond or a conjugated double bond. When considering a C_{60} molecule as a rolled-up carbon sheet, these bonds primarily stem from a sp^2 configuration, with an additional sp^3 character due to the non-

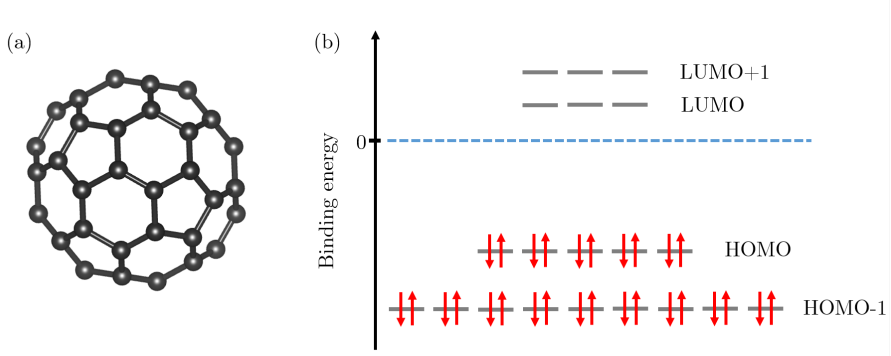

Figure (4.1) (a) Ball and stick model of a C_{60} molecule. The structural data for the model was taken from the molecular orbital data base of P. Puschnig, University of Graz [152]. (b) Energy level diagram of the molecular orbitals of a free C_{60} molecule. Similar to [153].

planarity of the bond configuration [149]. The remaining 60 electrons that do not contribute to localized bonds between neighboring carbon atoms occupy π-orbitals and are delocalized across the carbon cage [154].
In Figure 4.1 (b) the energy level diagram of C_{60} including the two highest occupied molecular orbitals (HOMOs) and the two lowest unoccupied molecular orbitals (LUMOs) is illustrated. Each molecular orbital is degenerate and consists of a multiplet of energy levels [153]. It is imperative to acknowledge that the orbital designated as HOMO-1 in Figure 4.1 (b) is, in strict terms, comprised of two distinct, irreducible orbitals (one 4-fold and the other 5-fold degenerate). These orbitals are closely spaced in energy, making differentiation between them challenging. Notwithstanding, they are generally treated as a single orbital in the extant literature [23, 46, 155]. In this work, this convention will be followed.
Following the presentation of the free C_{60} molecule, the subsequent step is to elucidate its properties on noble metal interfaces. The focus will be directed towards the Cu(111) surface.

4.2. Structural Properties and Adsorption Geometry of Monolayer C_{60} on Cu(111)

First, the adsorption geometry of C_{60} on noble metal surfaces, with a particular emphasis on the Cu(111) surface is discussed. Depending on the substrate, the adsorption behavior of C_{60} can exhibit significant variation. The molecular ordering is thereby defined by two aspects: strong molecule-substrate interactions and weaker intermolecular interactions. The former can be of two types: ionic or covalent. In the case of ionic bonding, charge is transferred between molecules and the substrate. Due to the large electron affinity of C_{60}, 1-3 electrons per C_{60} are transferred from the metal surface to the molecules, creating a permanent negative charge. The amount of transferred electrons depends on the adsorption configuration. These charges induce a positive counterpart by forcing a redistribution of the metal surface's mobile electrons, leading to an attractive potential between the molecules and the substrate. In the case of covalent bonding, electrons are shared between the substrate and the adsorbed molecules. The weaker intermolecular interactions are of van der Waals character [156]. The adsorption of C_{60} on Cu(111) is influenced by both covalent and ionic bonding [27].
Upon adsorption of C_{60} molecules on a surface, the molecules try to align with the surface's symmetry. This process dictates the specific part of the molecule that interacts with the surface, given that C_{60} possesses three distinct rotational symmetry axes, as previously delineated. The alignment of the unit cell vectors of the C_{60} superstructure with respect to the substrate determines the size and orientation of the resulting superstructure unit cell [156]. The adsorption geometries of C_{60} on the noble metal surfaces Cu(111), Ag(111) and Pt(111),

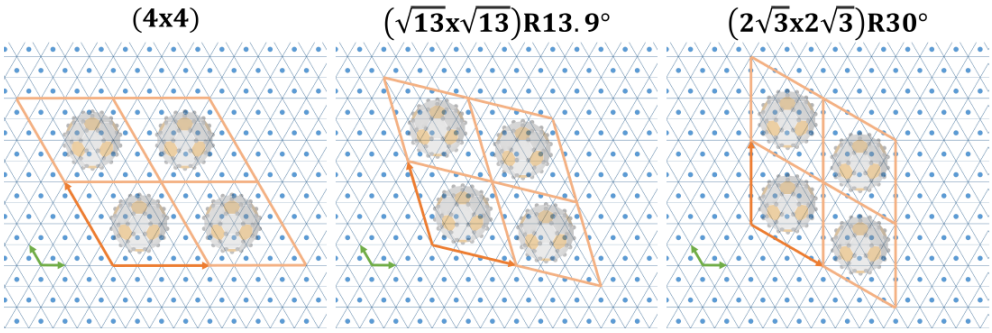

Figure (4.2) Unit cells of C_{60} monolayers on different noble metals. left: 4×4 superstructure on Cu(111), center: $(\sqrt{13} \times \sqrt{13})$R13.9° on Ag(111), right: $(2\sqrt{13} \times 2\sqrt{13})$R30° on Pt(111). Crossing points of the blue lines indicate positions of the substrate atoms of the first layer, whereas dots indicate the position of the second layer atoms. The orange and green arrows denote the lattice vectors of the C_{60} superstructure and metal substrates respectively. With courtesy of Norman Haag from [47], similar to [156].

will be discussed as an example. On all three surfaces, C_{60} forms commensurate, closed-packed superstructures, as illustrated in Figure 4.2. The blue lines in the figure represent the atomic rows of the metal substrates, with crossing points denoting the position of atoms from the uppermost layer. Positions of atoms in the second metal layer are indicated as blue dots. The orange and green arrows represent the lattice vectors of the C_{60} superstructure and metal substrates, respectively. The lattice constant of bulk C_{60} is approximately four times larger than the lattice constant of the Cu(111) surface, resulting in a 4×4 superstructure. Conversely, for Ag(111) and Pt(111), the disparity in lattice constants between the C_{60} bulk and the substrate proves to be too substantial, prompting a rotation of the superstructure unit cell to reduce strain [156]. This structural adjustment leads to the formation of a $(\sqrt{13} \times \sqrt{13})$R13.9° superstructure on Ag(111) and a $(2\sqrt{13} \times 2\sqrt{13})$R30° superstructure on Pt(111). This consideration of the superstructure geometries of C_{60} on different metal surfaces also illustrates the rational behind using the Cu(111) surface as a substrate in all subsequent experiments involving C_{60}. The congruence of the different symmetry domains of the surface and the molecules leads to coinciding signatures in momentum space, thereby simplifying the interpretation of measurement data. Consequently, the adsorption geometry of C_{60} on the Cu(111) surface will be discussed in more detail.

C_{60} molecules adsorb on Cu(111) in three distinct configurations [142, 143, 157]. The distinguishing characteristics of these configurations include the adsorption height of the molecules and the degree of reconstruction of the surface. Figure 4.3 provides a visual representation of these configurations in a ball-and-stick model, illustrating a side view and a top-down perspective. The latter includes four superstructure unit cells. To enhance visibility, the atoms of the distinct Cu layers are color-coded. For all three adsorption configurations, the C_{60} molecules are oriented with a hexagon pointing towards the Cu(111) surface. This configuration enables the molecules to align with the three-fold symmetry of the Cu(111) surface, as evidenced by the literature [156]. The first adsorption configuration is the unreconstructed surface. In this configuration, the molecules exhibit the greatest distance from the surface, positioned centrally over a Cu atom in the top most layer. In the second configuration the removal of the central Cu atom beneath the C_{60} molecules enables a closing-in of the molecules on the surface. This configuration is denoted as "single-atom vacancy". The final configuration is the nanopit, which is a seven-atom vacancy beneath the C_{60} molecules, allowing them to dig into the surface. This configuration enhances the molecule-metal interactions, as 15 carbon atoms form covalent bonds with the 12 surrounding copper atoms [142, 157]. This

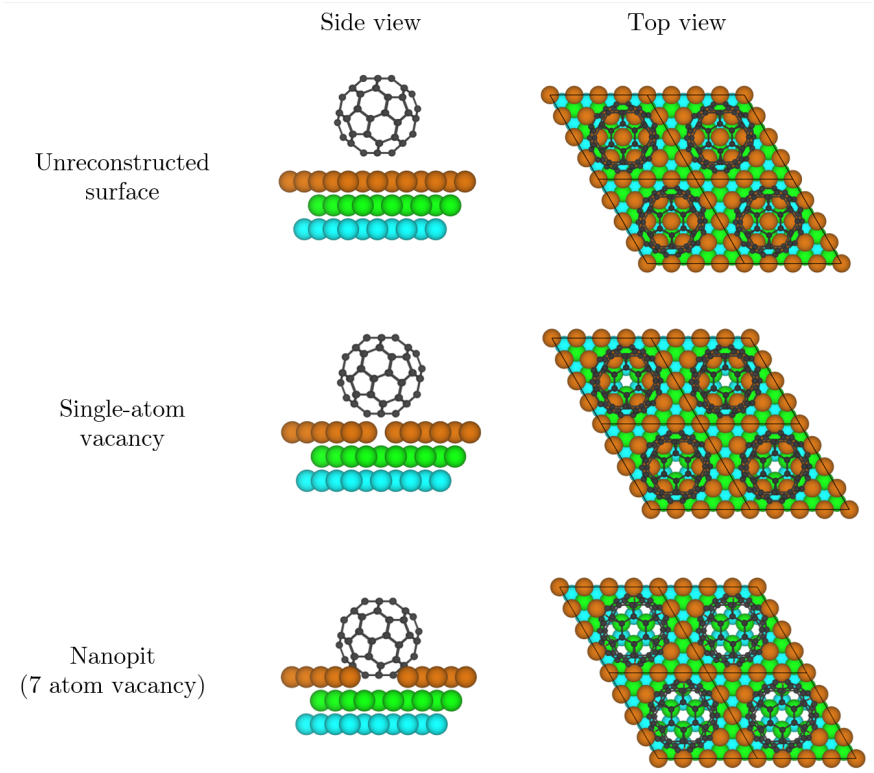

Figure (4.3) Three different adsorption configurations for C_{60} on Cu(111) with varying adsorption heights in a ball-and-stick representation. The left column shows a side view, omitting Cu atoms in the first layer for better visibility of the vacancies. The right column depicts a top view geometry of four neighboring unit cells. For better differentiation, the three Cu layers were colored dissimilar. Similar to [142, 143].

phenomenon, however, also results in a distortion of the first Cu layer, a detail that is not illustrated in Figure 4.3 [142]. The activation energy required for the formation of vacancies is counterbalanced by the shortening of the Cu-C_{60} bonds, thereby facilitating the formation of all three configurations at ambient temperature [143, 156]. Furthermore, post-growth annealing or C_{60} deposition under elevated sample temperatures favors the formation of the nanopit configuration, as this is the energetically most favorable one [142, 143, 157].
It is noteworthy that each of the three adsorption configurations enumerated above is also capable of occurring for a molecular orientation that has been rotated by 60° around the surface normal. This orientation differs from the previous one in that the C_{60} hexagons are surrounded by alternating pentagons and hexagons as bordering structures, resulting in a rotation axis that is only three-fold symmetric aligned with respect to the surface normal. Additionally, the formation of nanopits on Cu(111) is only possible due to matching lattice constants and aligning the molecular symmetry axes with the surface symmetry axes. In the case of Ag(111) or Pt(111), for instance, the single-atom vacancy is the preferred adsorption configuration. This phenomenon can be attributed to the reduced number of surface atoms per superstructure unit cell, which results in the single-atom vacancy configuration maximizing the potential for carbon-metal bonds [142].
Following this overview of the adsorption geometry of C_{60} on different metal surfaces, with a particular focus on Cu(111) as the substrate for all subsequent experiments, the investigation of the electronic properties of the sample system will be presented.

4.3. Momentum Microscopy of a Monolayer C_{60} on Cu(111)

The present study commences with an examination of the electronic structure of the monolayer C_{60}/Cu(111) sample system. According to the literature, C_{60} displays pronounced hybridization with the Cu(111) surface [27, 156]. The ensuing discourse will thus start with the identification of hybrid states and the determination of the influence of the molecule-substrate interaction on the electronic properties of the C_{60} molecule as well as the Cu substrate.
Monolayer C_{60} films were grown on the Cu(111) surface. For further elucidation regarding the sample preparation and the molecular deposition, please refer to Appendix A.1. The sample system was investigated through the use of momentum microscopy with the unpolarized He I_α line ($h\nu = 21.2\,\mathrm{eV}$) of a vacuum ultraviolet gas discharge lamp, model HIS 14 HD, manufactured by FOCUS GmbH. The relative intensity of the He I_β light emission is merely 1.2 to 1.8 % of the He I_α intensity [77]. It will be excluded from the further discussion since no features attributable to photoemission processes caused by He I_β light could be identified in the energetic region of interest.
The data presented was subjected to the data analysis procedure delineated in the Appendix A.2. It is imperative to underscore that the data underwent a symmetrization process to enhance contrast, in accordance with the $p3m1$ symmetry of the Cu(111) surface, unless specified otherwise.

As illustrated in Figure 4.4 (a), the photoelectron spectrum of the monolayer C_{60}/Cu(111) sample system (red) is compared with the photoelectron spectrum of the bare Cu(111) surface (blue) within the energy range encompassing the highest occupied molecular orbital (HOMO) and lowest unoccupied molecular orbital (LUMO). The total intensity within the photoemission horizon was integrated for every energy to obtain the spectra. In addition, a spectrum of the monolayer C_{60}/Cu(111) sample system that was extracted from a circular

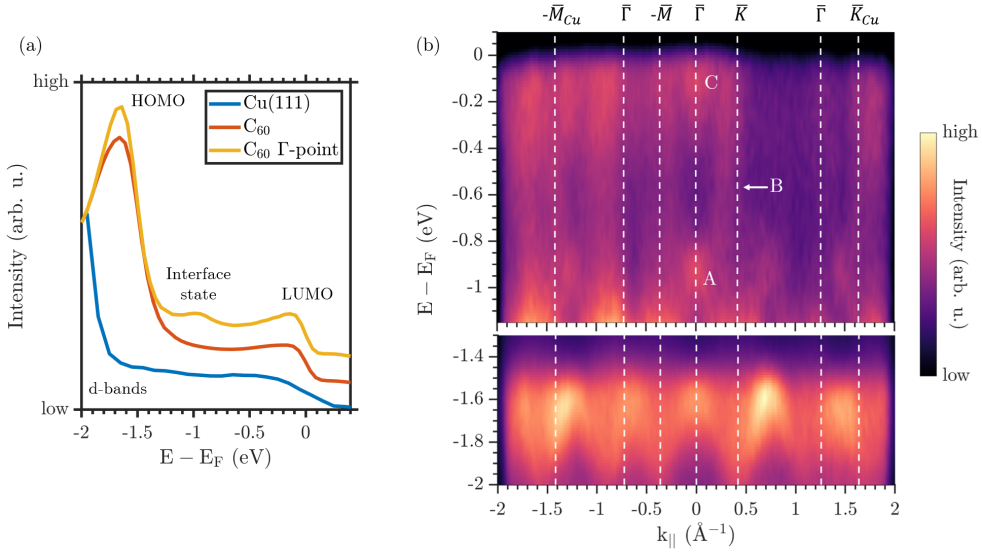

Figure (4.4) (a) Photoelectron spectra of the clean Cu(111) surface (blue) and the C_{60} monolayer on Cu(111) interface (red and orange). The red spectrum is integrate over the whole photoemission horizon, whereas the orange spectrum is extracted from a circular region with a radius of $0.15\,\mathrm{Å}^{-1}$ around the $\overline{\Gamma}$-point. The spectra are scaled independently for better visibility. (b) Energy distribution curve (EDC) of the monolayer C_{60}/Cu(111) sample system along the $-\overline{M\Gamma K}$-direction in the same energy range as depicted in the spectra. For better visibility the energy range was separated in two parts with independent adjustment of the contrast.

region with a radius of $0.15\,\text{Å}^{-1}$ around the $\overline{\Gamma}$-point is depicted in yellow. The spectrum of the Cu(111) surface displays the energetic region of the sp-bands. The substantial increase in intensity observed at approximately $E - E_F = -1.7\,eV$ corresponds to the onset of the Cu d-bands. At the onset, the HOMO is located at $E - E_F = -1.65\,eV$ within the valence band of the C_{60}/Cu(111) hybrid system. In addition, an increase in intensity is observed around the Fermi edge, which corresponds to the LUMO state. The LUMO is partially occupied by charge transfer from the Cu. This phenomenon can be attributed to the substantial electron affinity exhibited by C_{60} [158]. In the spectrum of the monolayer C_{60}/Cu(111) system that was extracted around the $\overline{\Gamma}$-point, an additional peak becomes visible at $E - E_F = -0.95\,eV$. This peak has been attributed to an interface state in the literature [27, 159]. The occurrence of an interface state serves as an indication of hybridization between the C_{60} molecules and the Cu substrate.

To further investigate the discussed energy region, it will be resorted to momentum-resolved photoemission data. The corresponding energy distribution curve (EDC) to the displayed spectra is depicted in Figure 4.4 (b). To enhance contrast and visibility, the EDC is segmented into two sections. The lower portion of the EDC illustrates the energy region of the HOMO. In the upper part of the figure, the energetic range is delineated from the onset of the HOMO up to the Fermi edge. The EDC paths were extracted along the $-\overline{M\Gamma K}$-direction. High symmetry points of the surface Brillouin zones (BZs) of the C_{60} superstructure and the Cu(111) surface are indicated by white dashed lines and labeled accordingly.

First, the lower EDC in Figure 4.4 (b), which illustrates the energetic region of the HOMO, is discussed. The EDC does not demonstrate a flat intensity distribution, which is characteristic of many molecular orbitals and localized molecular states. Instead, it exhibits a substantial dispersion. The visible dispersive band oscillates with a periodicity that is consistent with the C_{60} BZ, and its wave crests are located at the $\overline{\Gamma}$-points. A similar dispersion of the frontier valence orbitals has also been observed in the electronic structure of multilayer C_{60} films. This phenomenon can be attributed to the wave function overlap of neighboring C_{60} molecules' π-orbitals (see Section 5.3 and references [22, 23, 47]). In contrast to the multilayer C_{60} system, where two bands are observed in the energetic region of the HOMO, only one dispersive band is evident in the monolayer system on Cu(111). In addition, an elevated oscillation frequency is observed in the case of multilayer C_{60} films [22, 23, 47]. The observed discrepancies between the monolayer C_{60}/Cu(111) system and the C_{60} multilayer films are attributed to the significant impact of the Cu(111) surface on the molecular orbital.

In the following discussion, the upper EDC will be examined. As illustrated in Figure 4.4 (b), this EDC encompasses the energetic region of the onset of the HOMO peak until the partially filled LUMO and the Fermi edge. A variety of different states have been observed that do not resemble the sp-bands of the bare Cu(111) surface and span the whole energy range. The C_{60} molecule is characterized by the absence of states between the HOMO and LUMO. Consequently, the emergence of these states is attributed to the hybridization of C_{60} with the Cu substrate. Accordingly, the energy region illustrated is designated as the "interface region", as it is predominantly influenced by the hybridization between molecular and metal states at the interface.

The prominent feature at the $\overline{\Gamma}$-point, with an energy of approximately $E - E_F = -0.95\,eV$, is designated as "A". It corresponds to the observed interface state peak in the photoelectron spectrum extracted around the $\overline{\Gamma}$-point in Figure 4.4 (a). Subsequently, an upward-bending parabola, designated "B," comes into view, extending to the boundaries of the BZ around the Fermi edge. The aforementioned behavior was also observed by Tamai et al. [27]. Furthermore, an observation was made in [27] of a downward-bending parabola commencing at feature A. This state, however, is not as distinctly apparent in the data presented here. It has been posited that both parabolas and the bright feature A at the $\overline{\Gamma}$-point are interface states arising from a hybridization of the Cu atoms with the six lowest carbon atoms of C_{60}

that face the surface [27].
The bright feature at the $\overline{\Gamma}$-point close to the Fermi edge, labeled as "C", is the Shockley surface state of the Cu(111) surface, which has been shifted to higher energies as a result of the interaction between the molecule and the substrate [27]. Due to the limited visibility of the surface state, it remains impossible to ascertain whether the surface state is affected by hybridization or if its curvature remains unaltered and the observed shift is a consequence of the molecular layer exerting a push-back effect on the surface state electrons, thereby displacing them to the bulk. A substantial decrease in the intensity of the surface state is observed in comparison to the bare Cu(111) surface. The molecular adlayer is the reason for this phenomenon. It introduces the probability of additional scattering events for photoelectrons originating from the Cu substrate. The presence of the surface state is surprising, given that the C_{60} monolayer is closed and no free regions of the bare Cu substrate are expected. This is because the monolayer was prepared by desorption of the C_{60} multilayer (see Appendix A.1). The visibility of the Shockley surface state through a closed monolayer of adsorbate molecules is a common occurrence in weakly interacting systems; however, this phenomenon rarely occurs in the case of hybridized interface systems. In this particular instance, it is anticipated that the surface state will undergo quenching [160]. Its delocalization over the entire surface usually makes the Shockley surface state sensitive to hybridization, since the overlap of electron wave functions with the adsorbate is easily achieved. Tamai et al. hypothesized that the surface state survives due to an absence of hybridized or C_{60}-derived bands in the sp-projected band gap [27]. Despite the occurrence of momentum-selective hybridization [161], the complete absence of hybridization between the surface state and the C_{60} molecules due to a momentum mismatch is surprising.
It was determined in the literature that the surface state couples to the intramolecular C_{60} phonons, as evidenced by a reduced intensity at approximately $-0.16\,\mathrm{eV}$ for all parallel momenta [27]. This reduction in intensity is not observable in the data presented in Figure 4.4, presumably due to insufficient statistics and a coarse sample of the energy region in question. As illustrated in Figure 4.4 (b), the EDC of the interface region exhibits a complex momentum structure that deviates from the periodicity of the C_{60} superstructure. This can be observed in the absence of the feature A at the $\overline{\Gamma}$-points of the neighboring BZs. Therefore, a more thorough examination of the momentum space structures is warranted. To that end, the following discussion will focus on constant energy maps (CE maps) at select energies. The periodicity in momentum space, in combination with the width of the observable features, will provide insight into the localization and molecular or metallic character of the entities in question. To identify changes in molecular orbital fingerprints due to molecule-substrate interactions, the experimental CE maps will be compared to photoemission orbital tomography (POT) calculations of the free C_{60} molecule as a first estimate. The C_{60} multilayer sample system discussed in Section 5.3 incorporates intermolecular interactions without substrate influence. However, it is not feasible for comparison because the multilayer comprises a 2×2 superstructure of differently oriented molecules (see Section 5.2.1). This results in different CE maps. As a first step the HOMO will be examined in more detail.

In Figure 4.5 (a), an excerpt of the photoelectron spectrum is displayed depicting the energetic region of the HOMO of the monolayer C_{60}/Cu(111) system. The gray vertical lines mark the energetic position of the CE maps displayed in Figure 4.5 (b-d). The blue and green superimposed hexagons represent the first BZs of the C_{60} adsorbate and the Cu(111) substrate, respectively. All three CE maps show a complex pattern. As the energy is scanned, the patterns continually evolve into one another, indicating a strong dispersion of the HOMO level.
For the purpose of comparison, Figure 4.5 (e) presents the theoretical CE map of the C_{60} HOMO for a free molecule. The CE map was calculated using photoemission orbital to-

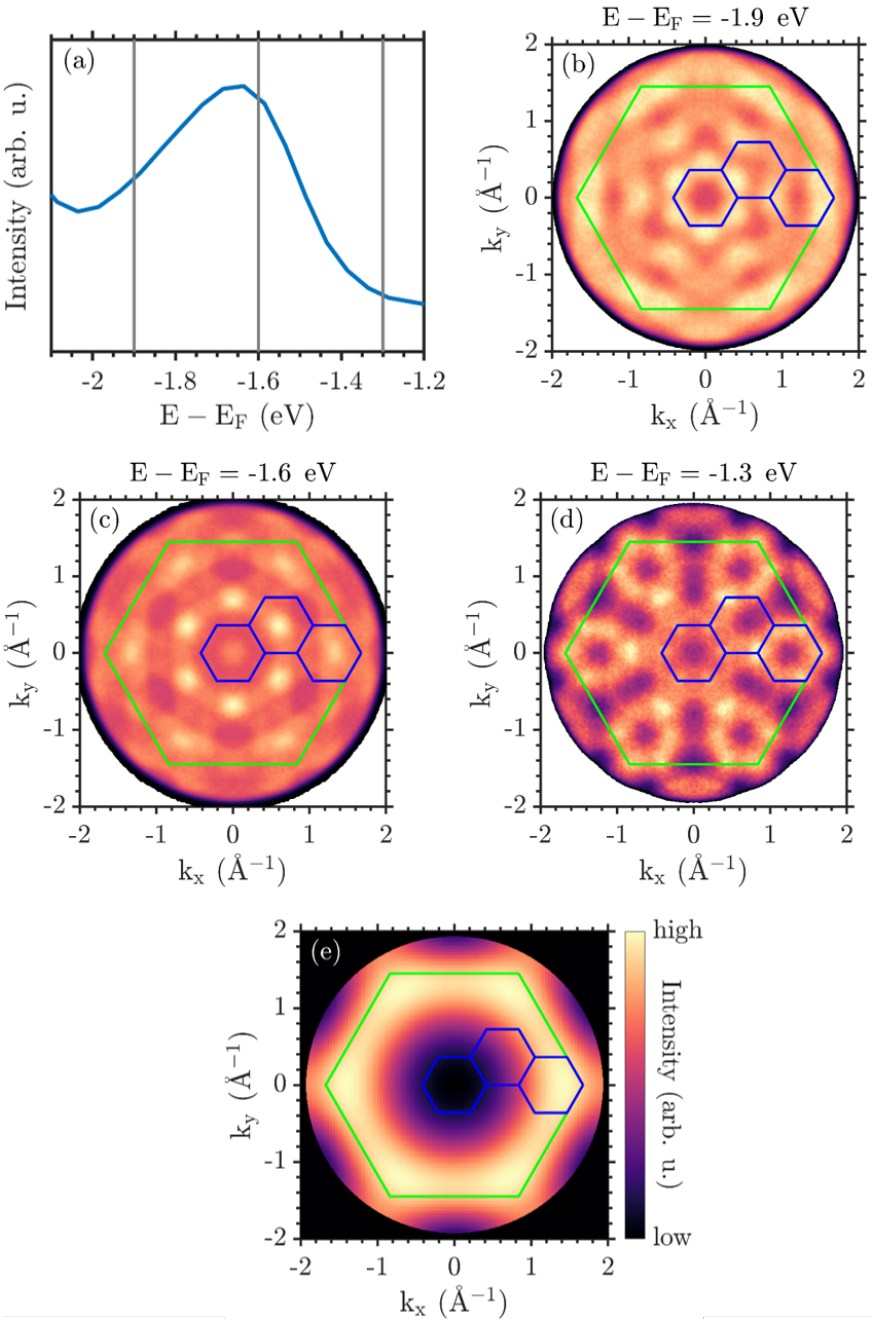

Figure (4.5) (a) Photoelectron spectrum of the energetic region of the HOMO of the monolayer C_{60}/Cu(111) system. (b-c) Selected CE maps of the HOMO. The surface Brillouin zones of the C_{60} and the Cu(111) surface are indicated in blue and green respectively. The energetic positions of the CE maps are indicated by vertical gray lines in the spectrum in (a). (e) Calculated CE map of the HOMO for non-interacting C_{60} molecules using POT. The CE map was generated using the software kMap.py [162] and the molecular orbital data base of P. Puschnig, University of Graz [152].

mography (POT) and symmetrized to account for all molecular orientations present in the monolayer on Cu(111) system. This model is intended to replicate the behavior of a monolayer in the absence of intermolecular and molecule-substrate interactions. The BZs of the monolayer constituents are drawn to better compare the spatial extent of the signatures with the experimental CE maps.
The CE maps of the monolayer C_{60}/Cu(111) system bear little resemblance to the theoretical one in Figure 4.5 (e), which depicts the emission pattern of the pure molecular orbital for all molecular orientations. Only the CE map extracted at the energetic peak position of the HOMO in Figure 4.5 (c) partially resembles the theoretical CE map with the six intensity maxima close to the border of the Cu BZ. The complexity of the patterns of the experimental CE map in comparison to the theoretical CE map of the free molecule demonstrates the strong influence of the molecule-substrate interactions on the electronic states in this energy range. Additionally, the smaller linewidth of the signatures indicates an enhanced electron delocalization compared to the free molecule.
The features surrounding the $\overline{\Gamma}$-points of the C_{60} BZs in the experimental map are reiterated in neighboring BZs. However, a modulation is present in the CE maps, which leads to slight differences in the features of neighboring BZs. Two phenomena contribute to this observation. First, the molecular dispersion is best visible within the momentum distribution of the molecular orbitals [16]. Therefore, the prominence of intermolecular interactions to the momentum space signatures is not identical for every BZ, but should be strongest in regions coinciding with the intensity maxima of the CE map of the free C_{60} molecule HOMO in Figure 4.5 (e). Second, hybridization can possibly affect the electronic wave functions of the HOMO, leading to dispersive signatures outside the momentum distribution of the molecular orbital. This can also lead to signatures that follow the periodicity of the BZ of the Cu(111) surface.

Next, the interface region will be discussed. For this purpose, Figure 4.6 (a) present a photoelectron spectrum of this energy region. The gray vertical lines indicate the energetic positions of the CE maps displayed in Figure 4.6 (b-d). The CE maps are extracted at selected energies, at which different contributions from the adsorbate and substrate are expected. The CE map in Figure 4.6 (b) is extracted at the energetic peak position of the interface state. The occurrence of the interface state is limited to the monolayer C_{60}/Cu(111) hybrid system and does not emerge for C_{60} layer adsorbed on other noble metal surfaces [27]. It exhibits significant signatures of the hybridization between the molecules and the copper substrate. A highly intricate momentum pattern is observed, which does not align with the periodicity of the C_{60} superstructure lattice. Remnants of the Cu sp-bands are still visible outside the first BZ of the Cu(111) substrate, highlighted by a blue dashed circle. Given the absence of these purely Cu features within the first BZ of the Cu(111) surface, it is anticipated that the momentum distribution will exhibit distinct variations between neighboring Cu BZs, akin to the observations in neighboring C_{60} BZs. This assumption cannot be validated due to the limited photoemission horizon.
In their observations, Tamai et al. directly discerned states that establish connections between $\overline{\Gamma}$-points of neighboring BZs at the energetic position of the interface state (see Figure 4.7). They deduced that these states exhibit delocalization along the nearest neighbor direction, while exhibiting localization along the next-nearest neighbor direction [27]. The researchers excluded the possibility of final state umklapp processes, in which Cu states would follow the C_{60} superstructure, as the origin of these states.

These states could not be resolved in the present study. It is suggested that the magnification of momentum space in this experiment may be inadequate for observing the findings reported by Tamai et al. [27]. The larger field of view resulted in fewer pixels on the detector to resolving the area inside the surface Brillouin zone, which may have been too coarse to

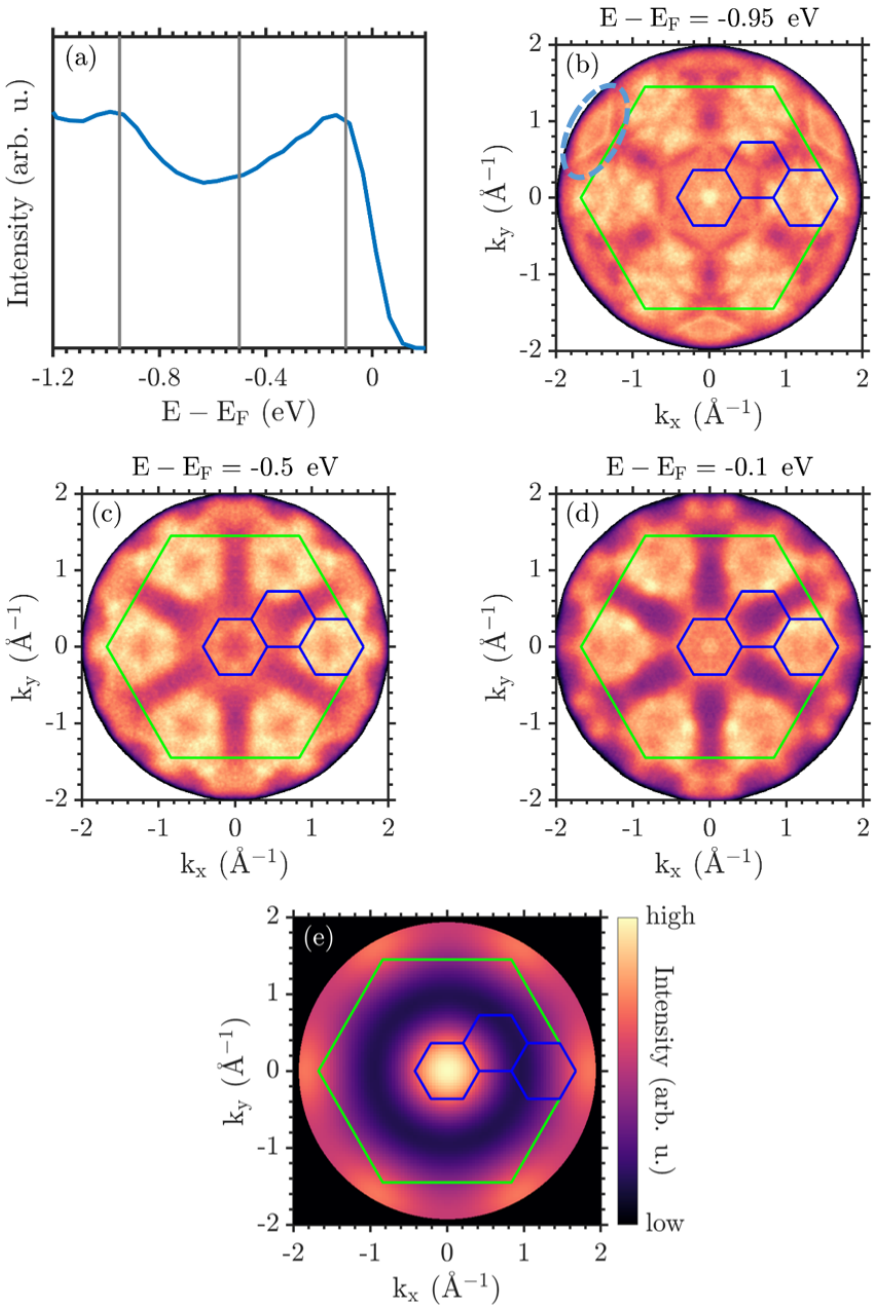

Figure (4.6) (a) Photoelectron spectrum of the interface region of the monolayer C_{60}/Cu(111) system. (b-c) Selected CE maps of the interface region. The CE maps were extracted at characteristic energetic positions of the hybrid system and its subsystems: (b) interface state, (c) sp-bands of Cu, (d) C_{60} LUMO. The surface Brillouin zones of the C_{60} and the Cu(111) surface are indicated in blue and green respectively. The energetic positions of the CE maps are indicated by vertical gray lines in the spectrum in (a). (e) Calculated CE map of the LUMO for non-interacting C_{60} molecules using POT. The CE map was generated using the software kMap.py [162] and the molecular orbital data base of P. Puschnig, University of Graz [152].

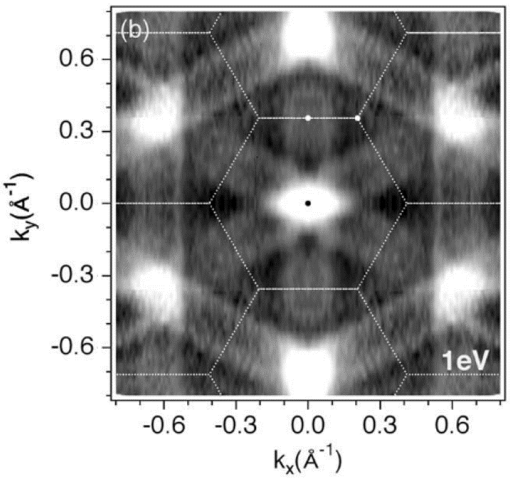

Figure (4.7) Constant energy map recorded at $E - E_F = -1\,eV$ using a photon energy of $h\nu = 21.2\,eV$. White values correspond to high intensity. The C_{60} surface Brillouin zones are drawn in white onto the CE map. Delocalized states connecting neighboring $\overline{\Gamma}$-points are observed. With permission from [27]. Copyright © 2008 American Physical Society.

resolve the states in question. In addition, the present experiments were conducted at ambient sample temperatures, in contrast to the experiments performed at 10 K in [27], which also hindered the observation. As illustrated in Figure 4.5 (c), analogous faint features that link the $\overline{\Gamma}$-points of neighboring BZs at the energetic peak position of the HOMO can be discerned. However, these features are not evident within the interface region. A potential explanation for this phenomenon is that the states delineated by Tamai et al. [27] stem from the HOMO and constitute a component of the C_{60} band structure that emerges as a consequence of the overlapping of π-electron wave functions among neighboring molecules (refer to Section 5.3 and [22, 23]). These states extend into the interface region due to the involvement of the HOMO in the hybridization process and are not resolved in the presented experiment due to lower momentum resolution.

The CE map illustrated in Figure 4.6 (c) is extracted at an energetic position in between the peak of the interface state and the onset of the LUMO. In the absence of hybridization, the CE map would be predominantly influenced by the Cu sp-bands as C_{60} lacks electronic states within this energy region. However, the displayed PAD does not resemble the electronic structure of the Cu(111) sp-bands. Rather, it shows broad features indicative of a partial molecular character of the electronic states involved.

Figure 4.6 (d) depicts a CE map in the energetic region of the partially filled LUMO, which is in close proximity to the Fermi edge. The features demonstrate only a marginal alteration in comparison to the CE map presented in Figure 4.6 (b). Therefore, it is hypothesized that the molecular contribution causing the broad features in momentum space originates from the LUMO participating in the hybridization with the Cu(111) substrate. It is proposed that the influence of the LUMO on the hybridization is stronger than that of the HOMO. This is due to the fact that the LUMO wave function is located further away from the carbon cages of the C_{60} molecules.

For comparison, Figure 4.6 (e) presents the theoretical POT CE map of the C_{60} LUMO for a free molecule. The CE map symmetrized to account for all rotation and mirror domains of the C_{60} monolayer and simulates the behavior of a monolayer in the absence of intermolecular and molecule-substrate interactions. It is evident that the theoretical CE map of the LUMO does not resemble the experimental one in Figure 4.6 (d). This indicates that the hybridization of the LUMO wave functions with those of Cu significantly reshapes the

emission patterns of the molecular orbitals of the hybrid system. However, the experimental CE map is not extracted at the energetic peak position of the LUMO since it is not fully occupied. It is therefore possible that in the case of a more occupied LUMO, an experimental CE map can be found (possibly near its energetic peak position) that shows more similarity to the theoretical CE map in Figure 4.6 (e). For the HOMO, it was observed that, despite the dispersion, the CE map that best corresponded to the theoretical CE map of a free C_{60} molecule was found at the center of the HOMO peak (see Figure 4.5 (c)).
In the case of PTCDA adsorbed on the Cu(100) surface, the hybridization of the molecules and the metal surface leads to PADs defined by those of the isolated molecule modified by intermolecular interactions [33]. The resulting intermolecular dispersion is enhanced by the hybridization with the substrate. In contrast, the observed band structure of the C_{60} monolayer on Cu(111) shows a stronger hybridization between the C_{60} molecules and the Cu substrate as thePADs are significantly modified. The observed interface region shows newly formed PADs that do not resemble those of the separate systems. It therefore indicates a stronger molecule-substrate interaction than for PTCDA chemisorbed on Cu(100) [163, 164]. Density functional theory (DFT) calculations have been employed by Tamai et al. to demonstrate that the six carbon atoms of C_{60} that are oriented towards the Cu surface hybridize with the Cu s-, p-, and d-states [27]. The resulting hybrid state is localized between the molecules and the Cu surface, and its energetic position coincides with the interface state observed in experiments. However, the DFT calculations in [27] exclusively considered the unreconstructed Cu surface. Given that the samples in [27] were fabricated by desorption of a C_{60} multilayer, it is expected that the unreconstructed Cu(111) surface is not the solely occurring adsorption configuration, as the annealing process can lead to an enhanced occurrence of the nanopit configuration (see Section 4.2). In the subsequent section, an in-depth examination of the PADs of the three distinct adsorption configurations of C_{60} on the Cu(111) surface is undertaken, employing the technique of photoemission orbital tomography (POT). A comparison will then be made between the simulated emission patterns of the different configurations and the experimental results.

4.4. Photoemission Orbital Tomography of the Different Adsorption Configurations

In this section, an effort is made to compare the experimental results obtained with photoemission orbital tomography (POT) calculations of the monolayer C_{60} on Cu(111) system. In contrast to the previous work by Tamai et al. [27], calculations for the three distinct adsorption configurations, unreconstructed surface, single-atom vacancy, and nanopit (refer to Section 4.2) are conducted. The primary objective is to discern disparities in molecule-substrate interactions and to identify discrepancies in band structure and hybridization that are attributable to the three distinct adsorption configurations. In addition, an effort is made to deduce the dominant adsorption geometry present in the sample.
The POT calculations were performed by Professor Peter Puschnig of the University of Graz. The electronic states were calculated employing density functional theory (DFT) calculations using the Vienna Ab Initio Simulation Package (VASP) version 5.4.4 [165, 166]. Six layers of the Cu(111) substrate were included in the simulation accompanied by a 20 Å vacuum layer between the periodic replica of the Cu slabs. Exchange-correlation effects and van der Waals contributions were incorporated by the usage of the Perdew-Burke-Ernzerhof (PBE) functional [167] and the D3 dispersion correction [168], respectively. Further, the projector-augmented wave (PAW) method [169] was utilized with an energy cutoff of 400 eV. A dipole layer is placed in the vacuum region to prevent spurious electrical fields [170]. The geometry relaxation is performed on a Monkhorst-Pack grid of $6 \times 6 \times 1$ k-points allowing all atoms except Cu atoms of the two lowest layers to relax until all forces are below the threshold of

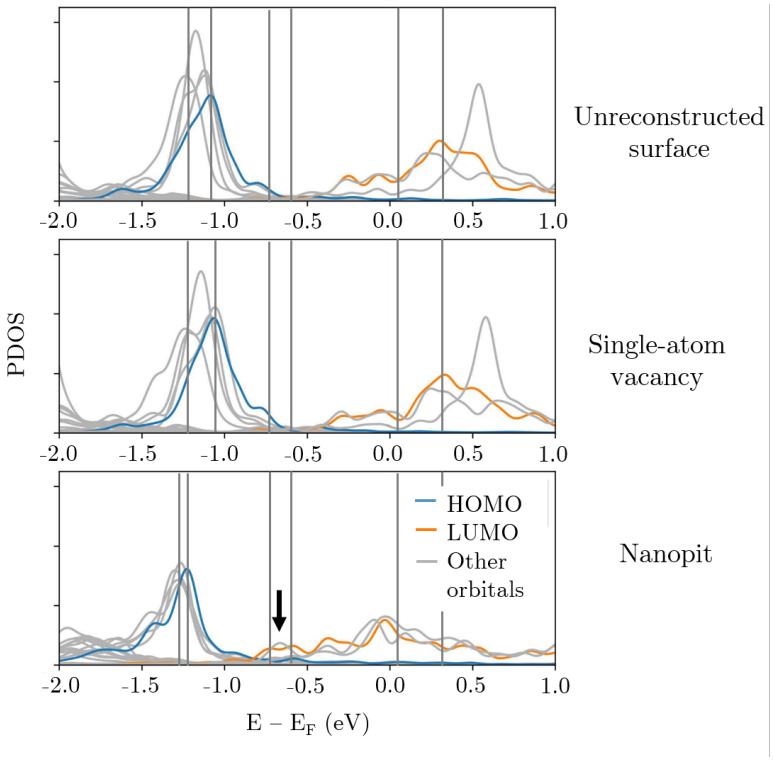

Figure (4.8) Projected density of states (PDOS) of the frontier orbitals for the three different adsorption configurations of a C_{60} monolayer on Cu(111). Note that in this particular case the PDOS of the HOMO and LUMO refer to two-electron energy levels. The other orbitals, shown in gray, represent the corresponding two-electron energy levels, which belong to the degenerate HOMO and LUMO (see Section 4.1). The vertical lines mark the energetic positions of CE maps discussed in more detail.

0.01 eV/Å. To obtain the photoemission data, the Kohn-Sham energies and orbitals are calculated from the relaxed geometry non-self-consistently on a k-point mesh of $12\times12\times3$. The photoemission angular distributions (PADs) are calculated employing the one-step model of photoemission [171] under the assumption of an exponentially damped plane wave final state between the substrate and the molecules [33]. This damping reproduces the mean free path of the photoelectrons and is needed to avoid an overestimation of bulk substrate states.

The projected density of states (PDOS) of the molecular orbitals resulting from the POT calculations is illustrated in Figure 4.8 for the three distinct adsorption configurations of the C_{60} monolayer on Cu(111) hybrid system. The PDOS of the HOMO and LUMO are highlighted in blue and orange, respectively. In this particular instance, HOMO and LUMO denote the highest occupied and unoccupied molecular orbital, respectively, with the capacity to accommodate two electrons. In the course of this work, HOMO and LUMO were invariably associated with a multiplet of degenerate two-electron orbitals (see Section 4.1). As illustrated in Figure 4.8, the remaining two-electron orbitals of these multiplets are represented by gray PDOS curves.
It is apparent that the maxima of the PDOS of the Kohn-Sham orbitals exhibit variation among the distinct adsorption geometries. A close examination reveals that the PDOS of the nanopit adsorption configuration is distinct from those of the other two configurations. In this instance, the maxima of all degenerate HOMO peaks are grouped at lower energies. In addition, it has been demonstrated that all of the LUMO levels in this adsorption configuration exhibit a maximum PDOS at the Fermi edge. This is in contrast to the adsorption configurations of the unreconstructed surface and the single-atom vacancy, which exhibit a

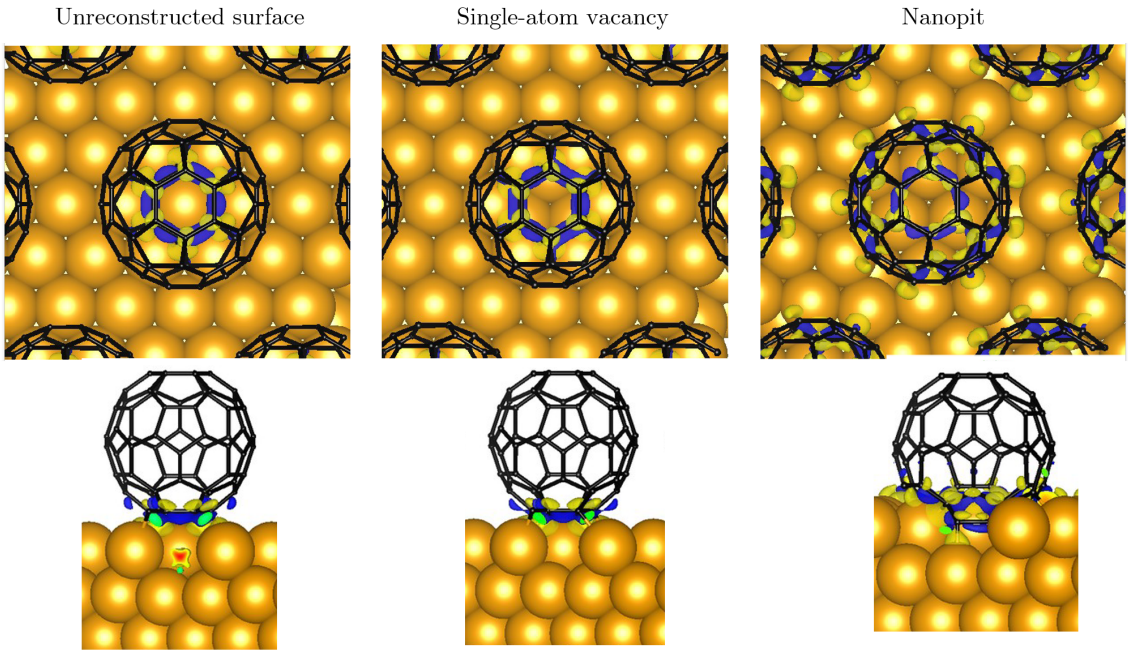

Figure (4.9) Kohn-Sham orbitals of the electronic states located on the lower carbon atoms involved in the hybridization with the Cu(111) substrate for the three different adsorption configurations. The orbitals are extracted at the at the energetic position of the Fermi edge. The yellow and blue isosurfaces correspond to different signs of the electron wave functions.

high degree of similarity. In both cases, the PDOS of the different two-electron orbitals are more spread out in energy and partially exhibit larger maxima. In addition, the maxima of the PDOS are shifted towards higher energies for both the occupied and unoccupied orbitals in comparison with the nanopit adsorption configuration. A further striking discrepancy between the nanopit adsorption configuration and the other configurations is the energetic position of a possibly emerging interface state. In the nanopit configuration, the possible interface state is emerges at approximately $-0.6\,\mathrm{eV}$ below the Fermi level. This state is derived from the LUMO. Conversely, the unreconstructed surface and the single-atom vacancy show a more pronounced feature derived from the HOMO manifesting at approximately $-0.75\,\mathrm{eV}$. ARPES experiments reported in literature attributed the interface state to be derived from the LUMO [142].

Figure 4.9 illustrates the isosurfaces orbital resolved electron densities of the lower carbon atoms of the C_{60} molecule that are involved in the hybridization process with the Cu(111) surface for the three distinct adsorption configurations. The wave functions are extracted at the energetic position of the Fermi edge. The different colors of the isosurfaces correspond to the different signs of the electron wave functions. It is apparent that the varying degrees of surface reconstruction are concomitant with the adsorption height of the C_{60} molecules. As illustrated in the side view images depicted in Figure 4.9, the adsorption height is largest for the unreconstructed Cu(111) surface and smallest for the nanopit configuration, where the molecules undergo partial sinking into the surface. The findings of different adsorption heights depending on the degree of surface reconstruction are consistent with existing literature on the subject [142, 143, 157].
Figure 4.9 further elucidates that the lowest carbon atoms of the C_{60} molecules that face the surface participate in the hybridization. Consequently, localized σ-bonds are formed between the carbon atoms in question and the nearest copper atoms thereby reducing the C-Cu bond lengths [143, 156]. It can be deduced that the interface state is located between the molecules

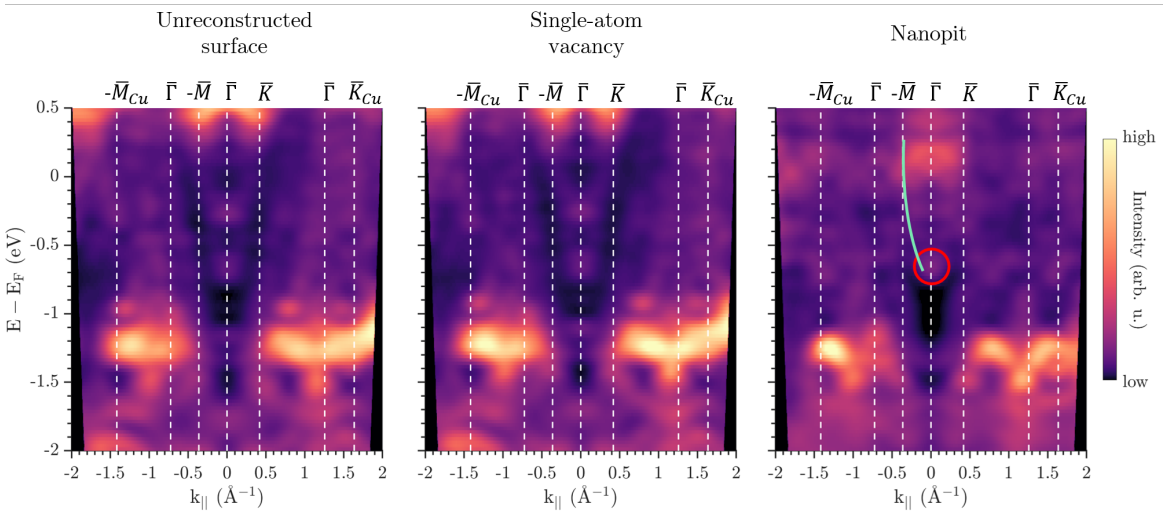

Figure (4.10) Comparison of calculated energy distribution curves of the monolayer C_{60}/Cu(111) of the three different adsorption configurations using photoemission orbital tomography. The EDCs were extracted along the $-\overline{M\Gamma K}$-direction. High symmetry points of the C_{60} adsorbate and the Cu(111) surface are indicated by vertical white dashed lines.

and the Cu surface. In the case of the unreconstructed surface and the single-atom vacancy configuration, solely the six carbon atoms directly facing the Cu(111) surface are capable of contributing to the hybridization process with the substrate. Conversely, within the nanopit configuration, 15 carbon atoms can form localized bonds with neighboring copper atoms, a consequence of the sinking of the C_{60} molecules into the nanopits. The strong interaction of the C_{60} molecules with the Cu surfaces induces a deformation of the Cu surfaces in the first layer, thereby further enhancing the interaction [142].
The reconstruction of the surface is concomitant with a change in the charge density of the first Cu layers. The outcome of this process is a modification of the work function, a phenomenon that is also subject to the influence of the molecule-substrate interaction. The results of the DFT calculations suggest a correlation between the degree of surface reconstruction and the change in work function. The nanopit configuration exhibited the largest increase, at more than 0.4 eV.
It was determined that this robust hybridization and reconstruction of the surface is a distinctive property of the C_{60} monolayer on Cu(111). This phenomenon is attributed to the lattice matching of the C_{60} adsorbate and the Cu(111) surface, resulting in the formation of the 4×4 superstructure [27, 142, 156]. In contrast, on other noble metal surfaces, both phenomena exhibit a significant decrease in magnitude. For instance, on Ag(111), the C_{60} exhibits a significantly diminished molecule-substrate interaction and does not form nanopits; rather, it generates predominately single-atom vacancies, which represent the highest degree of surface reconstruction on this surface. The underlying cause of this phenomenon is attributed to a discrepancy in the lattice parameters of the constituent materials resulting in the formation of the $(\sqrt{13} \times \sqrt{13})$R13.9° superstructure [156].

In the subsequent phase of this study, the momentum distributions of the Kohn-Sham orbitals for the three distinct adsorption configurations are compared. Therefore, Figure 4.10 displays the energy distribution curves (EDCs) of the three configurations. The presence of two possible rotational orientations of the C_{60} molecules, deviating by 60° (see Section 4.2), necessitated the summation of the POT data set with its correspondingly rotated counterpart. The EDCs were extracted along the $-\overline{M\Gamma K}$-direction. Several high symmetry points of the surface Brillouin zones of the C_{60} superstructure and the surface Brillouin zone of

the Cu substrate are indicated by vertical, white, dashed lines. It is important to note that the color map is nonlinear in order to achieve optimal contrast between regions of varying intensity levels.
Intricate momentum distributions are identified for all three adsorption configurations. Upon closer examination, it becomes clear that each of these is significantly richer in features than the experimental EDC depicted in Figure 4.4 (b). A comparison of the course of the PDOS depicted in Figure 4.8 indicates that the HOMO is located in the region of higher intensity between -1.5 and $-1\,\mathrm{eV}$ for all adsorption configurations. It is noteworthy that there is an absence of oscillating behavior in the HOMO, which has been observed in the experimental EDC. The interface state manifested as a prominent feature around the $\overline{\Gamma}$-point in the experiment. A comparison of the EDC of the nanopit in Figure 4.10 with the experimentally obtained EDC in Figure 4.4 (b) leads to the assignment of the feature at approximately $-0.7\,\mathrm{eV}$ (marked by a red circle) to the interface state. An upward-bending parabola is also observable (partially indicated by the green line). The downward bending parabola observed by Tamai et al. [27] is not distinguishable. This finding aligns with the experimental EDC. For the EDCs of the unreconstructed surface and the single-atom vacancy configuration, two prominent features at the $\overline{\Gamma}$-point can be observed. For these adsorption configurations, the feature at $-0.7\,\mathrm{eV}$ is also assigned to the interface state. The corresponding constant energy map shows better agreement with the experimental result (refer to Figure 4.12).
The samples in the conducted experiments were prepared by desorption of a C_{60} multilayer (see Appendix A.1). Therefore, the samples are expected to consist of the nanopit and the unreconstructed surface configurations. The single atom vacancy is energetically less favorable and therefore should be less abundant [142]. The same applies to the experiments of Tamai et al [27].
For a more detailed comparison of the POT calculations with the experimental PADs, CE maps extracted at different energetic positions are compared. A direct comparison of orbital energies is not possible due to the limitations of density functional theory [33, 172–174]. The aim is to identify the energetic positions of the electronic states by their characteristic momentum distributions. Therefore, different possible theoretical CE maps will be compared with the experimental ones.

Figure 4.11 compares the experimental CE map of the HOMO with possible corresponding theoretical CE maps for all three different adsorption configurations. The top row shows CE maps at the same energetic position of $-1.25\,\mathrm{eV}$. The CE maps of the different adsorption configurations are similar, reproducing the twelve main intensity maxima inside the BZ of the substrate. In the CE map of the nanopit configuration, the main maxima are more distinct. Furthermore, all theoretical CE maps show a more or less pronounced star-shaped pattern of increasing intensity near the $\overline{\mathrm{M}}$-points of the Cu BZ. This pattern cannot be distinguished in the experimental CE map. It is obvious that there is a discrepancy in the radial spacing of the features between theory and experiment. The main intensity maxima are not completely located at the $\overline{\Gamma}$-points of the C_{60} BZs. The mismatch is less severe for the CE map of the nanopit configuration. A possible origin of this discrepancy will be discussed later.
The bottom row shows alternative CE maps of different energies that could also be attributed to the HOMO orbital, judging from their momentum distributions. The CE map of the nanopit configuration was extracted at $-1.30\,\mathrm{eV}$, which is close to the energetic positions of the CE maps in the top row. Therefore, the pattern is similar with the main intensity maxima being less elongated. The CE maps of the unreconstructed surface and the single atom vacancy configuration are extracted at -0.95 and $-0.90\,\mathrm{eV}$, respectively. They show similar PADs with overall weaker intensity and smaller intensity maxima. The patterns do not fully resemble the experimental CE map of the HOMO. However, the radial positions of the maxima is in better agreement with the experimental ones compared to the CE maps of

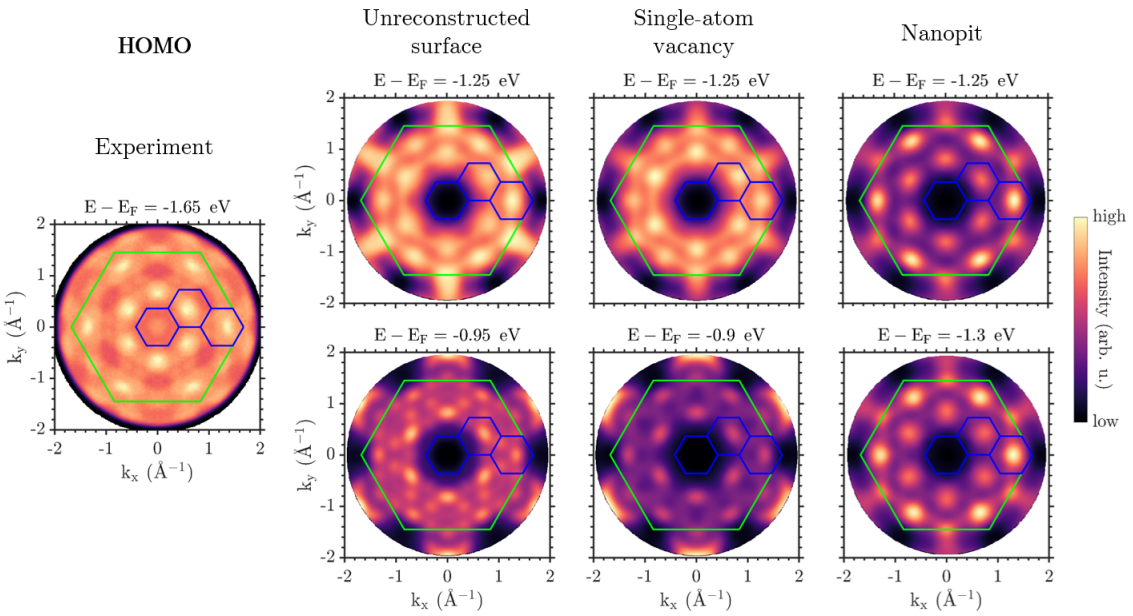

Figure (4.11) Comparison of the experimental HOMO CE map of the monolayer C_{60}/Cu(111) with calculated CE maps of the three different adsorption configurations using photoemission orbital tomography. Due to the incorrect absolute energy scale of the DFT calculations several possible matching calculated CE maps are depicted. The experimental CE map was extracted at the energetic peak position of the HOMO. The surface Brillouin zones of the C_{60} adsorbate and the Cu(111) surface are superimposed in blue and green, respectively.

these configurations in the top row. Furthermore, they show much weaker intensity around the $\overline{\text{M}}$-points of the Cu BZ, thus matching the experimental CE map better in these regions. Therefore, it is possible that these CE maps contribute to the observed experimental momentum distribution of the HOMO, but are superimposed by the CE map of the nanopit configuration.
Overall, the best agreement was obtained with the CE maps of the nanopit, indicating a higher occurrence of this adsorption configuration compared to the others.

Next, an experimental CE map characteristic of the interface state is compared with possible corresponding theoretical CE maps in Figure 4.12. The theoretical CE maps in the top row are extracted at an energy of $-0.6\,\text{eV}$ and those in the bottom row are extracted at $-0.7\,\text{eV}$. None of the theoretical CE maps fully reproduces the experimentally observed momentum distribution. In the top row, the CE maps of the unreconstructed surface and the single atom vacancy configuration show a ring-like structure consisting of several smaller intensity maxima. These small maxima resemble the lower parts of the six main features of high intensity in the experimental CE map. In addition, arcs of increased intensity are observed near the $\overline{\text{M}}$-points outside the BZ of the Cu surface. These arcs also appear in the experimental CE map, but with less prominence and are superimposed by remnants of the Cu sp-bands along three $\overline{\Gamma\text{M}}$-directions. The CE map of the nanopit configuration at $-0.6\,\text{eV}$ is different from the above. It shows intensity maxima near the $\overline{\text{K}}$-points of the Cu BZ. These maxima correspond to parts of the six main features of the experimental CE map. A combination of the CE maps of the unreconstructed surface and/or the CE map of the single-atom vacancy configuration together with the CE map of the nanopit configuration could reproduce the six main features along the $\overline{\Gamma\text{K}}$-directions in the experimental CE map. The nanopit CE map would thus contribute the parts of the features close to the edge of the Cu BZ, while the CE maps of the other configurations would contribute the rest of the

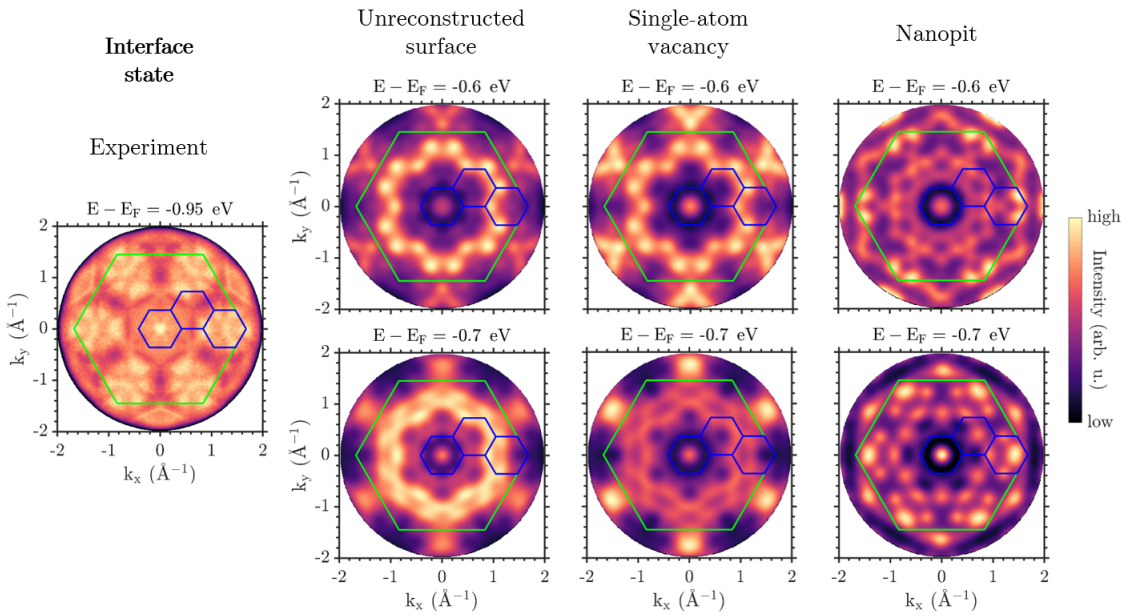

Figure (4.12) Comparison of the experimental interface state CE map of the monolayer C_{60}/Cu(111) with calculated CE maps of the three different adsorption configurations using photoemission orbital tomography. Due to the incorrect absolute energy scale of the DFT calculations several possible matching calculated CE maps are depicted. The experimental CE map was extracted at the energetic peak position of the interface state. The surface Brillouin zones of the C_{60} adsorbate and the Cu(111) surface are superimposed in blue and green, respectively.

features closer to the central $\overline{\Gamma}$-point.
An alternative composition of the experimental CE maps of the interface state might be possible with the theoretical CE maps in the bottom row of Figure 4.12. The theoretical CE maps are all extracted at an energy of −0.7 eV. In this case, the CE map of the nanopit configuration is similar to the experimental CE map. The maxima within the Cu BZ are more distinct than the features in the experimental CE map, but their arrangement reproduces the overall structure. The feature of highest intensity are located near the $\overline{\text{K}}$-points of the Cu BZ. A difference between the CE map of the nanopit configuration and the experimental CE map are the intensity maxima outside the Cu BZ near the $\overline{\text{M}}$-point. The experimental CE map does not show such spot-like maxima at this location. The CE maps of the unreconstructed surface or the single-atom vacancy configuration again show an increased intensity in a structured ring. For this energy the overall agreement with the experimental CE map is worse than for the CE maps at −0.6 eV. The CE maps show intensity maxima outside of the Cu BZ in proximity of the $\overline{\text{M}}$-points that do not occur in the experimental CE map. Nevertheless, they could complement the CE map of the nanopit configuration at −0.7 eV in a similar way as described for the CE maps in the top row.
It should be noted that in the EDCs in Figure 4.10 a feature at the $\overline{\Gamma}$-point at −0.3 eV was assigned as a possible main feature of the interface state for the unreconstructed surface and the single-atom vacancy configuration. No CE map at this energy was shown in the comparison to the experimental CE map of the interface state, as they are drastically different. The theoretical CE maps that show the best agreement with the experimental ones are extracted at the energetic position of the emergent state between the HOMO and the Fermi edge in the PDOS plot of the nanopit configuration in Figure 4.8 (marked with an arrow).
For the experimental CE map of the interface state, the best agreement is obtained by combining the CE map of the nanopit reconstruction and the unreconstructed surface, since the relative intensities in the single-atom vacancy configuration show less agreement with

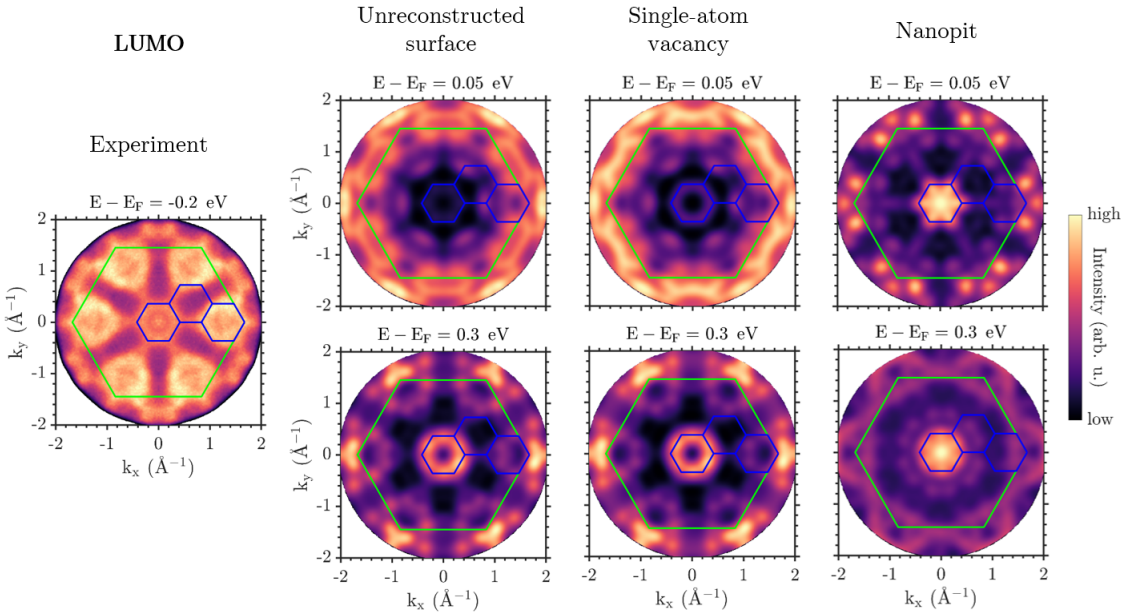

Figure (4.13) Comparison of the experimental LUMO CE map of the monolayer C_{60}/Cu(111) with calculated CE maps of the three different adsorption configurations using photoemission orbital tomography. Due to the incorrect absolute energy scale of the DFT calculations several possible matching calculated CE maps are depicted. The experimental CE map was extracted at the energetic peak position of the LUMO. The surface Brillouin zones of the C_{60} adsorbate and the Cu(111) surface are superimposed in blue and green, respectively.

the experiment. The nanopit configuration has the highest PDOS in the relevant energy range of the interface state (see Figure 4.8). Therefore, it is suggested that this adsorption configuration is the main contributor to the observed interface state in the experiment. The unreconstructed surface only contributes to a lesser extent.

Finally, a characteristic experimental CE map of the LUMO is compared with the results of the POT calculations in Figure 4.13. The experimental CE map consists of six broad maxima near the $\overline{\text{K}}$-points of the Cu BZ, which are connected to the $\overline{\Gamma}$-point. The theoretical CE maps are extracted at 0.05 and 0.3 eV for all adsorption configurations. The experimental CE map is best matched by the CE maps at 0.3 eV of the unstructured surface and the single atom vacancy configuration and the CE map at 0.05 eV of the nanopit configuration. The other CE maps either fail to reconstruct characteristic signatures in the momentum distribution or exhibit strongly deviating relative intensities. This could occur due to limitations in the DFT calculations or a wrong estimation of the mixing of molecular orbitals with electronic orbitals from the substrate. The CE map of the nanopit configuration at 0.05 eV mainly reproduces the main intensity maxima of the experimental CE map and their connecting features towards the $\overline{\Gamma}$-point. The features are more complex than in experiment. However, the relative intensity distribution does not agree with the experiment because the intensity inside the Cu BZ around the $\overline{\text{K}}$-points is too low compared to the intensity of the features outside the Cu BZ. The CE maps of the unreconstructed surface and the single-atom vacancy configuration at 0.3 eV are in better agreement with the experimental CE map. In particular, the overall structures are in better agreement. However, these CE maps also show an increased intensity outside the Cu BZ instead of inside as in the experiment. Furthermore, the features seem to be radially displaced closer to the photoemission horizon compared to the experiment. As mentioned above, this can be a result of the incorporation of the inner potential in the POT calculations.The experimental CE map of the LUMO is

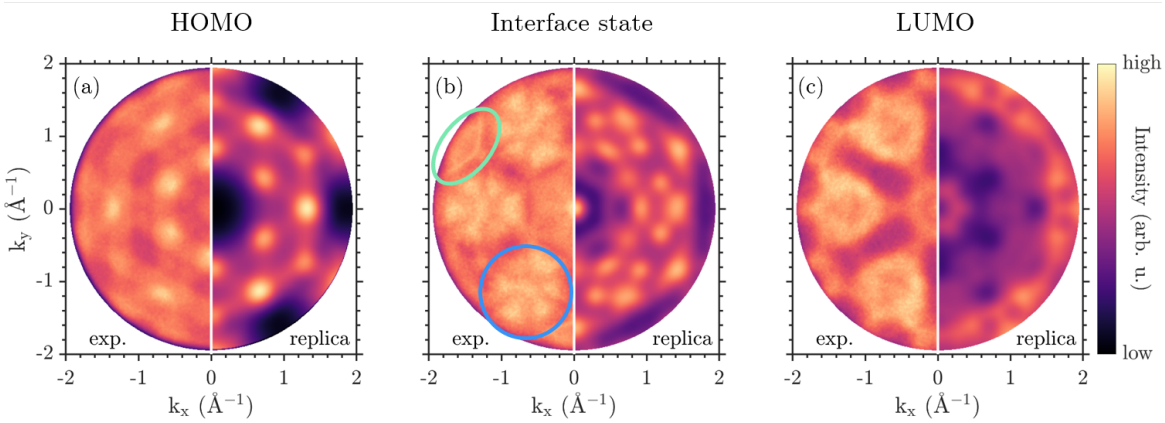

Figure (4.14) Replication of experimental CE maps of the (a) HOMO, (b) interface state, and (c) LUMO using the POT CE maps of the different adsorption configurations. The images are split in half with the left halves displaying the experimental CE maps and the right halves showing the corresponding replicas. The replicas were created by a 2D fitting routine.

best reproduced by the CE maps of the unreconstructed surface or the single-atom vacancy configuration at 0.3 eV. The nanopit configuration appears to contribute less to the experimental CE map, which is in contrast to the other electronic states that showed a strong contribution from the nanopit configuration. The reason for this is the smaller PDOS of the nanopit configuration at the considered energies compared to the PDOS of the other adsorption configurations. This is due to the larger linewidth of the LUMO for the nanopit configuration. Furthermore, the overall intensity of the CE map of the nanopit configuration at 0.3 eV is rather weak. This could lead to the false impression that the experimental CE map is only composed of contributions from the other adsorption configurations.

The next step is to reproduce the experimental CE maps of the HOMO, interface state, and LUMO using suitable combinations of the six possible corresponding theoretical CE maps (shown in Figures 4.11–4.13). This was done by fitting the experimental CE maps with linear combinations of POT CE maps using one CE map for each adsorption configuration. Figure 4.14 shows an example of the replica resulting from the 2D fitting of a selected combination of theoretical CE maps. The left halves of the CE maps display the experimental data, while the right halves show the corresponding replica. The HOMO replica in Figure 4.14 (a) is created using the bottom row of POT CE maps in Figure 4.11. There is a very good agreement between the replica and the experimental data. All of the main intensity maxima and minima are reproduced. However, a mismatch in the radial position of the intensity maxima is observable, which will be discussed later. Similarly, for the interface state in Figure 4.14 (b), a reasonable agreement between theory and experiment can be observed. The replica uses the bottom row of POT CE maps in Figure 4.12. The six main features (highlighted by a blue circle) are reproduced. However, in the experimental data, these features consist of six intensity maxima, whereas the replica only comprises four. Furthermore, the Cu sp-band signatures highlighted by the green ellipse are not reproduced because these states are absent from the CE maps of the POT calculations. Lastly, the LUMO replica in Figure 4.14 (c) reveals discrepancies between the experiment and the theory. While the replica reproduces the main intensity maxima, the overall intensity distribution does not match the experimental data.

The portion of coverage for each adsorption configuration can be calculated from the replication fit parameters. Table 1 shows the resulting values as a percentage for each CE map replicated. Significant variations in coverage can be observed depending on the underlying

Table (4.1) Composition of the monolayer C_{60}/Cu(111) with different adsorption configurations calculated from the fit parameters of the CE map replication. The coverage portions were calculated for each replica individually. The values are in percent.

	Unreconstructed surface	Single-atom vacancy	Nanopit
HOMO	44	0	56
Interface state	15	7	78
LUMO	45	0	55

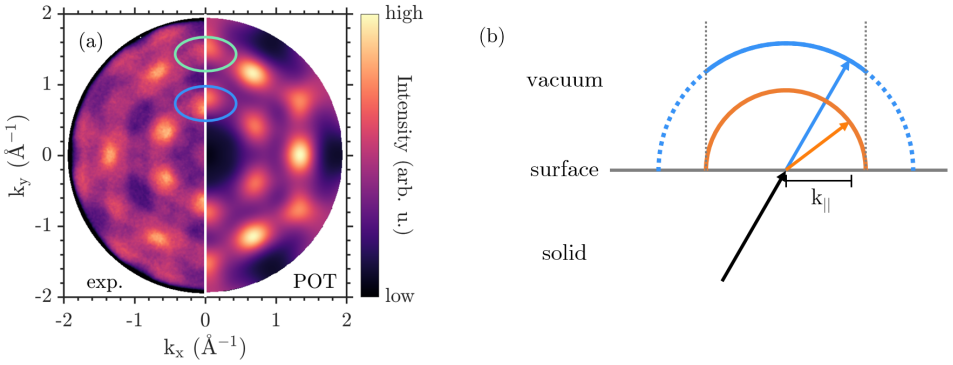

Figure (4.15) Problematic incorporation of the inner potential in POT. (a) CE map of the HOMO of monolayer C_{60}/Cu(111). The left half of the image depicts the experimental data, while the right half presents a corresponding CE map of the POT calculation of the nanopit adsorption configuration. It is evident that there is a radial mismatch in the alignment of the corresponding features highlighted by the ellipses. (b) Schematic depiction of the propagation of the photoelectrons through the surface in the applied POT formalism. The blue arrow illustrates the negligence of the inner potential in the POT calculation as it was accounted for by an enlargement of the photon energy, while the orange arrow depicts a correct incorporation of the inner potential resulting in a refraction of the photoelectron. The blue and orange semicircles represent the resulting PADs. To match the correct photoemission horizon the blue PAD has to be cut accordingly (dashed versus solid line). It is evident that the curvature of both PADs are different resulting in different distances between features upon a projection onto a planar detection screen.

POT CE maps used as a basis set in the 2D fitting. Due to these variations, no mean value is specified. Additionally, no error bounds resulting from the fitting procedure are provided, as using a different set of theoretical CE maps as a basis can result in significant changes to the resulting coverage portions. The magnitude of these changes is comparable to the variations between different replicas. As a general trend, it can be seen that the investigated sample spot is predominantly composed of the nanopit and unreconstructed surface configurations, the first occurring more often. The single-atom vacancy configuration occurs only to a small extent. This was expected since it is energetically unfavorable compared to the other configurations. The overall trend confirms the expectation that the nanopit configuration is the most frequently occurring adsorption configuration because of the annealing of the sample.

Before concluding this section, the radial displacements of features resulting from a simplified treatment of the inner potential in the POT calculations will be further explained. For this purpose, a CE map of the HOMO is shown in Figure 4.15 (a). The left half of the CE map shows the experimental results and the right half shows a corresponding CE map of the nanopit configuration. It is obvious that there is a discrepancy in the radial spacing between different features for theory and experiment. The distance between maxima in the outer hexagon (marked by a green ellipse) is smaller than the distance between maxima in

the inner hexagon (marked by a blue ellipse). The origin of the different maxima positions is the treatment of the inner potential in the POT calculations. The inner potential was considered by artificially increasing the photon energy. For clarity, Equation 4.1 repeats the energetic relationships between the inner potential V_0, the final state energy E_f, the kinetic energy outside the solid $E_\mathrm{kin,o}$, and the energetic onset of the atomic potential wells E_0.

$$E_f + |E_0| = E_\mathrm{kin,o} + V_0 = h\nu - E_\mathrm{B} - \Phi + V_0 \tag{4.1}$$

Conservation of energy is applied to rewrite the kinetic energy outside of the solid in terms of photon energy $h\nu$, binding energy E_B (related to the Fermi energy), and the work function Φ. Refer to Section 2.2.1 and Figure 2.3 for more information and a graphical representation of the energetic relationships. From Equation 4.1 it is apparent that energy is conserved if the photon energy is increased by the amount of the inner potential and the latter is then neglected. This means that the 3D cut through the band structure at constant energy is at the same position in momentum space. Thus, the inclusion of the inner potential by increasing the photon energy will lead to the PAD of the same electronic state as for an explicit treatment of the inner potential. The discrepancy in the position of the features arises during the conservation of momentum, which is shown schematically in Figure 4.15 (b). As mentioned above, the spherical cut inside the solid is the same in both cases of treating the inner potential. This is indicated by the black momentum vector in Figure 4.15 (b). For an explicit treatment of the inner potential, the electron is refracted as it leaves the solid, leading to a change in the parallel momentum component (indicated by an orange vector). This results in a reduction of the momentum component perpendicular to the surface. The resulting hemispherical distribution of photoelectrons outside the solid is represented by an orange semicircle. Conversely, if the inner potential is included by enlarging the photon energy, no refraction occurs at the surface. This results in the blue vector and the corresponding photoelectron distribution shown in blue. In order to obtain the correct size of the photoemission horizon (solid blue arc), the photoelectron distribution has to be cut off accordingly. For both treatments of the inner potential, the resulting photoelectron distributions show the same electronic states and have the same photoemission horizon. However, their curvature is different. The photoelectron distributions are projected onto a plane to simulate the detected constant energy map. The different curvatures result in different distances between neighboring features after the 2D projection, which is what is observed in the experiment.

This finding emphasizes the need for explicit treatment of the inner potential in POT calculations of 3D systems with large inner potentials and/or complex photoemission angular distributions. Furthermore, the explicit treatment is required when small differences between CE maps are investigated or a higher level of accuracy analysis based on the POT CE maps is the goal.

In this section, photoemission orbital tomography calculations have shown that the three different adsorption configurations of C_{60} on Cu(111) all have different projected densities of states of the molecular orbitals and distinct characteristic PADs. The PDOS as well as the PADs of the unreconstructed surface and the single-atom vacancy configuration show more similarity to each other than to the nanopit configuration. This is expected since the nanopit configuration shows a significantly enhanced interaction of the C_{60} molecules with the Cu surface.

The experimental CE maps of the HOMO and interface states were best described by the theoretical CE maps of the nanopit configuration. In contrast, the experimental CE maps of the LUMO showed a better agreement with the theoretical CE map of the unreconstructed surface. It is concluded that the investigated sample consists of coexisting nanopit and unreconstructed surface configurations. The annealing process during the sample preparation (refer to Appendix A.1) was apparently not sufficient to produce a sample completely com-

posed of the nanopit adsorption configuration. It seems that the nanopit is the prevalent adsorption configuration as the experimental CE maps of the HOMO and interface state showed a predominant contribution. The contribution of the single-atom vacancy to the observed CE maps is small. This is expected since the configuration has been reported to be energetically less favorable [142]. The varying degree of contribution of the adsorption configurations to the PADs at distinct energies results from the different magnitude of the PDOS.
A 2D fitting approach was used to calculate the relative contributions of each adsorption configuration to the composition of the monolayer C_{60}/Cu(111) sample system. Despite significant variations, a general trend was observed. The sample system is predominantly composed of the nanopit configuration, followed by the unreconstructed surface configuration. The single-atom vacancy configuration occurred in small amounts.

4.5. First Steps Towards the Investigation of Excited States

In the course of this chapter, the occupied electronic states of a C_{60} monolayer on Cu(111) have been investigated. As a next possible step, the focus can be shifted to the excited states. In the C_{60} bulk film, the unoccupied molecular orbitals were observed to exhibit a pronounced dispersion similar to that of the occupied orbitals [175]. The question can be asked if and to what extent these states and their dispersion are affected by the hybridization between the molecules and the substrate. In bulk C_{60} bound electron-hole pairs, so-called excitons, are formed upon optical excitation (see Section 5.2.2) [46, 67, 89, 155]. In contrast, in the C_{60} monolayer on Cu(111) it is expected that the hole created during the optical excitation of an electron to an unoccupied state will be efficiently screened due to the strong molecular-substrate interaction.
In order to study the unoccupied electronic states in the C_{60} monolayer on Cu(111) and to compare them with the free molecule and the C_{60} bulk, it is first necessary to determine their energetic positions. These are altered compared to the free molecule and the bulk due the molecule-substrate interaction. The energetic position of the unoccupied states can be determined by recording a photoelectron spectrum for different photon energies. Figure 4.16 shows the kinetic energy of the photoelectrons for different photon energies between 1.8 and 2.25 eV. The intensity of each data point is represented by the color of the plot. Each photoelectron spectrum is plotted vertically, parallel to the y-axis. The secondary electron background corresponds to the prominent maxima between 0 and 0.5 eV kinetic energy. Due to the low photon energy compared to the work function of 4.71 eV, the adsorption of at least three photons is required to excite an electron above the vacuum energy. As a result, possible unoccupied states are superimposed by the secondary electron background.

In Figure 4.16, three different unoccupied states can be identified, highlighted by the colored straight lines that were manually adjusted to the peak positions. As the photon energy is varied, the energetic positions of the observed states shift depending on the number of photons required to excite the electron above the vacuum energy (see Section 2.4). Thus, the magnitude of the slope of each colored straight line in Figure 4.16 represents the amount of photons needed to excited an electron from the observed state above the vacuum level.
The green line in Figure 4.16 has a slope of three. This indicates that the corresponding state is occupied because, as mentioned earlier, at least three photons in the given photon energy interval are required to overcome the work function. The observed state thus corresponds to the partially filled LUMO truncated by the Fermi level.
The dark and light blue lines both have a slope of one and are therefore intermediate states in the photoemission process. Since only one photon is needed to photoemit an electron from these intermediate states, two photons must be absorbed to populate them. This means

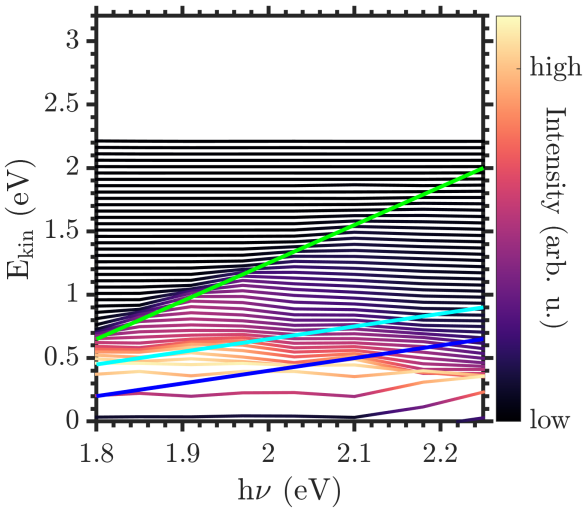

Figure (4.16) Determination of the energetic positions of the excited states in the monolayer C_{60}/Cu(111) system and the order of the photoemission process. The plot shows the kinetic energy of the photoelectrons versus the applied photon energy. The intensity at a given data point is color-coded. The evolution of three distinct electronic states are marked by the colored straight lines. The order of the photoemission process can be deduced from the slopes of the lines. The electronic state marked by the green line is photoexcited by a 3PPE process and the states marked by the light and dark blue lines are photoexcited by a 1PPE process.

that they are energetically closer to the vacuum energy than to the Fermi level. From the linear equation of the colored lines it is possible to determine the energetic positions of the observed intermediate states at 3.15 and 3.4 eV above the Fermi level. Due to the large band gap at the $\overline{\Gamma}$-point of the Cu(111) surface, which is about the size of the work function of the bare Cu surface [176], the observed intermediate states cannot be unoccupied states of the pure Cu(111) surface. A possible assignment to one of these states could be the LUMO+2 of the C_{60} molecules, as it has been reported to be about 3 eV above the Fermi energy of the C_{60} monolayer on the Cu(111) system [159, 175, 177, 178]. Thus, only one observed intermediate state can be assigned to a molecular orbital, whereas the other remains elusive. Other unoccupied molecular orbitals, such as the LUMO+3, were reported more than 1 eV away from the LUMO+2, and thus, despite the large bandwidth of these molecular orbitals, are not in question for the assignment of the second observed intermediate state [159, 177]. The LUMO+1 could not be observed in the literature for a monolayer of C_{60} on Cu(111). It is possible that the second state results from the hybridization of the C_{60} molecules with the Cu(111) substrate and is therefore an interface state. The occupied interface state below the Fermi level was observed most clearly in spectra limited to the $\overline{\Gamma}$-point (see Section 4.3). It is reasonable to assume the same for an unoccupied interface state. Due to the limited photoemission horizon in the nPPE study described above, the extracted photoemission spectra are mostly confined to the $\overline{\Gamma}$-point. This would argue for resolving possible interface states. The determination of the energetic position of unoccupied states in the literature was performed by inverse photoemission spectroscopy and near-edge x-ray absorption spectroscopy without the momentum space limitation [175, 177, 178]. It is proposed that this interface state was therefore not observed in the literature because its signal was too low to be resolved. The above considerations result in the energy level diagram shown in Figure 4.17.

To further investigate the observed unoccupied states and to determine the assignment of these states as interface states or molecular orbitals, a monument-resolved photoemission experiment should be conducted. Due to the limited photoemission horizon in the 3PPE experiment performed in this section, higher photon energies should be used to ensure a

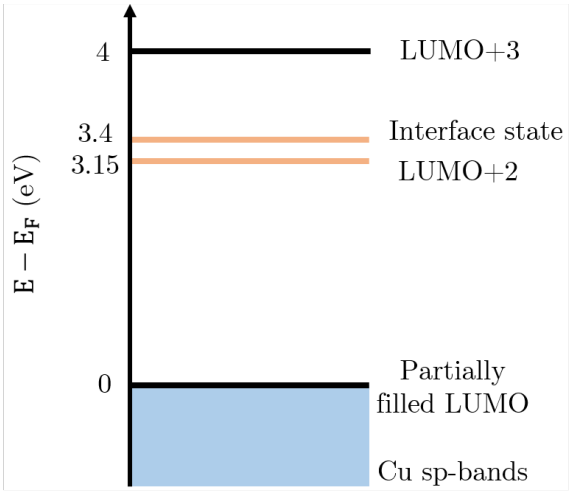

Figure (4.17) Energy level diagram of the excited states of a C_{60} monolayer on Cu(111). The energetic positions of the LUMO+2 and the interface state are obtained in this work, whereas the energetic position of the LUMO+3 is taken from reference [177]. The LUMO+1 was not observed in literature for a single monolayer of C_{60} on Cu(111).

sufficient field of view in momentum space. It is suggested to resolve at least the whole surface Brillouin zone of the Cu(111) surface to study the possible dispersion and hybridization effects, similar to the study of the occupied states in the previous sections. This would also overcome the problem of Bloch-like unoccupied states just above the vacuum energy. These states serve as final states in the photoemission process for low photon energies, superimposing the photoemission angular distributions of the intermediate states (refer to Section 5.4.1 for further details).

4.6. Summary and Outlook

This chapter has provided a qualitative understanding of significantly hybridized molecule-metal interfaces. As a sample system, a monolayer of C_{60} on a Cu(111) surface was investigated using momentum microscopy. The studies revealed a strong modification of the electronic structures of both components due to the molecule-substrate interaction. This modification occurred not only in the energetic region of the C_{60} HOMO and LUMO, but spanned the entire range of the Cu sp-bands. It was found that the HOMO contributes less to the hybridization between the molecules and the substrate than the LUMO. This can be explained by the larger spatial extension of the LUMO away from the C_{60} carbon cage. Furthermore, a parabolically dispersive interface state was observed at the $\overline{\Gamma}$-point, which has been reported in the literature [27]. All observed hybridized states are rather localized due to their broad features in momentum space.
The Shockley surface state of the bare Cu(111) surface was still observed shifted closer to the Fermi energy. The occurrence of the Shockley surface state for a closed molecular layer, despite significant hybridization with the substrate, has been explained in the literature by the absence of hybridized or C_{60}-derived bands in the sp-projected band gap of Cu(111).
C_{60} can adsorb on Cu(111) in three different geometries: the unreconstructed surface, the single-atom vacancy and the nanopit configuration. In order to distinguish the different adsorption configurations by their geometric and electronic properties and their different degrees of hybridization, photoemission orbital tomography calculations were performed for all three configurations. The results from the literature could be reproduced, attributing the highest adsorption height to the unreconstructed surface and the lowest to the nanopit

configuration [142, 143]. In the latter, the C_{60} molecules bury themselves in the seven-atom vacancy nanopit, allowing more carbon atoms to form localized bonds with neighboring copper atoms. For this reason, the calculated electronic structure displayed in the extracted energy distribution curve of the nanopit differed significantly from the ones of the unreconstructed surface and the single-atom vacancy configuration.
Theoretical constant energy maps could be assigned to the experimentally obtained CE maps of the HOMO, the interface state and the LUMO. The experimental CE maps of the HOMO and the interface state were best described by the corresponding theoretical CE maps of the nanopit configuration, with smaller contributions from the corresponding CE maps of the unreconstructed surface. For the experimental CE map of the LUMO it was vice versa, which was attributed to the lower projected density of states of the nanopit configuration in this energy range and the rather low overall intensity of the CE maps. It was concluded that the investigated sample consisted mainly of nanopit adsorption configurations with a portion of the unreconstructed surface remaining. The occurrence of the single-atom vacancy configuration is negligible. This was expected since it is energetically less favorable.
It was found that the inclusion of the inner potential in the photoemission orbital tomography calculations by increasing the photon energy leads to a radial shift between the momentum space signatures. The reason for this is the neglect of the refraction of the photoelectrons. Correct treatment of the inner potential is important for 3D systems with complex photoemission angular distributions.
Furthermore, first steps towards the study of the excited states of the monolayer C_{60} on Cu(111) system have been taken. By varying the photon energy, two energetically close excited states were observed and their energetic positions were determined. It is proposed that one state is derived from the LUMO+2 and the other is a possible interface state, which may only be resolved by limiting the photoelectron spectrum to the $\overline{\Gamma}$-point.

The chapter concludes with an outlook for possible future research. The study of the excited states of the monolayer C_{60}/Cu(111) sample system can be continued after the energetic position of two states has been determined. Using photoemission orbital tomography it is possible to validate the assignment of the two observed states as an interface state and a state derived from the LUMO+2. The influence of the hybridization on the excited states can be studied and possible differences for the three different adsorption geometries could be identified. The excited state dynamics could be resolved in a pump-probe experiment. Furthermore, the results regarding the band structure, the excited state dynamics and the (de)localization of the excited states could be compared to the C_{60} multilayer sample system. This would allow to answer the question whether the interaction with the substrate completely suppresses the formation of excitonic states.
The strong hybridization of C_{60} with the Cu(111) surface, accompanied by the severe possible reconstruction of the surface, is a special case of hybrid system. The magnitude of the phenomena is attributed to the matching of the adsorbate and substrate lattice constants. Less surface reconstruction and less hybridization have been reported for C_{60} on other noble metal surfaces, where the lattice constant of the superstructure is not a multiple of the substrate lattice constant [27, 179]. It has been proposed that the mismatch between the adsorbate and the substrate unit cell can lead to a reduced overlap in the molecule-metal wave function and thus to a reduced hybridization [27]. Future research could further investigate the influence of this mismatch on hybridization. Furthermore, the question can be asked whether other 3D aromatic molecules, show such a strong hybridization on noble metal surfaces and whether this hybridization is also influenced by the size and orientation of the superstructure unit cell with respect to the substrate. Rubrene on Pt(111) was reported to show chemisorption-like behavior and signs of hybridization and might serve as a good starting point [180].

Another possible class of molecular systems to investigate are endohedral fullerenes. These are fullerenes that contain one or more atoms inside their carbon cage. It has been shown that for $Sc_3N@C_{80}$ adsorbed on the Ag(111) surface, the Sc_3N core is distorted into a pyramidal shape due to charge transfer from the substrate to the LUMO [181]. The question now is how the electronic and geometric properties of the core of endohedral fullerenes are altered on surfaces where not only charge transfer occurs, but the molecular orbitals hybridize strongly with the metal states of the substrate, similar to the case of C_{60} on Cu(111). For this question, POT would be a suitable technique to probe the electronic structure of the system and to distinguish core and carbon cage states in momentum space.

5 Excitonic Structure in C_{60} Multilayer Films

This chapter discusses the momentum space signatures of the excitonic landscape of a multilayer film C_{60} on Cu(111). The objective of this study is to observe the dispersion of excitonic states which are a correlated electronic phenomenon and to determine the excitonic character based on momentum space signatures. Additionally, the use of ultraviolet photon energies, which provide an easy access with good statistics to the first surface Brillouin zone, is tested conceptually in the framework of exciton photoemission orbital tomography. All experiments are performed at low sample temperatures ($T \approx 130\,\mathrm{K}$) unless otherwise noted.
After a brief introduction to excitons in molecular crystals and the multilayer C_{60} sample system, the valence band structure of the sample system, which serves as the initial state in the photoemission studies of the excitonic structure, is discussed. Afterwards, the dispersive scattered final states that significantly influence the measurements of the excited states are debated. The measurements of the excitonic landscape of the sample system using ultraviolet photon energies will be discussed and compared to theory calculations and experiments conducted with extreme-ultraviolet photon energies. In the last part of the chapter, the temporal evolution of the excitonic momentum space signatures is discussed, and the results obtained at low sample temperatures compared to measurements at room temperature.

5.1. Excitons in Organic Semiconductors

Upon light absorption in organic semiconductors, electrons are excited from the ground state, leaving behind a vacancy with positive charge in the molecular orbital, a so-called hole. The electrons in organic semiconductors are localized on the respective molecules and therefore less mobile compared to electrons in metals. As a consequence, the remaining hole is not fully screened by the electron system and can still interact with the excited electron via Coulomb interaction. This leads to the formation of a bound electron-hole pair, a quasiparticle called an exciton. The formation of excitons is only possible if the Coulomb energy is larger than the thermal energy [182–185]. In general, this is the case for molecular solids with exciton binding energies in the range of several 100 meV [185].
The basic properties of excitons relevant to organic semiconductors will be described for the simple case where only one electron transition from the highest occupied molecular orbital (HOMO) to the lowest unoccupied molecular orbital (LUMO) contributes to the formation of an exciton, as shown in Figure 5.1. Two cases can be distinguished: The electron can either be promoted to the LUMO on the same molecule as the remaining hole or onto a neighboring molecular site [183]. The former scenario is referred to as a Frenkel exciton, while the latter is called a charge transfer (CT) exciton or a Davydov exciton [182, 183, 186, 187]. It is imperative to acknowledge that molecular orbitals are single-particle states consisting of a single electron wave function, whereas excitonic states are quasiparticle states consisting of many electron wave functions. As suggested by Zhu [184], both of these states can be represented within the same energy level diagram as in Figure 5.1, with the ionization potential serving as a reference point. The ionization potential is defined as the minimum energy required to ionize an electron from the HOMO level to the local vacuum level. The optical

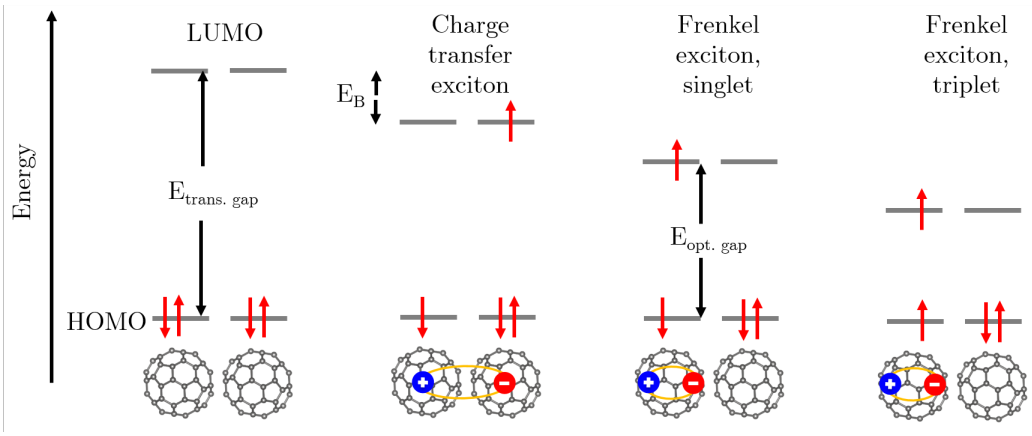

Figure (5.1) Schematic drawing of the energy level alignment of Frenkel and charge transfer excitons compared to the molecular orbitals. For simplification only one possible transition from the HOMO to the LUMO is considered contributing to the excitonic state. Similar to [185]. The structural data for the ball and stick model of C_{60} was taken from the data base of P. Puschnig, University of Graz [152].

gap $E_{\text{opt gap}}$ of the material is then defined as the energy distance between the ground state and the first optically accessible excitonic state. Conversely, the transport gap $E_{\text{trans gap}}$ is defined as the energy distance between the HOMO and LUMO of the many-body system. The exciton binding energy E_{B} is defined as the amount of energy required to generate free charge carriers, that is, the distance between the excitonic state and the LUMO.

Frenkel excitons and CT excitons are charge-neutral. The CT exciton is characterized by a larger charge separation and an associated dipole moment. Consequently, CT excitons are more easily separated into free charge carriers [182]. Due to the rather weak intermolecular interactions compared to the binding energies of the electrons, the wave functions of both types of excitons can be expressed as a product of molecular wave functions [182, 183]. Specifically, Frenkel excitons comprise excited molecular wave functions, while CT excitons consist of ionic wave functions. The wave functions are distributed throughout the entire crystal. However, the resulting wave packet describing the exciton is localized with finite spread.
According to the Pauli principle, molecular orbitals have the capacity to contain two electrons with antiparallel spin. Consequently, the promotion of an electron from the HOMO to the LUMO can result in the formation of a singlet or a triplet state. This can significantly affect the energy level alignment of Frenkel excitons because the exchange interaction between both electrons on the same molecular site is comparably large. As a result, the Frenkel excitonic states are split into triplet and singlet states in a 3:1 ratio [183]. The triplet states are lower in energy and have a much longer lifetime because a spin flip process is necessary for the electron to return back into the singlet ground state. In the context of CT excitons, the distinction between singlet and triplet states is rendered negligible due to the small exchange interaction between the promoted and the remaining electron.
The transition from an isolated molecule to a molecular aggregate results in the splitting of excitonic levels, thereby forming quasi-continuous bands whose width is contingent upon the dipole-dipole interaction [183]. The width of the aforementioned bands is also dependent on molecular and lattice vibrations [187].
Excitons can furthermore exhibit dispersive band structures that can be characterized by a tight-binding model. The magnitude of band oscillations is greater for CT excitons than for Frenkel excitons due to their enhanced delocalization [188, 189].
Following the above discussion, some remarks need to be made: Firstly, it should be ac-

knowledged that the discussion has been limited to a simplified model, involving a single HOMO → LUMO transition in the process of exciton formation. However, for actual sample systems, multiple transitions from distinct orbitals can contribute to a single excitonic state [66, 67]. Secondly, it is often assumed that CT excitonic states are located at higher energies compared to the ground state than Frenkel excitons due to the larger separation of charges. However, this is not universally valid, and its validity is contingent on the molecular packing and alignment [190]. Furthermore, Frenkel and charge transfer excitons are borderline cases of excitons. A definitive distinction between the two types of excitons may not be feasible in certain instances [183].

5.2. Multilayer C_{60} films on Cu(111)

This section discusses the structural and electronic properties of C_{60} multilayer films on a Cu(111) sample. Special emphasis is given to the excitonic landscape of the system.

5.2.1. Structural and Geometric Properties

Due to the substantial diameter of the C_{60} molecules, films comprising three to five monolayers can be regarded as decoupled from the substrate. These films exhibit properties that are characteristic of the C_{60} bulk phase [191, 192].
At room temperature C_{60} forms a face centered cubic (fcc) crystalline structures on different noble metals, thereby following the geometric structure of the monolayer system [156]. As outlined in Section 4.2 C_{60} growths in a 4×4 superstructure on Cu(111), resulting in a lattice constant of the C_{60}(111) surface of approximately 10 Å [156, 193]. As a result of the growth along the high-symmetry direction of the Cu(111) substrate, the C_{60} multilayer does not exhibit any additional rotational or mirror domains, leading to significantly less complex low energy electron diffraction (LEED) patterns and momentum space structures compared to C_{60} multilayer films grown on other substrates like Ag(111) or Pt(111). In contrast, C_{60} multilayers grown on Ag(111) follow the $(2\sqrt{3} \times 2\sqrt{3})$R30° superstructure of the monolayer (refer to Section 4.2 for further details). The presence of additional rotation and mirror domains introduces complexity to the momentum space signatures and diffraction patterns. Cu(111) is hence selected as a substrate for the multilayer system due to the aforementioned complications.
The unit cell of the C_{60}(111) multilayer system contains one molecule, as indicated by the orange unit cell vectors in Figure 5.2 (a). At ambient temperature, all molecules exhibit unrestricted rotation. However, upon cooling below 260 K, the C_{60} crystal undergoes a phase transition from a fcc to a sc crystal structure [149, 193–197]. This transition exerts a negligible effect on the lattice constant, with a reduction of approximately 1 % [193]. The transition temperature of the surface is lower than the one for the bulk and lies in between 225 and 235 K [197]. In the region below the fcc-sc phase transition temperature, the C_{60} molecules exhibit a transition to a rotationally ordered state. The molecules retain only one rotational degree of freedom around the <111> axes (see Figure 5.2 (b)) [149, 193–197]. The molecules do not rotate freely around these axes, but make rigid jumps between positions that are 60° apart. This results in the inequality of neighboring molecular sites, leading to a 2x2 superstructure with respect to the structural phase containing one molecule per unit cell. The resulting superstructure unit cell thus consist of four molecules (see blue unit cell in Figure 5.2 (a)). The rather high temperature at which this reorientation occurs can be explained by the bond optimization of adjacent molecules. The molecules reorient in such a manner that pentagon centers with low electron density of the C_{60} carbon cage face electron-rich double bonds, thus stabilizing the overall structure [149, 195]. The remaining rotational degree of freedom, i.e., the jump reorientation around the <111> axes, is frozen

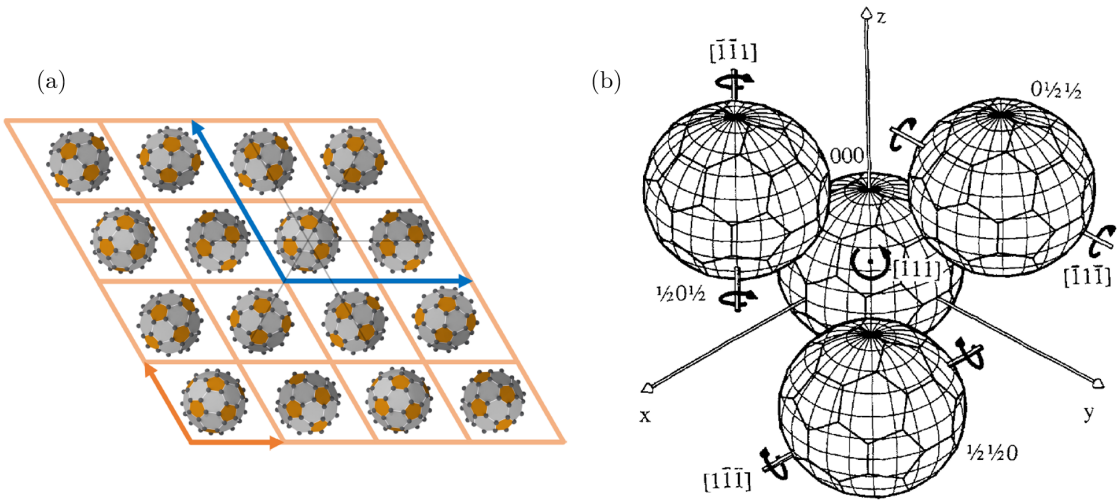

Figure (5.2) Structure of a C_{60} multilayer at low temperature. (a) Surface structure as seen from the top. The orange arrows display the unit cell of the molecular arrangement. The blue arrows indicate the superstructure also considering molecular orientation. One C_{60} molecule in the unit cell is oriented in a hexagon-prone geometry while the other three have double-bonds facing the surface. The latter three molecules are rotated by 120° with respect to each other. The black lines mark a three fold symmetry with a hexagon-prone C_{60} in its center. With permission from [47]. (b) Bulk unit cell of the C_{60} crystal at temperatures between 90 and 260 K. Only one rotational degree of freedom is remaining with a jump reorientation around the indicated axes. Copyright © 1993, Informa UK Limited, trading as Taylor & Francis Group [194].

out below 90 K. This results in the molecular arrangement depicted in Figure 5.2 (a). In the large unit cell (illustrated in blue), three of the four molecules are aligned with double bonds facing towards the surface, while the fourth molecule has a hexagonal site pointing down [197].

5.2.2. Electronic and Excitonic Properties

This section presents a selected literature-based overview of the electronic and excitonic properties of a C_{60} multilayer film, building on the structural characteristics discussed in the preceding section.
C_{60}, like rubrene, is a special case of an organic semiconductor with a pronounced dispersive band structure [18–23, 198–200]. The phenomenon of dispersive band formation is attributed to the overlap of the π-electron system of neighboring molecules, which is therefore constrained to the energetically higher-lying occupied molecular orbitals and unoccupied orbitals [21–23, 142, 175]. It has been determined that both the HOMO and the HOMO-1 consist of two highly dispersive, counterpropagating bands [22, 23]. The developed bands possess a relatively narrow bandwidth between 300 and 600 meV compared to inorganic semiconductors or metallic systems [21, 22]. In contrast, lower-lying orbitals, beginning at about 5 eV binding energy, exhibit a σ-orbital character and manifest as ring-like dispersionless signatures in momentum space. As previously mentioned in Section 4.1, the orbitals referred to as HOMO and LUMO, as well as all other frontier orbitals of the C_{60} molecule, are degenerate and consist of several energy levels. The difference arising from intermolecular interaction between these energy levels in the multilayer is negligible.

Upon optical excitation, electrons can occupy excitonic states. In a C_{60} multilayer, as is the case with organic semiconductors in general, two types of excitons can exist: Frenkel and charge transfer (CT) excitons. Their fundamental properties and differences were discussed

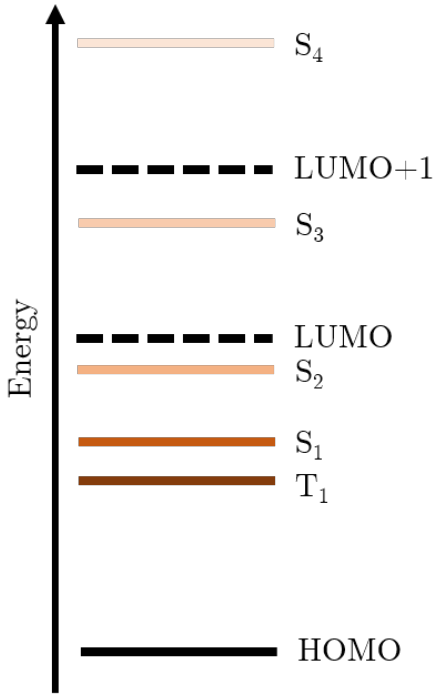

Figure (5.3) Schematic drawing of the excitonic energy levels and the single particle molecular orbitals of interest.

in Section 5.1. As illustrated in Figure 5.3, a energy level diagram is provided that offers a comprehensive overview of the most significant excitonic states in solid C_{60}, with respect to the single-particle molecular orbitals in the energetic vicinity. S and T represent the singlet and triplet states, respectively. The LUMO and LUMO+1 are single particle states, meaning that the electron occupying this state is not bound to a hole. The energetic positions of all drawn states, as well as the lifetimes of an electronic excitation into these states, are listed in Table 5.1. It has been determined that there exist three excitonic states below the LUMO and one excitonic state between the LUMO and the LUMO+1. The lifetimes of all excitations decrease with increasing energetic distance from the HOMO. It should be noted that the listed values, particularly the lifetimes, are significantly influenced by the quality of the sample the thickness of the molecular film [46, 89, 155, 201].
A major property of the excitonic states is their character, i.e. whether they are Frenkel or charge transfer excitons. The T_1, S_1, and S_4 excitons exhibit Frenkel character, while the S_3 exciton manifests a CT character [46, 67, 155]. The S_2 exciton's character remains a subject of debate. While some studies suggest a Frenkel character, others indicate a CT character [46, 67, 155].
Emmerich et al. investigated the exciton formation depending on the molecular coverage and the light polarization [155]. Their findings revealed that the population of the S_3 exciton upon direct excitation is contingent on the light polarization, exhibiting maximum excitation efficiency for p-polarized light. Conversely, the subsequent formation of S_2 and S_1 excitons via decay is not influenced by the light polarization, as the ratio between CT and Frenkel excitons remains constant. The molecular coverage exhibited no discernible influence on the exciton population or their respective characteristics, but on the depopulation times of the excitonic levels. An increase in depopulation times was observed with increasing film thickness.
In the remaining portion of this chapter, the focus will be exclusively on the S_1-S_3 excitons.

Table (5.1) Energetic peak positions and quasi particle lifetimes of the the excitonic states (S = singlet, T = triplet) as well as an electronic excitation in the single particle molecular orbitals LUMO and LUMO+1 from literature. The energetic positions were referenced to the HOMO with the position of the Fermi edge at $E - E_{\mathrm{HOMO}} = 1.9\,\mathrm{eV}$ [89]. The listed values, especially for the lifetimes, can strongly depend on the sample quality and thickness [89, 155, 201, 202]. A more detailed overview of the energetic positions can be found in [89].

	$E - E_{HOMO}$ (eV)	Lifetime	Reference
S_4	3.6	$< 50\,\mathrm{fs}$	[67]
LUMO+1	3.4 - 4.0	48 fs	[201, 203, 204]
S_3	2.8 - 3.0	$38 - 45\,\mathrm{fs}$	[46, 67, 89, 155]
LUMO	2.3 - 2.4	$0.73 - 2.51\,\mathrm{ps}$	[201, 203, 204]
S_2	2.0 - 2.2	$2.0 - 134\,\mathrm{ps}$	[46, 67, 89, 205–207]
S_1	1.7 - 1.9	$1.23 - 1.3\,\mathrm{ns}$	[46, 67, 89, 205]
T_1	1.45	$15 - 22.3\,\mu\mathrm{s}$	[89, 205]

5.3. Valence Band Structure of C_{60} Multilayer Films

First, an investigation of the general electronic structure of the occupied states will be conducted before the excitonic structure in a C_{60} multilayer film on Cu(111) is discussed. This will establish a foundation for the subsequent investigation of excitonic states, as the frontier valence orbitals serve as initial states in the photoemission process. The following investigation will entail a comparison of the findings from experiments on multilayer films of C_{60} grown on Cu(111) with those from prior studies of C_{60} multilayer films on Ag(111) by Haag et al. [23] and of bulk C_{60} on Bi_2Se_3 by Latzke et al. [22].
The subsequent experiments were conducted at temperatures between 120 and 140 K, which is below the phase transition temperature of the C_{60} multilayer. As delineated in Section 5.2.1, this results in a sc unit cell and the suppression of two out of three molecular rotations [193–197]. A vacuum ultraviolet (VUV) gas discharge lamp, the HIS 14 HD model from FOCUS GmbH, emitting the He I_α line ($h\nu = 21.2\,\mathrm{eV}$), was utilized as an unpolarized light source. The relative intensity of the He I_β light emission is only about 1.2 to 1.8 % compared to the He I_α intensity [77]. In the further discussion, it will be omitted because no sign of electrons emitted by He I_β light is visible in the data.

Figure 5.4 (a) illustrates the photoelectron spectrum of the first two frontier valence orbitals of the C_{60} multilayer. The energetic peak position of the highest occupied molecular orbital (HOMO) serves as a reference due to the abundance of a Fermi edge in this semiconducting system. The visible molecular orbital peaks were fitted using a combination of two Gaussian functions and a background contribution. The resulting values for the energetic peak positions and the full width at half maximum (FWHM) are listed in Table 5.2 and are in agreement with literature [21, 84, 149, 199, 202]. The disparity in the intensity of the orbital peaks can be attributed to the different degree of degeneracy of HOMO and HOMO-1)(see Figure 4.1 (b)) and varying cross sections, which exhibit a dependence on photon energy [199].
As illustrated in Figure 5.4 (b), an energy distribution curve (EDC) depicts the same energetic region as in the photoelectron spectrum. The cut orientation is selected along the $\overline{\Gamma\mathrm{K}}$ direction for negative momenta and along the $\overline{\Gamma\mathrm{M}}$ direction for positive momenta, respectively. The vertical white lines indicate the boundary of the first surface Brillouin zone

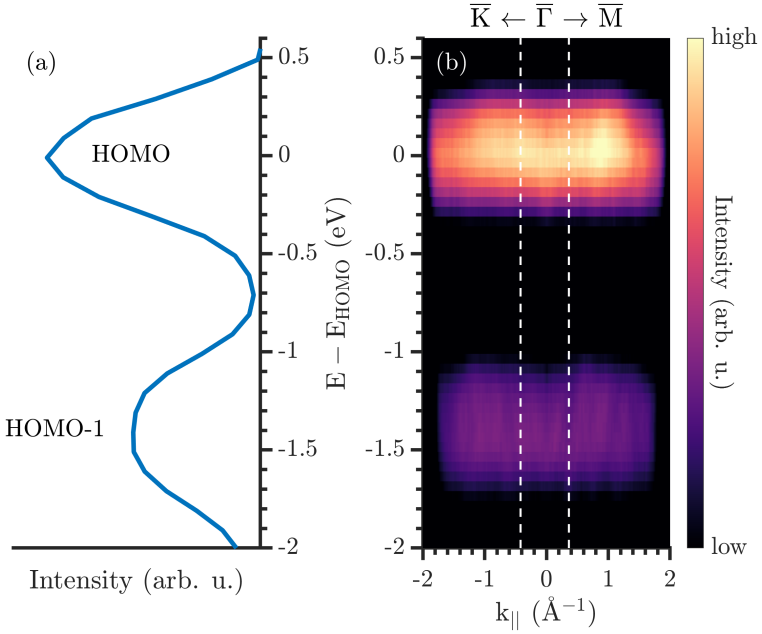

Figure (5.4) Photoelectron spectrum (a) and energy distribution curve (EDC) (b) of the two frontier valence orbitals of a C_{60} multilayer on Cu(111) ($h\nu = 21.2\,eV$). For the extraction of the EDC the 3D ARPES data set was cut along the $\overline{KT}\overline{M}$-direction. The vertical white lines indicate the border of the first surface Brillouin zone.

Table (5.2) Energetic peak positions referenced to the HOMO and FWHM of the highest valence orbitals.

	$E - E_{HOMO}$ (eV)	FWHM (eV)
HOMO	0	0.56
HOMO-1	-1.41	0.67

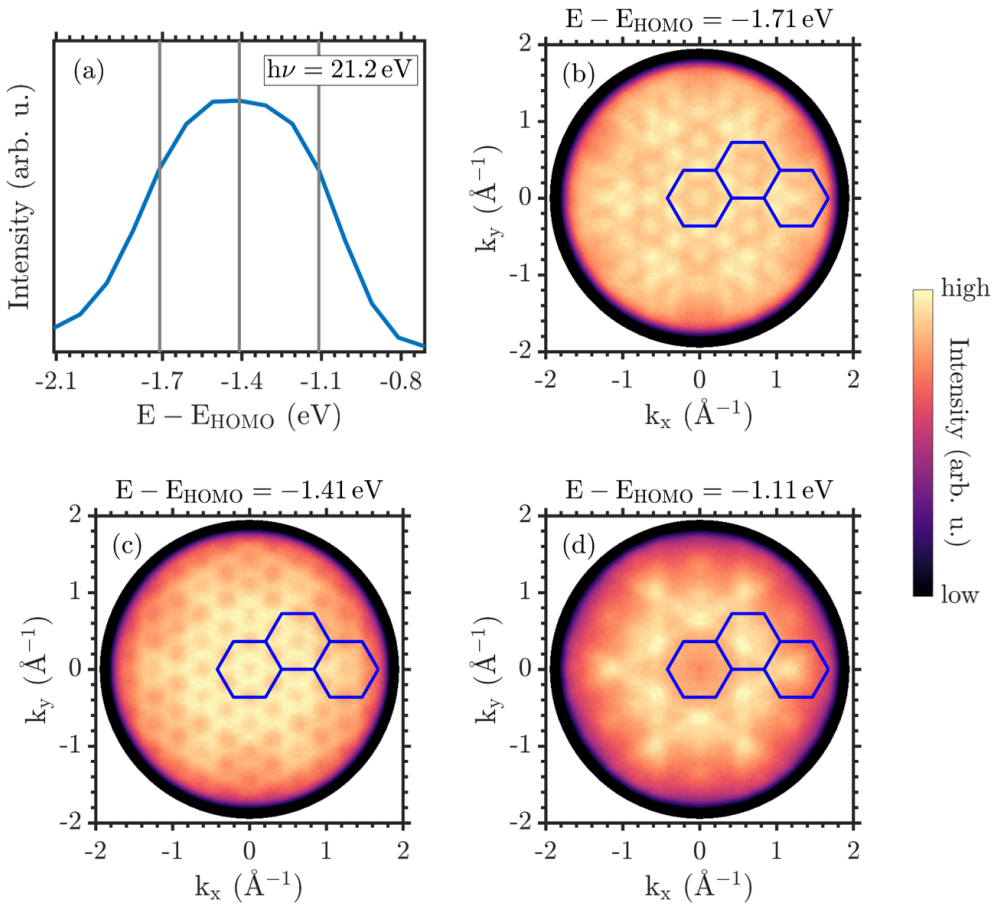

Figure (5.5) Constant energy maps (b-d) of the HOMO-1 orbital of a C_{60} multilayer film on Cu(111). The maps are extracted at the energetic positions indicated by the gray lines in the photoelectron spectrum (a). The CE maps show a dispersive structure showing rich signatures with the first BZ superimposed in blue.

(BZ), i.e. the first $\overline{\text{K}}$-point and the first $\overline{\text{M}}$-point. The data was symmetrized according to the sample symmetry, as explained in Appendix A.2, and interpolated in energy to enhance visibility. As anticipated, the molecular features manifest as broad regions of intensity. Inside each region of the HOMO and HOMO-1 a dispersion is visible. In the case of the HOMO-1, two strongly dispersive bands can be observed, as referenced in the relevant literature [21–23, 199, 208]. However, for the HOMO, the two expected bands are barely distinguishable. The atomic crystal-like band structure arises from the overlap of the π-orbitals of neighboring molecules [18, 22, 23, 198].

A more thorough examination of the band dispersion by means of constant energy maps (CE maps) of the two frontier valence orbitals will be conducted in the following section. The examination will begins with the HOMO-1 and its corresponding CE maps, which are depicted in Figure 5.5 (b)-(d). The energetic positions at which the CE maps were extracted are marked in the spectrum in Figure 5.5 (a) by gray lines. All CE maps exhibit well-defined patterns that show complex structures which follow a sixfold symmetry. This behavior is also observed in the raw data before symmetrization. For low energies, a dot-like pattern with a superimposed hexagon of lower intensity is observed (see Figure 5.5 (b)). The hexagonal pattern is significantly larger than the first BZ drawn in blue, exhibiting a 30° rotation towards the latter. In proximity to the photoemission horizon along the $\overline{\Gamma\text{M}}$-direction areas of reduced intensity are also identified. The CE map at the energetic peak position of the HOMO-1 (Figure 5.5 (c)) exhibits a honeycomb structure. The larger hexagonal structure

and the aforementioned areas show an overall higher intensity. The CE map on the higher energetic side of the HOMO-1 signal (Figure 5.5 (d)) displays a star-like pattern exceeding the first BZ. The transition of the different dot- and stripe-like features into each other for the different energies illustrates the dispersive nature of the molecular band structure.

The HOMO displays comparable characteristics to the HOMO-1, as can be seen in Figure 5.6 (b)-(d). However, its CE maps exhibit slightly less clarity and less well-defined structures. The energetic positions at which the CE maps were extracted are again marked in the spectrum in Figure 5.6 (a) by gray lines. For lower energies, the CE map displays a spot-like pattern that resembles the pattern of the HOMO-1 at lower energies. In this case, a star-like area of reduced intensity is discernible in the center. At the energetic position of the peak maximum, the photoemission pattern of the HOMO consist of six broad maxima located along the $\overline{\Gamma\mathrm{M}}$ direction. This configuration evolves into a prominent hexagon at higher energies, as illustrated in Figure 5.6 (d).
The observed photoemission angular distributions (PADs) strongly resemble to those reported by Latzke et al. in [22] and are characteristic of the two frontier dispersive bands in a commensurate bulk C_{60} film. The reason for this similarity despite the different substrates is that C_{60} can adopt its natural packing arrangement in both cases. In the case of Cu(111), this is possible due to a match between the lattice constants of the substrate and the adsorbate surface. On Bi_2Se_3, on the other hand, the interaction through van der Waals forces is so weak that the C_{60} molecules can adopt this preferred arrangement indefinitely. In contrast, the PADs observed for a multilayer C_{60} film on Ag(111) exhibit a significantly more complex pattern [23]. This discrepancy can be attributed to the growth pattern of C_{60} molecules, which adopt a $2\sqrt{3} \times \sqrt{3}\mathrm{R}30°$ structure, resulting in the formation of additional rotational and mirror domains.
The CE maps for the HOMO-1 and HOMO in Figures 5.5 and 5.6 reveal that not all discernible emission signatures align with the periodicity of the C_{60} BZ. Instead, there are larger signatures that extend across multiple BZs. To ascertain whether these larger signatures can be attributed to PADs of single molecular orbitals, a theoretical CE map of the C_{60} HOMO calculated by photoemission orbital tomography (POT) is shown in Figure 5.6 (e). The CE map was generated by summing the PADs of the HOMO for each molecular orientation present in the multilayer film. Thus, this represents a CE map of the C_{60} multilayer film in the absence of intermolecular interactions. It can be seen that the CE map of the HOMO calculated by POT shows only a ring close to the photoemission horizon. The reason for the absence of more detailed signatures is the PADs of the different molecular orientations in the unit cell are complementary to each other cancelling out most signatures during their superposition. Thus also the larger signatures in the experimental CE maps originate due to molecular interactions.
It has been demonstrated for two-dimensional (2D) molecules that the PAD of the molecular orbital defines the global intensity distribution and thus the regions where dispersion is best visible in the experiment [16]. Due to its 3D nature, complex orbitals, and one active degree of rotation, the HOMO and HOMO-1 of the investigated C_{60} multilayer sample system contribute to the respective PADs over the entire accessible momentum space. This results in large-scale patterns that exceed the C_{60} BZ. Furthermore, this allows the small signatures of the dispersive band structure, which follow the periodicity of the C_{60} BZ, to arise over the whole accessible momentum space.
It is noteworthy that C_{60} displays a dispersive band structure in spite of one remaining active rotation of the molecules. This observation indicates that the formation of the band structure is solely dependent on the overlap of adjacent molecules, with their relative orientation being negligible [22, 47]. It is suggested that this is due to the high symmetry of the C_{60} molecules, leading to the formation of a dispersive band structure even at room temperature

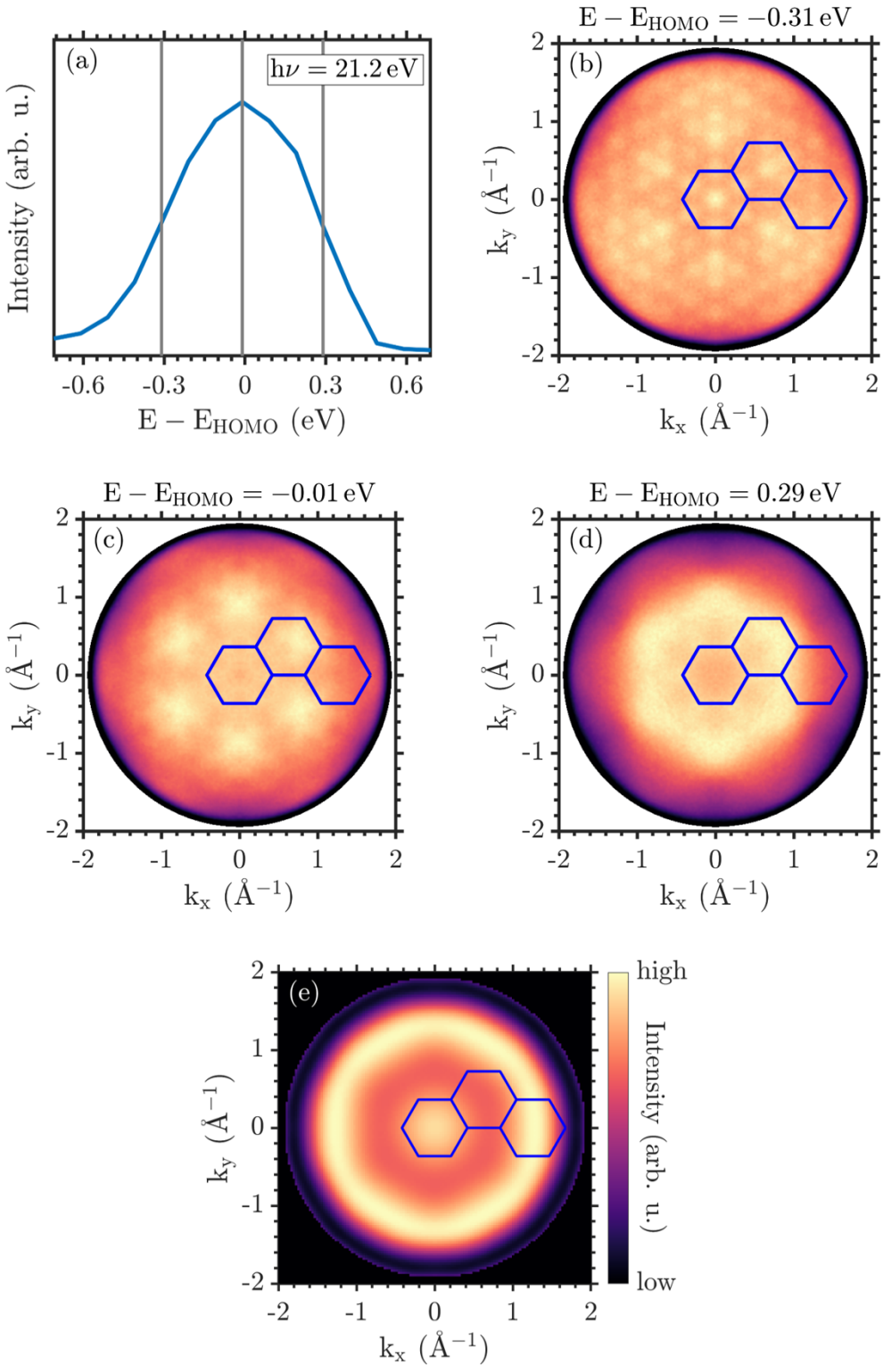

Figure (5.6) Constant energy maps (CE maps) (b-d) of the HOMO orbital of a C_{60} multilayer film on Cu(111). The maps are extracted at the energetic positions indicated by the gray lines in the photoelectron spectrum (a). As for the HOMO-1 in Figure 5.5, the CE maps show distinct signatures evolving over the whole energetic range of the molecular orbital. (e) Theoretical CE map of the HOMO of free molecules calculated by POT. The CE map was generated using the software kMap.py [162] and the molecular orbital data base of P. Puschnig, University of Graz [152]. The first BZ is superimposed in blue.

with all rotational degrees of freedom active [47].
As stated in Section 5.2.1 and illustrated in Figure 5.2 (a), the C_{60}(111) surface displays a 2x2 superstructure due to the different orientation of neighboring molecules. Despite the presence of active molecular rotations around one axis, the superstructure remains present due to the uniaxial rotations around the differently oriented axes of the molecules (see Figure 5.2 (b)). It is important to note that the superstructure is not visible in our ARPES or LEED experiments. This outcome arises from the high symmetry of the C_{60} molecules. The resulting signatures of the superstructure are too faint to be resolved. In the case of the LEED experiments, the situation is analogous to the 1x2 superstructure of $K_{0.5}$PTCDA on Ag(111) (refer to Section 3.2 for further information) [99]. In this context, the significant similarity of the form factors of the distinct molecules results in diffraction spots with intensities below the detection threshold.
In summary, it was shown that the electronic structure of the two frontier valence orbitals of multilayer C_{60} on Cu(111) was found to exhibit strong dispersive bands, in accordance with the findings reported in literature [21–23, 199, 208]. The interplay between overlapping π-orbitals of neighboring molecules and the correlation between band structure and molecular emission patterns was thoroughly examined. The search for the signatures of the 2×2 superstructure was unsuccessful due to the high symmetry of the C_{60} molecules.
The occupied electronic states of C_{60}, as discussed in this section, will function as the initial states in the photoemission process. This process will be used to study the excitonic states, which are the focus of the remainder of this chapter. In the following sections, the question of whether the excitonic states exhibit pronounced dispersion will be explored.

5.4. Momentum Space Signatures of Excitonic States of C_{60} Multilayer Films

In this section, the results of the investigation of the excitonic momentum space signatures of excitonic states in C_{60} multilayer sample systems will be presented. The presentation will commence with a thorough exposition of the excitation scheme and the measured photoelectron angular distributions (PADs). This will be followed by an in-depth discussion of the involved final states in the photoemission process. This becomes relevant due to the small probe photon energy used in the experiments. Afterwards an approach intended to remove the contributions of the final states is presented. In the final section of this study, the excitonic PADs will be replicated using simple geometrical assumptions. This will allow the validation of the findings after the approximate removal of the final state contributions.

Figure 5.7 provides a schematic representation of the measurement and excitation scheme for the 2PPE experiment, which aims to investigate the momentum signatures of excitonic states in a multilayer C_{60}. Electrons are excited into the S_3 excitonic state by a femtosecond (fs) laser pulse with a photon energy of 2.95 eV. Consequently, the electrons can scatter and cascade into the lower lying S_2 and S_1 states. A delayed UV pulse ($h\nu = 5.90\,\mathrm{eV}$) can then excite electrons from each excitonic level leading to photoemission. Consequently, the electrons of each excitonic state are ultimately found in a corresponding final state, designated as F_1 - F_3. In the following treatment of the excitonic states the energy will be referenced to the energetic position of the HOMO. For delimitation, the kinetic energy referenced to the vacuum level will be stated in the discussion of final states. As previously stated in Section 5.2.2, the excitonic states of C_{60} have been observed to exhibit a dispersion [188, 209]. The use of probe pulses with ultraviolet photon energies ($h\nu = 5.90\,\mathrm{eV}$) results in a photoemission horizon that is only slightly larger than the first BZ. This allows to study the intermolecular dispersion but not the orbital signatures. This photon energy can be achieved by frequency up-conversion of a Ti:Sa oscillator laser output (see Section 2.2.3). The high repetition

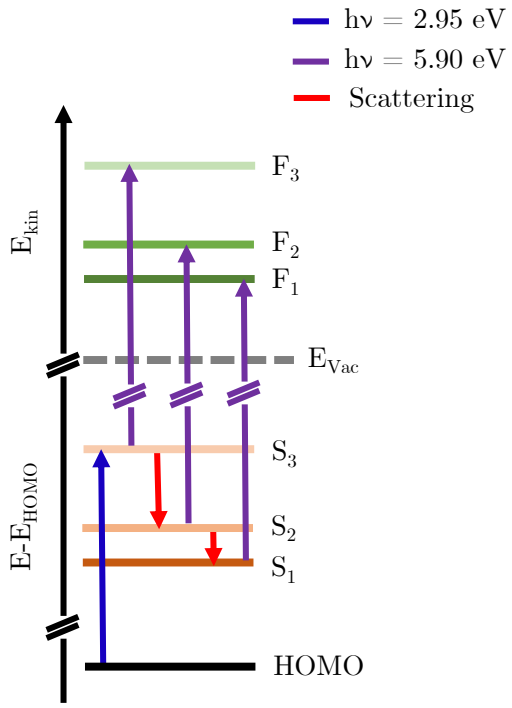

Figure (5.7) Pump-probe excitation scheme of excitonic states of a C_{60} multilayer. After excitation of the S_3 exciton with a visible fs laser pulse ($h\nu = 2.95\,\mathrm{eV}$), the electrons can subsequently scatter into the lower lying excitonic states S_2 and S_1. A delayed UV laser pulse ($h\nu = 5.90\,\mathrm{eV}$) then photoemits electrons from each excited state into a corresponding final state F_1 - F_3 above the vacuum level. The energetic positions of the excitonic states are referenced to the HOMO. Final states are discussed in terms of kinetic energy referenced to the vacuum level.

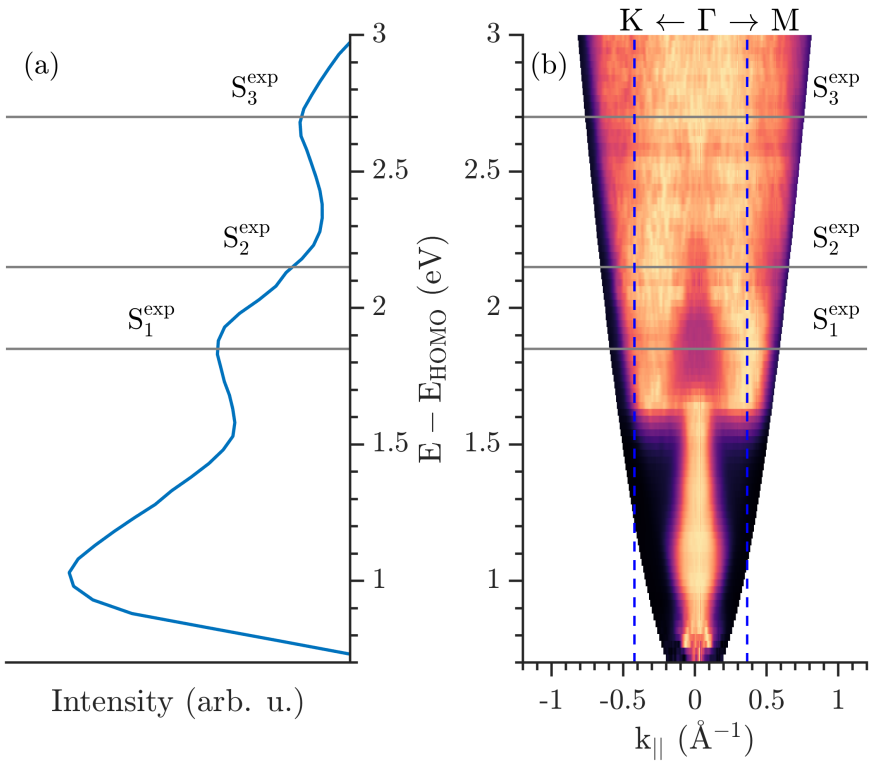

Figure (5.8) Photoelectron spectrum (a) and energy distribution curve (EDC) (b) of the excitonic states energy region of a C_{60} multilayer on Cu(111) following the excitation scheme in Figure 5.7. The EDC was extracted along the $\overline{\text{KΓM}}$-direction. The energetic positions of the excitonic states S_1-S_3 are highlighted by horizontal gray lines. The blue dashed vertical lines indicate the $\overline{\text{K}}$- and $\overline{\text{M}}$-point of the first surface Brillouin zone.

rate of the oscillator laser system of approximately 80 MHz enables sufficient resolution and statistics to study the dispersion in such a pump-probe experiment.

Figure 5.8 (a) depicts the photoemission spectrum of the investigated excitonic states. The spectrum was measured in a pump-probe experiment exciting the electronic transitions shown in Figure 5.7 with zero delay between pump and probe pulses. The intensity axis has been plotted logarithmically to accentuate the visibility of minute signatures in comparison to the substantial secondary electron peak that is located around 1 eV. The spectrum displays three discernible features at 1.90, 2.15 and 2.70 eV. By comparing the energetic positions of these three features with literature they could be attributed to the S_1, S_2 and S_3 exciton signatures respectively [46, 67, 89, 155, 205]. It is noteworthy that in certain literature, these excitonic states are designated as singlet exciton (S_1), charge transfer exciton 1 (CT_1), and charge transfer exciton 2 (CT_2), respectively.

As illustrated in 5.8 (b), an energy distribution curve (EDC) is presented, delineating the distribution of energy along the $\overline{\text{KΓM}}$-direction within the accessible momentum space. The energetic positions of the excitonic states S_1-S_3 identified in the photoemission spectrum are highlighted by horizontal gray lines. For the secondary electron region, a pronounced feature emerges at the $\overline{\Gamma}$-point up to $E - E_{HOMO} = 1.6$ eV where the photoemission intensity undergoes a sudden redistribution to the boundary of the photoemission horizon. Space charge effects may be partially responsible for the intensity at the $\overline{\Gamma}$-point and its prominent intensity. For energies larger than 1.6 eV no signatures of space charger are visible anymore as the intensity around the $\overline{\Gamma}$-point approaches a pronounced minimum.
A more detailed examination of the measured momentum distributions at the energetic po-

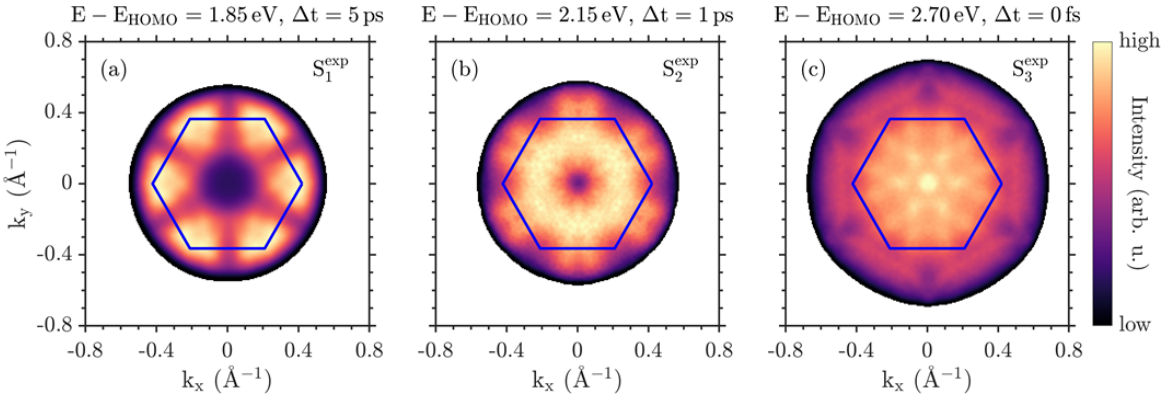

Figure (5.9) Experimentally obtained constant energy maps of the excitonic states S_1-S_3 of a C_{60} multilayer following the excitation scheme in Figure 5.7. The maps are extracted at the energetic positions indicated by the gray lines in Figure 5.8. The first BZ is superimposed in blue.

sitions of the excitonic states is enabled by the CE maps in Figure 5.9. The CE maps are extracted at the energetic positions marked by the gray lines in Figure 5.8. It is noteworthy that the CE map pertaining to the S_1 exciton is not extracted at the energetic position of the peak maximum, but rather at a smaller energies. This results in a reduction of the energetic overlap with the S_2 exciton because the large FWHM of both excitonic states is reduced ($FWHM_{S1} = 0.36\,eV$ and $FWHM_{S2} = 0.40\,eV$ [67]). Given that the S_1 and S_2 excitons are populated by inelastic scattering, the corresponding CE maps are extracted at the time of their maximum population where most of the population of the higher-lying excitonic states has already decayed. This approach also serves to minimize the potential superposition of different excitonic states in the measured photoelectron distributions.
The first BZ, corresponding to the real space unit cell with a single C_{60} molecule (orange unit cell in Figure 5.2 (a)), is marked in blue in each CE map of Figure 5.9. Only this BZ is used subsequently as a reference because the molecular orientation is less important for the dispersion of electronic states due to the high symmetry of the C_{60} molecules. This was also found for the occupied states of the band structure shown in Section 5.3.
While all CE maps in Figure 5.9 demonstrate a complex intensity distribution, some similarities and differences are evident. In particular, the CE maps associated with the S_1 and S_2 excitons show a pronounced intensity minimum at the $\overline{\Gamma}$-point, while the CE map of the S_3 exciton displays a maximum. Furthermore, a shift in the areas of highest intensity is observed from the boundary of the first BZ to its center, comparing the CE maps of the S_1-S_3 excitons. Another notable difference is, that the higher the energetic position of the excitonic state, the more detailed the intensity distributions become. A common feature of all three CE maps shown are the six stripe-like areas of low intensity along the $\overline{\Gamma M}$-directions. Having discussed the general shape and structure of the PADs, it is now necessary to examine a possible influence of the photoemission final state.

5.4.1. Scattered Final States

In the photoemission process, the final state can exert a considerable influence on the photoemission angular distribution, particularly at low photon energies [68–72]. This phenomenon can be attributed to the fact that the unoccupied region of the band structure of a crystalline sample extends far above the vacuum energy level. The unoccupied Bloch states of a crystalline sample can act as final states in the photoemission process, exhibiting significant dispersion. [68–72]. As previously stated in Section 2.2.2, these Bloch-like final states are regarded as scattered states [68–70]. The outgoing photoelectron wave can be subdivided into two components: one that is directly emitted into a plane wave final state propagating

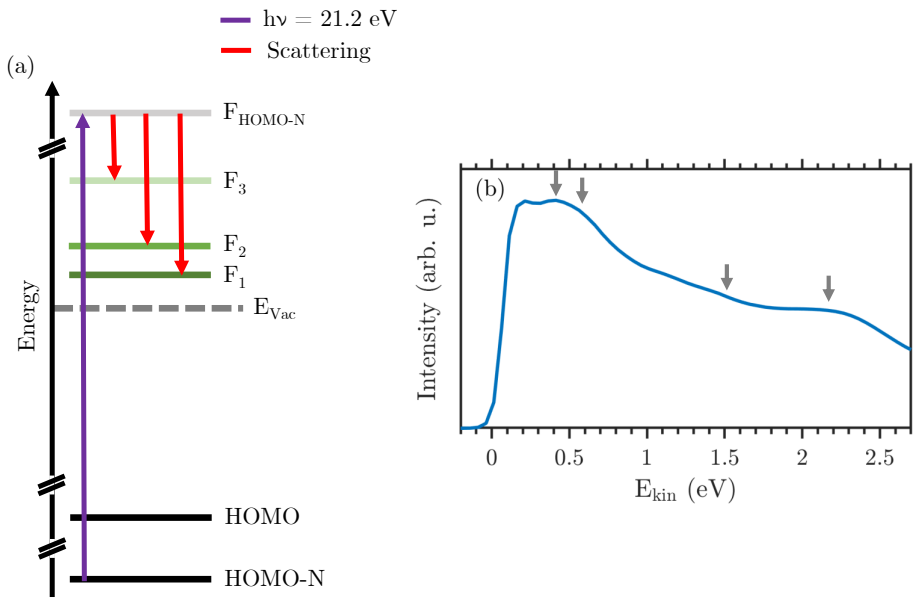

Figure (5.10) (a) Occupation scheme of the empty molecular states with scattered secondary electrons starting from an arbitrary occupied molecular orbital as initial state. (b) Photoelectron spectrum of the secondary electron region of a C_{60} multilayer film. The peaks in the curve progression marked by gray arrows indicate empty molecular states occupied by scattered secondary electrons.

towards the detector and one that propagates to the surface and is coherently backscattered by the surrounding atoms or molecules (see Figure 2.4 in Section 2.2.2). The latter displays a Bloch-like character due to the scattering at the periodic potential of the scattering centers. Consequently, both components contribute to the measured PAD on the detector in a coherent superposition.

A more in-depth examination of the CE maps presented in the preceding section (Figure 5.9) necessitates a comprehension of the structure of the final states. This can be obtained using secondary electron emission [71, 72, 210, 211] and an excitation scheme as depicted in Figure 5.10 (a). Electrons are excited from molecular orbitals of the C_{60} multilayer film using a vacuum ultraviolet (VUV) lamp with the $He\,I_\alpha$ line. During the photoemission process, some electrons scatter inelastically, thereby losing the energy and momentum relation to their initial states. This corresponds to the second step in the three-step model of photoemission. The scattered electrons can subsequently occupy the previously unoccupied Bloch-like states situated above the vacuum energy level following the scattering process [71, 72, 210, 211]. Secondary electrons can thus be used to map the empty band structure above the vacuum in an energetic region of the secondary electron background, as depicted in the photoelectron spectrum in Figure 5.10 (b). The spectrum exhibits multiple peaks in the otherwise smooth course of the secondary electron background whihc are indicated by gray arrows in the spectrum in Figure 5.10 (b). This observation indicates the existence of empty molecular states that are occupied during the scattering process. These empty molecular states have been previously observed using photoemission spectroscopy [212] and inverse photoemission [175].

In Figure 5.11 (a), an EDC of the secondary electron region is presented. The energy distribution curve (EDC) reveals the presence of strongly dispersive bands. These bands extend over several eV, thereby verifying the Bloch-like character of the final states. With higher kinetic energy, the observable signatures become broader and more smeared out. It is con-

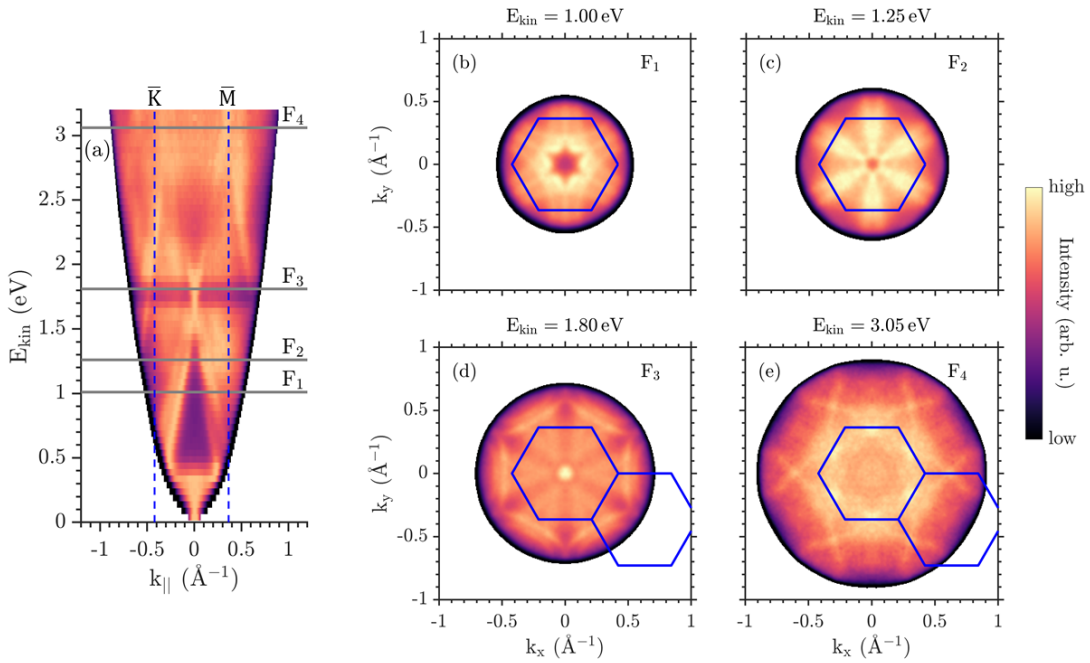

Figure (5.11) EDC (a) and selected CE maps (b-e) of the secondary electron region of the multilayer C_{60} sample system showing structurally rich momentum distributions of final states occupied by scattered electrons. The energetic positions of the CE maps are highlighted by horizontal gray lines in the EDC. The blue lines indicate the first BZ corresponding to the real space unit cell containing a single C_{60} molecule. For the CE maps at higher kinetic energies (d, e) also a neighboring BZ is indicated.

ceivable that within this energy range, occupied σ-states are being excited into the scattered final states. These initial σ-states manifest as broad ring-like features in their PADs and may contribute to a large extent to the obtained CE maps [23].
To obtain a more detailed perspective on the dispersive nature of the scattered final states, selected CE maps of the secondary electron region are presented in Figures 5.11 (b)-(e). Their energetic positions are marked by gray horizontal lines in the corresponding EDC in Figure 5.11 (a). The CE maps in (b)-(d) are extracted at the same kinetic energies as the ones measured in the pump-probe experiment in Figure 5.9. The CE map in Figure 5.11 (e) serves as an illustrative example for the PADs at higher kinetic energies. This implicates that the states observed at the energetic positions F_1-F_3 are final states for the corresponding excitonic states S_1-S_3. Consequently, all PADs that exclusively represent Bloch-like scattered final states are designated as F_i, and those of the excitonic states that include contributions of Bloch-like scattered final states as measured in the pump-probe experiment are designated as S_i^{exp}. In the next section an approximate removal of the final state contributions from the excitonic state PADs S_i^{exp} will be performed.
The first surface Brillouin zone (BZ) corresponding to the real space unit cell containing a single C_{60} molecule (illustrated as the orange unit cell in Figure 5.2 (a)) is superimposed on all CE maps. All CE maps in Figure 5.11 exhibit features that evolve towards the border of the BZ. However, a definitive conclusion regarding the evolution of these features beyond the first BZ remains ambiguous due to the restricted accessible momentum space. This is especially the case for lower kinetic energies, as evidenced by the CE maps in Figure 5.11 (b) and (c). At higher kinetic energies, the periodicity of the BZs is reflected in the momentum distributions. This phenomenon is further demonstrated in Figure 5.11 (d) and (e). For better differentiation, a neighboring BZ is delineated. For the F_3 final state CE map (Figure 5.11 (d)), the features along the $\overline{\Gamma M}$-direction appear to repeat outside the larger BZ, but are distorted due to the projection of the spherical electron wavefront on the flat detector screen.

The features at the border of the photoemission horizon along the $\overline{\Gamma M}$-directions may be the same features observed at the $\overline{\Gamma}$-point. In the case of the F_4 final state (Figure 5.11 (e)), the crossing lines at the $\overline{M}$-points, which are best visible at higher momenta, can also be observed in the central BZ. An increase of intensity along the $\overline{\Gamma M}$-direction near the photoemission horizon could correspond to the $\overline{\Gamma}$-point of the second BZ. However, it appears that there is an additional intensity modulation between the central BZ and the neighboring ones in form of a bright disc around the border of the central BZ. This modulation might emerge from molecular orbitals analogous to the intensity modulations of the occupied states, as discussed in Section 5.3. The momentum space features at larger momenta demonstrate a similar distortion induced by the projection onto the detector, as previously discussed for the F_3 CE map.
The complexity of the final state structure and its dispersion imposes a challenge for the further analysis of C_{60} PADs using low photon energies. As illustrated in Figure 5.7, under the pump-probe excitation scheme, the photoelectrons can populate the dispersive final states previously discussed in two ways: either directly or via elastic scattering. Consequently, any discernible structure observed in the CE maps depicted in Figure 5.9 must be contemplated in the context of its potential origin: Emission patterns could either stem from the excitonic state, the final state, or from a coherent superposition of both.

Now, the CE maps containing information about the excitonic states and scattered final states, S_i^{exp} in Figure 5.9, will be compared to the CE maps of the pure final states F_i obtained by secondary electron emission in Figure 5.11. Figure 5.12 (a) illustrates the energy distribution curve along the $-\overline{K\Gamma K}$-direction, which is divided into two segments by a vertical white line at the $\overline{\Gamma}$-point. The left side of the figure displays the EDC of the excited states, while the right side exhibits the EDC of the scattered final states. Each energy slice has been normalized to its maximum intensity to enhance visibility at higher energies. It is apparent that the EDCs exhibit numerous similarities, particularly in the energetic region of the involved excitonic states S_1-S_3 and their corresponding final states F_1-F_3, as indicated by the gray horizontal lines. The most striking difference is found for $E - E_{HOMO} < 1.6\,eV$ which can be partly attribute to a signature of space charge for the pump-probe experiment. In the excitonic data, a feature can be seen that evolves toward the $\overline{\Gamma}$-point with increasing energy (marked with a blue arrow). A corresponding feature can also be observed in the EDC of the scattered final states. However, this feature evolves faster towards the $\overline{\Gamma}$-point. Since the dispersive feature in the EDC of the excitonic states spans the entire energy range of the three excitonic levels, it presumably originates from intramolecular interactions. Intermolecular interactions would manifest themselves in dispersive features within the linewidth of each excitonic state. A more detailed discussion will be given in the following sections after an approximate removal of the final state contributions from the excitonic PADs.
A further difference between the EDCs is the band evolving towards the $\overline{\Gamma}$-point in the energetic region of the F_3 final state (marked by a blue arrow). This band could not be detected in the pump-probe experiment. A reason for this may be insufficient statistics.
The constant energy maps of the excitonic states are shown in Figure 5.12 (b)-(d) for negative momenta and the CE maps of the corresponding pure scattered final states F_1 to F_3 are displayed for positive momenta. A comparison of the momentum distributions obtained by the pump-probe experiment with the scattered final states reveals that the emission pattern of the S_1 exciton exhibits minimal commonalities with the pattern of the scattered final state (Figure 5.12 (a)). The emission maxima of the final state are, in fact, located on local minima of the momentum distribution of the excitonic state. This finding indicates that the influence of the final state F_1 on the CE map of the S_1^{exp} exciton is negligible. The CE maps attributed to the S_2 and S_3 excitons resemble those of the CE maps of the corresponding final states, F_2 and F_3. Despite the prevalence of the final state in the CE maps of the S_2

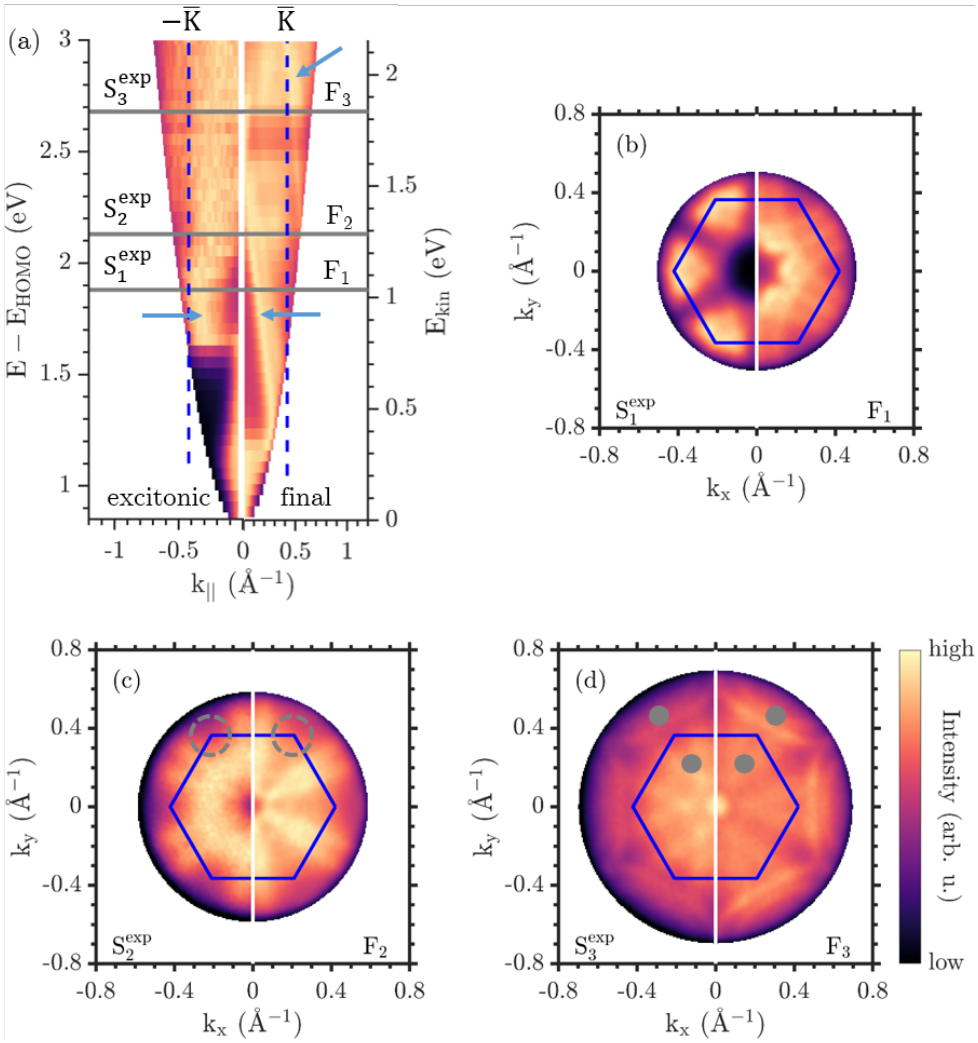

Figure (5.12) Comparison of the momentum distributions of the excitonic states (shown at negative momenta for all images) and scattered final states (shown at positive momenta for all images) separated by vertical white lines. (a) EDC along the $-\overline{\mathrm{KTK}}$-direction. For each energy the intensity was normalized to its maximum intensity for better visibility. The gray horizontal lines indicate the energies at which the CE maps were extracted. (b)-(d) CE maps of the excitonic states S_1^{exp} to S_3^{exp} for negative momenta and the corresponding scattered final states F_1 to F_3 at positive momenta. The first BZ of the unit cell containing a single C_{60} molecule is marked in dark blue.

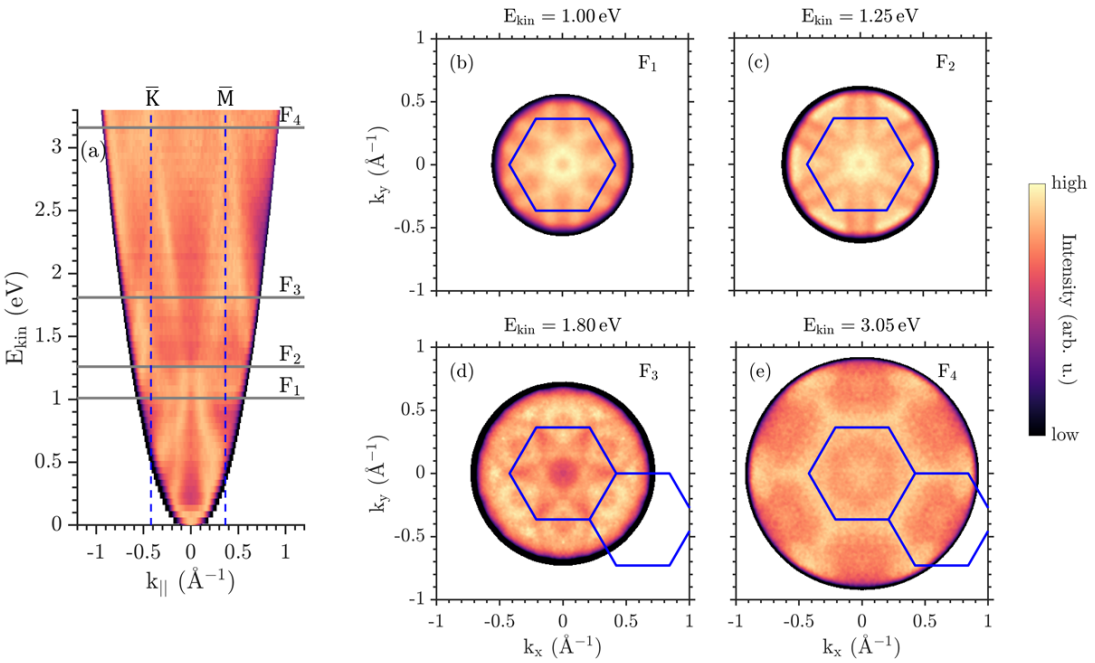

Figure (5.13) EDC (a) and selected CE maps (b-e) of the secondary electron region of the monolayer C_{60}on Cu(111) sample system discussed in Chapter 4. Structurally rich momentum distributions of final states occupied by scattered electrons are visible. The energetic positions of the CE maps are highlighted by gray horizontal lines in the EDC. The blue lines indicate the first BZ corresponding to the real space unit cell containing a single C_{60} molecule. For the CE maps at higher kinetic energies (d, e) also a neighboring BZ is indicated.

and S_3 excitons, discernible differences emerge, which may be indicative of excited state signatures. As illustrated in Figure 5.12 (c), the intensity surrounding the $\overline{K}$-points is notably higher in the CE map of the S_2 exciton compared to its scattered final state counterpart. This is highlighted for two $\overline{K}$-points by gray dashed circles. A similar observation can be made in the area of the BZ in the CE map of the S_3 exciton in Figure 5.12 (d), where the intensity within the BZ is elevated relative to the intensity outside of it. This can best be seen by comparing the regions marked with gray dots. These differences in the momentum space signatures may be indicative of the momentum distributions of the pure intermediate states.

Dispersive scattering end states are not only present in the C_{60} multilayer film, but also occur in the C_{60}/Cu(111) monolayer sample system discussed in Chapter 4. The scattered final states of both systems are compared. The secondary electron region of the monolayer C_{60}/Cu(111) sample system is depicted in the EDC in Figure 5.13 (a). A comparison of the two systems reveals the presence of similar dispersive bands, suggesting comparable behavior in both systems. Two bands can be observed crossing at the $\overline{\Gamma}$-point and evolving towards the $\overline{K}$- and $\overline{M}$-point. It is noteworthy that these two bands are also discernible in the multilayer sample system. However, their crossing point is at lower kinetic energies. Furthermore, the intensity minimum at the $\overline{\Gamma}$-point below the crossing point is much more pronounced in the C_{60} multilayer.
A further comparison of the scattered Bloch states above the vacuum level is displayed in Figure 5.13 (b-d), which presents the CE maps of the C_{60} monolayer on Cu(111) system at the same kinetic energies as the ones of the multilayer sample system in Figure 5.11. The depicted CE maps bear a certain resemblance to those of the multilayer sample system, yet they also exhibit notable discrepancies. For example, the CE maps of the F_1 and F_2 final states show a star-like pattern of higher intensity in both systems. In contrast, the CE maps

of the F_3 final states both show a star-like pattern of lower intensity, but rotated by 30° with respect to each other. One potential explanation for these discrepancies could be attributed to a constant energy shift between the scattered Bloch states of the two sample systems, as would be expected given that the observed crossing points in the EDCs are located at different energies. If this is indeed the case, then the CE map of the F_2 scattered Bloch state of the monolayer sample system in Figure 5.13 (c) should approximately correspond to the CE map of the F_3 state of the multilayer system in Figure 5.11 (d). However, a close examination reveals that the CE maps in question exhibit no discernible similarities. Specifically, the outwards evolving features of low intensity are rotated by 30° between the two CE maps. Consequently, it is inferred that the disparity in the scattered Bloch states does not stem from a mere energy shift. Instead, it is proposed that the underlying cause of the distinct dispersion of the scattered Bloch states above the vacuum level of the monolayer C_{60} sample system is the influence of the Cu(111) substrate. The extent of the substrate's influence on the dispersion of the scattered Bloch states remains elusive; that is, it cannot be ascertained whether the photoelectrons are partially backscattered on the first layer of the Cu(111) substrate due to their rather large inelastic mean free path greater than 10 nm at these low kinetic energies [38]. Alternatively, the hybridization between the C_{60} molecules and the Cu(111) surface might also effect scattered states such far above the vacuum level. The resolution of this outstanding question may be possible through the implementation of a dedicated density functional theory calculation.
It should be noted that increasing the energy of photons to avoid the final state energy region under discussion may present a significant challenge. It has been demonstrated that final states with higher kinetic energies are less prone to manifesting Bloch-like characteristics, as the electrons are energetically further away from the crystal potential. This phenomenon has been observed in various experiments, including those conducted on a C_{60} multilayer [23, 67]. However, the necessary magnification of the small momentum space region of the first surface Brillouin zone, as well as the low signal-to-noise ratio of commonly available light sources capable of delivering the necessary photon energies, impose significant experimental challenges. However, the advent of pulsed femtosecond extreme ultraviolet light sources operating at MHz repetition rates may render this a viable prospect in the future.
In this chapter, it was demonstrated that for the S_2 and S_3 excitonic states, the obtained photoemission angular distributions predominantly characterized by the pattern of the corresponding final states F_2 and F_3. While subtle distinctions potentially originating from the excitonic states were discerned, their overall configuration and structure of the momentum distributions remain ambiguous. Consequently, the subsequent section aims to extract the excitonic features from the CE maps discussed herein by partially disentangling the excitonic and final state contributions through a simplified approximation.

5.4.2. Approximate Removal of the Scattered Final State Contributions

The photoemission angular distribution of the excitonic states S_2 and S_3, measured with low photon energies, are predominantly influenced by scattered final states. The objective is now to approximately remove these final state contributions and extract momentum space signatures of the excitonic states. The two contributions to the photoemission signal at low photon energies, namely the direct emission into a plane wave final state and the indirect emission backscattered from the surrounding molecules, are coherently superimposed [68, 69]. Consequently, disentangling these contributions can be challenging.
In the following discussion, the superposition of the PADs is treated as incoherent, which is a crude approximation. Consequently, the composite PAD of the excitonic and final states can be straightforwardly regarded as a weighted sum of the PADs of the respective states. To approximate the separation of excited and final state contributions, the CE maps of the pure scattered final states, discussed in Section 5.4.1, are subtracted from the composite CE

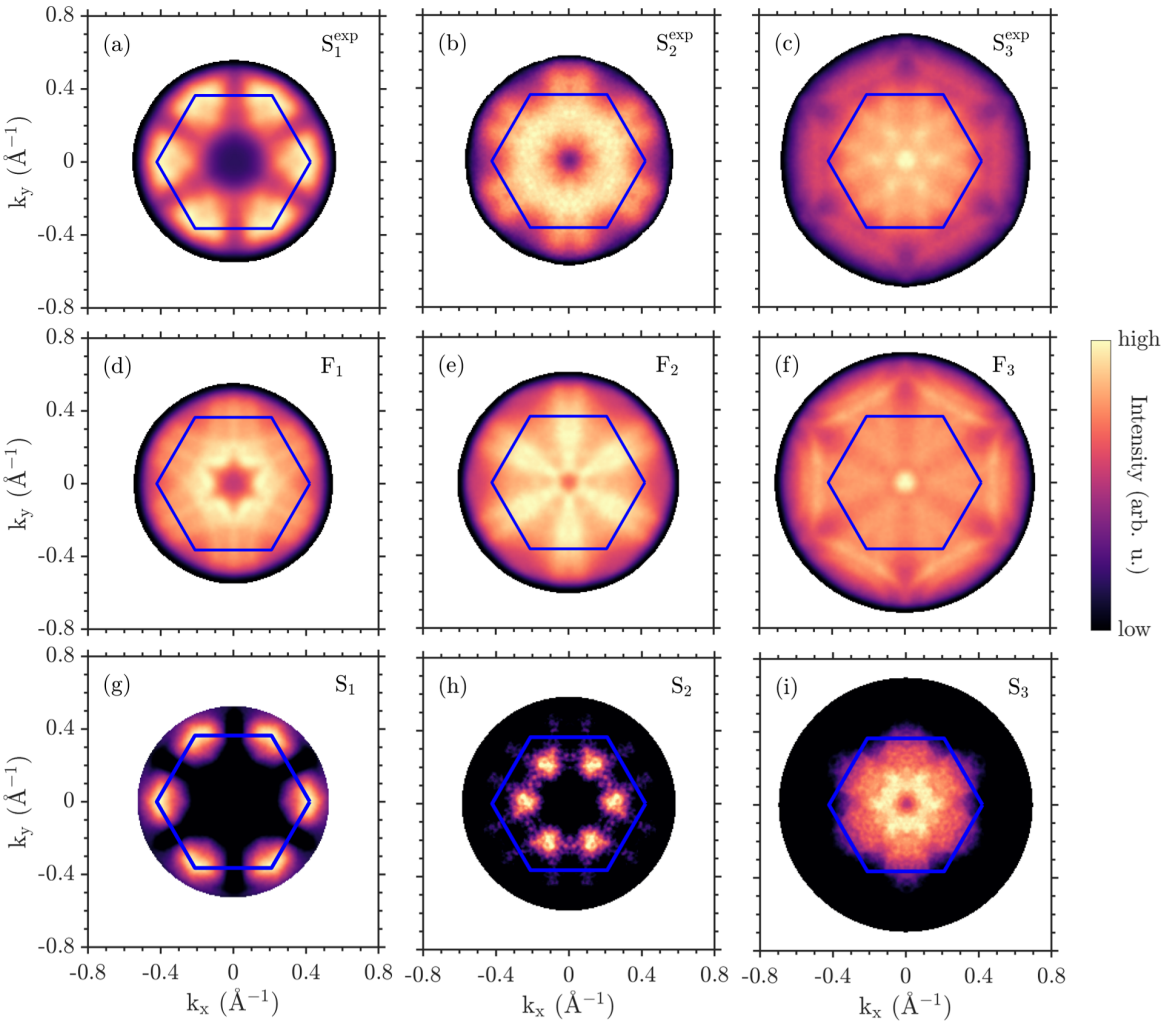

Figure (5.14) Comparison of the composite excitonic and final state (a-c), purely final state (d-f) and the final state adjusted CE maps (g-i). The bottom row CE maps emerges from suitable scaling and subtraction of the first two rows. The first BZ corresponding to the real space unit cell containing a single C_{60} molecule is indicated in dark blue.

maps obtained in the pump-probe experiment. The crude approximation of an incoherent superposition of excitonic and final states provides a feasible method of reducing the number of free parameters influencing the formation of the obtained PADs. This is particularly crucial given that the examined differences and details are rather small in comparison to the overall signal and its amount of contributing factors. This approach does not entirely eliminate all contributions from the final states. Signatures in the CE maps resulting coherent interference of the scattered electron wave with the direct emission into a plane wave final state will persist. Nevertheless, it allows for the verification of the presence of excitonic state contributions as well as a better estimate of the shape and extent of their photoemission angular distributions. The respective PADs will be designated as S_i.
A subsequent discussion of the differentiation of excitonic and final state contributions to the measured CE maps will be constrained to one energy per excitonic state. Additionally, the focus will be on the delay steps that were previously identified. It is important to note that the comprehensive evaluation procedure is carefully applied to all the delay steps obtained to ensure the results are consistent.

Figure 5.14 shows the constant energy maps of the composite PADs of exciton and final

state S_i^{exp} (top row), the pure final state PADs F_i (middle row), and the PADs of the excitonic states after subtraction of the final state contribution (bottom row). Prior to the subtraction, a proper scaling of the photoemission intensities of the different measurements is performed. A variety of scaling methods have been considered (see A.3.1 for further information), yielding qualitatively similar results, thereby underscoring the robustness of the remaining signatures in the momentum distributions towards the analysis procedure. Furthermore, the kinetic energy of the subtracted final state was varied by 0.05 eV to ascertain the optimal match between the final state CE map and the composite maps obtained. This approach also accounts for potential inaccuracies in energy calibration due to space charge and poorer energy resolution in the pump-probe experiment. The best correlation between the CE maps of pure final states F_i and the composite CE maps S_i^{exp} was observed when both were measured at the same kinetic energy. This outcome is consistent with previous findings and further underscores the negligible impact of space charge effects in the pump-probe experiment.
A comparison of the CE map of the S_1 exciton after final state adjustment with the composite CE map and the one of its corresponding final state (first column in Figure 5.14) reveals that the six major intensity maxima remain constant. As discussed in Section 5.4.1, the momentum distribution of the final state is more or less complementary to the momentum distribution of the excitonic state S_1^{exp}, yielding maxima along the $\overline{\Gamma\mathrm{M}}$-direction where the excitonic PAD has pronounced minima. The CE map of the S_1 exciton does not change substantially due to the removal of the incoherent final state contributions. Thus it serves as a validation of the approximation and the subtraction approach.
As illustrated in Figure 5.14 (h), the PAD of the S_2 exciton after final state adjustment in Figure 5.14 (h) shows six bright maxima near the $\overline{\mathrm{K}}$-points within the first BZ. From each maximum in the CE map in Figure 5.14 (h), two lines are observed to evolve outwards. A comparison with the CE map with purely final state contributions, F_2 (see Figure 5.14 (e)), reveals the ambiguity in attributing the origin of these features. Given the tendency of molecular states to exhibit broad momentum distributions due to the localization of electrons on the molecules, it is unexpected that such thin and detailed lines would serve as autonomous signatures of a molecular excitonic state.
For the S_3 exciton, following the adjustment of the final state, a blossom-like pattern is observed in the photoemission angular distribution, that scarcely exceeds the first BZ Of particular note is the intensity minimum at the $\overline{\Gamma}$-point, which persists under all scaling methods (see Appendix A.3), albeit with varying degrees of prominence. A star-shaped pattern is observable around the intensity minimum. To ascertain whether these features could potentially be attributed to an incomplete subtraction of the final state, a comparison was made between the composite CE map S_3^{exp} in Figure 5.14 (c) and the corresponding CE map with pure final state contributions F_3 in (f). This comparison reveals that the composite CE map exhibits six intensity maxima surrounding the $\overline{\Gamma}$-point, a feature not observed in the CE map of the pure final state. However, the question remains whether these maxima are independent or interconnected, as illustrated in Figure 5.14 (i). Additionally, a disc-like region of elevated intensity, approximately equivalent in size to the larger BZ, is observed in the composite CE map S_3^{exp}, yet it is absent in the CE map of the pure final state F_3. The question of whether this region of elevated intensity should have such a blossom-like shape as in the resulting CE map S_3 in Figure 5.14 (i) remains unresolved.

The S_1 and S_3 excitons are of Frenkel and charge transfer character, respectively. The case of the S_2 exciton is more ambivalent. In the existing literature, the S_2 has been assigned a charge transfer character [46, 89, 155]. A recent study using exciton photoemission orbital tomography (exPOT) has suggested a purely Frenkel-like character for the S_2 exciton. It should be noted, however, that the exPOT calculation simulated only the interaction between

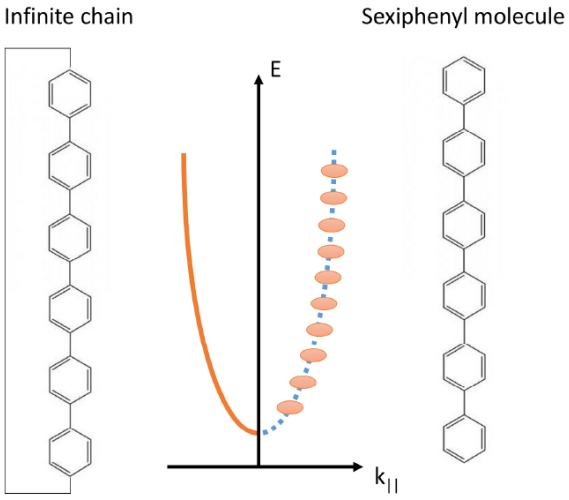

Figure (5.15) Schematic depiction of the intramolecular dispersion of the sexiphenyl molecule. If the molecule would be extended to an infinite chain, a smooth dispersive band would form (left side). Due to the finite size of sexiphenyl emission maxima follow the infinite band dispersion separated by band gaps between molecular orbitals (right side). With permission from Norman Haag [47].

C_{60}-dimers and thus did not include all possible intermolecular interactions. The momentum space signatures of the excitonic states shown in Figure 5.14 do not allow a reliable identification of the excitonic character. A possible relationship between the excitonic character and the momentum space signatures could be their line width. The hypothesis could be that a larger charge separation for charge transfer excitons results in a reduced linewidth in momentum space compared to Frenkel excitons. The PADs of the S_1 and S_2 excitons in Figure 5.14 (g) and (h) would be consistent with this hypothesis, but the observed PAD of the S_3 exciton in Figure 5.14 (i) contradicts it.

A comparison of the PADs of the different excitonic states reveals that they are all distinct from one another. Indeed, the intensity undergoes a redistribution from the border of the Brillouin zone towards the $\overline{\Gamma}$-point going from the energetically lowest to the highest exciton. This phenomenon may be indicative of intramolecular dispersion, a consequence of the delocalization of electrons within the molecule's limited size. A notable example of this phenomenon is sexiphenyl [15]. The location of maxima for a variety of molecular orbitals was found to be consistent with the shape of a dispersive parabola (as illustrated schematically on the left side of Figure 5.15). In the event that the molecule's length were infinite, the parabolic dispersive band would manifest as a smooth surface. However, due to its limited size, the parabolic dispersive band is segmented between different molecular orbitals (see right side of Figure 5.15). A similar effect was also observed for the localized sigma orbitals of C_{60} [23, 47]. It is hypothesized that a similar effect might be present in the excitonic levels of C_{60}.
It is conceivable that features of the incoherent contribution of the scattered final states persist in the respective CE maps due to an inadequate subtraction. For instance, potential sources of subtraction deficiencies may include small translations, rotations, shearing, or radial expansions between the CE images, resulting in the subtraction of non-coinciding features. In an effort to address this issue, an image registration algorithm analogous to the one utilized for the correction of the flat field has been employed (see the explanation of the data analysis methods in Appendix A.2). As the majority of momentum space features are broad, the algorithm is constrained to the correction of potential translations between images. This is necessary because the efficacy of the algorithm is diminished if corrections for rotation or shearing are permitted. The underlying reason for this limitation is multifaceted, including

the width of the momentum space features, the high symmetry of the CE maps, and the relatively high background intensity within the photoemission horizon. Consequently, adjustments were made to account for rotation, radial expansion, and any potential shearing, which were performed manually. As previously mentioned in the section above and further elaborated in Appendix A.3, the details of the individual CE maps strongly depend on the scaling of the intensities in the CE maps used for subtraction. As previously mentioned, the scaling of the intensities of the CE maps is necessary due to the different light sources used to observe the excited states and obtain the purely scattered final state momentum distributions.
In this section, estimates of the photoemission angular distributions of the excitonic states S_1-S_3 were obtained after subtraction of the incoherent part of the scattered final states. It was observed that all PADs are distinct and evolve from the main intensity at larger momenta to its relocation close to the $\overline{\Gamma}$-point when going from S_1 to S_3. This phenomenon is indicative of an intramolecular dispersive nature of the excitonic bands within a C_{60} multilayer. Furthermore, the complex emission patterns of the excitonic states may be indicative of dispersive excitonic states due to intermolecular interactions. As mentioned in the previous section, the emergence of these dispersive excitonic bands can be attributed to the dispersive behavior of the unoccupied molecular orbitals involved in the formation of the investigated excitons, particularly the LUMO and LUMO+1.
The shape and structure of the excitonic PADs in this section have demonstrated robustness against various data evaluation approaches (see Appendix A.3). However, given the residual ambiguities concerning specific details in the received PADs of the S_2 and S_3 excitonic states following the approximate removal of incoherent final state contributions, the subsequent section is devoted to verifying the findings presented herein.

5.4.3. Replication of the Excitonic Photoemission Angular Distributions

In the preceding section, an approximation of an incoherent superposition of excited and scattered final states was made, and a subsequent subtraction of the incoherent final state contributions was performed to obtain an estimate of the photoemission angular distributions of the S_1-S_3 excitons. However, the origins of certain signatures observed in the momentum maps derived from this approach remain ambiguous. The objective of this section is twofold: first, to resolve the ambiguities that remain, and second, to verify the structure and details of the PADs acquired in the previous section.
Details of the emission patterns in the excitonic CE maps, subsequent to subtraction of the incoherent scattered final state contributions, may originate from disparate sources. These details may either be part of the excitonic states' PADs or emerge from the coherent superposition of the excitonic state's plane wave component with the scattered final state. Another possibility is that features might be remnants of the incoherent scattered final state contributions due to insufficient subtraction. As enumerated in the preceding section, potential sources of subtraction deficiencies encompass small translations, rotations, shearing, or radial expansions between the CE images, resulting in a subtraction of non-coinciding features. Furthermore, the scaling of the the CE maps before subtraction influences the prominence of the different momentum space signatures. Consequently, a thorough examination of the resulting CE maps in Figure 5.14 (g-i) is imperative, particularly concerning their minor features.
The verification approach employed in this section is distinct from the subtraction method outlined in Section 5.4.2. Rather than extracting the excited states contributions from the measured CE maps, as was previously done, the measured CE maps S_i^{exp} will be replicated by adding the purely incoherent final state with simple estimates of the excitonic PADs. The replication approach will be illustrated with the S_2 exciton as an example. As in the previous section, the discussion will focus on the CE map of a specific time step within the

pump-probe scheme. Furthermore, the replication of the S_1 exciton will not be performed because in this case, excitonic and final state momentum space signatures can be easily distinguished due to the complementary nature of both.
Subsequent to the subtraction of the incoherent component of the scattered final state contributions in the CE map of the S_2 exciton, a salient question emerges: Can the outgoing lines in Figure 5.14 (h) be ascribed to the excited state, or are they remnants of an insufficient subtraction of the said scattered final state? Assuming the latter as a starting point, only the six intensity maxima are assigned to the excited state. The objective is then to identify a suitable, yet simple estimate of the shape of the intensity maxima in order to replicate the CE map.

Figure 5.16 (a) shows the intensity profile along the $k_y = 0$ direction through the right maximum of the S_2 exciton CE map. The cut direction of the intensity profile is indicated by a gray line in the inset. The intensity profile consists of two distinct components: a primary peak and a shoulder. The intensity maxima will be approximated in first order as two-dimensional Gaussian peaks, estimating each maximum to be rotational symmetric and neglecting the observed shoulder as well as its non-uniform distribution around the main peak of each maximum. The positions of the 2D Gaussian peak estimates were determined through a fit of the intensity profile in Figure 5.16 (a), utilizing the center positions of the main maxima and enforcing a $p3m1$ symmetry for the entire 2D emission pattern. The widths of these peaks were adjusted for different estimates (see Appendix A.3.2). The resulting estimate of the S_2 exciton PAD that produced the best results in the replication approach is displayed in Figure 5.16 (b).
It is possible to examine whether the created estimate resembles the main features of the CE map of the S_2 exciton after subtraction of the final state contributions. Figure 5.16 (c) provides a useful reference for this examination. In this figure, the estimate (blue) is superimposed on the aforementioned CE map (red). It is apparent that the estimate accurately reproduces the primary intensity maxima of the S_2 CE map. However, the intensity between the maxima is weaker. In addition, the peak width of the estimate is larger than in the experimental CE map.
In order to replicate the CE map of the S_2 exciton obtained in the pump-probe experiment (see Figure 5.14 (b)) a 2D fitting approach similar to the one applied for the cesiated PTCDA monolayers in Section 3.3 is performed.

$$f_{S_2^{exp}} = a_1 \cdot CE_{S_2,estimate} + a_2 \cdot CE_{F_2} + a_3 \cdot CE_{S_1^{exp}} + a_4 \tag{5.1}$$

Equation 5.1 specifies the incoherent weighted sum of the various components incorporated within the 2D fit function $f_{S_2^{exp}}$. In this equation, $CE_{S_2,estimate}$ refers to the estimate of the S_2 contributions, as illustrated in Figure 5.16 (b). CE_{F_2} is the CE map of the corresponding final state F_2 (see, for example, 5.14 (e)) measured with secondary electron emission. The term $CE_{S_1^{exp}}$ accounts for possible contributions of the S_1 as measured in the pump-probe experiment (see Figure 5.14 (a)), due to a possible energetic overlap of the S_1 and S_2 excitons. Finally, a constant background over the entire CE map is accounted for with a_4. The function $f_{S_2^{exp}}$ is fitted pixel-wise to the CE map of the S_2^{exp} exciton measured in the pump-probe experiment using the least-square method.
The result is shown in the right part of Figure 5.16 (d). In contrast to the preceding figures, the CE map at 0 ps delay is presented. The most successful replication was attained for this time step. The replicated CE map demonstrates a strong resemblance to the measured one. It is observed that the six Gaussian peaks coalesce with the structures of the final state, resulting in a circular feature as observed in the experimental CE map. The intensity of the outwards evolving lines originating from the final state PAD remains comparatively lower close to the photoemission horizon than in the measured CE map S_2^{exp}. The contribution

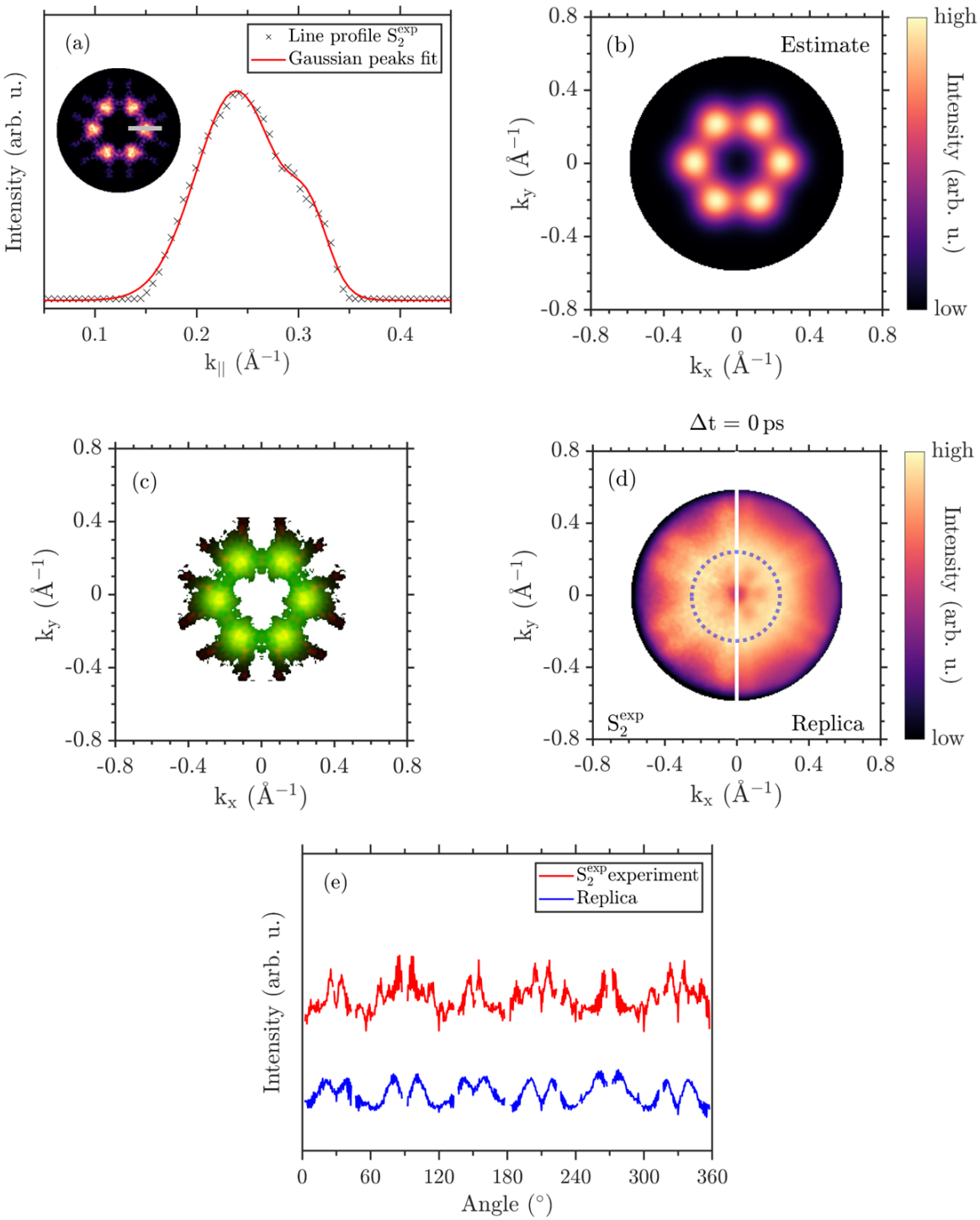

Figure (5.16) Replication of the S_2 exciton PAD. (a) Radial intensity profile of the obtained S_2 exciton PAD after subtraction of the incoherent final state contributions. The cut direction of the line profile is shown in the inset. The curve is fitted using two Gaussian functions. (b) Estimate of the S_2 exciton PAD using Gaussian peaks. (c) Overlay of the S_2 PAD (red) and its estimate (green). (d) S_2^{exp} CE map of the exciton including incoherent final state contributions (left) and its replica using Gaussian peak estimates (right). (e) Intensity profile of the S_2^{exp} exciton PAD (red) and its replica (blue) extracted along a circle as indicated in (d). The lines are shifted with respect to each other for better visibility.

of the S_1 exciton is found to be one order of magnitude lower than that of the final state F_2 and of the S_2 exciton. This observation suggests the possibility of overestimation of the contributions of the S_1 exciton, given its complementary nature to the S_2^{exp} CE map. This hypothesis is further substantiated by the observation of a comparatively low constant background, which is most likely diminished in the event of an overestimation of the S_1 exciton contribution.
To check whether the estimate of the S_2 exciton and the final state CE map F_2 merge sufficiently in the replication approach, the intensity along the blue circle in Figure 5.16 (d) is extracted for the S_2^{exp} CE map and its replica. The resulting intensity profiles are displayed in Figure 5.16 (e) and show a striking similarity. Both intensity profiles oscillate with the same frequency and phase. Two spikes occur in each oscillation cycle, corresponding to the position of the outgoing lines. These spikes are also reproduced in the replica and demonstrate that estimate of the S_2 exciton and the final state CE map F_2 can merge to a circular feature that precludes further discernment. Estimates of the S_2 exciton with smaller width of the Gaussian peaks do not from such a homogeneous circular feature and also do not reproduce the spikes observed in the intensity profile. An example is shown in Appendix A.3.2.
The excellent agreement between replica and experimental CE map demonstrates that the replication of the S_2^{exp} exciton CE map, incorporating final state contributions, is feasible with a rudimentary estimate of the S_2 exciton comprising six Gaussian peaks. This suggests that the PAD of the S_2 exciton is predominantly composed of six maxima, as illustrated in 5.14 (h). The intensity between the six maxima is a remnant due to a limited subtraction of the scattered final state. This assertion is further substantiated by the striking similarity observed in the intensity profiles depicted in Figure 5.16 (e). However, it is postulated that components of the radially outward-pointing lines may originate from the coherent superposition of scattered final state and excited state PADs. While their contribution along the circular cut used for the intensity profiles could be reproduced well, their relative intensities at larger momenta were always too weak in the replica.
It should be noted that only a limited number of different peak widths for the estimates were tested, but no quantitative analysis in terms of a fitting routine was performed. This approach of replicating the pump-probe experiment's measured CE map S_2^{exp} assumes an incoherent superposition of plane wave component and scattered final state, which appears to be only appropriate for qualitative investigations.

The identical approach is implemented for the CE map of the S_3 exciton. The objective is to verify the blossom-like shape of the excitonic PAD extracted in the preceding section (see Figure 5.14 (i)). Its complex structure is approximated using a flat disc. In the event that the replication of the S_3^{exp} CE map is successful with this disc, it can be concluded that the detailed structure in the S_3 CE map in Figure 5.14 (i) still belongs to the incoherent part of the F_3 final state.

Figure 5.17 (a) illustrates a cut through the excitonic CE map of Figure 5.14 (i) along the $k_x = 0$ direction to ascertain an appropriate size for the disc. The direction of the cut is visualized in the inset. The resulting intensity profile is fitted using a one-dimensional higher order Gaussian function, as outlined in Equation 5.2.

$$f(k_{||}) = a \cdot exp(-(\frac{k_{||}}{w})^6) + b \tag{5.2}$$

After determining the fit parameters, substituting $k_{||}$ with $\sqrt{k_x^2 + k_y^2}$ yields the function specifying the disc-like estimate of the S_3 exciton CE map. The resulting estimate is depicted in Figure 5.17 (b). Figure 5.17 (c) presents an overlay image of the aforementioned disc-like

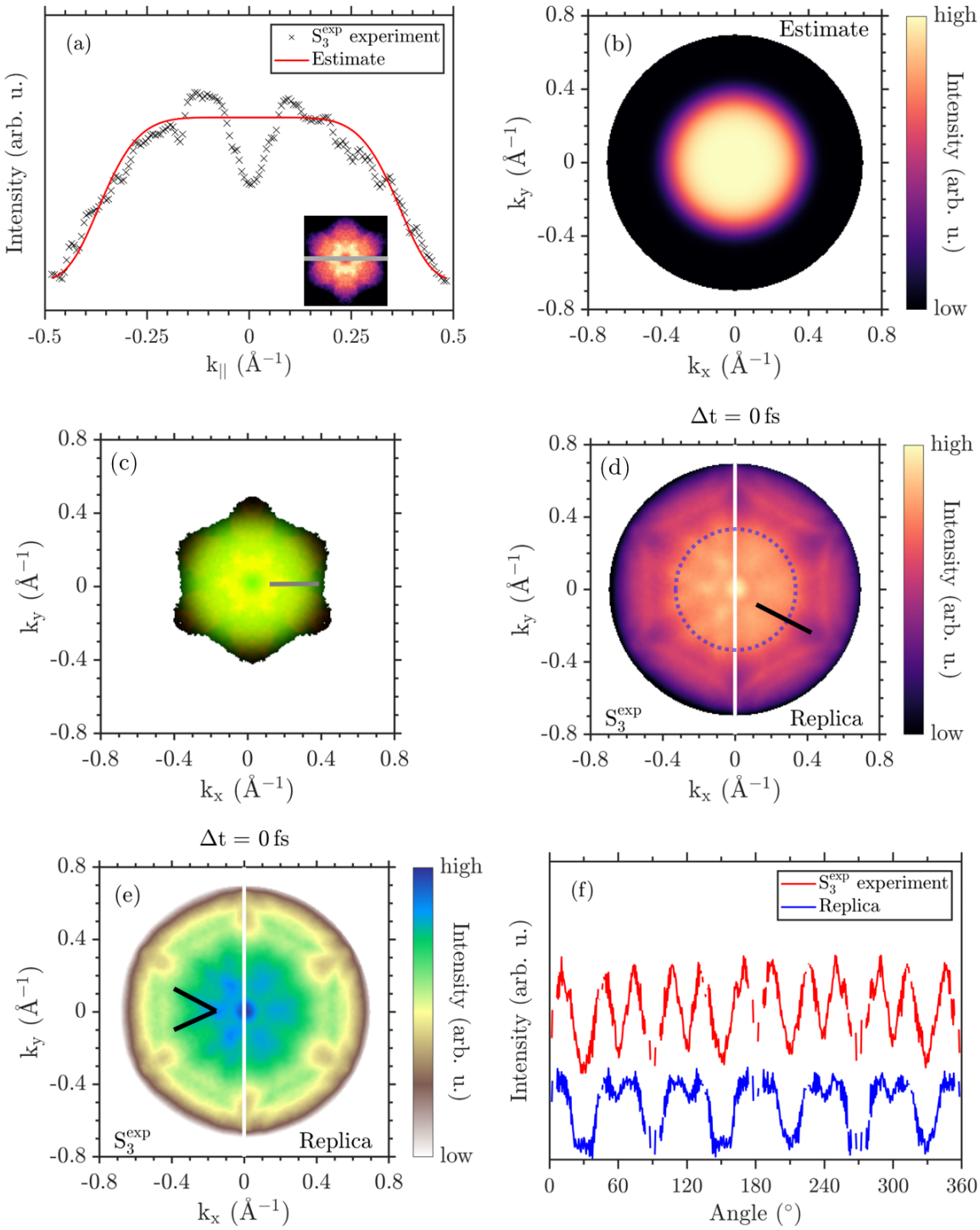

Figure (5.17) Replication of the S_3 exciton PAD. (a) Intensity profile of the obtained S_3 exciton PAD at $k_x = 0$ after subtraction of the incoherent final state contributions. (b) Estimate of the S_3 exciton PAD using a disc-like intensity distribution. (c) Overlay of the S_3 PAD (red) and its replication (green). (d) S_3^{exp} CE map of the exciton including incoherent final state contributions (left) and its replica using a disc-like intensity estimate (right). (e) Same as in (d), but with different color map and contrast. (f) Intensity profile of the S_3^{exp} exciton PAD (red) and its replica (blue) extracted along a circle as indicated in (d). The lines are shifted with respect to each other for better visibility.

estimate in blue and the S_3 PAD after scattered final state subtraction in red. It is apparent that the width of the estimate and the S_3 PAD demonstrate good agreement.

The replication is executed in a manner analogous to that of the S_2 exciton, employing a pixel-wise fit that utilizes the least-square method in accordance with the fit function delineated in Equation 5.3.

$$f_{S_3^{exp}} = a_1 \cdot \mathrm{CE}_{S_3,\mathrm{estimate}} + a_2 \cdot \mathrm{CE}_{F_3} + a_3 \tag{5.3}$$

$\mathrm{CE}_{S_3,\mathrm{estimate}}$ is the CE map of the disc-like estimate, as depicted in Figure 5.17 (b) and CE_{F_3} is the CE map of the corresponding scattered final state obtained by secondary electron emission, as illustrated in Figure 5.14 (f). The function $f_{S_3^{exp}}$ is fitted to the S_3^{exp} CE maps of the S_3 exciton, as determined in the pump-probe experiment, encompassing all contributions from the final state (see Figure 5.14 (c)). The resulting replication is shown in the right part of Figure 5.17 (d). The left part of the figure illustrates the S_3^{exp} CE map for reference. The correspondence between the measured CE map and the replica is highly significant. The reproduction of all features was successful. A salient difference is evident in the S_3^{exp} CE map, where features attributed to the final state are more blurry. The discrepancy can be attributed to the disparity in statistics between the pump-probe experiment and secondary electron emission. In addition, certain features within the blue dotted circle exhibit a higher relative intensity in the experimental CE map compared to the replica.
In order to facilitate a more precise comparison of relative intensity, Figure 5.17 (e) presents the same images as Figure 5.17 (d), but with a different color map and adjusted contrast. The circular intensity distribution, which is represented by the color green, possesses an identical radius in both the experimental S_3^{exp} CE map and the replica. This indicates that the spatial extent of the disc-like S_3 estimate is in good agreement with the experiment. Therefore, it can be concluded that the blossom-like intensity in the S_3 CE map does not belong to the incoherent part of the scattered final state. Rather, it is suggested that this intensity is part of the excitonic signatures. In addition, the alignment of this intensity distribution validates the normalization methods employed to derive the S_3 CE map depicted in Figure 5.14 (i). For a more exhaustive examination of this topic, please refer to the Appendix A.3.2.
A difference between the experimental CE map and the replica lies in the intensity of the V-shaped features colored in blue in Figure 5.17 (e). For better visibility, the edges of one feature are exemplary outlined with black lines. It is apparent that the features are more defined in the experimental CE map with increased relative intensity at the tips.

These V-shaped features and the overall blossom-like shape of the S_3 exciton PAD shall be elucidated in more detail. Therefore, intensity profiles are extracted along the indicated circle in Figure 5.17 (d) and plotted in Figure 5.17 (f). A comparison of the intensity profiles reveals that they exhibit the same periodicity; however, the intensity minima in the experimental S_3^{exp} CE map are equally pronounced, while for the profile of the replica only every second minimum is as distinctive. The distinct minima in the intensity profile of the replica correspond to the stripe-like minima that are observed along the $\overline{\Gamma\mathrm{M}}$-direction highlighted by a black line in Figure 5.17 (d). These minima originate from the F_3 final state. The other minima in the line profiles are not as pronounced in the replica as in the experiment. Therefore, this pronunciation in the experiment is not due to the incoherent contribution of the scattered final state. The minima in the line profile that are not sufficiently reproduced in the replication are located along the directions where the blossom-like signatures of the S_3 exciton have an indentation in radius (indicated by a gray line in Figure 5.17 (c)). The drop in intensity near these indentations is captured by the extracted line profile. Thus, it is possible that the blossom-like shape of the S_3 exciton extracted in the previous section is the shape of the excitonic PAD. It is not an artefact of the subtraction approach, despite the

overall well-fitting replication using a disk-shaped estimate of S_3 CE map. If the blossom-like pattern is a remnant of insufficient subtraction, the intensity profile of the replica is expected to show the same pronounced minima as in the experiment. However, it could also result from the coherent superposition of the plane wave final state and the scattered final state. The same reasoning applies to the different relative intensities of the V-shaped features.
In this section, the PADs excluding the incoherent scattered final state contributions of the S_2 and S_3 excitons, which were presented in the previous section, were verified by means of a replication approach. This approach employed simple geometric structures as estimates of the excitonic contributions. It was determined that the S_2 PAD is predominantly composed of six maxima. Other structures in the resulting CE maps after scattered final state subtraction were assigned to remnants of the incoherent scattered final state contribution due to insufficient subtraction. The S_3 PAD can be adequately approximated by a disc. However, not all details could be reproduced, suggesting a more blossom-like structure of the PAD of the S_3 exciton. Differences in relative intensities were attributed to effects of coherent superposition of excited and scattered final states for both excitons. This analysis reinforced the results of the subtraction approach in the previous section. To investigate the influence of the coherent superposition of the plane wave and scattered final states, the purely excitonic PAD has to be accessed experimentally. Therefore, it is necessary to modify the photon energy of the probing laser pulse in such a way that the electrons reach a pure plane wave final state, as described above.

5.5. Exciton Photoemission Orbital Tomography

Having ascertained and corroborated a suitable estimation of the PADs of the excitonic states, it is aimed to interpret the results and derive conclusions. For this purpose, the recently developed extension of photoemission orbital tomography to excitonic states is employed, which is referred to as exciton photoemission orbital tomography (exPOT). Prior to the presentation of simulated CE maps corresponding to the measurement settings, a concise introduction to the formalism of exPOT, its findings, and its implications will be provided. Subsequently, the primary steps undertaken in the application of exPOT to the C_{60} multilayer systems, as conducted by Bennecke et al. [67], will be deliberated. Finally, a comparison will be made between our experimental results and simulated CE maps of the excitonic states. This will serve to establish a connection with the results previously obtained by Bennecke et al.

5.5.1. Introduction to Exciton Photoemission Orbital Tomography

Photoemission orbital tomography is an exemplary technique for interpreting photoemission angular distributions obtained in an ARPES experiment for occupied molecular orbitals. It is apparent that the theoretical framework, as delineated in Section 2.3, rapidly reaches its limitations when attempting to describe the PADs of excited electronic states in molecular systems. In the context of the POT formalism, the conventional approach of employing the single-particle wave function of the unoccupied molecular orbital to which the electron is excited as the initial state has been demonstrated to yield correct results only in certain specific cases [34]. The particular complexity of excitons, particularly their entanglement, is not adequately addressed by the POT formalism.
The extension of the framework of POT to the excitonic regime is referred to as exciton photoemission orbital tomography (exPOT). The following exposition shall elucidate the fundamental principles and ramifications of exPOT, as they have been delineated in the seminal work of Kern et al. [34]. In addition, a delimitation of exPOT and time dependent density functional theory (TDDFT) calculations will be furnished. For a thorough exposition

of the derivation, please refer to the relevant literature [34]. Expressing the photoemission matrix element in a many-body formulation enables the connection of excitonic wave functions to their corresponding measured constant energy maps, allowing for their interpretation as the Fourier-transform of the coherent sum of the electronic part of the exciton wave function. This facilitates their interpretation as the Fourier transform of the coherent sum of the electronic part of the exciton wave function. As a surprising revelation, the state of the remaining photohole has been demonstrated to only exert an influence on the kinetic energy spectrum of the photoelectrons [34].
The photoemission process is once more describe by Fermi's golden rule in the dipole approximation.

$$\omega \propto \frac{2\pi}{\hbar} |\langle \Psi_f | \mathbf{Ap} | \Psi_i \rangle|^2 \delta(E_f - E_i - h\nu) \tag{5.4}$$

In this case, the initial state of the photoemission process is the exciton wave function. It can be expressed terms of the product basis of single-particle electron $\chi_c(\mathbf{r_e})$ and hole functions $\phi_v(\mathbf{r_h})$. The wave function of the m-th exciton with an excitation energy of Ω_m is subsequently derived as the sum over all valence and conduction states v, c, as outlined in Equation 5.5.

$$\psi_m(\mathbf{r_h}, \mathbf{r_e}) = \sum_{v,c} X_{vc}^{(m)} \phi_v^*(\mathbf{r_h}) \chi_c(\mathbf{r_e}) \tag{5.5}$$

The coefficients of the transition density matrix $X_{vc}^{(m)}$ define the contributions of electron and hole states to the exciton wave function. It has been demonstrated that this particular representation of the exciton wave function satisfies the Bethe-Salpeter equation [67].
As indicated by Fermi's golden rule, this expression for the excitonic wave function is employed as an initial state for the photoemission process. Assuming the sudden approximation, the plane wave final state approximation inherent to POT and switching to Dyson orbitals in the treatment of the electron system, the statement for the photoemission intensity in Equation 5.6 can be found. This equation resembles the standard equation of POT (refer to Equation 2.17 as a reference) connecting the photoemission intensity with Fourier-transformed electronic wave functions.

$$I_m(\mathbf{k}) \propto |\mathbf{Ak}|^2 \sum_j |\sum_c X_{jc}^{(m)} \mathrm{FT}[\chi_c](\mathbf{k})|^2 \times \delta(h\nu - E_{\mathrm{kin}} - \epsilon_j + \Omega_m) \tag{5.6}$$

In this context, $\mathrm{FT}[\chi_c]$ denotes the Fourier transform of the unoccupied molecular orbital χ_c, ϵ_j signifies the ionization potential of the j-th excited state, and $|\mathbf{Ak}|^2$ represents the polarization factor that modulates the photoemission intensity.
It is evident from Equation 5.6 that the hole does not contribute to the photoemission angular distribution; rather, it only influences its energetic position via the ionization potential ϵ_j in the energy conservation. It is important to note that if multiple states of the hole are possible in the formation of the exciton, the same excitonic state may manifest at different positions in the photoelectron spectrum.

A thorough examination of the predictions of Equation 5.6 is warranted, and it can be conducted by assessing all possible generic cases of the excitonic structure in Figure 5.18 within the simplest system of two valence and two conduction states. The upper portion of the figure illustrates the involved electronic transitions, while the lower portion depicts the exPOT predictions on the corresponding PADs in the black boxes and the photoelectron spectrum. In case (i), it is demonstrated that a single transition from the highest occupied to the lowest unoccupied molecular orbital and the corresponding wave functions are involved the exciton formation. The excitonic PAD is subsequently determined by the Fourier transform of the unoccupied orbital χ_1, which occurs at a specific position within the photoelectron spectrum

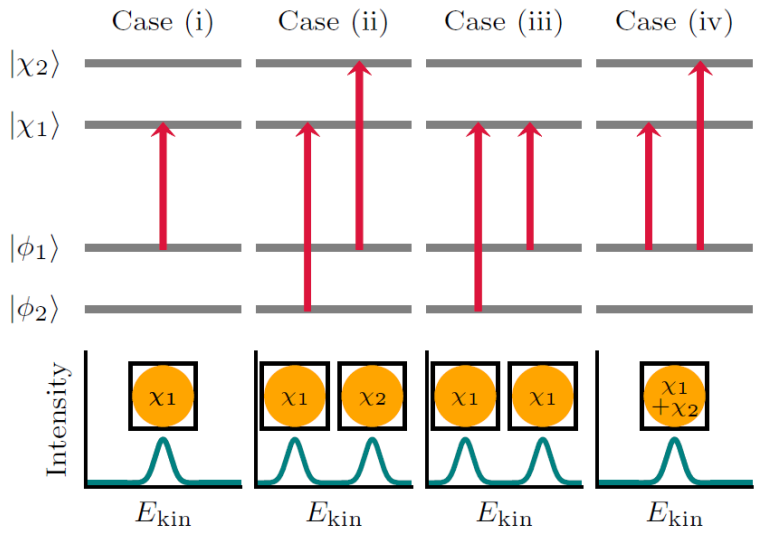

Figure (5.18) exPOT predictions of a generic exciton structure involving two electron and two hole states. For the four cases the involved electron transitions (top) as well as the implications on the PADs and photoelectron spectrum (bottom) are given.

($E_{\mathrm{kin}} = h\nu - \epsilon_1 + \Omega_1$). This phenomenon has been observed in a multitude of organic systems, representing the lowest excitonic excitation [64].
Case (ii) involves two transitions in the formation of the exciton: $|\phi_2\rangle \rightarrow |\chi_1\rangle$ and $|\phi_1\rangle \rightarrow |\chi_2\rangle$. Given the possibility of two different states of the photohole, the signatures of the exciton appear at two different kinetic energies. The observable PADs at these two energies are also different. The PAD at lower kinetic energies represents the momentum map of the χ_1 orbital, while the PAD at higher energies shows the Fourier transform of the χ_2 orbital. This exciton case is a simple illustration of a genuinely entangled state.
Case (iii) also involves two transitions, but is dissimilar to case (ii). Both transitions start at different occupied orbitals. However, it is notable that both transitions ultimately terminate at the lowest unoccupied orbital, designated as χ_1. In regard to case (ii) the excitonic signatures manifest at two distinct kinetic energies. However, both PADs depict the Fourier transform of the χ_1 orbital independent of the state of the photohole.
In the final prototypical case (iv), both excitonic transitions involve the highest occupied orbital, ϕ_1. As there is only one possible state of the photohole, the exciton contributes to a single energetic position within the photoelectron spectrum. According to Equation 5.6, the corresponding PAD consists of the coherent sum of the Fourier-transformed orbitals χ_1 and χ_2.
Notwithstanding their generic nature, each case has a corresponding example in real molecular systems [34]. As will be demonstrated in the next section, within the multilayer C_{60} system, the cases (i) and (iv) can be identified, as well as a combination of these two.
In summary, exciton photoemission orbital tomography is a thorough framework for understanding photoemission angular distributions of excitonic states. Accordingly, the state of the photohole only determines the energetic positions of the excitonic contributions to the photoemission intensity. In comparison to an accurate photoemission simulation using TDDFT, exPOT is computationally more efficient. Furthermore, exPOT allows for the incorporation of any functional describing excited states, which is a capability lacking in TDDFT. The restriction of exPOT to the plane wave final state approximation has been effectively implemented in numerous systems (see Section 2.3). In addition, recent advancements have been made to address these limitations and explore potential extensions to POT that facilitate the incorporation of final state effects [66].

In the following section, the initial implementation of the exPOT framework within the C_{60} multilayer system by Bennecke et al. will be examined and compared to our findings.

5.5.2. Exciton Photoemission Orbital Tomography of a C_{60} Multilayer

The framework of exciton photoemission orbital tomography has been previously implemented in the analysis of a C_{60} multilayer film by Bennecke et al. [67]. The initial investigation focused on the first four excitonic bands, designated as S_1-S_4. The excitation of the S_1-S_3 excitonic states occurred with a pump photon energy that was nearly equivalent to the one in the pump-probe experiment described in Section 5.4. The S_4 exciton was resonantly excited with a photon energy of 3.6 eV. The system was probed with extreme ultraviolet light ($h\nu = 26.5\,\text{eV}$). It should be noted that, given the large photon energy of the probe pulses, no contributions from the final state were required to be considered. Constant energy maps of the excitonic states were acquired for comparison with ab-initio calculations. In the following Section 5.5.2, an overview of the findings reported by Bennecke et al. [67] will be provided. It is especially important to emphasize the theoretical calculations involved, since the same approach with an altered probe photon energy will be applied to the excitonic PADs obtained in this work in Section 5.5.2.

ExPOT of a C_{60} Multilayer Using Extreme Ultraviolet Photon Energies

Figure 5.19 (a) shows the unit cell of the C_{60} superstructure, taking into account the varying orientations of neighboring molecules. The utilization of ab-initio calculations for the description of the entire unit cell is computationally demanding. Therefore, the unit cell was subdivided into C_{60} dimers, which were then embedded in a crystalline C_{60} environment. This configuration will be referred to as the "dimer model" in the following discussion. For symmetry reasons it is sufficient to consider only two dimers: the dimer 1-2 and 3-4, according to the labeling in Figure 5.19 (a). Other possible dimer combinations can be acquired by suitable rotation of the aforementioned ones.

A hybrid-functional DFT calculation is performed. The resulting single-particle energies are corrected self-consistently by the GW approximation, resulting in the energies enumerated in the energy level diagram depicted in Figure 5.19 (b). The line thickness equates to the amount of involved electronic states. The four bands under consideration are labeled according to the corresponding orbitals of the gas phase C_{60} molecule (see Section 4.1). The solution of the Bethe-Salpeter-Equation, derived from the GW single-particle energies, yields the exciton energies, Ω_m, as depicted in the absorption spectrum in the bottom panel of Figure 5.19 (c). The excitation coefficients, $X_{\nu c}^{(m)}$, are also derived from this solution. The absolute square of the latter indicates the extent to which each electron-hole transition, $\Phi_\nu \chi_c$, contributes to a specific exciton Ψ_m. This is represented by the black bars in Figure 5.19 (c). It is noteworthy that excitons can comprise multiple electron-hole transitions. The S_3 exciton is an example of this phenomenon, consisting of a HOMO $\rightarrow$ LUMO transition and, to a lesser extent, a HOMO $\rightarrow$ LUMO+1 transition (see blue and purple panels in Figure 5.19 (c)). It is also important to note that the HOMO $\rightarrow$ LUMO transition (abbreviated H $\rightarrow$ L) is the primary transition part of all three excitons, S_1-S_3.
As illustrated in Figure 5.19 (d), the anticipated composition of the excitonic wave function and the CE maps is represented schematically for the four excitonic bands, S_1-S_4. It is important to note that the energetically highest exciton S_4 cannot be addressed using a pump photon energy of 2.95 eV. The two key aspects of any state observed in photoemission are its energetic position in the photoelectron spectrum as well as its photoemission angular distribution. As outlined in the preceding section, the energetic position of excitonic states is defined by the energetic position of the hole. Conversely, the emission pattern is determined

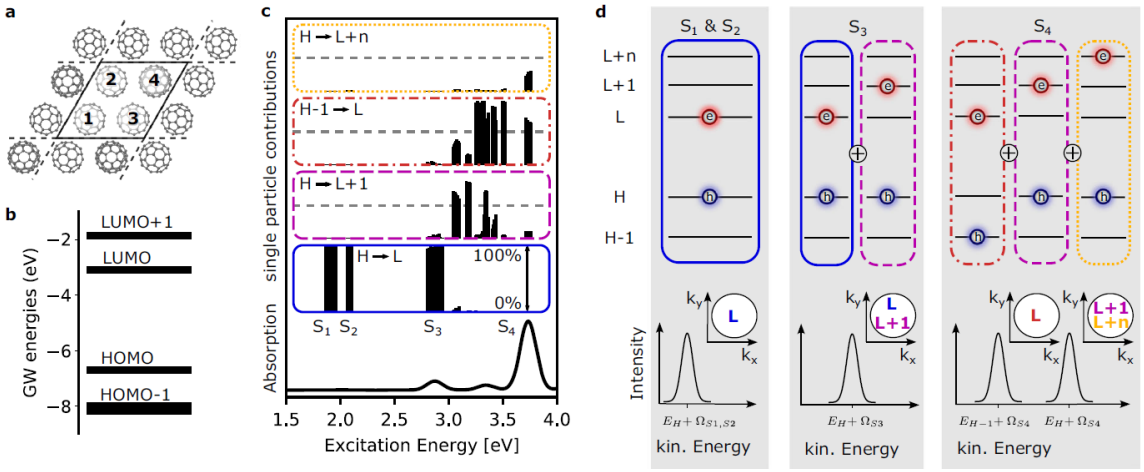

Figure (5.19) (a) Superstructure unit cell of the top most layer of a C_{60} multilayer film. Out of the four molecules with different orientation, dimers were formed for the ab-initio calculations. (b) Energy diagram of the two frontier occupied and unoccupied orbitals involved in the exciton formation in the dimer model. The line thickness represents the amount of involved single particle orbitals. (c) Absorption spectrum (bottom) as a function of exciton energy and electron-hole pair contributions to the different exciton wave functions arranged by the orbital transitions involved. HOMO and LUMO are abbreviated as H and L respectively. (d) Visualization of the orbital contributions to the exciton wave functions S_1-S_4 (top). The shown molecular levels represent single particle states. Schematic drawing of the expected PAD patterns and their energetic locations (bottom). The figure is taken from [67] under the CC BY 4.0 license (`https://creativecommons.org/licenses/by/4.0/`), copyright © by 2024 Springer Nature Limited.

by a coherent superposition of all contributing orbitals to which the electron is excited. In the case of the excitons relevant to this work, S_1-S_3, the first two consist exclusively of HOMO → LUMO transitions resulting in a PAD determined by the LUMO orbital. In contrast, the S_3 exciton encompasses HOMO → LUMO+1 transitions, thereby manifesting a PAD that originates from the coherent sum of the Fourier-transformed LUMO and LUMO+1. It has been demonstrated that the three excitons under consideration contain transitions in which the hole ultimately resides in the HOMO. Consequently, the corresponding PADs occur at a single kinetic energy.

The case of the S_4 exciton, however, is different. It is anticipated to manifest at two distinct kinetic energies within the photoemission signal, exhibiting different PADs. One PAD displays the emission pattern that is characteristic of the LUMO orbital, while the other displays a superposition of the LUMO+1 and several higher unoccupied orbitals, denoted as LUMO+n.

Bennecke et al. were able to extract constant energy maps for the S_1-S_3 excitons, and subsequently compared these maps with theoretical exPOT calculations within the framework of the dimer model. They found a good agreement between the experimental and theoretical CE maps. Furthermore, the degree of charge separation of the investigated excitons could be ascertained, thereby indicating a Frenkel-like behavior for the S_1 and S_2 excitons and a charge transfer character for the S_3 exciton. Differences observed in the CE maps of the S_3 exciton can be attributed to the limitations inherent in the dimer approach. It is evident that, given its status as the smallest entity capable of modeling charge transfer processes, the dimer is inadequate for the description of dispersion effects. It is also posited that the assignment of Frenkel character to the S_2 exciton may be indicative of limitations inherent to the dimer model, as other studies suggest a charge transfer character [46, 155].

Following this outline of the initial application of exPOT to the multilayer C_{60} sample system, as previously documented, the subsequent section will address our findings employing

a comparable approach with a reduced probe photon energy.

ExPOT of a C_{60} Multilayer Using Ultraviolet Photon Energies

An exPOT analysis will be carried out on our C_{60} multilayer data with 6 eV probe photon energy, as discussed in the preceding section and outlined in [67]. The ab-initio calculations were carried out by Andreas Windischbacher in the research group led by Peter Puschnig at the University of Graz.

Figure 5.20 shows a comparison between the experimental CE maps after subtraction of the incoherent scattered final state contributions (a-c) and the theoretical equivalents obtained in the exPOT formalism (d-i). The CE maps (d-f) were calculated in analogy to the description in Bennecke et al. [67], employing a dimer model. The sole discrepancy lies in the probe photon energy, which was adjusted to 6 eV. All calculation results, including the exciton energies, the contribution of orbital transitions to the exciton wave functions, and their spatial spread remain the same as depicted in Figure 5.19 and discussed in [67].
In order to better account for dispersion effects, the dimer model was advanced to a trimer model. Accordingly, the interactions between molecules 2-3-4 (see Figure 5.19 (a) or Figure 5.21 (a) for labeling) embedded in a suitable environment were calculated. It should be noted that the presented trimer calculation does not encompass the entirety of the unit cell. This limitation is attributable to computational constraints, which necessitated the calculation of a single trimer (comprising molecules 2, 3, and 4). In order to calculate the entire unit cell, it would be necessary to employ a calculation for an additional trimer (comprising molecules 1, 2, and 3) which has not been done. The arithmetic mean of the two trimer calculations would then provide a description of the entire BZ. Instead, the missing trimer 1-2-3 was approximated by an adequate mirroring of the calculated trimer, with molecule 4 projected onto the position of molecule 1. The simulated unit cell of the trimer model thus contains the molecules 4-2-3-4 with an additional molecule 4 instead of molecule 1. It is depicted in Figure 5.21 (a).
As demonstrated in Figure 5.21 (b), the resulting changes on the contributing orbital transitions to the excitonic states and the altered adsorption spectrum from the trimer calculation can be observed. The incorporation of an additional molecule increases the amount of contributing electron transitions to the excitonic states as well as the total amount of possible excitons. As the contributions to the S_1 and S_2 exciton remain mostly unchanged, the amount of HOMO $\rightarrow$ LUMO+1 transitions that contribute to the S_3 exciton is increased. Moreover, the S_3 exciton exhibits enhanced energetic broadening, attributable to an increase in HOMO $\rightarrow$ LUMO transitions. The observation of a considerable change in the number of transitions contributing to the S_3 exciton is an indication that its charge transfer character is better described in the trimer model compared to the dimer model. In addition, the unaltered contributions to the S_2 exciton suggest a Frenkel character. As in the case of the dimer model, the assignment of a Frenkel character to the S_2 exciton may be due to an incomplete description of the intermolecular interactions. To include all possible intermolecular interactions in the unit cell would require the calculation of a tetramer, which is computationally demanding.

A comparison of the CE maps in Figure 5.20 of both the dimer and trimer model with the experimental CE maps after subtraction of the incoherent, scattered final state contributions, reveals significant discrepancies. Only for the S_1 exciton theory and experiment exhibit a notable degree of concurrence, as depicted in the left column of Figure 5.20. Both the dimer and the trimer models replicate the six intensity maxima observed in the experimental CE map (Figure 5.20 (a)). A discernible observation is the enhancement in reduction of linewidth and narrowing of features during the transition from the dimer model to the

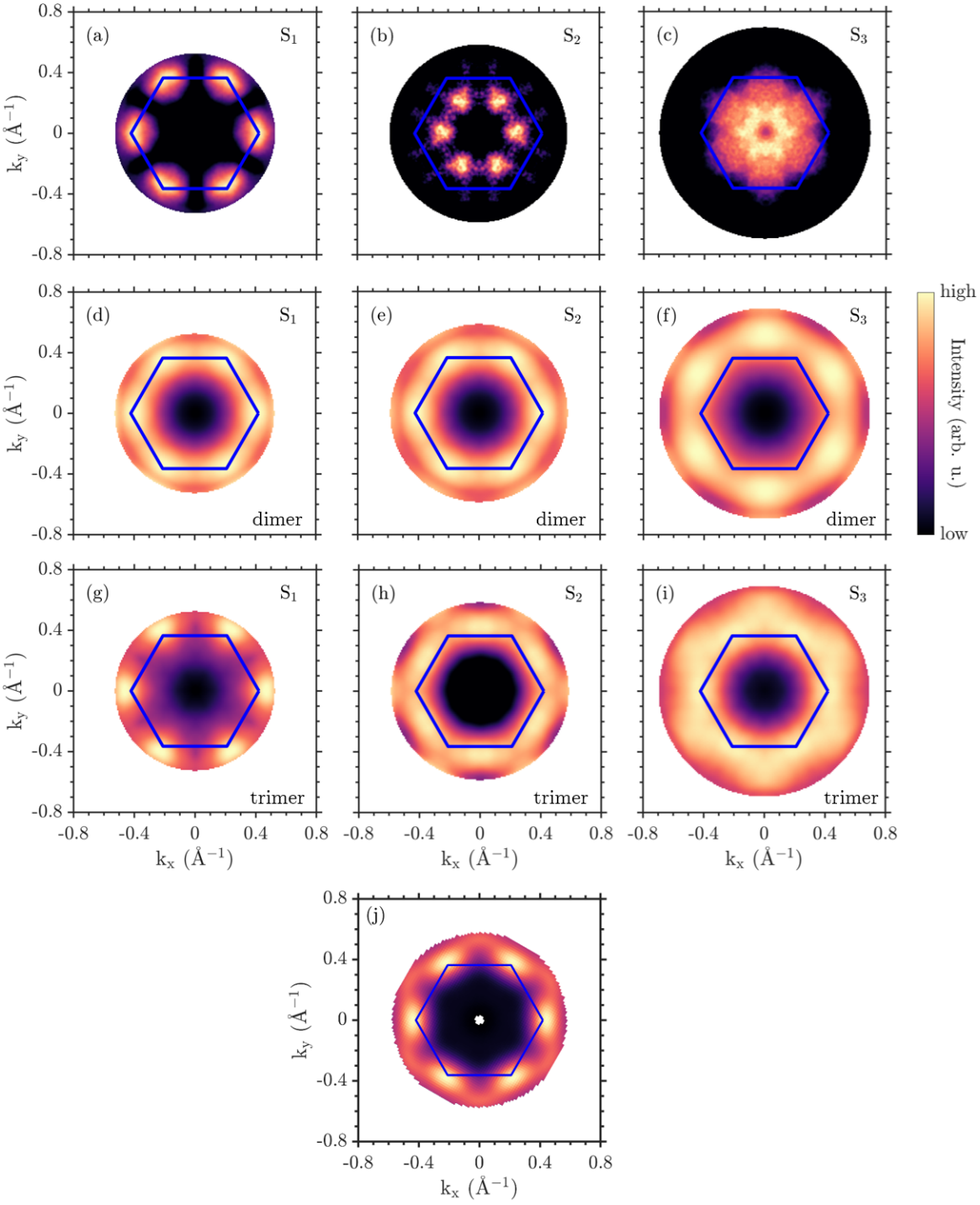

Figure (5.20) Constant energy maps of the S_1-S_3 excitons using exPOT: (a-c) Measured CE maps after subtraction of the incoherent part of the scattered final states. (d-f) CE maps from exPOT calculations using a dimer model to describe the C_{60} interactions. (g-i) CE maps from exPOT calculations using a trimer model to describe the C_{60} interactions. (j) CE map the LUMO of a non-interacting C_{60} multilayer film. The CE map was generated using the software kMap.py [162] and the molecular orbital data base of P. Puschnig, University of Graz [152]. The BZ of the single-molecule unit cell is indicated in dark blue.

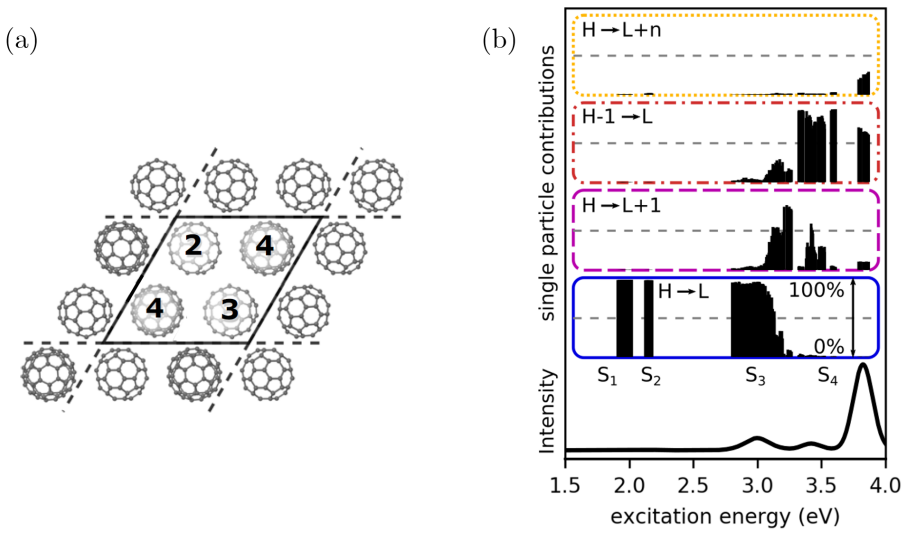

Figure (5.21) (a) Superstructure unit cell of the top most layer of a C_{60} multilayer film. Out of the four molecules with different orientation, a trimer comprising of the molecules 1-2-3 was formed for the ab-initio calculations. (b) Absorption spectrum (bottom) and electron-hole pair contributions to the different exciton wave functions for the C_{60} trimer. The different contributions are arranged by the involved molecular orbitals. HOMO and LUMO are abbreviated as H and L respectively. Subfigure (a) is modified from [67] under the CC BY 4.0 license (`https://creativecommons.org/licenses/by/4.0/`), copyright © by 2024 Springer Nature Limited. Subfigure (b) was created by Andreas Windischbacher, University of Graz.

trimer model. One potential explanation for this phenomenon is that the incorporation of an additional C_{60} molecule contributes to the transition to a fully periodic structure. As demonstrated in Section 5.3, the frontier occupied orbitals exhibit a pronounced dispersion. This phenomenon was also reported for the unoccupied orbitals [175]. The inclusion of an additional C_{60} molecule in the exPOT calculations enables the integration of more delocalized orbital wave functions within the excitonic description. Consequently, this results in the manifestation of more narrow emission maxima in momentum space, a consequence of the Fourier transformation. However, an alternative explanation could also be that the maxima for the S_1 exciton in the trimer calculations are more narrow due to the absence of contributions from the trimer 1-2-3, which is necessary to describe the entire unit cell. It is possible that the summation of the CE maps for both trimers could yield a result that resembles the dimer CE map in Figure 5.20 (d).
As illustrated in the middle column of Figure 5.20, the calculated CE maps for the S_2 exciton exhibit partial deviation from the experimentally obtained ones. As discussed in the preceding sections, the predominant momentum space signatures associated with the S_2 exciton are manifested as the six intensity maxima depicted in Figure 5.20 (b). While the exPOT calculations in the dimer model also yield six intensity maxima for the S_2 exciton, these maxima are considerably broader and located at larger momentum values than those observed in the experiment. As illustrated in Figure 5.19 (c), it is evident that both the S_2 exciton and the S_1 exciton are predominantly comprised of HOMO $\rightarrow$ LUMO transitions. For comparison, Figure 5.20 (j) shows the PAD of the LUMO of a non-interacting C_{60} multilayer. To obtain the CE map, POT calculations of free C_{60} molecules for all molecular orientations in the unit cell were performed and the resulting CE maps were summed. The CE map of the LUMO also consists of six main intensity maxima located at the $\overline{\text{K}}$-point. The similarity between the CE map of the LUMO and the CE maps of the S_1 and S_2 excitons shows that the electronic wave function of the LUMO is the crucial property of the excitonic emission patterns.

The emission pattern of the S_2 exciton in the trimer model depicted in Figure 5.20 (h) is an exception. It also consists of six intensity maxima, however they are now located along the $\overline{\Gamma}\overline{\mathrm{M}}$-directions. The rotation of the maxima is surprising as due to little changes in the electronic transitions contributing to the S_2 exciton when going from the dimer to the trimer model, similar CE maps are expected. A 30° rotation of the intensity maxima, however is quite a substantial difference. Unfortunately, no statement regarding the origin of this rotation can be made at this time. The missing contributions from the second trimer appear improbable as the origin of the rotated maxima. The CE maps of both trimers will possess an equivalent intensity level. Consequently, an averaging process would not result in a complete redistribution of the maxima toward the $\overline{\mathrm{K}}$-points. One potential origin of this phenomenon could be the diminished number of electron wave functions in the molecular orbital description of the trimer model in comparison to the dimer model. This reduction of wave functions is a limitation of the trimer model necessitated by the increased number of interacting electrons resulting from the third molecule. It is therefore a trade-off for including additional intermolecular interactions.
Also for the trimer model, the analysis of the electron and hole positions in the exPOT calculations of the S_2 exciton suggests that it has a pure Frenkel-like character. Thus, this model also cannot explain the charge transfer character of the S_2 exciton reported in the literature [46, 155].

The results of the ab-initio calculation of the S_3 exciton in both models exhibit significant discrepancies with the experimental CE map (right column in Figure 5.20). The two theoretical CE maps demonstrate a pronounced minimum inside the BZ whereas in the experiment intensity was found exclusively in this region. A notable distinction emerges between the dimer and trimer models with respect to the intensity maxima predicted. Specifically, the dimer model forecasts six intensity maxima, while the trimer model predicts a star-like feature. Both theoretical CE maps should resemble the emission pattern of the LUMO in Figure 5.20 (j). This is due to the fact that HOMO $\rightarrow$ LUMO transitions are the dominant contribution. However, the features in the CE maps are rotated by 30° whit respect to to each other. A possible explanation is that both models are deficient in their ability to incorporate the required intermolecular interactions to adequately describe the charge transfer S_3 exciton on the length scale of the first surface Brillouin zone.
A comparison of the present results with those obtained by Bennecke et al. [67] indicates that, in both cases, the discrepancies between experiment and theory were most significant for the S_3 exciton, a finding that is consistent with the same reasoning. Nevertheless, the overall congruence between the dimer model calculations and the experimental CE map is considerably more substantial in [67]. This phenomenon is attributed to the effect that imaging the full photoemission horizon at a photon energy of 26.5 eV predominantly probes the molecular orbital character of the investigated excitons. It is possible that dispersive effects may still be discernible, albeit merely as a small modulation superimposed upon the molecular orbital fingerprints [16]. The experiment's sensitivity to possible dispersion effects is enhanced by focusing exclusively on the surface Brillouin zone, utilizing lower probe photon energies of 5.9 eV. This would provide a rationale for the marked discrepancy between experiment and exPOT calculations as presented in this work.
It should be mentioned that the presented exPOT calculations incorporated the incorrect inner potential, as evidenced by the POT calculations of the C_{60} monolayer on Cu(111) in Section 4.4. This results in momentum mismatch of identical emission signatures between experimental and theoretical CE maps. It should also be noted that the probe photon energy of 5.9 eV used in the C_{60} multilayer study produces a much smaller hemispherical cut through momentum space compared to VUV radiation. Therefore, the discrepancy between the curvature of the experiment and that of the theory should be more pronounced. The

aforementioned spherical cut may also result in minor variations in emission patterns, given the substantial dispersion of C_{60} along the k_z-direction.
In summary, a comparison was made between the experimental results outlined in the previous sections and CE maps generated using exciton photoemission orbital tomography. In the exPOT formalism, the C_{60} film was replicated through the implementation of a dimer and trimer approach. The correspondence between theoretical and experimental findings is noteworthy for the energetically lowest S_1 exciton in both models. For S_1 and S_1 excitonic states, experiment and theory differed significantly. Possible reasons for these differences are the limitations of the dimer and trimer models. Both models do not include all intermolecular interactions. In addition, it is necessary to reduce the number of atomic orbitals in the linear combination of the molecular orbitals and to limit the energy range to which the GW correction is applied in the trimer model due to computational restraints.
In order to enhance the outcomes exhibited in this study, it is essential to more effectively incorporate dispersion and intermolecular delocalization effects in the exPOT calculation of a C_{60} multilayer. One potential approach involves the calculation of a tetramer, thereby computing the behavior of a complete unit cell. Although such a simulation is computationally feasible, it is imperative to reduce the utilized atomic basis set and the GW-corrected energy window further to achieve convergence. A more precise characterization of intermolecular interactions using a tetramer model could potentially enhance the congruence between theory and experiment. However, the constraints imposed on the utilized atomic basis and the GW-correction may contribute to additional discrepancies with experimental observations. A time dependent density functional theory calculation of the C_{60} multilayer, incorporating the potential effects of final states, could be a conceivable next step. Nonetheless, this approach is computationally intensive and may provide a more limited degree of insight into the underlying physical phenomena, as it lacks the intuitive nature characteristic of the exPOT formalism.
The next section will discuss a possible temporal evolution of the momentum space signatures of the excitonic states.

5.6. Time Dependency of the Excitonic Photoemission Angular Distributions

The emphasis will now be directed towards the temporal evolution of the excitonic momentum maps. As previously mentioned in Section 5.2.2, the decay dynamics of excitons in a C_{60} multilayer, as well as the various influences on them, have been extensively studied [46, 89, 155, 201, 205, 207, 213]. Causa et al. discovered, that upon optical excitation with 2.76 eV light, the created charge transfer exciton (corresponding to the S_3 exciton in this work) is not in its ground state but rather in an energetically higher vibrational state [213]. Additional research supports the hypothesis that excitonic peaks observed in the photoemission spectra of C_{60} multilayers undergo a vibrational broadening. [214, 215]. As has been previously documented, the signatures in the PADs of such vibrational states can exhibit discrepancies when compared to the PAD of the respective ground state [216]. The objective of this study is to examine this phenomenon in the context of a C_{60} multilayer.
In order to investigate exciton dynamics on a femtosecond time scale, it is necessary to utilize a laser source that can provide sufficiently short pulses. The temporal width of the laser pulses was estimated to be 94 fs for the pump beam and approximately 230 fs for the probe beam. The determination of the pulse duration can be found in Appendix A.3.3.
The energy interval of photoelectrons integrated for each excitonic CE maps is approximately 100 meV wide. This is large in comparison to the energetic spacing of the vibrational states in solid C_{60} [201, 214, 217]. The energy of the vibrational states ranges between 2 and 50 meV with smaller values for intermolecular vibrations and larger values for intramolecu-

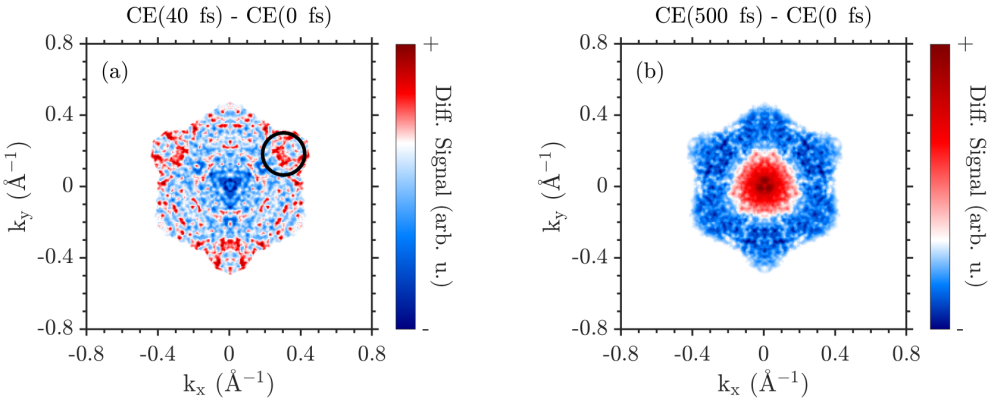

Figure (5.22) Difference maps of the CE maps of the S_3 exciton for selected time steps. The CE maps at different delays used to generate the difference maps are stated in the title. Red areas indicate an increase, blue areas a decrease in intensity.

lar vibrations [218]. Consequently, transitions between distinct vibrational states cannot be discerned by alterations in the energetic distribution over time. Instead, these transitions should become evident through changes in the momentum map at a constant energy level. In order to enhance small variations and discern potential transitions between vibrational states, constant energy maps at different time steps, i.e. varying delays between pump and probe pulse, are subtracted from each another. The CE maps of the excitonic states without incoherent contributions of the final states S_i (see Figure 5.14) are employed in the generation of the difference maps. In the event that the experimental CE maps S_i^{exp}, incorporating all final state contributions, are employed, the subtraction of different time steps will principally culminate in the elimination of the incoherent component of the scattered electron final state. This means that a subtraction of the CE maps S_i^{exp} from each other result in CE maps in the kind of S_i. The reason for this is that the final state is present for all time steps with similar relative intensity. The resulting CE maps will be similar to the CE maps depicted in Figure 5.14, which complicates the discernment of subtle variations due to the decay of excited vibrational states.

Each momentum map is normalized by its sum of all pixels before subtraction. This procedure serves to facilitate the visualization of relative changes. This results in difference maps as exemplary displayed for the S_3 exciton in Figure 5.22. Red areas indicate an increase, blue areas a decrease in relative intensity. To discriminate genuine vibrational features from potential experimental artefacts, a systematic comparison of difference maps across multiple delay steps is performed. The CE map acquired at a delay time closest to the maximum population of the excitonic state is designated as the reference. Subsequent this reference is individually subtracted from CE maps recorded at later delay times to generate a series of difference maps. To correctly assign emerging features to the transition between vibrational states, it is necessary to compare difference maps with different delay steps. The CE map closer to time zero is kept as a reference and the CE map at later delay steps is varied. If a given feature originates from a vibrational transition, it is expected to manifest consistently across difference maps involving progressively longer delay times. This persistence arises from the assumption that the emission pattern does not undergo a complete reversion to its initial intensity distribution due to the unlikelihood of a second identical excitation or decay pathway. Consequently, recurrent features across the delay series can be attributed to vibrational transitions, whereas transient or inconsistent features are more likely to result from noise, fluctuations, or experimental artefacts.
Figure 5.22 (a) displays the difference map of the CE maps of the S_3 exciton at 40 and 0 fs. The difference map exhibits a pronounced speckled pattern. The speckles originate from

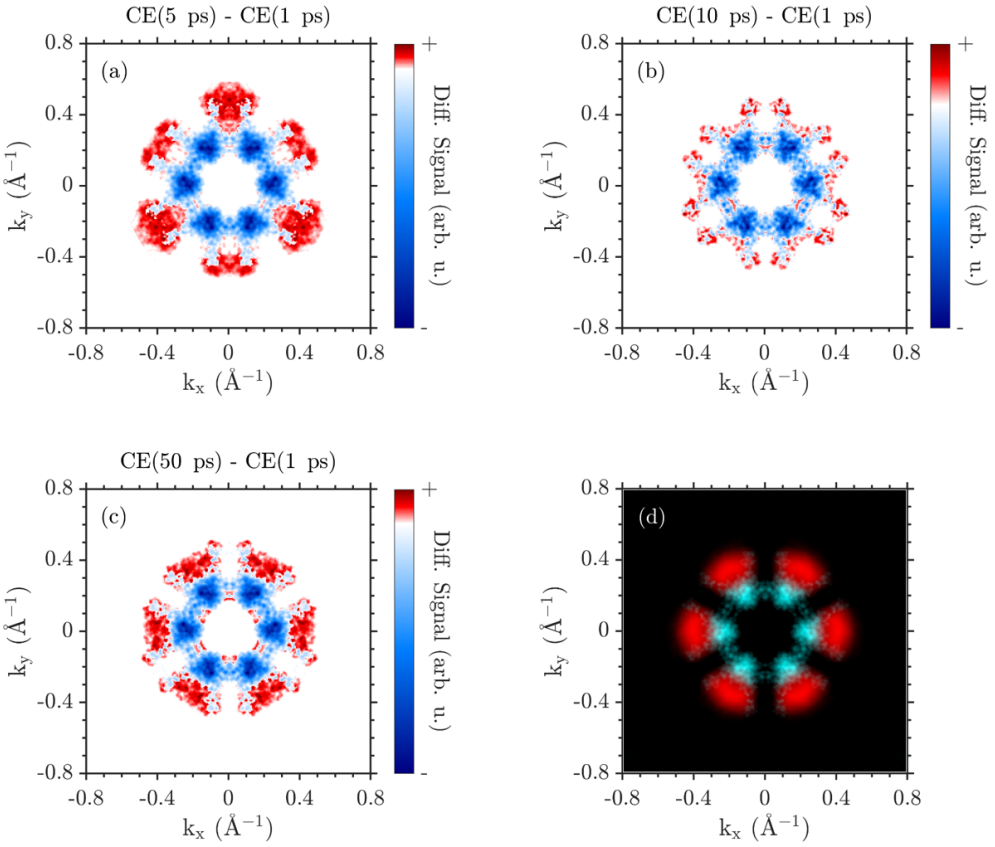

Figure (5.23) Difference maps of the CE maps of the S_2 exciton for selected time steps (a-c). The CE maps at different delays used to generate the difference maps are stated in the title. Red areas indicate an increase, blue areas a decrease in intensity. (d) Overlay image of the PADs of the S_1/S_2 (red/cyan) exciton.

the presence of noise on the subtracted CE maps that is amplified in the subtraction. This phenomenon predominately occurs when the underlying CE maps at different time steps exhibit the same pattern and similar relative intensity. The three slightly larger red areas at the outer parts of the S_3 momentum pattern (marked by a black circle in Figure 5.22 (a)), in conjunction with the blue feature at the $\overline{\Gamma}$-point, are addressed to artifacts.
As depicted in Figure 5.22 (b), the difference map of the S_3 exciton CE maps at 500 and 0 fs reveals the presence of two distinct regions. The red center indicates that at 500 fs, there is an increased relative intensity surrounding the $\overline{\Gamma}$-point in comparison to the intensity at 0 fs. The majority of the population in the S_3 excitonic state has already decayed after 500 fs (compare Table 5.1). This observation indicates that the feature surrounding the $\overline{\Gamma}$-point does not constitute an excitonic state. As previously stated in Section 5.4, the presence of space charge in the measurements was evident, manifesting as a bright spot surrounding the $\overline{\Gamma}$-point. It was further pointed out that the influence of space charge on the structures of the exitonic CE maps is negligible. However, it is more prominent at time steps with low measurement signal as for the CE map of the S_3 exciton at 500 fs pump-probe delay. This phenomenon is further amplified by subtracting different CE maps from one another.

Preceding with the S_2 exciton, Figure 5.23 (a) presents the difference map of the CE maps at 5 and 1 ps. A redistribution of intensity is observable from the blue regions, corresponding to the primary maxima of the S_2 momentum signature, to the red areas. Figure 5.23 (b) illustrates the difference map of the CE maps of the S_2 exciton at 10 and 1 ps. The red signatures observed in Figure 5.23 (a) remain elusive. The difference map resembles the CE map of the S_2 exciton. Therefore, the redistribution of intensity observed in the difference

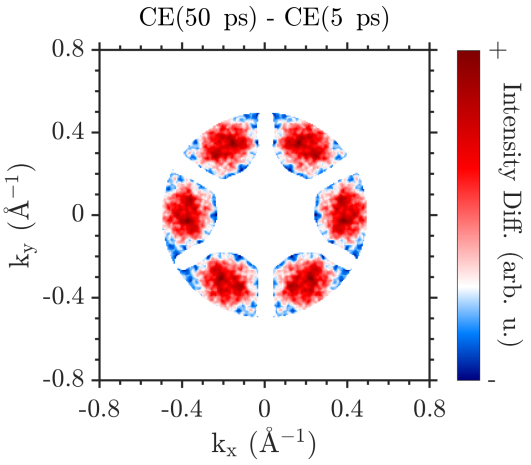

Figure (5.24) Difference map of the CE maps of the S_1 exciton at 50 and 5 ps pump-probe delay. Red areas indicate an increase, blue areas a decrease in intensity.

map involving smaller delays in Figure 5.23 (a) is attributed to an artifact resulting from the subtraction method. This artifact is hypothesized to originate from variations in the statistics of the raw data of the underlying CE maps. In particular, the 5 ps delay CE map has a much lower signal-to-noise ratio than the other CE maps involved in the formation of the difference maps in Figure 5.23. It should be noted that the observed change in the difference maps, as depicted in Figure 5.23 (a), is not anticipated to result from a vibrational transition, as it would substantially modify the excitonic wave function. As indicated by the extant literature, the reported changes are more subtle, retaining the overall shape of the momentum distribution pattern [216].
By increasing the delay between the underlying CE maps of the S_2 exciton to subtract, a subsequent redistribution of intensity is observed in the difference map (see Figure 5.23 (c)). In this instance, the intensity is redistributed from the primary maxima in a radial outward direction, resulting in the formation of six new maxima, which are colored red. This indicates the occupation of the S_1 exciton. It is evident from the comparison of the FWHM of the S_1 and S_2 excitonic levels ($FWHM_{S1} = 0.36$ eV and $FWHM_{S2} = 0.40$ eV [67]) that the they are overlapping in the investigated energy region. To verify the attribution of the emerging features to the S_1 exciton, refer to Figure 5.23 (d). This panel presents an overlay image of the PADs of the S_2 exciton, depicted in cyan, and the S_1 exciton, shown in red. The overlay image exhibits a strong resemblance to the difference map in Figure 5.23 (c). This supports the assignment of the emerging pattern as a transition from the S_2 to the S_1 exciton.

Finally, the case of the S_1 exciton is elucidated. A selected difference map of the exciton state involving the CE maps at 50 and 5 ps is presented in Figure 5.24. The primary emission maxima of the S_1 PAD are indicated by the color red, signifying an elevated relative intensity in the later delay step. Given that this is the case for most difference maps and inverses contrast, if CE maps of negative time delays are used in the subtraction, it can be concluded that this behavior merely visualizes the rise in population of the S_1 exciton. The reason why the population increase of the S_1 exciton can be observed in the difference map is that this increases the peak-to-background ratio of the six main intensity maxima and thus changes the relative intensity. Alternative normalization approaches have been employed, such as normalizing each CE map to the mean intensity of one of the six main maxima, in order to possibly visualize small changes in the emission pattern during the increase in population. However, these approaches have only produced artefacts.
In summary, the momentum space signatures of the excitonic bands did not exhibit any indications of vibrational transitions. The underlying rationale for this phenomenon may be

attributable to the subtle nature of the accompanying changes in emission patterns, which may have been too small to be resolved. It is particularly noteworthy that all underlying constant energy maps were generated by removing the incoherent contribution of the scattered final states. It is possible that during this procedure, signatures indicating the transitions between different vibrational states may be lost. The utilization of CE maps, including all final state contributions, is also not appropriate for the subtraction approach delineated in this section. This is due to the fact that it would function as a removal of the incoherent scattered final state contributions, as outlined in Section 5.4.2. Therefore, the discrepancy in images exclusively illustrates the extracted excitonic PADs of Figure 5.14 and minor alterations in emission patterns across varying delay steps do not exhibit adequate augmentation.
An alternative explanation for the absence of any observed vibrational transition is that the statistical dataset from the pump-probe experiment remains insufficient compared to the noise level, particularly in the context of the requisite data processing procedures. Finally, it is possible that any vibrational transition may not manifest as a resolvable change in the excitonic emission patterns. Theoretical calculations of the excitonic PADs of different vibrational sublevels could shed some light on this question. However, this is not feasible given the available computational resources.
The data presented so far was obtained at low temperatures, resulting in a simple-cubic arrangement of the C_{60} multilayer films with a single rotational degree of freedom remaining (see Section 5.2.1). The subsequent section will undertake a comparative analysis of the low-temperature results with data obtained at room temperature.

5.7. Excitonic Momentum Space Signatures at Room Temperature

Following extensive discussion, the photoemission data of the excitonic states at low-temperature (LT) will be compared with data taken at room temperature (RT). At the latter temperature all rotational degrees of freedom are active within the solid phase. Therefore, all lattice positions are equivalent, resulting in a real space unit cell that contains a single molecule (orange unit cell in Figure 5.2 (a)). As demonstrated in Section 5.2.1, beneath the fcc - sc phase transition temperature, only rotations around single rotation axis persist. Given the orientation of the rotation axes for neighboring molecules, a distinction in molecular positions is observed, resulting in a superstructure unit cell containing four differently oriented molecules (see blue unit cell in Figure 5.2 (a)). As demonstrated by Haag et al. [23, 47], the photoemission angular distribution from a C_{60} multilayer exhibits no evidence of periodicity with respect to the surface Brillouin zone of the superstructure. As substantiated by the preceding sections, the autonomy from molecular orientations is attributed to the high-symmetry of the C_{60} molecule and its molecular orbitals. A comparison of the results obtained so far with a data set pertaining to the excitonic states at room temperature will serve as a secondary verification of the subordinate role of the molecular orientation. In addition, the general influence of temperature on the excitonic PADs will be investigated.

Figure 5.25 (a) depicts a comparison of the logarithmic photoelectron spectra of the different temperature phases at 0 fs pump-probe delay. The energetic positions of the excitonic states investigated for the low-temperature (LT) phase are indicated by gray lines for reference. Evidently, the spectral signatures of the S_2 and S_3 excitons exhibit a notable decrease in intensity at room temperature (RT) in comparison to their intensity at low temperatures. The phenomenon can be attributed to the presence of phonons at room temperature, which act as additional scattering partners. This leads to a decrease of the photoelectron yield from the S_3 exciton and an increase in the photoelectron yield from the S_1 exciton.

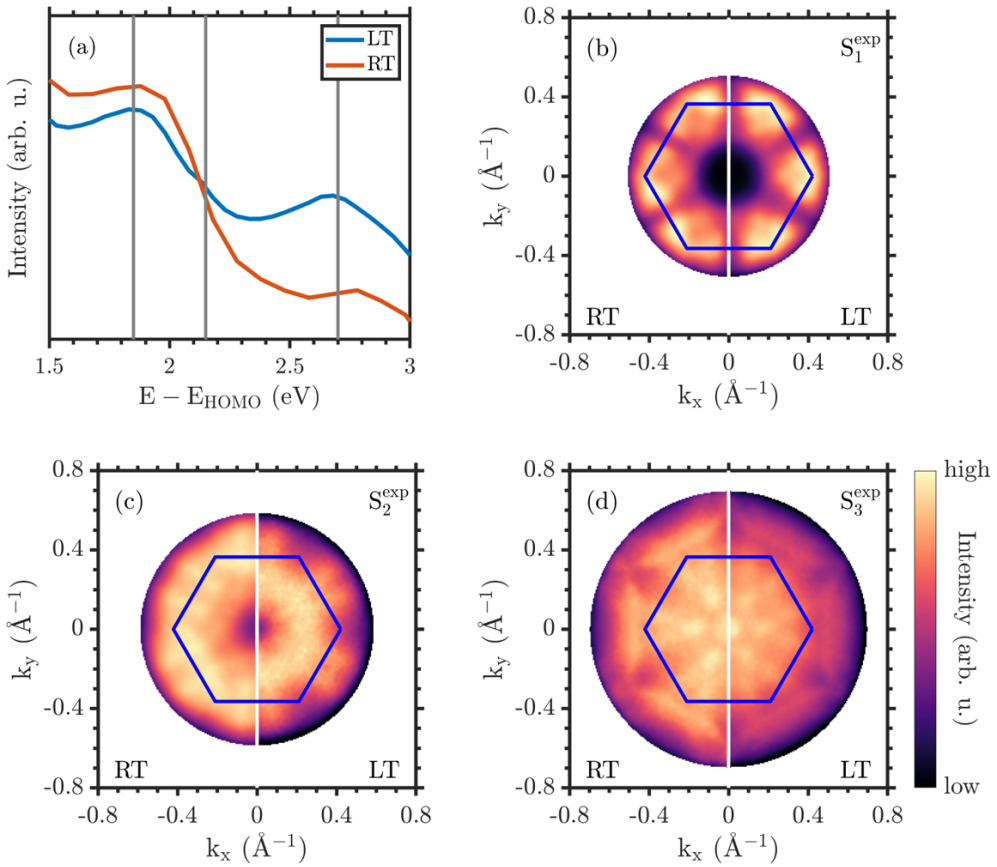

Figure (5.25) (a) Photoemission spectra of the energy region of the investigated excitonic states at room temperature (RT) and at low temperature (LT, $T \approx 130\,\mathrm{K}$). The y-axis is scaled logarithmically for better comparability. (b-d) Comparison of the CE maps of the S_1-S_3 excitons including incoherent scattered final state contributions. The left halves of all images show the CE maps at room temperature, the right halves the low temperature ones. The first BZ is indicated in blue.

Table (5.3) Parameters of the constant energy maps for the room temperature (RT) and low temperature (LT) measurements.

	RT			LT		
	S_1	S_2	S_3	S_1	S_2	S_3
$E - E_{HOMO}$ (eV)	1.85	2.2	2.8	1.85	2.15	2.7
Δt (ps)	5	2	0	5	1	0

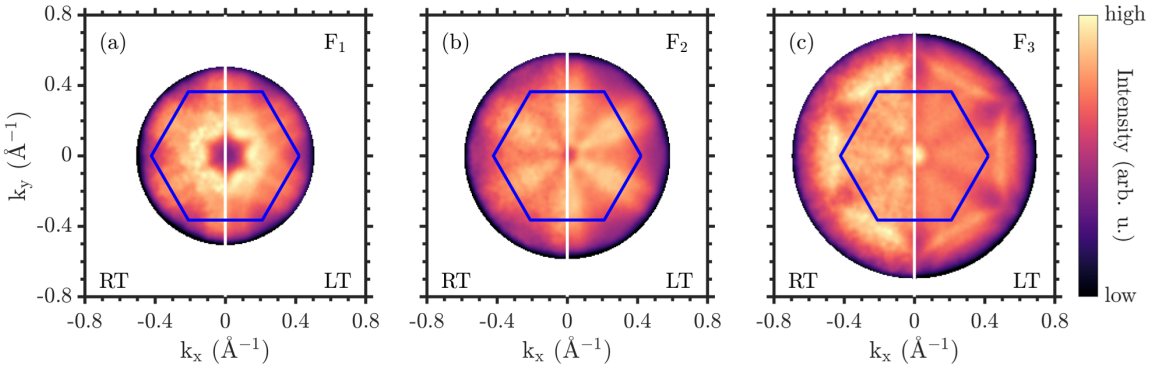

Figure (5.26) Comparison of the CE maps of the scattered final state CE map F_1-F_3 measured with secondary electron emission. The left halves of all images show the CE maps at room temperature (RT), the right halves those at low temperature (LT, $T \approx 130\,\mathrm{K}$). The first BZ is indicated in blue.

To further facilitate comprehension of the momentum space signatures, Figure 5.25 (b-d) illustrates the constant energy maps of the excitonic states of interest, incorporating all final state contributions. Accordingly, the left halves of the figures depict the results for the RT phase, while the right halves illustrate the LT phase that have been previously presented in this chapter (see Section 5.4). It is important to note that the parameters at which the CE maps were recorded differed slightly between room and low-temperature. Table 5.3 provides an overview of the energetic position and the pump-probe delay of the CE maps that are subject of this section.

In room temperature measurements, the increased number of phonons results in an increased number of scattering partners, which leads to a higher noise level. The excitonic CE maps exhibit a comparable overall structure in both temperature phases. Minor discrepancies have been observed. As illustrated in Figure 5.25 (b), the S_1 exciton displays a hexagonal pattern of reduced intensity, accompanied by rounded edges near the six primary maxima, which is more pronounced in the RT phase. The CE map of the S_2 exiton at room temperature demonstrates increased intensity at larger momenta and therefore a reduction in intensity closer to the $\overline{\Gamma}$-point than its low-temperature counterpart. Finally, the S_3 exciton exhibits similar momentum maps at both temperatures.

In the subsequent stage of the analysis, a comparison of the photoemission final states will be made with the results from Section 5.4.1. This will facilitate the subsequent removal of their incoherent contribution to the CE maps. The measurement of the final states is once again conducted using secondary electron emission. The final states are detected in the secondary electron background of a vacuum ultraviolet photoelectron spectrum. Photoelectrons that scatter into these Bloch-like final states during the photoemission process lose their energy and momentum relation of the initial state and subsequently exhibit only the PAD corresponding to the scattered final state. The resulting CE maps of the scattered final states that are populated during the investigation of the excitonic states are displayed

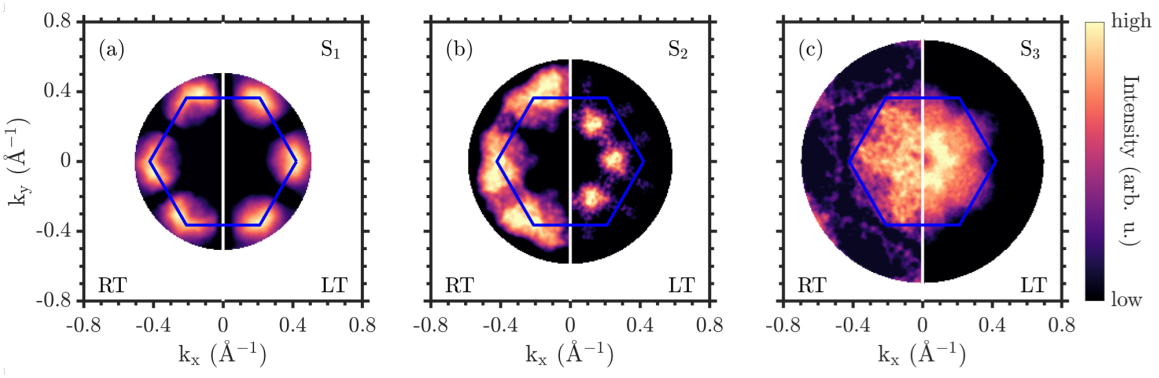

Figure (5.27) Comparison of the CE maps of the S_1-S_3 excitons after removal of incoherent scattered final state contributions. The left halves of all images show the CE maps at room temperature (RT), the right halves the low temperature (LT, $T \approx 130\,\mathrm{K}$) ones. The first BZ is indicated in blue.

in Figure 5.26. As previously mentioned, the room temperature results are plotted in the left halves, while the low temperature results are plotted in the right halves of the figures. A thorough examination reveals no discernible structural disparities, suggesting that in the context of a C_{60} multilayer, the resulting final state momentum maps are autonomous of molecular orientation and rotations. It appears that molecular position is the only relevant factor. This outcome aligns with the observation that the band structure of the occupied molecular orbitals is independent of molecular orientations.
Notwithstanding the potential for molecular rotation, the C_{60} multilayer is also known to exist in a distinct Bravais lattice, characterized by equivalent symmetry, at ambient temperature. The change from a face centered cubic to a simple cubic structure during the cooling process is accompanied by a lattice contraction with a decrease in the surface lattice constant from $a_0 = 10.02\,\text{Å}$ to $a_0 = 9.93\,\text{Å}$ [193]. The alteration in the lattice constant is small, rendering it undetectable in the experiment. Therefore, the phase transition of the crystalline arrangement cannot be directly tracked in momentum space.

In the final step of the procedure, the incoherent contributions of the scattered final states are removed from the measured RT CE maps. This is accomplished using the subtraction approach outlined in Section 5.4.2. This facilitates a more effective comparison of the PADs of the excitonic states. The results are listed in Figure 5.27. The extracted RT PADs of the S_1 (a) and S_3 exciton (c) have a high similarity to their LT counterparts. The minima inside the main intensity spots of S_3 exciton CE map are more pronounced in the RT phase. The observed asymmetry of these spots is a result of the symmetrization of the data. The room temperature CE map of the S_3 exciton exhibits a single, broadened feature at low temperatures. The elevated intensity in proximity of the $\overline{\Gamma}$-point remains a matter of debate, as discussed for the low temperature measurements in Sections 5.4.2 and 5.4.3. The residual faint intensity observed at the photoemission horizon is attributed to a remnant of inadequate incoherent final state subtraction, a phenomenon that is compounded by the elevated noise level.
The case of the S_2 exciton, however, is different. In this instance, the six maxima identified in the LT phase are prove indistinguishable at room temperature. The resulting features bear a striking resemblance to signatures of the S_1 exciton and are hence assigned as such. The enhanced manifestation of S_1 exciton characteristics within the CE map of the S_2 exciton is attributable to the comparatively diminished lifetime of the latter, a consequence of its interaction with phonons [89, 219]. The population in the S_2 undergoes a faster decay, concurrently populating the S_1 excitonic state and enhancing its contributions to the CE map. It is also important to note that the room temperature data was acquired at a 2 ps

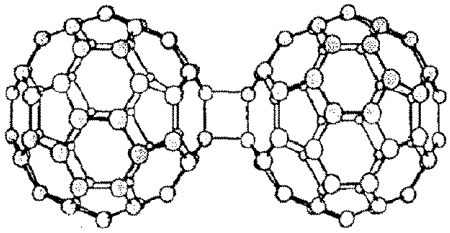

Figure (5.28) Schematic drawing of the "2 + 2" cycloaddition in C_{60}. With permission from [221], copyright © 1993 Published by Elsevier B.V.

pump-probe delay, whereas the low-temperature CE map was taken at 1 ps delay. This further amplifies the observed difference.
It is important to note that pump-probe measurements conducted at ambient temperature have the potential to exhibit radiation-induced damage. The excited C_{60} molecules, can undergo a "2 + 2" cycloaddition [220, 221]. In this process two parallel oriented double bonds are broken, forming a new four-sided bond between two adjacent C_{60} molecules (see Figure 5.28). The occurrence of this photoinduced cycloaddition is only possible above a temperature of $T_0 = 250\,\mathrm{K}$ [221]. At temperatures below this threshold, the double bonds of neighboring molecules avoid each other by rotating around differently oriented <111> directions [194]. The investigation revealed small traces of photopolymerization in the sample under study. These traces manifested as a broadening of the molecular orbitals and an emergence of a novel signature in proximity to the HOMO-1. However, no direct effects could be detected in the initial, excitonic or final state momentum maps, indicating that the amount of photopolymerized molecules is still negligible.
In summary, the momentum maps of the S_1-S_3 excitonic states at room temperature were compared to the previously discussed ones at $T \approx 130\,\mathrm{K}$. As for the low temperature ones, the incoherent contributions of the scattered final states occupied in the photoemission process were removed, resulting in an estimate of the excitonic photoemission angular distributions. The two additional rotational degrees of freedom populated at room temperature do not result in any discernible differences in emission patterns when compared to those observed at low temperatures, both for final state PADs and excitonic ones. This finding lends further support to the hypothesis that the photoemission angular distributions of the excitonic states, as well as the band structure of the scattered final states, are independent of molecular orientation. Instead, these phenomena appear to be contingent solely on the absolute overlap of adjacent molecules. This finding aligns with the results reported for the occupied molecular band structure [47].

5.8. Summary and Outlook

This chapter presents a detailed investigation of the first three excitonic states S_1 - S_3 in a C_{60} multilayer system using momentum microscopy. High repetition rate ultraviolet light sources allowed high resolution measurements of the photoemission angular distributions (PADs) within the first Brillouin zone. A dispersion over all three excitonic levels was observed, which was attributed to intramolecular interactions. The obtained excitonic PADs were found to be coherently superimposed with Bloch-like scattered final states. Therefore, special attention was given to isolate the momentum-resolved signatures of the excitonic states by a subtraction approach. This method removed the incoherent contributions of the scattered final states from the CE maps, yielding an approximation of the purely excitonic PADs. The emission signatures of the S_1 exciton could be unambiguously identified, which was not the case for the S_2 and S_3 excitons. Therefore, a replication approach using simple

geometric structures was used. This allowed to distinguish between excitonic signatures, artifacts of the subtraction approach, and remnants of the coherent contributions of the scattered final states.
Exciton photoemission orbital tomography calculations using a dimer and a trimer model to approximate the C_{60} superstructure unit cell showed good agreement with experiment for the S_1 exciton and partial agreement for the S_2 and S_3 excitons. Discrepancies were attributed to incomplete treatment of intermolecular interactions. In the case of the trimer model, not all molecular orientations in the unit cell were considered. In addition, the number of electron wave functions included in the description of the molecular orbitals had to be reduced due to computational limitations. A comparison with experimental data from Bennecke et al. [67] suggests that the exPOT framework more accurately captures the orbital character of excitons, while showing challenges in accounting for intermolecular interactions.
Efforts to resolve vibrational sublevels within the excitonic states by analyzing temporal changes in the CE maps were inconclusive. The subtle nature of these transitions may have been masked by the subtraction of incoherent contributions of the scattered final states or limited by the acquired statistics of the data set. Future attempts using higher photon energies might enable access to plane wave final states, facilitating better access to observing these vibrational states.
A temperature-dependent analysis revealed no differences between low- and room-temperature PADs of the excitonic states, suggesting that variations in crystal structure and an increased number of active rotational degrees of freedom have negligible impact within the resolution limits of the current setup. Instead, the excitonic PADs are primarily determined by the spatial overlap of adjacent molecules, independent of their respective orientation. This is consistent with the results for the occupied molecular orbitals and can be attributed to the high symmetry of the C_{60} molecules.
In conclusion, momentum-resolved signatures of the first three excitons in a C_{60} multilayer film were successfully identified. The observed excitonic dispersion pointed to predominantly intramolecular interactions, yet no clear momentum-space distinction between Frenkel and charge transfer excitons was observed. The conceptual application of ultraviolet photon energies within the framework of exciton photoemission orbital tomography revealed significant challenges due to the influence of dispersive scattered final states. These findings underscore both the potential and current limitations of momentum microscopy in mapping excitonic phenomena in complex molecular systems.

Several follow-up questions arise from this work. One open question is whether the momentum distributions of excitons differ when they are populated resonantly versus via decay of higher-energy excitons. In the C_{60} multilayer system, the S_1 exciton is a promising candidate for resonant excitation due to its distinct PAD features, which can be easily distinguished from contributions from the scattered final state.
Future studies could also explore the coherence between excitons and the exciting light field. This involves a coherent population and depopulation of an excitonic state. This would involve examining whether momentum distributions change as coherence is lost, requiring a phase-stabilized interferometer setup.
Another possible direction is to analyse the nature of the Bloch-like scattered final states themselves. For higher kinetic energies, the observed final state PADs become simpler in structure, contracting to a ring-like feature before becoming indistinguishable in the CE maps. Investigating the transition from Bloch-like to plane-wave final states could reveal whether such changes in momentum space reflect a change in final state character. Density functional theory calculations would help to clarify the orbital nature of these states.
This work highlights fundamental challenges in applying exciton photoemission orbital tomography to systems such as C_{60} at ultraviolet photon energies, where Bloch-like scattered

final states dominate the excitonic PADs, complicating interpretation. To resolve the purely excitonic PADs and possibly observe dispersion of the individual excitonic levels, i.e. intermolecular dispersion of the excitonic states, higher photon energies and a restricted momentum field of view (spanning only a few Brillouin zones) are required. This must be combined with high repetition rate light sources to maintain statistical reliability.
Modeling the full C_{60} superstructure unit cell proved to be computationally demanding. Given the current limitations, future research should focus on simpler systems, either with smaller molecules or fewer molecules per unit cell. Planar molecules such as PTCDA, pentacene, or sexiphenyl may be more suitable for exPOT-based exciton studies. Their 2D character avoids complications of the correct inclusion of the inner potential. Furthermore, multilayer films of these molecules exhibit π-orbital overlap across layers, potentially leading to out-of-plane dispersion and interlayer charge transfer excitons. These systems may help to resolve whether Frenkel and charge transfer excitons can be distinguished in momentum space.

6 Conclusion and Outlook

This chapter summarizes the most important results of this work and draws a general conclusion. In addition, an outlook on possible further research of photoemission orbital tomography using ultraviolet photon energies will be given.

6.1. Conclusion

In order to contribute to the fundamental understanding of band structure design in π-conjugated molecular systems on surfaces this work investigated electronic wave function coupling and correlated electronic effects through momentum microscopy and photoemission orbital tomography (POT). The influence of adsorption geometry, molecular orientation and intermolecular interactions on the energy level alignment, electronic structure and excitonic landscape was investigated. The focus was on three prototypical π-conjugated organic molecular systems on surfaces, including cesium-doped monolayer films of PTCDA on Ag(111), monolayer C_{60} films on Cu(111), and multilayer C_{60} films on Cu(111).
First, the examination of cesium-doped PTCDA monolayers on Ag(111) revealed weak molecule-substrate hybridization. Cesium doping induced a molecular reorientation into two distinct point-on-line phases, solely dependent on the dopant concentration. Despite differences between cesium and potassium, similar structural phases suggest that the alkali metal character of the dopant atoms primarily drives molecular arrangement. Energy level alignment in this weakly hybridized point-on-line structure was found to be determined by molecular orientation. Next, a strongly hybridized interface of a monolayer C_{60} on Cu(111) was studied. The overall band structure of the system was altered by the hybridization, even in energy regions where no molecular states are present. The emergence of a new interface state located between the molecules and the metal substrate was observed. Different adsorption configurations led to varying degrees of hybridization, with the most reconstructed surface showing the strongest coupling between molecular and metal electronic states. Finally, excitonic states in a C_{60} multilayer film were analyzed, with momentum-resolved signatures of the first three excitons observed. The observed dispersion pointed to intramolecular interactions, but no clear distinction between Frenkel and charge transfer excitons was found in momentum space.
A complementary variant of the exciton photoemission orbital tomography (exPOT) technique was explored conceptually, utilizing ultraviolet probe photon energies and operating at high repetition rates of approximately 80 MHz. Due to the lower photon energies, this approach restricts access to the first surface Brillouin zone in momentum space. However, the high repetition rate enables detailed tracking of exciton dynamics and the acquisition of photoemission angular distributions (PADs) with high statistical accuracy. This, in turn, facilitates the observation of subtle momentum-space features and dispersion signatures that are less apparent in the conventional exPOT approach, which employs extreme ultraviolet photon energies and is primarily sensitive to the orbital character of excited molecular states [67]. Despite these advantages, the interpretation of experimental data remains challenging due to the presence of dispersive, scattered final states that are coherently superimposed

with the exciton PADs. To address this, a method for the approximate removal of incoherent contributions arising from these scattered final states is presented. Furthermore, a validation strategy based on the reconstruction of experimental PADs using simple geometric structures to assess the effectiveness of the removal of the incoherent final state contributions is introduced.
Overall, this thesis provides new insights into the coupling of electronic wave functions and excitonic states in π-conjugated organic molecular systems on surfaces. It demonstrates how molecular orientation, adsorption configuration as well as intermolecular interactions critically shape the electronic properties of the systems from weak physisorption to strong hybridization. The excitonic landscape is governed by intra- and intermolecular coupling. These findings contribute to a more detailed, fundamental understanding of how molecular-scale structure and interactions govern electronic and excitonic behavior, which constitutes an essential step towards the rational design of organic electronic and optoelectronic devices.

6.2. Outlook

In this work, the use of ultraviolet photon energies in the context of (exciton) photoemission tomography was conceptually tested. It was found that the occurrence of dispersive Bloch states above the vacuum level poses significant challenges. These unoccupied Bloch states serve as final states in the photoemission process for ultraviolet photon energies. As a consequence, the measured photoemission angular distributions (PADs) of the studied states are coherently superimposed by the PADs of the final states. In Section 5.4.2, an approach for the approximate removal of the final state contributions from the measured PADs was presented. Since this approach has its limitations, an outlook is given on how to avoid the challenges of dispersive final states in the photoemission experiment.
The obvious option is to use larger photon energies. It has been shown that final states with larger kinetic energies are less prone to manifest Bloch-like properties because the electrons are energetically further away from the crystal potential. This phenomenon has been observed in various experiments, including those performed on a C_{60} multilayer [23, 67, 71]. In addition, the larger photon energies lead to an increased photoemission horizon, which also allows the study of systems where the region of interest is located at larger momenta. Examples are orbitals of planar molecular systems, e.g. PTCDA (see Chapter 3) or the Dirac cones in graphene. However, it should be noted that increasing the photon energy to avoid the energy region of dispersive final states can be an experimental challenge if only small regions around the $\overline{\Gamma}$-point are to be investigated, as was the case in the study of the excitonic landscape in multilayer C_{60} films in Chapter 5. The necessary magnification of the small momentum space region, as well as the low signal-to-noise ratio of commonly available light sources capable of providing the necessary photon energies, pose significant experimental challenges. However, pulsed femtosecond extreme ultraviolet light sources operating at repetition rates of tens of MHz may make this a viable prospect in the future.
A second possibility is to restrict the analysis to systems that do not exhibit dispersive, scattered final states near the vacuum energy. Due to the limited photoemission horizon when using ultraviolet photon energies, these systems additionally require either small surface Brillouin zones (BZs), corresponding to large real space unit cells, or the states of interest must be located near the $\overline{\Gamma}$-point. One class of materials that meets these requirements are topological insulators, like Bi_2Se_3. Topological insulators exhibit a unique topologically protected surface state within the conduction and valence band gap [222–227]. This surface state, with its linear dispersion relation, has the shape of a Dirac cone and is located at the $\overline{\Gamma}$-point. Angel-resolved photoemission spectroscopy (ARPES) experiments with ultraviolet photon energies have demonstrated the absence of dispersive scattered final states near the vacuum energy. The strong confinement of the topological surface state in energy

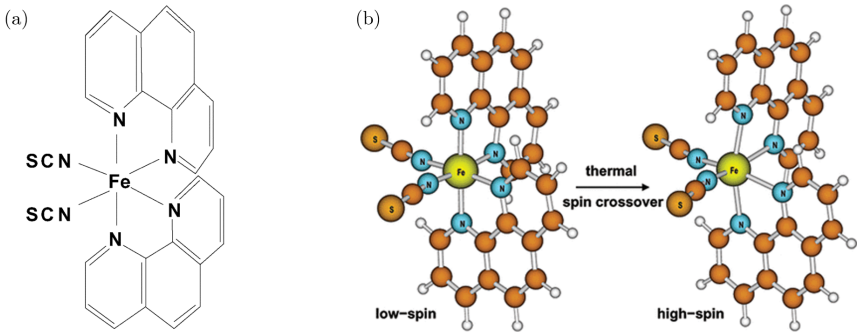

Figure (6.1) (a) Structure of the $Fe(phen)_2(NCS)_2$ complex. (b) Molecular deformation of the ligand field around the central iron atoms during the low-spin to high-spin transition. Taken with permission from [228]. Copyright © 2002 American Chemical Society.

and momentum requires high resolution experiments with sufficient photon flux. Therefore, topological insulators are an ideal candidate for ARPES with ultraviolet photon energies.

A fascinating open question in the field of topological insulators is the manipulation of surface state electrons and their dynamics in the presence and absence of time-reversal symmetry [141]. This is particularly interesting since time-reversal symmetry prevents the backscattering of surface state electrons [227, 229]. Several methods for breaking the time-reversal symmetry and subsequently modifying the surface state electrons by magnetic proximity have been proposed and realized. The methods include the use of magnetic dopants or adatoms [230, 231], molecular adsorbates with magnetic moments [136, 141], and ferromagnetically coupled metal-organic networks [140, 232]. A similar approach to Caputo et al. [141] and Cuxart et al. [136] using molecular adsorbates with magnetic moments is proposed in this work. Instead of metal-centered phthalocyanines, spin crossover molecular complexes are proposed as adsorbates, in particular $Fe(phen)_2(NCS)_2$. The structure of the $Fe(phen)_2(NCS)_2$ complex is schematically shown in Figure 6.1 (a). These molecules exhibit magnetic bistability, which involves two different spin states: a singlett state with no magnetic moment ($S = 0$), called low-spin state, and a high-spin state with non-zero magnetic moment ($S = 2$). The spin states result from an energetic splitting of the 3d atomic orbitals of the central iron atom depending on the structure of the ligand field [233, 234]. External stimuli such as pressure, temperature or optical excitation can change the spin state of the molecules [235, 236]. Figure 6.1 (b) shows the structural deformation of the ligand field for the two different spin states of $Fe(phen)_2(NCS)_2$. At room temperature the molecules are in the high-spin state.
A first ARPES study of a monolayer of $Fe(phen)_2(NCS)_2$ spin crossover molecules on the topological insulator Bi_2Se_3 has been performed. Figure 6.2 (a) shows the energy distribution curve (EDC) of the bare Bi_2Se_3 surface in the region of the topological surface state. As a light source the He I_α line ($h\nu = 21.2\,eV$) of a vacuum ultraviolet gas discharge lamp was used. The conduction band is partially filled due to the dissociation of adsorbed residual gas molecules under extreme ultraviolet radiation [237]. In comparison, Figure 6.2 (b) shows the EDC in the region of the surface state of the Bi_2Se_3 surface covered with a $Fe(phen)_2(NCS)_2$ monolayer. The molecular adsorption leads to a further filling of the conduction band. In addition, the valence band, the conduction band and the surface state are flattened. A gap is observed between the valence and conduction band. This proves that the magnetic moments of the spin crossover complexes break time-reversal symmetry due to magnetic proximity, resulting in a topologically trivial insulator.

The results presented here are very promising, but only preliminary and should be repro-

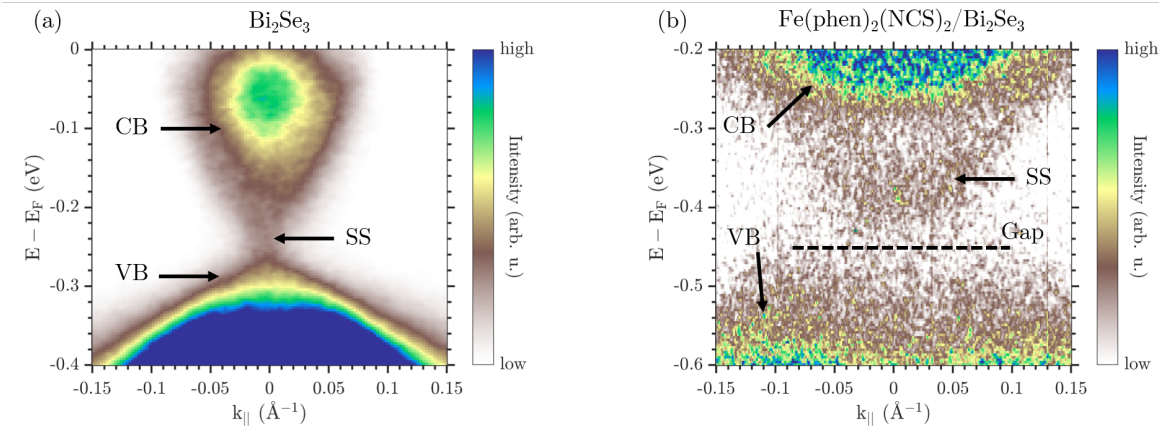

Figure (6.2) Energy distribution curves of the topological surface state of pristine Bi_2Se_3 (a) and $Fe(phen)_2(NCS)_2$ on Bi_2Se_3. The arrows mark the conduction band (CB), the surface state (SS) and the valence band (VB). The molecular adsorption leads to a further occupation of the conduction band. A gap in the surface state is indicated by the dashed line.

duced with better statistics. In addition, the decomposition of $Fe(phen)_2(NCS)_2$ molecules under extreme ultraviolet irradiation needs to be monitored. For further research, the study of the transition from a topologically non-trivial to a topologically trivial phase could be investigated using time-resolved ARPES by optically switching the spin crossover complex from low- to high-spin states [236]. This would provide insight into the fundamental aspects of topological protection.

A Supplementary Information

A.1. Sample Preparations

Since all the experiments presented in this thesis are surface sensitive, their results depend strongly on the quality of the sample surface and thus on its preparation. In this chapter the different methods of sample preparation are summarized, starting with the preparation of a cesium-doped monolayer of PTCDA on Ag(111) discussed in Chapter 3, followed by a description of the preparation of a C_{60} monolayer on a Cu(111) single crystal investigated in Chapter 4. This system serves as a starting point for the growth of the C_{60} multilayer films discussed in Chapter 5. All samples were prepared in ultrahigh vacuum with a base pressure better than $2 \cdot 10^{-9}$ mbar.

A.1.1. Cleaning of the Metal Substrates

The Ag(111) and Cu(111) single crystals used in the experiments were cleaned by repeated cycles of Ar^+ sputtering followed by annealing. The ion beam was focused and rapidly scanned over the surface with an exposure time per sample spot of $300\,\mu s$ and an Ar pressure of $\approx 2.2 \cdot 10^{-7}$ mbar. The acceleration voltage was gradually reduced from 1500 to 800 V over the course of the various sputter/anneal cycles. After 30 min of sputtering, the samples were heated for $30 - 45$ min ($T_{Ag(111)} = 723$ K, $T_{Cu(111)} = 773$ K).
The surface quality was checked with low energy electron diffraction (LEED) and angle-resolved photoelectron spectroscopy (ARPES), confirming that no traces of previous adsorbate layers remained. A well-ordered surface is characterized by sharp diffraction spots and the clear presence of the Shockley surface state.

A.1.2. Cs-doped PTCDA Monolayers on Ag(111)

After the cleaning of the Ag(111) single crystal PTCDA monolayer films were grown by physical vapor deposition of the molecules from a three-pocket TCE Knudsen cell evaporator by *Kentax UHV equipment*. The evaporation temperature was set at 583 K while the sample was held at 353 K to ensure a higher mobility of the molecules on the surface and consequently a better ordered structure. The evaporation time was chosen to be 10 min, resulting in more than monolayer coverage. The sample was then heated to 423 K for all molecular layers except the first to desorb because the first layer is more strongly bound to the surface due to the stronger metal-molecule interaction compared to intermolecular interactions [100]. The successful growth of a well ordered PTCDA layer was confirmed in LEED (see Figure 3.2 (a) for the characteristic diffraction pattern).
The samples were doped by exposing the PTCDA monolayer to a cesium flux from a dispenser by *SAES Getter* and then annealed above 373 K for several minutes to improve the film quality. We expect no phase transition from this annealing procedure since the activation energy in the comparable potassium doped system is above 473 K [99].

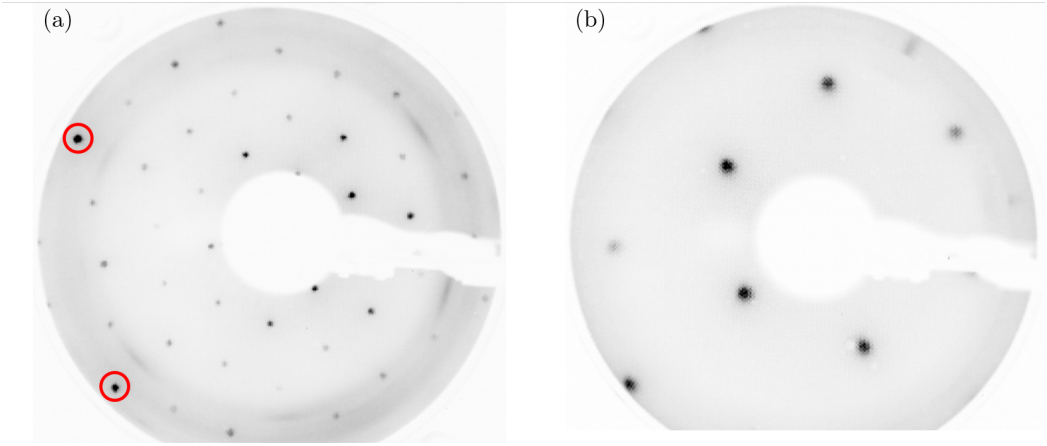

Figure (A.1) (a) LEED image of a C_{60} monolayer on Cu(111) ($E = 80.5\,\text{eV}$). The 0^{th} order is obscured by the electron gun. The diffraction spots marked with red circles belong to the 1^{st} diffraction order of the Cu(111) surface. (b) LEED image of a C_{60} multilayer film on Cu(111) ($E = 17.0\,\text{eV}$). The 0^{th} order and partially the 1^{st} order are obscured by the electron gun. The LEED images were taken at room temperature.

A.1.3. C_{60} Monolayer Film on Cu(111)

To prepare a monolayer of C_{60} on Cu(111), a multilayer film is first prepared by evaporating C_{60} molecules from the Knudsen cell set to $T_{\text{evap}} = 678\,\text{K}$ for 90 min. All additional layers except the first are desorbed in a subsequent annealing of the sample to 678 K for 50 min, as also for C_{60} the interaction of the first layer with the Cu surface is stronger than the intermolecular interaction between the C_{60} layers [149, 179, 197]. Furthermore, the thermal activation allows the C_{60} molecules to improve the adsorption sites and molecular orientation, thus optimizing the bond geometry [156].
The presence of a C_{60} monolayer was investigated in LEED by the appearance of first order diffraction spots of the Cu(111) substrate, as highlighted by the red circles in the LEED image in Figure A.1 (a). These spots are strongly attenuated starting from the second layer [47].
The annealing process leads to a burial of the C_{60} molecules and a consequent reconstruction of the Cu(111) surface [143].

A.1.4. C_{60} Multilayer Film on Cu(111)

The preparation of a C_{60} monolayer on Cu(111) as described above in Section A.1.3 serves as the starting point for the preparation of the multilayer films. The monolayer sample is kept at an elevated temperature of about 403 K while C_{60} molecules are evaporated for another 90 min under the same conditions as above. This second evaporation on the monolayer at elevated substrate temperatures results in an improved molecular order of the fabricated C_{60} multilayer film [149].
The quality of the thick C_{60} films was investigated by LEED and ARPES. Sharp diffraction spots (see Figure A.1 (b)) and a pronounced minimum between the HOMO-1 and HOMO peak in the photoelectron spectrum (see Figure 5.4 (a)) are indicators of a well ordered film. Furthermore, the contrast and sharpness of the PAD of the S_1 excitonic state was used as a reference for the sample quality (see Figure 5.9 (b)).

A.2. Data Analysis Methods

This section provides an overview of the data analysis process. We begin with a discussion of the general steps that are applied to each data set by default (unless otherwise noted). These include flat-field camera correction, averaging of different runs, calibration of the constant energy maps, distortion correction, and image symmetrization. Individual steps of the data analysis are not explained here (for example, the 2D tomographic fitting routine), but can be found in the corresponding sections of the main part of this thesis.

A.2.1. Flat-Field Correction

All data in this work are acquired using a momentum microscope, which measures photoemission angular distributions at constant energies, so-called constant energy maps (CE maps) (see Section 2.2.3). The CE maps are recorded by a cahrge-coupled device (CCD) camera from a fluorescence screen after signal enhancement by a matched pair of microchannel plates (MCPs). The different channels of the MCPs are structured by a honeycomb pattern that is visible in the raw data. To remove this honeycomb pattern and to balance the sensitivity of different regions of the MCPs, a flat-field correction is applied.

$$CorrectedImage = (RawImage - DarkFrame) \cdot \frac{mean(FlatField - DarkFrame)}{(FlatField - DarkFrame)} \quad \text{(A.1)}$$

The raw data are corrected according to Equation A.1 [238]. The flat-field is a uniformly illuminated image of the MCPs and the screen without any sample information and depends on the applied MCP voltage. The dark-frame image is taken without any illumination of the imaging unit, thus correcting for any dark current of the CCD camera.

A.2.2. Averaging of Different Runs

Each CE map of an experiment is measured several times to improve the statistics. The different runs are averaged to produce a single image. The averaging is done using an intensity-based image registration algorithm to account for image drift between runs. The first run is used as a fixed reference. For all subsequent runs, the algorithm finds the necessary transformations to make the structures of the current image coincide with the reference. Only image translations are allowed to minimize the induction of possible errors. Image registration is performed on Sobel-filtered images. The Sobel filter enhances all edges, including the photoemission horizon, allowing a better matching of the structural momentum space signatures in the image registration.
After averaging all runs, the resulting CE map is smoothened with an adaptive median filter to remove bright, isolated pixels.

A.2.3. Momentum Calibration of the Constant Energy Maps

After the flat field correction and averaging of all runs, the resulting CE maps are calibrated to obtain the conversion factor between pixel and $Å^{-1}$. To do this, the edge of the photoemission horizon is located in each image by a Canny edge detection algorithm [239]. Then an ellipse is fitted to the photoemission horizon. The position of the center of the photoemission parabola is obtained from the ellipse parameters, and the desired conversion factor between pixel and $Å^{-1}$ is determined by fitting the semi-major and semi-major axes with the free electron dispersion relation in Equation A.2.

$$r^2 = \frac{2m}{\hbar^2} E \quad \text{(A.2)}$$

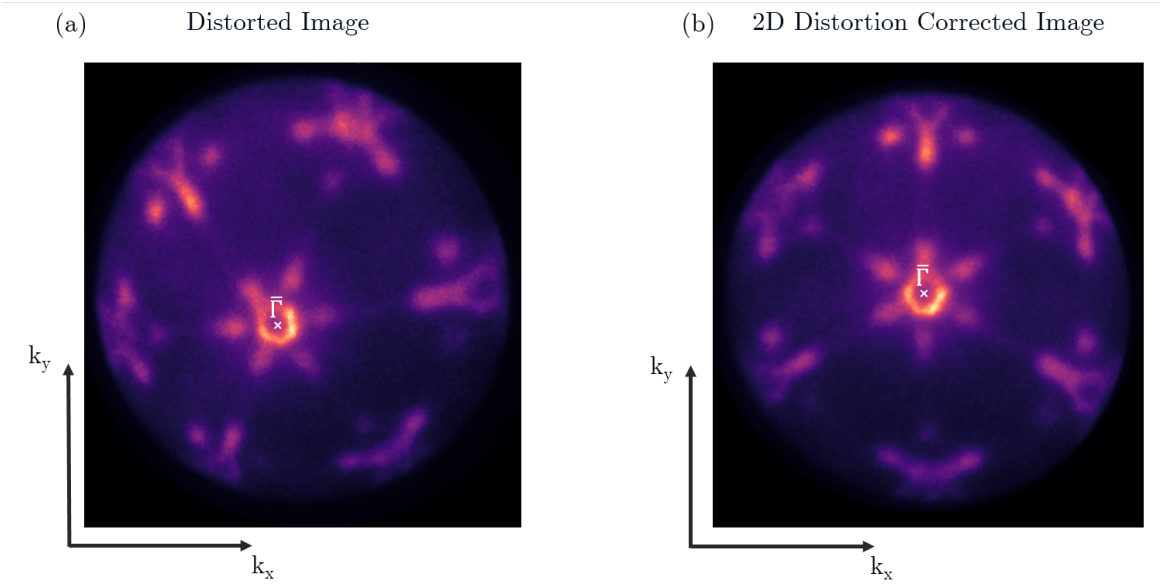

Figure (A.2) Comparison of a Bi_2Se_3 CE map before (a) and after (b) distortion correction. The CE map shows the Bi_2Se_3 valence band ($E - E_F = 0.25\,eV$). The visible features are centered around $\overline{\Gamma}$-points. After distortion correction the $\overline{\Gamma}$-points are centered in the photoemission horizon.

It is also possible to compensate for any difference between the semi-major and semi-major axis resulting from sample tilt and/or suboptimal stigmator settings to obtain a circular photoemission horizon.

A.2.4. Distortion Correction

If the microscope is misaligned or the sample is tilted, the CE maps can be distorted. Since there is no possibility to adjust the sample tilt at the NanoESCA setup in Kaiserslautern, this has to be taken into account in the data analysis.
Figure A.2 shows an example of CE maps of Bi_2Se_3 before and after distortion correction. Each star-like feature is centered around a $\overline{\Gamma}$-point. For the $Bi_2Se_3(0001)$, a $\overline{\Gamma}$-point is expected in the center of the photoemission horizon with the same distance to all neighboring $\overline{\Gamma}$-points. Since distortion usually occurs only in one direction due to tilt, the distortion correction described by Wei et al. [240] is applied only along the x-direction after a suitable rotation of the images. This rotation aligns the distortion axis with the x-axis. The direction of the distortion can usually be found from the movement of the ellipse center for different energies obtained in the calibration process. The results of the distortion correction can be verified by applying a symmetrization of the image according to the sample symmetry. The linewidth of the features in the CE map serves as an indicator of the success of the distortion correction procedure, since it is the smallest after symmetrization of a distortion-free image.

A.3. Supplementary Information Excitonic Structure in C_{60} Multilayer Films

This section provides supplemental information for Chapter 5, "Excitonic Structure in **C_{60}** Multilayer Films".

A.3.1. Approximate Removal of the Scattered Final State Contributions

In the subtraction approach, incoherent final state contributions are subtracted from the excitonic PADs. Thus, CE maps with pure final state contributions F_i are subtracted from those obtained in the pump-probe experiment, S_i^{exp}. These final state CE maps F_i are obtained through secondary electron emission using a vacuum ultraviolet gas discharge lamp. Since the final state and excitonic CE maps are obtained in different experiments, their total intensities are not comparable. Therefore, each CE map must be normalized prior to subtraction. This work tested different normalization methods:

- Normalization of each CE map to its **total intensity**. This method yielded the best results and was commonly used in this study.

- Normalization to the **maximum intensity** of each CE map. This method produced results similar to normalization based on total intensity. Therefore, it is not shown in Figures A.3 - A.5. However, in cases involving very large intensity maxima compared to the overall intensity level of the CE maps or image saturation, this method does not perform well.

- Normalization to the **mean intensity** of the CE map. This method showed analogous behavior with respect to the normalization to the maximum intensity.

- Normalization to the mean intensity of a selected **region of interest**. The regions of interest were chosen based on prominent features or regions with a significant contribution from the scattered final state.

The results of the various normalization methods used in the subtraction approach are shown in Figures A.3 - A.5. For the normalization to a region of interest (ROI), the ROI is depicted in a CE map before the final state subtraction, next to the resulting CE map. For the S_1 and S_3 exciton the normalization to the total intensity was chosen. For the S_2 exciton the normalization to the region of interest depicted in Figure A.4 (d) was chosen. This leads to a larger prominence of the outwards pointing lines in the CE maps, which are attributed to remnants of the incoherent final state contributions in Section 5.4.3. These features are less prominent in the normalization to the mean intensity of the region of interest depicted in Figure A.4 (b). However, the width of the main intensity maxima differs more strongly for the different delay steps. Hence the ROI in A.4 (d) was chosen.

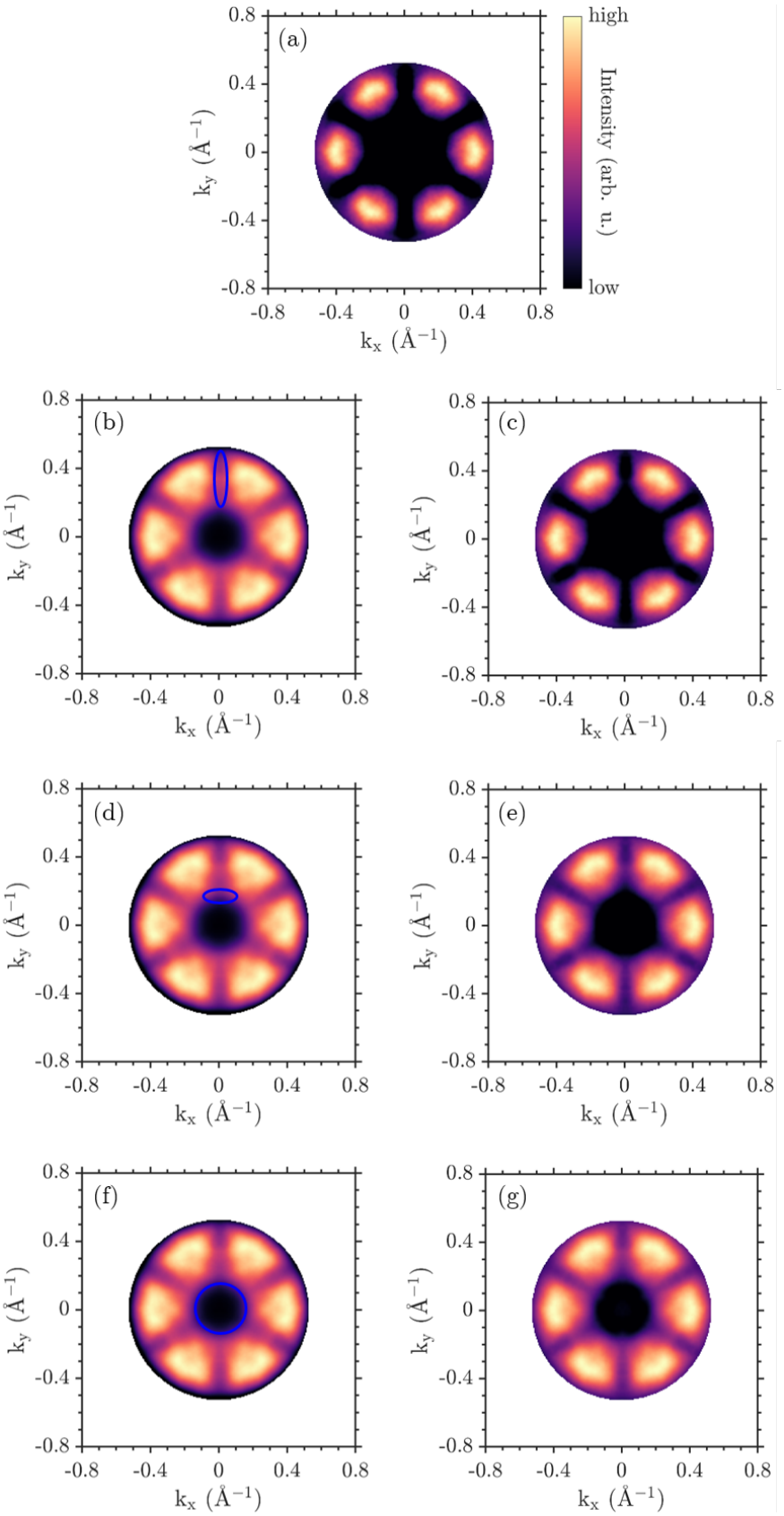

Figure (A.3) A comparison of the different normalization methods tested in the subtraction of the incoherent scattered final state contributions of the S_1 exciton PAD at a delay step of $\Delta t = 5$ ps. (a) The resulting CE map for normalizing the individual CE maps in the subtraction approach based on their total intensity. (c, e, g) The resulting CE map for normalizing the individual CE maps in the subtraction approach based on the mean intensity of selected regions of interest. The corresponding regions of interest are marked in blue in (b, d, f). The normalization to the total intensity was used in the discussion in Chapter 5.

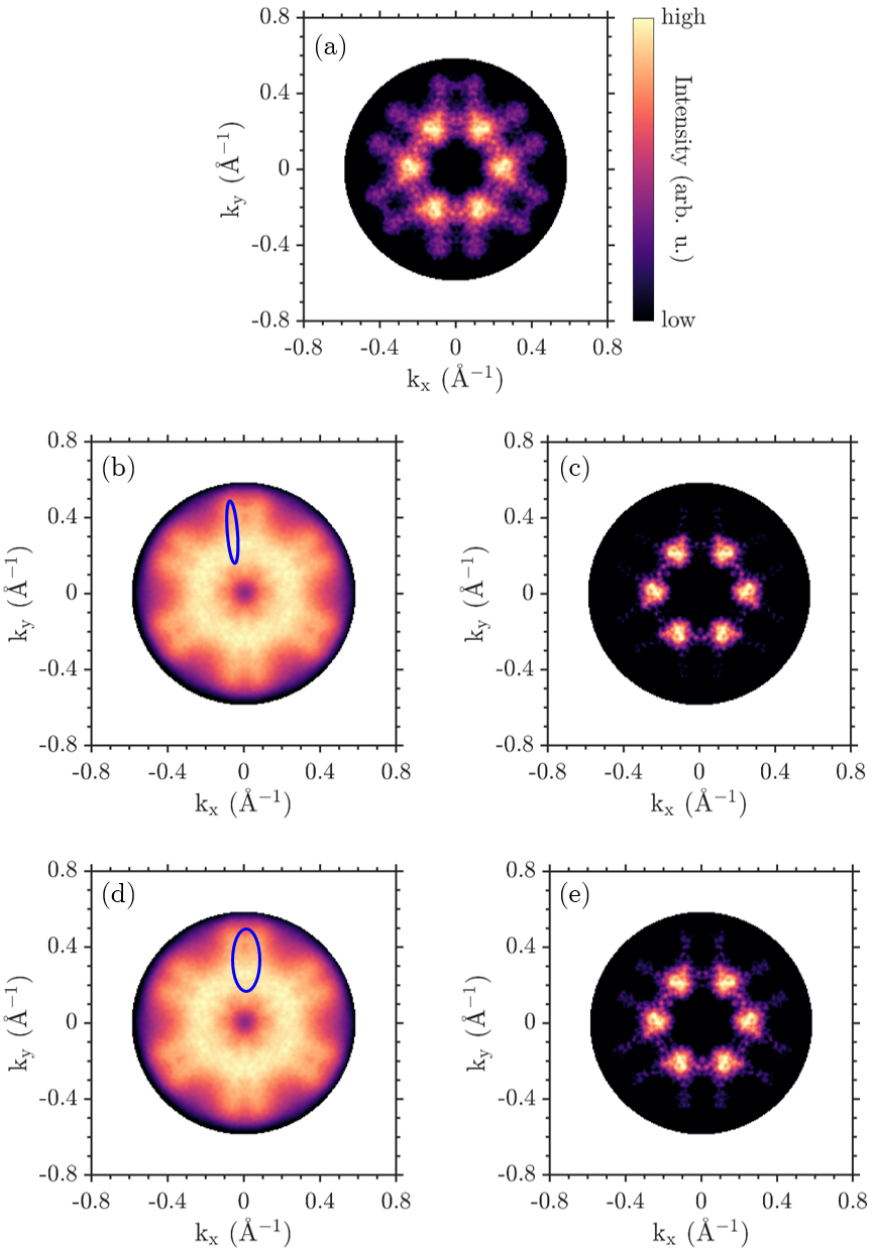

Figure (A.4) A comparison of the different normalization methods tested in the subtraction of the incoherent scattered final state contributions of the S_2 exciton PAD at a delay step of $\Delta t = 1\,\mathrm{ps}$. (a) The resulting CE map for normalizing the individual CE maps in the subtraction approach based on their total intensity. (c, e, g) The resulting CE map for normalizing the individual CE maps in the subtraction approach based on the mean intensity of the selected regions of interest. The corresponding regions of interest are marked in blue in (b, d, f). The normalization to the region of interest in (d) was used in the discussion in Chapter 5.

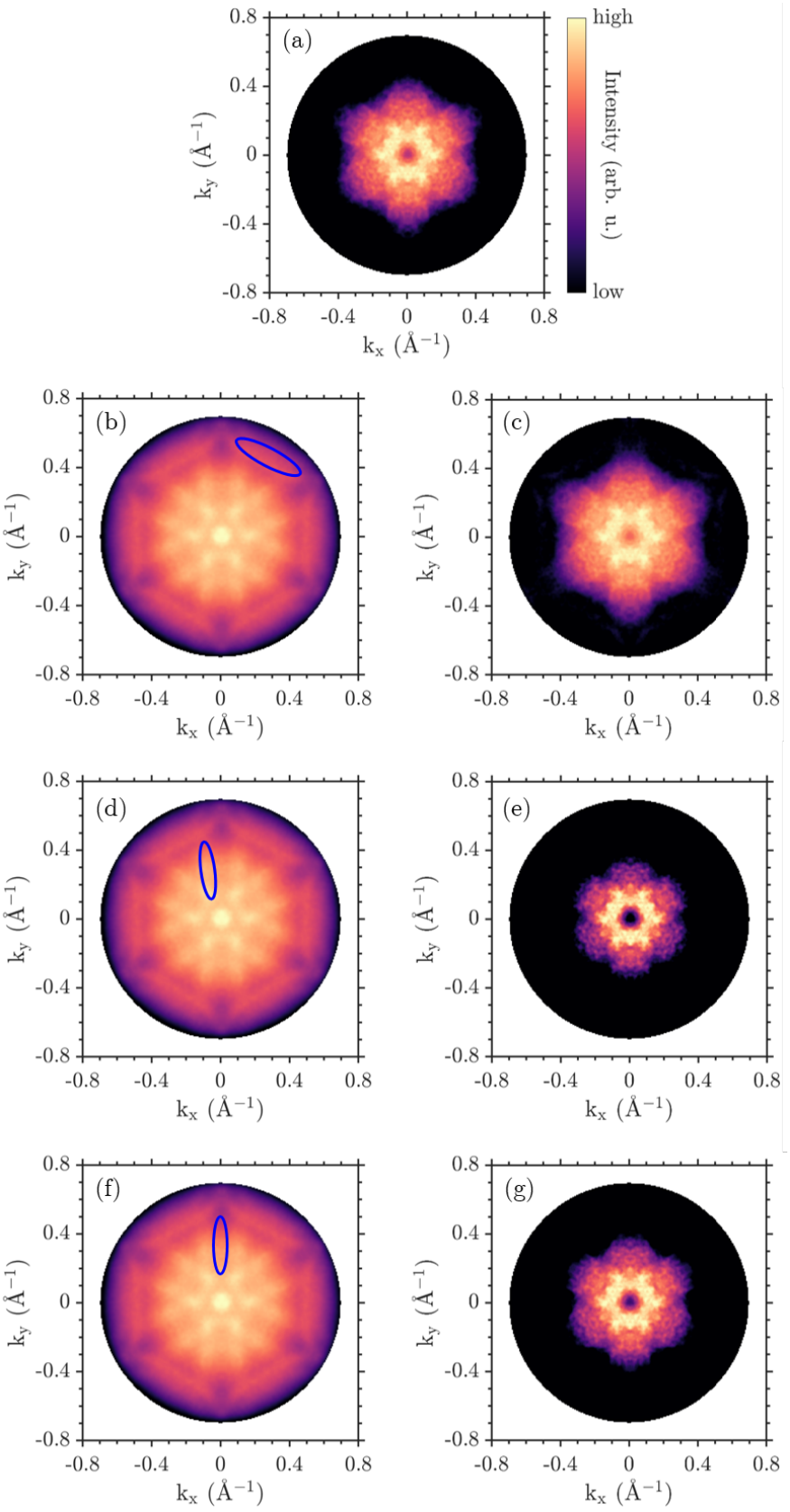

Figure (A.5) A comparison of the different normalization methods tested in the subtraction of the incoherent scattered final state contributions of the S_3 exciton PAD at a delay step of $\Delta t = 0$ fs. (a) The resulting CE map for normalizing the individual CE maps in the subtraction approach based on their total intensity. (c, e, g) The resulting CE map for normalizing the individual CE maps in the subtraction approach based on the mean intensity of the selected regions of interest. The corresponding regions of interest are marked in blue in (b, d, f). The normalization to the total intensity was used in the discussion in Chapter 5.

A.3.2. Replication of the Excitonic Photoemission Angular Distributions

This subsection provides supplementary details on the replication method presented in Section 5.4.3. Figure A.6 (a) shows the replication of the S_2 exciton PAD, similar to Figure 5.1, using smaller Gaussian peaks to estimate the main intensity maxima. The experimental data are depicted on the left and the resulting replica on the right of the CE map. It can be observed that the signatures of the estimate and of the corresponding final state F_2 do not merge into a single circular feature as in Figure 5.1 (d). Figure A.6 (b) shows the corresponding intensity profiles extracted along a circular cut through the main intensity of (a) (indicated by a dashed circle). The intensity profile of the replica reproduces the main oscillations in the experimental data. However, it fails to reproduce the two spikes in each oscillation cycle. The deviation of the replica from the experimental CE map and the different intensity profiles indicate that the widths of the Gaussian peaks used are insufficient to describe the intensity distribution of the S_2 exciton PAD. After testing different Gaussian peak widths, a suitable estimate was found, which is depicted and discussed in Section 5.4.3.

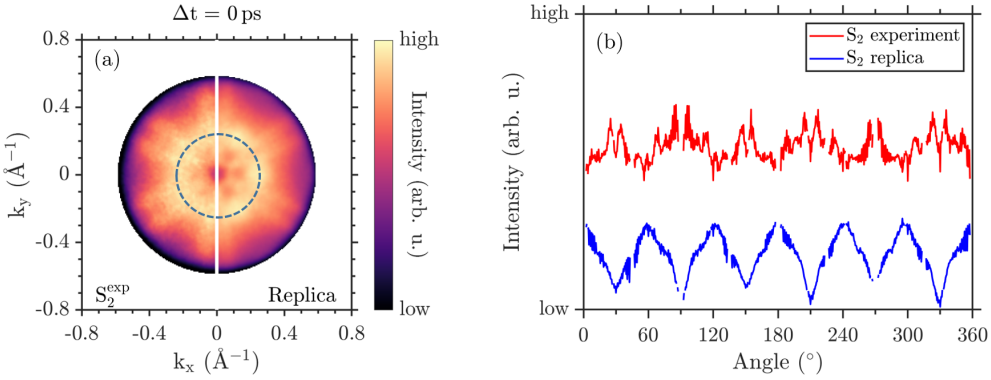

Figure (A.6) Replication of the S_2 exciton PAD using smaller Gaussian peaks for the estimates of the main intensity maxima. (a) The experimental data are depicted in the left half and the resulting replica in the right half of the CE map. The signatures of the estimate and of the final state do not merge. (b) Extracted intensity profiles along a circular cut through the main intensity maxima as sketched in (a) by the dashed circular line. The intensity profile of the replica fails to reproduce the two spikes in every oscillation cycle of the experimental data.

Figure A.7 depicts the replication of the S_3 exciton PAD, similar to Figure 5.3 (e). The experimental data are depicted in the left half and the resulting replica in the right half of the CE map. For this replication, a smaller disc-shaped estimate was used compared to the estimate in Figure 5.3. The width of this estimate corresponds to the extension of the intensity distribution of the S_3 exciton after subtraction of the incoherent final state contributions in Figure A.5 (g). This PAD was created by normalizing the CE maps involved in the subtraction method to the mean intensity of the region of interest in Figure A.5 (f). The thus resulting smaller disc-like estimate leads to a replica in decent agreement with the experimental data. However, the extension of the intensity distribution colored green in Figure A.7 does not match between the replica and the experiment. This indicates that the width of the estimate was too small. Similarly, the extension of the intensity distribution in the CE map in Figure A.5 (g) is too small, indicating that the correct intensity distribution of the S_3 exciton is broader. This demonstrates that the replication approach also validates the normalization method used to subtract incoherent final state contributions.

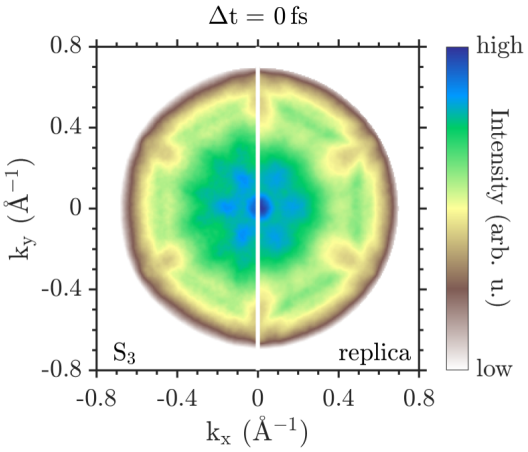

Figure (A.7) Verification of the normalization method via replication of the S_3 exciton PAD. The experimental data are depicted in the left half and the resulting replica in the right half of the CE map. The smaller width of the disc-like estimate used in replication corresponds to the width of the intensity distribution after subtraction of the incoherent final state contributions in Figure A.5 (g). This CE map was created using a normalization to the mean intensity of a region of interest depicted in Figure A.5 (f). The mismatch of the intensity distributions colored green between experiment and replica indicates that the width of the estimate was too small.

A.3.3. Determination of the Temporal Pulse Widths

For a time-resolved investigation of the photoemission angular distributions of excitonic states in C_{60} multilayer films in Section 5.6, the temporal widths of the laser pulses δt used in the pump-probe experiment must be determined. Therefore, the autocorrelation of the pump beam was measured using the Shockley surface state of a clean Cu(111) surface. The data were fitted using a sech^2-function (see Figure A.8 (a)) that yielded a temporal pulse width of $\delta \mathrm{t}_{\mathrm{pump}} = 94\,\mathrm{fs}$. The determination of the error bounds is omitted because the error in the determination of the temporal width of the probe pulses is much larger and thus defines the temporal resolution of the two-color pump-pulse experiment.
The temporal pulse width of the fourth harmonic probe pulses ($h\nu = 5.9\,\mathrm{eV}$) was determined on the C_{60} multilayer film sample as a system with a high work function is required. The S_3 excitonic state was used as an intermediate state and excited by the second harmonic pump pulses ($h\nu = 2.95\,\mathrm{eV}$, $\delta \mathrm{t}_{\mathrm{pump}} = 94\,\mathrm{fs}$). The experimental data shown in Figure A.8 (b) were fitted using a convolution of the pump pulse intensity $I_{\mathrm{pump}}(t)$ with a Green's function $G(t, T_{S_3})$. The cross-correlation of this convolution and the probe pulse intensity $I_{\mathrm{probe}}(t)$ results in the fit function in Equation A.3.

$$f(\Delta t) = [I_{\mathrm{pump}}(t) \circ G(t, T_{S_3})] \otimes I_{\mathrm{probe}} \tag{A.3}$$

The intensities of both pulses are described by a sech^2-function as in Equation A.4.

$$I(t) = A \cdot sech^2(\frac{t-b}{\delta t}) \tag{A.4}$$

$$G(t, T_{S_3}) = \Theta(t-b) exp(-\frac{t-b}{T_{S_3}}) \tag{A.5}$$

The Green's function in Equation A.5 describes the population of the S_3 exciton with its lifetime T_{S_3}. The pulse duration of the pump pulse and the lifetime of the S_3 exciton were used as fit parameters. The best fit of the experimental data resulted in a temporal width of the probe pulse of $\delta \mathrm{t}_{\mathrm{probe}} = 230 \pm 48\,\mathrm{fs}$. This fit also gave a pulse duration of the pump pulse of $\delta \mathrm{t}_{\mathrm{pump}} = 92\,\mathrm{fs}$, which is consistent with the 94 fs pulse duration found in the

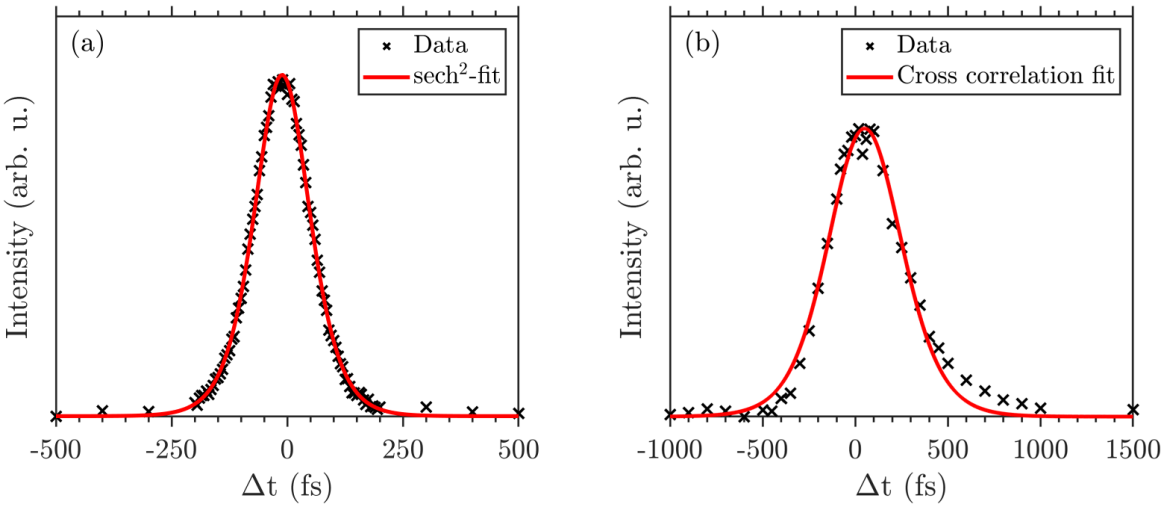

Figure (A.8) Determination of the temporal pulse widths of the pump and probe pulses used in the time-resolved investigation of the excitonic states in C_{60} multilayer films. (a) Autocorrelation of the pump pulses ($h\nu = 2.95\,\mathrm{eV}$). The sech^2-fit results in a temporal pulse width of $\delta t_{\mathrm{pump}} = 94\,\mathrm{fs}$. (b) Cross-correlation of the probe pulses ($h\nu = 5.9\,\mathrm{eV}$). The fit results in a temporal pulse width of $\delta t_{\mathrm{probe}} = 230\,\mathrm{fs}$.

autocorrelation. The lifetime of the S_3 exciton was determined to be $T_{S_3} = 46\,\mathrm{fs}$, which agrees with the lifetime of 45 fs reported in the literature [46]. The poorer agreement of the fit at the tails of the cross-correlation curve may result from a deviation of the laser pulses from a sech^2-shape.

A.4. Artificial Intelligence Tools

For the preparation of this thesis, the artificial intelligence tools ChatGPT and DeepL Write were used for linguistic and grammatical improvements of my own text.

List of Abbreviations

1PPE one-photon photoemission

2PPE two-photon photoemission

3PPE three-photon photoemission

ARPES angle-resolved photoelectron spectroscopy

BSE Bethe-Salpeter-Equation

BZ surface Brillouin zone

CE map constant energy map

CT charge transfer

DFT density functional theory

EDC energy distribution curve

exPOT exciton photoemission orbital tomography

fcc face centered cubic

FWHM full width at half maximum

HB heringbone

HOMO highest occupied molecular orbital

IDEA imaging double energy analyser

LEED low energy electron diffraction

LT low-temperature

LUMO lowest unoccupied molecular orbital

NIXSW normal incident X-ray standing wave

nPPE multi-photon photoemisssion

NTCDA 1,4,5,8-naphtalene-tetracarboxylic-dianhydride

OPO optical parametric oscillator

PAD photoemission angular distribution

PC phthalocyanine

PDOS projected density of states

PEEM photoemission electron microscope

PES photoemission spectroscopy

POT photoemission orbital tomography

PTCDA 3,4,9,10-Perylenetetracarboxilic Dianhydride

RT room temperature

sc simple cubic

SHG second harmonic generation

SPA-LEED spot profile analysis low energy electron diffraction

STM scanning tunneling microscopy

STS scanning tunneling spectroscopy

TCNQ tetracyanoquinodimethane

TDDFT time dependent density functional theory

TI topological insulator

UPS ultraviolet photoelectron spectroscopy

VUV vacuum ultraviolet

List of Figures

Bibliography

[1] Y. Zhou and S. Ramanathan, Critical Reviews in Solid State and Materials Sciences **38**, 286 (2013).

[2] Z.-Q. You and C.-P. Hsu, International Journal of Quantum Chemistry **114**, 102 (2014).

[3] H. Kim, Y. Won, H. W. Song, Y. Kwon, M. Jun, and J. H. Oh, Advanced science (Weinheim, Baden-Wurttemberg, Germany) **11**, e2306191 (2024).

[4] Q. Wang, T. O'Carroll, F. Shi, Y. Huang, G. Chen, X. Yang, A. Nevar, N. Dudko, N. Tarasenko, J. Xie, L. Shi, G. Wu, and D. Zhang, Electrochemical Energy Reviews **7**, 10.1007/s41918-024-00218-9 (2024).

[5] L. Chen, L. Wang, Z. Shuai, and D. Beljonne, The journal of physical chemistry letters **4**, 2158 (2013).

[6] X. Dong, Z. Peng, T. Chen, L. Xu, Z. Ma, G. Liu, K. Cen, Z. Xu, and G. Zhou, Applied Surface Science **561**, 150038 (2021).

[7] G. Pasquale, Z. Sun, K. N. Čerņevičs, R. Perea-Causin, F. Tagarelli, K. Watanabe, T. Taniguchi, E. Malic, O. V. Yazyev, and A. Kis, Nano letters **22**, 8883 (2022).

[8] M. Dvorak, S.-H. Wei, and Z. Wu, Physical Review Letters **110**, 016402 (2013).

[9] M. Grunert, M. Großmann, and E. Runge, Physical Review B **110**, 10.1103/PhysRevB.110.075204 (2024).

[10] A. Chernikov, T. C. Berkelbach, H. M. Hill, A. Rigosi, Y. Li, O. B. Aslan, D. R. Reichman, M. S. Hybertsen, and T. F. Heinz, Physical Review Letters **113**, 076802 (2014).

[11] J. Li, R. Yang, R. Li, and C. P. Grigoropoulos, Adv. Opt. Mater. **13**, 2403137 (2025).

[12] C. Ambrosch-Draxl, K. Hummer, S. Sagmeister, and P. Puschnig, Chemical Physics **325**, 3 (2006).

[13] A. M. Valencia, D. Bischof, S. Anhäuser, M. Zeplichal, A. Terfort, G. Witte, and C. Cocchi, Electronic Structure **5**, 033003 (2023).

[14] R. Temirov, S. Soubatch, A. Luican, and F. S. Tautz, Nature **444**, 350 (2006).

[15] G. Koller, S. Berkebile, M. Oehzelt, P. Puschnig, C. Ambrosch-Draxl, F. P. Netzer, and M. G. Ramsey, Science (New York, N.Y.) **317**, 351 (2007).

[16] T. Ules, D. Lüftner, E. M. Reinisch, G. Koller, P. Puschnig, and M. G. Ramsey, Physical Review B **90**, 10.1103/PhysRevB.90.155430 (2014).

[17] G. Szulczewski, S. Sanvito, and M. Coey, Nature materials **8**, 693 (2009).

[18] S.-i. Machida, Y. Nakayama, S. Duhm, Q. Xin, A. Funakoshi, N. Ogawa, S. Kera, N. Ueno, and H. Ishii, Physical Review Letters **104**, 156401 (2010).

[19] S. Yanagisawa, Y. Morikawa, and A. Schindlmayr, Physical Review B **88**, 10.1103/PhysRevB.88.115438 (2013).

[20] J. Nitta, K. Miwa, N. Komiya, E. Annese, J. Fujii, S. Ono, and K. Sakamoto, Scientific reports **9**, 9645 (2019).

[21] G. Gensterblum, J. Pireaux, P. A. Thiry, R. Caudano, T. Buslaps, R. L. Johnson, G. Le Lay, V. Aristov, R. Günther, A. Taleb-Ibrahimi, G. Indlekofer, and Y. Petroff, Physical Review B **48**, 14756 (1993).

[22] D. W. Latzke, C. Ojeda-Aristizabal, S. M. Griffin, J. D. Denlinger, J. B. Neaton, A. Zettl, and A. Lanzara, Physical Review B **99**, 10.1103/PhysRevB.99.045425 (2019).

[23] N. Haag, D. Lüftner, F. Haag, J. Seidel, L. L. Kelly, G. Zamborlini, M. Jugovac, V. Feyer, M. Aeschlimann, P. Puschnig, M. Cinchetti, and B. Stadtmüller, Physical Review B **101**, 10.1103/PhysRevB.101.165422 (2020).

[24] A. Kraft, R. Temirov, S. K. M. Henze, S. Soubatch, M. Rohlfing, and F. S. Tautz, Physical Review B **74**, 10.1103/PhysRevB.74.041402 (2006).

[25] L. Kilian, A. Hauschild, R. Temirov, S. Soubatch, A. Schöll, A. Bendounan, F. Reinert, T.-L. Lee, F. S. Tautz, M. Sokolowski, and E. Umbach, Physical Review Letters **100**, 136103 (2008).

[26] J. Ziroff, F. Forster, A. Schöll, P. Puschnig, and F. Reinert, Physical Review Letters **104**, 233004 (2010).

[27] A. Tamai, A. P. Seitsonen, F. Baumberger, M. Hengsberger, Z.-X. Shen, T. Greber, and J. Osterwalder, Physical Review B **77**, 10.1103/PhysRevB.77.075134 (2008).

[28] M. Cinchetti, V. A. Dediu, and L. E. Hueso, Nature materials **16**, 507 (2017).

[29] M. Marks, N. L. Zaitsev, B. Schmidt, C. H. Schwalb, A. Schöll, I. A. Nechaev, P. M. Echenique, E. V. Chulkov, and U. Höfer, Physical Review B **84**, 10.1103/PhysRevB.84.081301 (2011).

[30] N. Armbrust, F. Schiller, J. Güdde, and U. Höfer, Scientific reports **7**, 46561 (2017).

[31] A. Thomas, T. Leoni, O. Siri, C. Becker, M. Unzog, C. Kern, P. Puschnig, and P. Zeppenfeld, Physical Chemistry Chemical Physics **24**, 9118 (2022).

[32] P. Puschnig, S. Berkebile, A. J. Fleming, G. Koller, K. Emtsev, T. Seyller, J. D. Riley, C. Ambrosch-Draxl, F. P. Netzer, and M. G. Ramsey, Science (New York, N.Y.) **326**, 702 (2009).

[33] D. Lüftner, S. Weiß, X. Yang, P. Hurdax, V. Feyer, A. Gottwald, G. Koller, S. Soubatch, P. Puschnig, M. G. Ramsey, and F. S. Tautz, Physical Review B **96**, 10.1103/PhysRevB.96.125402 (2017).

[34] C. S. Kern, A. Windischbacher, and P. Puschnig, Physical Review B **108**, 10.1103/PhysRevB.108.085132 (2023).

[35] M. Reutzel, G. S. M. Jansen, and S. Mathias, Advances in Physics: X **9**, 10.1080/23746149.2024.2378722 (2024).

[36] H. Lüth, *Solid Surfaces, Interfaces and Thin Films*, fourth, revised and extended edition ed., Advanced Texts in Physics (Springer, Berlin and Heidelberg, 2001).

[37] L. Lyu, *Quantum engineering in two-dimensional organic porous networks*, Dissertation, RPTU Kaiserslautern-Landau, Kaiserslautern (2023).

[38] M. P. Seah and W. A. Dench, Surface and Interface Analysis **1**, 2 (1979).

[39] G. Ertl, R. Gomer, M. A. van Hove, W. H. Weinberg, and C.-M. Chan, *Low-Energy Electron Diffraction*, Vol. 6 (Springer Berlin Heidelberg, Berlin, Heidelberg, 1986).

[40] H. Hertz, Annalen der Physik **267**, 983 (1887).

[41] W. Hallwachs, Annalen der Physik **269**, 301 (1888).

[42] A. Einstein, Annalen der Physik **322**, 132 (1905).

[43] H. Ishii, K. Kudo, T. Nakayama, and N. Ueno, *Electronic Processes in Organic Electronics*, Vol. 209 (Springer Japan, Tokyo, 2015).

[44] S. Hüfner, *Photoelectron Spectroscopy: Principles and Applications*, third revised and enlarged edition ed., Advanced Texts in Physics (Springer, Berlin and Heidelberg, 2003).

[45] I. Fernández Torrente, K. J. Franke, and J. Ignacio Pascual, Journal of Physics: Condensed Matter **20**, 184001 (2008).

[46] B. Stadtmüller, S. Emmerich, D. Jungkenn, N. Haag, M. Rollinger, S. Eich, M. Maniraj, M. Aeschlimann, M. Cinchetti, and S. Mathias, Nature communications **10**, 1470 (2019).

[47] N. Haag, *Exploring the Potential of 3D Molecules for Orbital Tomography*, Dissertation, Technische Universität Kaiserslautern, Kaiserslautern (2017).

[48] T. Eul, *Polarization-dependent photoelectron momentum distributions from interband transitions at nobel metal surfaces*, Dissertation, RPTU Kaiserslautern-Landau, Kaiserslautern (2021).

[49] E. Noether, in *Gesammelte Abhandlungen - Collected Papers*, Springer Collected Works in Mathematics, edited by E. Noether and N. Jacobson (Springer Berlin Heidelberg, Berlin, Heidelberg, 1983) pp. 231–239.

[50] A. Damascelli, Physica Scripta **T109**, 61 (2004).

[51] J. W. Gadzuk, Physical Review B **10**, 5030 (1974).

[52] P. Puschnig, E.-M. Reinisch, T. Ules, G. Koller, S. Soubatch, M. Ostler, L. Romaner, F. S. Tautz, C. Ambrosch-Draxl, and M. G. Ramsey, Physical Review B **84**, 10.1103/PhysRevB.84.235427 (2011).

[53] B. Stadtmüller, M. Willenbockel, E. M. Reinisch, T. Ules, F. C. Bocquet, S. Soubatch, P. Puschnig, G. Koller, M. G. Ramsey, F. S. Tautz, and C. Kumpf, EPL (Europhysics Letters) **100**, 26008 (2012).

[54] H. Offenbacher, D. Lüftner, T. Ules, E. M. Reinisch, G. Koller, P. Puschnig, and M. G. Ramsey, Journal of Electron Spectroscopy and Related Phenomena **204**, 92 (2015).

[55] P. Puschnig and D. Lüftner, Journal of Electron Spectroscopy and Related Phenomena **200**, 193 (2015).

[56] S. Weiß, D. Lüftner, T. Ules, E. M. Reinisch, H. Kaser, A. Gottwald, M. Richter, S. Soubatch, G. Koller, M. G. Ramsey, F. S. Tautz, and P. Puschnig, Nature communications **6**, 8287 (2015).

[57] M. Hollerer, D. Lüftner, P. Hurdax, T. Ules, S. Soubatch, F. S. Tautz, G. Koller, P. Puschnig, M. Sterrer, and M. G. Ramsey, ACS nano **11**, 6252 (2017).

[58] C. Udhardt, F. Otto, C. Kern, D. Lüftner, T. Huempfner, T. Kirchhuebel, F. Sojka, M. Meissner, B. Schröter, R. Forker, P. Puschnig, and T. Fritz, The Journal of Physical Chemistry C **121**, 12285 (2017).

[59] P. Puschnig and M. G. Ramsey, in *Encyclopedia of Interfacial Chemistry* (Elsevier, 2018) pp. 380–391.

[60] X. Yang, I. Krieger, D. Lüftner, S. Weiß, T. Heepenstrick, M. Hollerer, P. Hurdax, G. Koller, M. Sokolowski, P. Puschnig, M. G. Ramsey, F. S. Tautz, and S. Soubatch, Chemical communications (Cambridge, England) **54**, 9039 (2018).

[61] L. Egger, B. Kollmann, P. Hurdax, D. Lüftner, X. Yang, S. Weiss, A. Gottwald, M. Richter, G. Koller, S. Soubatch, F. S. Tautz, P. Puschnig, and M. G. Ramsey, New Journal of Physics **21**, 043003 (2019).

[62] X. Yang, L. Egger, P. Hurdax, H. Kaser, D. Lüftner, F. C. Bocquet, G. Koller, A. Gottwald, P. Tegeder, M. Richter, M. G. Ramsey, P. Puschnig, S. Soubatch, and F. S. Tautz, Nature communications **10**, 3189 (2019).

[63] C. Metzger, M. Graus, M. Grimm, G. Zamborlini, V. Feyer, M. Schwendt, D. Lüftner, P. Puschnig, A. Schöll, and F. Reinert, Physical Review B **101**, 10.1103/PhysRevB.101.165421 (2020).

[64] R. Wallauer, M. Raths, K. Stallberg, L. Münster, D. Brandstetter, X. Yang, J. Güdde, P. Puschnig, S. Soubatch, C. Kumpf, F. C. Bocquet, F. S. Tautz, and U. Höfer, Science (New York, N.Y.) **371**, 1056 (2021).

[65] T. G. Boné, A. Windischbacher, M. S. Sättele, K. Greulich, L. Egger, T. Jauk, F. Lackner, H. F. Bettinger, H. Peisert, T. Chassé, M. G. Ramsey, M. Sterrer, G. Koller, and P. Puschnig, The Journal of Physical Chemistry C **125**, 9129 (2021).

[66] C. S. Kern, A. Haags, L. Egger, X. Yang, H. Kirschner, S. Wolff, T. Seyller, A. Gottwald, M. Richter, U. de Giovannini, A. Rubio, M. G. Ramsey, F. C. Bocquet, S. Soubatch, F. S. Tautz, P. Puschnig, and S. Moser, Physical Review Research **5**, 10.1103/PhysRevResearch.5.033075 (2023).

[67] W. Bennecke, A. Windischbacher, D. Schmitt, J. P. Bange, R. Hemm, C. S. Kern, G. D'Avino, X. Blase, D. Steil, S. Steil, M. Aeschlimann, B. Stadtmüller, M. Reutzel, P. Puschnig, G. S. M. Jansen, and S. Mathias, Nature communications **15**, 1804 (2024).

[68] A. Liebsch, Physical Review Letters **32**, 1203 (1974).

[69] J. W. Gadzuk, Surface Science **53**, 132 (1975).

[70] A. Liebsch, Physical Review B **13**, 544 (1976).

[71] M. Bovet, V. N. Strocov, F. Clerc, C. Koitzsch, D. Naumović, and P. Aebi, Physical review letters **93**, 107601 (2004).

[72] G. Wan, A. Croot, N. A. Fox, and M. Cattelan, Advanced Functional Materials **31**, 2007319 (2021).

[73] M. Escher, N. Weber, M. Merkel, C. Ziethen, P. Bernhard, G. Schönhense, S. Schmidt, F. Forster, F. Reinert, B. Krömker, and D. Funnemann, Journal of Physics: Condensed Matter **17**, S1329 (2005).

[74] B. Krömker, M. Escher, D. Funnemann, D. Hartung, H. Engelhard, and J. Kirschner, The Review of scientific instruments **79**, 053702 (2008).

[75] H. Ibach, ed., *Electron Spectroscopy for Surface Analysis*, Topics in Current Physics (Springer Berlin Heidelberg, Berlin, Heidelberg, 1977).

[76] F. Haag, T. Eul, P. Thielen, N. Haag, B. Stadtmüller, and M. Aeschlimann, The Review of scientific instruments **90**, 103104 (2019).

[77] FOCUS GmbH, VUV Source HIS 13 / HIS 14 HD and HIS Mono: Instructional Manual: Version 3.4 (2018).

[78] S.-P. MKS Instruments, Mai-Tai-Datasheet (10.2023).

[79] KMLABS, km_labs_Giffin_datasheet_180125.

[80] S.-P. MKS Instruments, Inspire-Datasheet (07.2024).

[81] A. M. Bradshaw and D. P. Woodruff, New Journal of Physics **17**, 013033 (2015).

[82] R. J. Smith, J. Anderson, and G. J. Lapeyre, Physical Review Letters **37**, 1081 (1976).

[83] C. Schott, *Tailoring geometric and electronic properties of a molecule-metal interface by utilization of 2D-materials*, Dissertation, RPTU Kaiserslautern-Landau, Kaiserslautern (25.07.2024).

[84] S. Hasegawa, T. Miyamae, K. Yakushi, H. Inokuchi, K. Seki, and N. Ueno, Physical Review B **58**, 4927 (1998).

[85] M. Bauer, A. Marienfeld, and M. Aeschlimann, Progress in Surface Science **90**, 319 (2015).

[86] M. Weinelt, Journal of Physics: Condensed Matter **14**, R1099 (2002).

[87] H. Ueba and B. Gumhalter, Progress in Surface Science **82**, 193 (2007).

[88] D. Velic, E. Knoesel, and M. Wolf, Surface Science **424**, 1 (1999).

[89] A. C. Rosenfeldt, B. Göhler, and H. Zacharias, The Journal of chemical physics **133**, 234704 (2010).

[90] E. Umbach, Progress in Surface Science **35**, 113 (1990).

[91] S. R. Forrest, Chemical reviews **97**, 1793 (1997).

[92] F. S. Tautz, Progress in Surface Science **82**, 479 (2007).

[93] K. Stallberg, A. Namgalies, S. Chatterjee, and U. Höfer, The Journal of Physical Chemistry C **126**, 12728 (2022).

[94] F. Ling, Q. Du, Y. Zhang, X. Zheng, A. Wang, C. Zhu, W. Wang, F. Wang, and S. Qin, Organic Electronics **124**, 106942 (2024).

[95] D. Kumar, M. Hendy, J. Hellerstedt, J. Hewes, S. Kolomoisky, C. Krull, and A. Schiffrin, The Journal of Physical Chemistry C **128**, 1404 (2024).

[96] A. Jeindl, J. Domke, L. Hörmann, F. Sojka, R. Forker, T. Fritz, and O. T. Hofmann, ACS nano **15**, 6723 (2021).

[97] C. Zwick, A. Baby, M. Gruenewald, E. Verwüster, O. T. Hofmann, R. Forker, G. Fratesi, G. P. Brivio, E. Zojer, and T. Fritz, ACS nano **10**, 2365 (2016).

[98] A. Baby, M. Gruenewald, C. Zwick, F. Otto, R. Forker, G. van Straaten, M. Franke, B. Stadtmüller, C. Kumpf, G. P. Brivio, G. Fratesi, T. Fritz, and E. Zojer, ACS nano **11**, 10495 (2017).

[99] C. Zwick, M. Meissner, F. Sojka, R. Forker, and T. Fritz, Physical Review Materials **3**, 10.1103/PhysRevMaterials.3.085604 (2019).

[100] K. Glöckler, C. Seidel, A. Soukopp, M. Sokolowski, E. Umbach, M. Böhringer, R. Berndt, and W.-D. Schneider, Surface Science **405**, 1 (1998).

[101] B. Krause, A. C. Dürr, K. Ritley, F. Schreiber, H. Dosch, and D. Smilgies, Physical Review B **66**, 10.1103/PhysRevB.66.235404 (2002).

[102] L. Kilian, E. Umbach, and M. Sokolowski, Surface Science **573**, 359 (2004).

[103] Y. Zou, L. Kilian, A. Schöll, T. Schmidt, R. Fink, and E. Umbach, Surface Science **600**, 1240 (2006).

[104] M. Rohlfing, R. Temirov, and F. S. Tautz, Physical Review B **76**, 10.1103/PhysRevB.76.115421 (2007).

[105] L. Romaner, D. Nabok, P. Puschnig, E. Zojer, and C. Ambrosch-Draxl, New Journal of Physics **11**, 053010 (2009).

[106] A. Hauschild, R. Temirov, S. Soubatch, O. Bauer, A. Schöll, B. C. C. Cowie, T.-L. Lee, F. S. Tautz, and M. Sokolowski, Physical Review B **81**, 10.1103/PhysRevB.81.125432 (2010).

[107] E. Umbach, K. Glöckler, and M. Sokolowski, Surface Science **402-404**, 20 (1998).

[108] F. Würthner, Chemical communications (Cambridge, England) , 1564 (2004).

[109] B. Stadtmüller, *Study of intermolecular interactions in hetero-organic thin films: Zugl.: Aachen, Techn. Hochsch., Diss., 2013*, Schriften des Forschungszentrums Jülich Reihe Schlüsseltechnologien, Vol. Bd. 61 (Forschungszentrum Jülich, Jülich, 2013).

[110] H. Marchetto, U. Groh, T. Schmidt, R. Fink, H.-J. Freund, and E. Umbach, Chemical Physics **325**, 178 (2006).

[111] O. Bauer, G. Mercurio, M. Willenbockel, W. Reckien, C. Heinrich Schmitz, B. Fiedler, S. Soubatch, T. Bredow, F. S. Tautz, and M. Sokolowski, Physical Review B **86**, 10.1103/PhysRevB.86.235431 (2012).

[112] M. Willenbockel, D. Lüftner, B. Stadtmüller, G. Koller, C. Kumpf, S. Soubatch, P. Puschnig, M. G. Ramsey, and F. S. Tautz, Physical Chemistry Chemical Physics **17**, 1530 (2015).

[113] M. Willenbockel, B. Stadtmüller, K. Schönauer, F. C. Bocquet, D. Lüftner, E. M. Reinisch, T. Ules, G. Koller, C. Kumpf, S. Soubatch, P. Puschnig, M. G. Ramsey, and F. S. Tautz, New Journal of Physics **15**, 033017 (2013).

[114] J. Wuesten, C. Ziegler, and T. Ertl, Physical Review B **74**, 10.1103/PhysRevB.74.125205 (2006).

[115] F. S. Tautz, M. Eremtchenko, J. A. Schaefer, M. Sokolowski, V. Shklover, and E. Umbach, Physical Review B **65**, 10.1103/PhysRevB.65.125405 (2002).

[116] J. Wüsten, K. Heimer, S. Lach, and C. Ziegler, Journal of Applied Physics **102**, 023708 (2007).

[117] J. Wüsten, S. Berger, K. Heimer, S. Lach, and C. Ziegler, Journal of Applied Physics **98**, 10.1063/1.1935763 (2005).

[118] E. Annese, J. Fujii, I. Vobornik, and G. Rossi, The Journal of Physical Chemistry C **116**, 2382 (2012).

[119] F. Bussolotti, S. Kera, and N. Ueno, Physical Review B **86**, 10.1103/PhysRevB.86.155120 (2012).

[120] Y. Hasegawa, Y. Yamada, and M. Sasaki, The Journal of Physical Chemistry C **118**, 24490 (2014).

[121] S. S. Batsanov, Inorganic Materials **37**, 871 (2001).

[122] L. H. Ahrens, Geochimica et Cosmochimica Acta **2**, 155 (1952).

[123] J. L. Bredas and G. B. Street, Accounts of chemical research **18**, 309 (1985).

[124] M. Wießner, D. Hauschild, A. Schöll, F. Reinert, V. Feyer, K. Winkler, and B. Krömker, Physical Review B **86**, 10.1103/PhysRevB.86.045417 (2012).

[125] J. Felter, M. Franke, J. Wolters, C. Henneke, and C. Kumpf, Nanoscale **11**, 1798 (2019).

[126] R. C. Haddon, A. F. Hebard, M. J. Rosseinsky, D. W. Murphy, S. J. Duclos, K. B. Lyons, B. Miller, J. M. Rosamilia, R. M. Fleming, A. R. Kortan, S. H. Glarum, A. V. Makhija, A. J. Muller, R. H. Eick, S. M. Zahurak, R. Tycko, G. Dabbagh, and F. A. Thiel, Nature **350**, 320 (1991).

[127] R. C. Haddon, Accounts of chemical research **25**, 127 (1992).

[128] O. Gunnarsson, Nature materials **7**, 176 (2008).

[129] J. Wüsten, S. Berger, M. Salomo, A. Mönnich, M. Bauer, S. Lach, M. Aeschlimann, and C. Ziegler, Physical Review B **78**, 10.1103/PhysRevB.78.195326 (2008).

[130] T. Dienel, A. Krause, R. Alle, R. Forker, K. Meerholz, and T. Fritz, Advanced materials (Deerfield Beach, Fla.) **22**, 4064 (2010).

[131] P. J. Blowey, B. Sohail, L. A. Rochford, T. Lafosse, D. A. Duncan, P. T. P. Ryan, D. A. Warr, T.-L. Lee, G. Costantini, R. J. Maurer, and D. P. Woodruff, ACS nano **14**, 7475 (2020).

[132] G. Hlawacek, F. S. Khokhar, R. van Gastel, B. Poelsema, and C. Teichert, Nano letters **11**, 333 (2011).

[133] A. J. Martínez-Galera and J. M. Gómez-Rodríguez, The Journal of Physical Chemistry C **115**, 23036 (2011).

[134] T. Bathon, P. Sessi, K. A. Kokh, O. E. Tereshchenko, and M. Bode, Nano letters **15**, 2442 (2015).

[135] A. .2018Della Pia, S. Lisi, O. de Luca, D. A. Warr, J. Lawrence, M. M. Otrokov, Z. S. Aliev, E. V. Chulkov, R. G. Agostino, A. Arnau, M. Papagno, and G. Costantini, Chemphyschem : a European journal of chemical physics and physical chemistry **19**, 2405 (2018).

[136] M. G. Cuxart, M. A. Valbuena, R. Robles, C. Moreno, F. Bonell, G. Sauthier, I. Imaz, H. Xu, C. Nistor, A. Barla, P. Gargiani, M. Valvidares, D. Maspoch, P. Gambardella, S. O. Valenzuela, and A. Mugarza, ACS nano **14**, 6285 (2020).

[137] H.-H. Yang, Y.-H. Chu, C.-I. Lu, C. J. Butler, R. Sankar, F.-C. Chou, and M.-T. Lin, Nano letters **15**, 6896 (2015).

[138] S. Sarkar, J. Yang, L. Z. Tan, A. M. Rappe, and L. Kronik, Chemistry of Materials **30**, 1849 (2018).

[139] B. Yan, B. Stadtmüller, N. Haag, S. Jakobs, J. Seidel, D. Jungkenn, S. Mathias, M. Cinchetti, M. Aeschlimann, and C. Felser, Nature communications **6**, 10167 (2015).

[140] M. M. Otrokov, E. V. Chulkov, and A. Arnau, Physical Review B **92**, 10.1103/PhysRevB.92.165309 (2015).

[141] M. Caputo, M. Panighel, S. Lisi, L. Khalil, G. Di Santo, E. Papalazarou, A. Hruban, M. Konczykowski, L. Krusin-Elbaum, Z. S. Aliev, M. B. Babanly, M. M. Otrokov, A. Politano, E. V. Chulkov, A. Arnau, V. Marinova, P. K. Das, J. Fujii, I. Vobornik, L. Perfetti, A. Mugarza, A. Goldoni, and M. Marsi, Nano letters **16**, 3409 (2016).

[142] W. W. Pai, H. T. Jeng, C.-M. Cheng, C.-H. Lin, X. Xiao, A. Zhao, X. Zhang, G. Xu, X. Q. Shi, M. A. van Hove, C.-S. Hsue, and K.-D. Tsuei, Physical Review Letters **104**, 036103 (2010).

[143] L. Forcieri, S. Taylor, P. Moriarty, and S. P. Jarvis, Physical Review B **104**, 10.1103/PhysRevB.104.205428 (2021).

[144] E. Osawa, Kagaku , 854 (1970).

[145] H. W. Kroto, J. R. Heath, S. C. O'Brien, R. F. Curl, and R. E. Smalley, Nature **318**, 162 (1985).

[146] R. E. Haufler, J. Conceicao, L. P. F. Chibante, Y. Chai, N. E. Byrne, S. Flanagan, M. M. Haley, S. C. O'Brien, C. Pan, and et al., The Journal of Physical Chemistry **94**, 8634 (1990).

[147] R. D. Johnson, D. S. Bethune, and C. S. Yannoni, Accounts of chemical research **25**, 169 (1992).

[148] R. D. Johnson, G. Meijer, and D. S. Bethune, Journal of the American Chemical Society **112**, 8983 (1990).

[149] M. S. Dresselhaus, *Science of fullerenes and carbon nanotubes* (Academic Press, San Diego, 1996).

[150] C. Kusch, B. Winter, R. Mitzner, A. Gomes Silva, E. Campbell, and I. V. Hertel, Chemical Physics Letters **275**, 469 (1997).

[151] V. Saltas and C. A. Papageorgopoulos, Surface Science **488**, 23 (2001).

[152] P. Puschnig, Organic Molecule Database: a database for molecular orbitals of pi-conjugated organic molecules based on the atomic simulated environment (ASE) ans NWChem as the DFT calculator.

[153] R. C. Haddon, L. E. Brus, and K. Raghavachari, Chemical Physics Letters **125**, 459 (1986).

[154] F. Rioux, Journal of Chemical Education **71**, 464 (1994).

[155] S. Emmerich, S. Hedwig, B. Arnoldi, J. Stöckl, F. Haag, R. Hemm, M. Cinchetti, S. Mathias, B. Stadtmüller, and M. Aeschlimann, The Journal of Physical Chemistry C **124**, 23579 (2020).

[156] X.-Q. Shi, M. A. van Hove, and R.-Q. Zhang, Journal of Materials Science **47**, 7341 (2012).

[157] G. Xu, X.-Q. Shi, R. Q. Zhang, W. W. Pai, H. T. Jeng, and M. A. van Hove, Physical Review B **86**, 10.1103/PhysRevB.86.075419 (2012).

[158] K. Kanai, K. Akaike, K. Koyasu, K. Sakai, T. Nishi, Y. Kamizuru, T. Nishi, Y. Ouchi, and K. Seki, Applied Physics A **95**, 309 (2009).

[159] G. Dutton and X.-Y. Zhu, The journal of physical chemistry. B **106**, 5975 (2002).

[160] F. Baumberger, T. Greber, B. Delley, and J. Osterwalder, Physical Review Letters **88**, 237601 (2002).

[161] X. Yang, M. Jugovac, G. Zamborlini, V. Feyer, G. Koller, P. Puschnig, S. Soubatch, M. G. Ramsey, and F. S. Tautz, Nature communications **13**, 5148 (2022).

[162] D. Brandstetter, X. Yang, D. Lüftner, F. S. Tautz, and P. Puschnig, Computer Physics Communications **263**, 107905 (2021).

[163] S. Gärtner, B. Fiedler, O. Bauer, A. Marele, and M. M. Sokolowski, Beilstein journal of organic chemistry **10**, 2055 (2014).

[164] S. Weiß, I. Krieger, T. Heepenstrick, S. Soubatch, M. Sokolowski, and F. S. Tautz, Physical Review B **96**, 10.1103/PhysRevB.96.075414 (2017).

[165] G. Kresse and J. Hafner, Physical Review B **47**, 558 (1993).

[166] G. Kresse and D. Joubert, Physical Review B **59**, 1758 (1999).

[167] J. P. Perdew, K. Burke, and M. Ernzerhof, Physical Review Letters **77**, 3865 (1996).

[168] S. Grimme, J. Antony, S. Ehrlich, and H. Krieg, The Journal of chemical physics **132**, 154104 (2010).

[169] P. E. Blöchl, Physical Review B **50**, 17953 (1994).

[170] J. Neugebauer and M. Scheffler, Physical Review B **46**, 16067 (1992).

[171] P. J. Feibelman and D. E. Eastman, Physical Review B **10**, 4932 (1974).

[172] S. Kümmel and L. Kronik, Reviews of Modern Physics **80**, 3 (2008).

[173] M. Dauth, T. Körzdörfer, S. Kümmel, J. Ziroff, M. Wiessner, A. Schöll, F. Reinert, M. Arita, and K. Shimada, Physical Review Letters **107**, 193002 (2011).

[174] D. Lüftner, S. Refaely-Abramson, M. Pachler, R. Resel, M. G. Ramsey, L. Kronik, and P. Puschnig, Physical Review B **90**, 10.1103/PhysRevB.90.075204 (2014).

[175] Jost, Troullier, Poirier, Martins, Weaver, Chibante, and Smalley, Physical Review B **44**, 1966 (1991).

[176] K. Schubert, A. Damm, S. V. Eremeev, M. Marks, M. Shibuta, W. Berthold, J. Güdde, A. G. Borisov, S. S. Tsirkin, E. V. Chulkov, and U. Höfer, Physical Review B **85**, 10.1103/PhysRevB.85.205431 (2012).

[177] K.-D. Tsuei, J.-Y. Yuh, C.-T. Tzeng, R.-Y. Chu, S.-C. Chung, and K.-L. Tsang, Physical Review B **56**, 15412 (1997).

[178] K.-D. Tsuei and P. D. Johnson, Solid State Communications **101**, 337 (1997).

[179] C.-T. Tzeng, W.-S. Lo, J.-Y. Yuh, R.-Y. Chu, and K.-D. Tsuei, Physical Review B **61**, 2263 (2000).

[180] K. Rothe, A. Mehler, N. Néel, and J. Kröger, Beilstein journal of nanotechnology **11**, 1157 (2020).

[181] J. Seidel, L. L. Kelly, M. Franke, G. van Straaten, C. Kumpf, M. Cinchetti, M. Aeschlimann, and B. Stadtmüller, Physical Review B **98**, 10.1103/PhysRevB.98.085434 (2018).

[182] G. Lanzani, *The photophysics behind photovoltaics and photonics*, online-ausg ed. (Wiley-VCH, Weinheim, 2012).

[183] C. J. Bardeen, Annual review of physical chemistry **65**, 127 (2014).

[184] X.-Y. Zhu, The journal of physical chemistry letters **5**, 2283 (2014).

[185] X.-Y. Zhu, Journal of Electron Spectroscopy and Related Phenomena **204**, 75 (2015).

[186] A. S. Davydov, Soviet Physics Uspekhi **7**, 145 (1964).

[187] W. Y. Liang, Physics Education **5**, 226 (1970).

[188] B. Pac, P. Petelenz, A. Eilmes, and R. W. Munn, The Journal of chemical physics **109**, 7923 (1998).

[189] R. Schuster, M. Knupfer, and H. Berger, Physical Review Letters **98**, 037402 (2007).

[190] J. Tanaka, Bulletin of the Chemical Society of Japan **36**, 1237 (1963).

[191] M. C. Cottin, J. Lobo-Checa, J. Schaffert, C. A. Bobisch, R. Möller, J. E. Ortega, and A. L. Walter, New Journal of Physics **16**, 045002 (2014).

[192] P. Merino, C. Große, A. Rosławska, K. Kuhnke, and K. Kern, Nature communications **6**, 8461 (2015).

[193] P. A. Heiney, J. E. Fischer, A. R. McGhie, W. J. Romanow, Denenstein, McCauley, A. B. Smith, and Cox, Physical Review Letters **66**, 2911 (1991).

[194] J. R. D. Copley, W. I. F. David, and D. A. Neumann, Neutron News **4**, 20 (1993).

[195] W. I. F. David, R. M. Ibberson, J. C. Matthewman, K. Prassides, T. J. S. Dennis, J. P. Hare, H. W. Kroto, R. Taylor, and D. R. M. Walton, Nature **353**, 147 (1991).

[196] W. I. F. David, R. M. Ibberson, T. J. S. Dennis, J. P. Hare, and K. Prassides, EPL (Europhysics Letters) **18**, 219 (1992).

[197] H. Wang, C. Zeng, B. Wang, J. G. Hou, Q. Li, and J. Yang, Physical Review B **63**, 10.1103/PhysRevB.63.085417 (2001).

[198] H. Ding, C. Reese, A. J. Mäkinen, Z. Bao, and Y. Gao, Applied Physics Letters **96**, 10.1063/1.3446849 (2010).

[199] P. J. Benning, C. G. Olson, D. W. Lynch, and J. H. Weaver, Physical Review B **50**, 11239 (1994).

[200] G. Gensterblum, Journal of Electron Spectroscopy and Related Phenomena **81**, 89 (1996).

[201] M. Shibuta, K. Yamamoto, T. Ohta, M. Nakaya, T. Eguchi, and A. Nakajima, Scientific reports **6**, 35853 (2016).

[202] S. Link, A. Scholl, R. Jacquemin, and W. Eberhardt, Solid State Communications **113**, 689 (2000).

[203] R. W. Lof, M. A. van Veenendaal, B. Koopmans, H. T. Jonkman, and G. A. Sawatzky, Physical Review Letters **68**, 3924 (1992).

[204] M. Shibuta, K. Yamagiwa, T. Eguchi, and A. Nakajima, Applied Physics Letters **109**, 10.1063/1.4967380 (2016).

[205] J. P. Long, S. J. Chase, and M. N. Kabler, Chemical Physics Letters **347**, 29 (2001).

[206] K. Kuhnke, R. Becker, and K. Kern, Chemical Physics Letters **257**, 569 (1996).

[207] R. Jacquemin, S. Kraus, and W. Eberhardt, Solid State Communications **105**, 449 (1998).

[208] P. He, S. Bao, C. Yu, and Y. Xu, Surface Science **328**, 287 (1995).

[209] E. L. Shirley, L. X. Benedict, and S. G. Louie, Physical Review B **54**, 10970 (1996).

[210] V. N. Strocov, H. I. Starnberg, and P. O. Nilsson, Physical Review B **56**, 1717 (1997).

[211] V. N. Strocov, H. I. Starnberg, P. O. Nilsson, H. E. Brauer, and L. J. Holleboom, Physical Review Letters **79**, 467 (1997).

[212] Benning, Poirier, Troullier, Martins, Weaver, Haufler, Chibante, and Smalley, Physical Review B **44**, 1962 (1991).

[213] M. Causa', I. Ramirez, J. F. Martinez Hardigree, M. Riede, and N. Banerji, The journal of physical chemistry letters **9**, 1885 (2018).

[214] L. Kjeldgaard, T. Käämbre, J. Schiessling, I. Marenne, J. N. O'Shea, J. Schnadt, C. J. Glover, M. Nagasono, D. Nordlund, M. G. Garnier, L. Qian, J.-E. Rubensson, P. Rudolf, N. Mårtensson, J. Nordgren, and P. A. Brühwiler, Physical Review B **72**, 10.1103/PhysRevB.72.205414 (2005).

[215] K. Tvingstedt, J. Benduhn, and K. Vandewal, Materials Horizons **7**, 1888 (2020).

[216] M. Graus, M. Grimm, C. Metzger, M. Dauth, C. Tusche, J. Kirschner, S. Kümmel, A. Schöll, and F. Reinert, Physical review letters **116**, 147601 (2016).

[217] P. A. Brühwiler, O. Karis, and N. Mårtensson, Reviews of Modern Physics **74**, 703 (2002).

[218] S. Huant, J. B. Robert, G. Chouteau, P. Bernier, C. Fabre, and A. Rassat, Physical Review Letters **69**, 2666 (1992).

[219] A. Kolmakov, V. Stankevitch, N. Svechnikov, P. Dudin, N. Artemev, H. Berger, G. Clerc, G. Margaritondo, M. Kamada, S. Hirose, K. Kanno, I. Akimoto, and T. Matsumoto, Journal of Electron Spectroscopy and Related Phenomena **78**, 449 (1996).

[220] A. M. Rao, P. Zhou, K.-A. Wang, G. T. Hager, J. M. Holden, Y. Wang, W.-T. Lee, X.-x. Bi, P. C. Eklund, D. S. Cornett, M. A. Duncan, and I. J. Amster, Science (New York, N.Y.) **259**, 955 (1993).

[221] P. Zhou, Z.-H. Dong, A. M. Rao, and P. C. Eklund, Chemical Physics Letters **211**, 337 (1993).

[222] F. D. Haldane, Physical Review Letters **61**, 2015 (1988).

[223] C. L. Kane and E. J. Mele, Physical Review Letters **95**, 226801 (2005).

[224] L. Fu, C. L. Kane, and E. J. Mele, Physical Review Letters **98**, 106803 (2007).

[225] M. König, S. Wiedmann, C. Brüne, A. Roth, H. Buhmann, L. W. Molenkamp, X.-L. Qi, and S.-C. Zhang, Science (New York, N.Y.) **318**, 766 (2007).

[226] H. Zhang, C.-X. Liu, X.-L. Qi, X. Dai, Z. Fang, and S.-C. Zhang, Nature Physics **5**, 438 (2009).

[227] M. Z. Hasan and C. L. Kane, Reviews of Modern Physics **82**, 3045 (2010).

[228] M. Reiher, Inorganic chemistry **41**, 6928 (2002).

[229] P. Roushan, J. Seo, C. V. Parker, Y. S. Hor, D. Hsieh, D. Qian, A. Richardella, M. Z. Hasan, R. J. Cava, and A. Yazdani, Nature **460**, 1106 (2009).

[230] L. A. Wray, S.-Y. Xu, Y. Xia, D. Hsieh, A. V. Fedorov, Y. S. Hor, R. J. Cava, A. Bansil, H. Lin, and M. Z. Hasan, Nature Physics **7**, 32 (2011).

[231] C.-Z. Chang, P. Wei, and J. S. Moodera, MRS Bulletin **39**, 867 (2014).

[232] L. Hernández López, *Electronic and magnetic properties of 2D metal-organic networks*, Dissertation, University of Zaragoza, Zaragoza (2023).

[233] P. Gütlich, Y. Garcia, and H. A. Goodwin, Chemical Society reviews **29**, 419 (2000).

[234] S. Rohlf, J. Grunwald, M. Kalläne, J. Kähler, F. Diekmann, S. Ossinger, B. Flöser, F. Tuczek, K. Rossnagel, and M. Gruber, The Journal of Physical Chemistry C **125**, 14105 (2021).

[235] J. A. Real, A. B. Gaspar, and M. C. Muñoz, Dalton transactions (Cambridge, England : 2003) , 2062 (2005).

[236] C. B. Viswanatha, J. Stöckl, B. Arnoldi, J. Knippertz, F. Haag, H. Paulsen, J. A. Wolny, M. Aeschlimann, V. Schünemann, and B. Stadtmüller, Impact of Cooperativity on the Spatial and Temporal Evolution of the Light-induced Spin-State Switching of the $Fe(phen)_2(SCN)_2$ Spin-Crossover Complex.

[237] E. Frantzeskakis, S. V. Ramankutty, N. de Jong, Y. K. Huang, Y. Pan, A. Tytarenko, M. Radovic, N. C. Plumb, M. Shi, A. Varykhalov, A. de Visser, E. van Heumen, and M. S. Golden, Physical Review X **7**, 10.1103/PhysRevX.7.041041 (2017).

[238] G. Emerson and S. Little, JAAVSO (1999).

[239] J. Canny, IEEE Transactions on Pattern Analysis and Machine Intelligence **PAMI-8**, 679 (1986).

[240] G.-Q. Wei and S. D. Ma, IEEE Transactions on Pattern Analysis and Machine Intelligence **16**, 469 (1994).

Ralf Hemm, Dipl. Physiker

Beruflicher Werdegang

08/2020 – heute **Promotion**

Experimentalphysik im Bereich Ultraschneller Phänomene an Oberflächen, RPTU Kaiserslautern-Landau

- Untersuchung molekularer Halbleiterschichtsysteme mittels Photoelektronenspektroskopie
- Aufbau, Wartung und Instandhaltung von Ultrahochvakuumanlagen und Lasersystemen zur Oberflächenanalytik

10/2018 – 04/2019 **Industriepraktikum**

Carl Zeiss Meditec AG, Oberkochen

- Entwicklung und Aufbau eines Prototyps zur spektralen Untersuchung von Tumorgewebe
- Kalibration und Auslieferung des Prototyps an internationale Kooperationspartner
- Schulung der Kooperationspartner im Umgang mit dem Prototyp

06/2018 – 08/2018 **wissenschaftliche Hilfskraft**

Photonik-Zentrum Kaiserslautern e.V., Kaiserslautern

- Aufbau eines Teststands für Photodioden

02/2015 – 02/2018 **wissenschaftliche Hilfskraft**

Arbeitsgruppe Aeschlimann, TU Kaiserslautern

- Weiterentwicklung von Messoftware zur Photoelektronenspektroskopie in Python und LabView

08/2014 – 12/2014 **wissenschaftliche Hilfskraft**

Fraunhofer ITWM, Kaiserslautern

- Testung und Fehleranalyse von Simulationssoftware

Ausbildung

08/2020 – heute	**Promotion in Physik** RPTU Kaiserslautern-Landau Titel der Dissertation: *„Structural Reorientation, Hybridization, and Excitonic States in Organic Molecules on Surfaces “*
10/2014 – 07/2020	**Diplomstudium der Physik** Technische Universität Kaiserslautern ▪ Schwerpunkte: Experimentelle Festkörperphysik, Laserphysik und nichtlineare Optik, organische Halbleiter, Vakuumphysik) ▪ Abschlussnote: Sehr gut (1,0)
09/2005 – 03/2014	**Schulausbildung** Sickingen-Gymnasium, Landstuhl Allgemeine Hochschulreife, Note sehr gut (1,0)

Publikationen

- S. Emmerich, S. Hedwig, B. Arnoldi, J. Stöckl, F. Haag, **R. Hemm**, M. Cinchetti, S. Mathias, B. Stadtmüller, and M. Aeschlimann. Ultrafast Charge-Transfer Exciton Dynamics in C60 Thin Films. The Journal of Physical Chemistry C, 124(43):23579–23587, 2020. doi: 10.1021/acs.jpcc.0c08011.

- W. Bennecke, A. Windischbacher, D. Schmitt, J. P. Bange, **R. Hemm**, C. S. Kern, G. D’Avino, X. Blase, D. Steil, S. Steil, M. Aeschlimann, B. Stadtmüller, M. Reutzel, P. Puschnig, G. S. M. Jansen, and S. Mathias. Disentangling the multiorbital contributions of excitons by photoemission exciton tomography. Nature communications, 15(1):1804, 2024. doi: 10.1038/s41467-024-45973-x.

Danksagung

Zum Schluss möchte ich mich noch bei allen Menschen bedanken, die mich während der Promotion unterstützt und begleitet haben.

Ein besonderer Dank geht an Prof. Benjamin Stadtmüller für die gute Betreuung während meiner Promotion. Du hast dir immer Zeit für meine Fragen genommen und mir wertvolle Anregungen in wissenschaftlichen Diskussionen gegeben. Deine lockere und ruhige Art hat ein sehr angenehmes Arbeitsklima geschaffen.

Ein weiterer Dank geht an Prof. Martin Aeschlimann für die Übernahme des Zweitgutachtens und die Möglichkeit Teil seiner Arbeitsgruppe zu sein. Danke für das Ermöglichen der Teilnahme an diversen Workshops und Konferenzen sowie eines Forschungsaufenthalts in Tucson.

Danke auch an Prof. Peter Puschnig und Dr. Andreas Windischbacher für das Beitragen von Theoriedaten zu dieser Arbeit und die Zeit, die ihr euch genommen habt die Fragen eines Experimentalphysikers zu beantworten.

Ich möchte mich herzlich bei der gesamten Arbeitsgruppe bedanken. Die Zusammenarbeit mit euch, unsere gemeinsamen Kaffeepausen, Schachpartien und das ein oder andere wohlverdiente Feierabendbier haben mir viel Freude bereitet und den Alltag bereichert.
Ein besonderer Dank gilt Tobias Eul für viele anregende Diskussionen und hilfreiche Beiträge bei wissenschaftlichen Fragestellungen.
Für die Unterstützung beim Betrieb der Laser und der dazugehörigen Laserstrecken danke ich Eugen Nosenko.
Ein besonderes Dankeschön geht an das Kammer-6-Team. Ohne euren Einsatz und eure Tatkraft wäre vieles nicht möglich gewesen. Ich danke meinen Supervisoren Florian Haag und Tony Yu – von euch konnte ich viel über Elektronenoptik, Lasertechnik und Datenverarbeitung lernen. Ihr habt euch stets Zeit für meine Fragen und Herausforderungen genommen, was ich sehr zu schätzen weiß.
Mein Dank gilt auch Martin Mitkov, Lukas Kau und Tony Yu für euren Einsatz an Kammer 6, eure gute Laune und die gemeinsame Zeit innerhalb und außerhalb der Universität. Diese Zeit habe ich sehr genossen.
Abschließend möchte ich mich bei Lu Lyu, Martin Mitkov, Tony Yu und Sebastian Hedwig für das Korrekturlesen dieser Arbeit bedanken. Eure Rückmeldungen und Hinweise waren mir eine große Hilfe.

Meinen Studienkollegen Andrea Nagel, Anna Friedel und Martin Will möchte ich danken für all die fröhlichen Abende abseits der Uni und die guten Lerngruppen während des Studiums. Ohne euch wäre es deutlich langweiliger gewesen.

Danke auch an meine Freunde Marco Hussong und Maximilian Vierling für die gute Freundschaft, Unterstützung und tollen Erinnerungen in den ganzen Jahren. Ich hoffe es werden

noch viele mehr!

Zum Schluss möchte ich meiner Familie danken, besonders meinen Eltern und meiner Partnerin Eva, für die Unterstützung bei meinen ganzen Vorhaben, Sorgen und Problemen. Ihr wart die ganzen Jahre immer für mich da und habt mir all dies erst ermöglicht.
Danke auch an meinen Hund Hilda für die aufmunternden Begrüßungen nach der Arbeit.

Fachbereich Physik

Rheinland-Pfälzische Technische
Universität Kaiserslautern Landau

Postfach 3049
67653 Kaiserslautern, Germany

www.physik.rptu.de/